



Virginia Commonwealth University
VCU Scholars Compass

Theses and Dissertations

Graduate School

2012

Hierarchical Templates and Their Application to Multimodal Porous Materials Fabrication

Bo Zhao
Virginia Commonwealth University

Follow this and additional works at: <https://scholarscompass.vcu.edu/etd>

 Part of the [Chemistry Commons](#)

© The Author

Downloaded from

<https://scholarscompass.vcu.edu/etd/303>

This Dissertation is brought to you for free and open access by the Graduate School at VCU Scholars Compass. It has been accepted for inclusion in Theses and Dissertations by an authorized administrator of VCU Scholars Compass. For more information, please contact libcompass@vcu.edu.

© Bo Zhao 2011
All Rights Reserved

**Hierarchical Templates and Their Application to Multimodal Porous Materials
Fabrication**

A dissertation submitted in partial fulfillment of the requirements for the degree of
Doctor of Philosophy at Virginia Commonwealth University.

by

Bo Zhao

Master of Science, Chinese Academy of Science, China, 2007

Bachelor of Science, Northeast Normal University, 2004

Director: Maryanne M. Collinson

Professor, Department of Chemistry

Virginia Commonwealth University

Richmond, Virginia

December, 2011

Acknowledgement

I am appreciative to my advisor Professor Maryanne M. Collinson for the opportunity to work in her research group and for her abundant help and invaluable assistance, support and guidance through my entire study process. This research project would not have been possible without her. I would like to thank my husband for his love and support during my graduate study. I would also like to thank my parents and friends, who always show understanding and encourage me. Dr. Dmitry Pestov is gratefully acknowledged for his instructions and help concerning instrumental analysis. I am also thankful to all my lab mates for useful discussions and encouragement during the whole study as well as the many hours of conversation, relaxation, and inspiration.

Table of Contents

	Page
Acknowledgements	iii
List of Figures	viii
List of Tables	xix
List of Abbreviations	xxi
Abstract	xxiv
Chapter 1: Introduction	1
1.1 Introduction	1
1.2 Overview of porous material	1
1.3 Introduction of templating methods	6
1.3.1 Hard templating	7
1.3.2 Soft templating	8
1.3.3 Sacrificial templating	9
1.3.4 Other templating	9
1.4 Introduction to hierarchical porous structure	10
1.5 Strategies of hierarchical porous structures fabrication	12
1.5.1 Dual templates	13
1.5.2 Porous material employment	16
1.5.3 Templating method combined with other chemical or physical method.....	17
1.5.4 Other strategies	19

1.6 Potential applications of hierarchical porous material	19
1.6.1 Catalysis and sensors	19
1.6.2 Separation	20
1.6.3 Drug delivery	22
1.6.4 Superhydrophobic surfaces and biomimic	22
1.6.5 Other potential applications	22
1.7 Summary of Objectives	23
Chapter 2: Characterization Techniques	25
2.1 Introduction	25
2.2 Transmission Electron Microscopy (TEM)	25
2.3 X-ray Photoelectron Microscopy (XPS)	27
2.4 Scanning Electron Microscopy (SEM)	28
2.5 Atomic Force Microscopy (AFM)	31
2.6 Nitrogen autosorb (BET)	33
2.7 Mercury intrusion	34
2.8 Electrochemical studies	35
2.8.1 Cyclic Voltammetry	36
2.8.2 Chronoamperometry/Chronopotentiometry	39
Chapter 3: Hierarchical templates	41
3.1 Introduction	41
3.2 Background and specific aim for hierarchical templates	41
3.3 Coupling mechanisms	44

3.4 Templates fabrication	47
3.4.1 Raspberry shaped templates	48
3.4.2 Strawberry shaped templates	48
3.5 Separation of hierarchical templates.....	52
3.6 Characterization	52
3.7 Packing of spheres.....	59
3.8 Advantages of the hierarchical templates	66
3.9 Introduction of the applications of the hierarchical templates	68
3.10 Conclusion	69
Chapter 4: Multimodal porous silica monolith	71
4.1 Introduction	71
4.2 Background and purpose for multimodal porous silica	71
4.3 Fabrication process	72
4.4 Characterizations and discussion	73
4.5 Conclusion	82
Chapter 5: Bimodal porous gold electrode	84
5.1 Introduction	84
5.2 Specific aim for bimodal porous gold film	84
5.3 Fabrication process	86
5.3.1 Synthesis of hierarchical porous gold electrodes by potentiostatic deposition.....	89
5.3.2 Synthesis of hierarchical porous gold electrodes by galvanostatic deposition.....	92
5.4 Characterizations of hierarchical porous gold electrodes.....	97

5.4.1 Surface characterization (XPS)	97
5.4.2 Surface area measurement	101
5.5 Electrochemical studies	104
5.5.1 FcCH ₂ OH in KCl	105
5.5.2 FcSH adsorbed redox system.....	113
5.5.3 Protein biofouling study	118
5.6 Conclusion	133
Chapter 6: Hollow sphere with well defined windows on the shell	135
6.1 Introduction.....	135
6.2 Background.....	135
6.3 Fabrication process	137
6.4 Characterizations	138
6.5 Discussion	149
6.6 Summary.....	153
Chapter 7: Conclusion and future directions	155
7.1 Conclusion	155
7.2 Future work	156
References	159
Vita	177

List of Figures

Chapter 1

- Figure 1.1** Transport mechanism through the pores 5
- Figure 1.2** Three pore categories and their transport mechanisms. 5
- Figure 1.3** Overview of the templating process used to prepare porous materials in various forms for different applications..... 6
- Figure 1.4** Schematic process of porous thin film fabrication via the hard templating method. First, pack the templates on a surface, and then impregnate the desired material into the empty spaces in the template packing. After template removal by post treatment, the structure that remains on the surface is a porous thin film. 8
- Figure 1.5** (A) An example of dual templating with polystyrene and silica beads, (B) 3D-assembled mesoporous silica colloids and their different internal structures, and (C) Mixed micellar phases of nonmiscible surfactants: mesoporous silica with bimodal pore size distribution via the nanocasting process. 15
- Figure 1.6** A dual templating approach to obtain trimodal hierarchical porous materials, (A) Hybrid material (silica: gray; polymer colloid: blue; BC micelle: dark blue; LC micelle: red). (B) Corresponding silica material after calcination or extraction of the three templates 16
- Figure 1.7** Example of lithography combined with templating (A to D) SEM images at different magnifications of hierarchically ordered mesoporous silica. A lattice of the macroporous framework skeleton is visible in (B) and (D). Pluronic F127 block copolymer was used as the structure-directing agent. 18

Figure 1.8 Hierarchically ordered macro-/mesoporous silica monolith for size-selective adsorption of proteins SDS-polyacrylamide gel electrophoresis analysis results of (a) the mixture solution containing BSA and cytochrome c before the adsorption, (b) the mixed solution after the adsorption by the sample hierarchically ordered porous silica monoliths without macropore entrance, and (c) hierarchically ordered porous silica monoliths with 50 nm size macropore entrance 21

Chapter 2

Figure 2.1 Schematic image of the components of a transmission electron microscope..... 26

Figure 2.2 X-ray photoelectron spectroscopy theoretical background. The incoming X-ray knocks out an inner layer electron; the kinetic of the leaving electron equals the X-ray energy minus the binding energy 28

Figure 2.3 Illustration of radiation and electrons generated when the electron beam bombards the sample surface 30

Figure 2.4 Illustration of the components of a scanning electron microscope 31

Figure 2.5 Illustration of the components of an atomic force microscope 33

Figure 2.6 A typical three electrode cell setup 36

Figure 2.7 Cyclic potential sweep 36

Figure 2.8 A typical cyclic voltammogram of gold working electrode in 1 mM FcCH₂OH/ 0.1 KCl solution at 0.1 V/s scan rate 37

Figure 2.9 Cyclic voltammogram for the reduction and subsequent reoxidation of an

electrochemically reversible adsorbed redox couple. 39

Chapter 3

Figure 3.1 The development process of multimodal porous material 41

Figure 3.2 Schematic images of hierarchical templates (a) raspberry-like template and (b) strawberry-like template 43

Figure 3.3 Reaction mechanisms (a) Carbodiimide--Amine (EDC) (b) Aldehyde--Amine (c) Epoxy-Amine. 45

Figure 3.4 Simplified reaction schemes for the preparation of (A) raspberry-like hierarchical spheres and (B) strawberry-like hierarchical spheres via carbodiimide chemistry and (C) raspberry-like hierarchical spheres via epoxy chemistry. 51

Figure 3.5 SEM images of raspberry-like hierarchical templates (A) 340 nm/29 nm templates, (B) 710 nm/29 nm templates (C) 710 nm/60 nm (D)1200 nm/29 nm (E) 1200 nm/60 nm prepared by coupling PS-NH₂ spheres with PS-Epoxy/Sulfate spheres. 53

Figure 3.6 SEM images of raspberry-like hierarchical templates (A) 450 nm/80 nm templates, (B) 1500 nm/110 nm templates prepared by coupling PS-COOH spheres with PS-NH₂ spheres. Insets are the blowups of each template 54

Figure 3.7 SEM images of 1500/110 nm “raspberry-like” templates (A, E), and “strawberry-like” templates synthesized at a Triton X-100 concentration of 0.05 wt % (B, F), 1 wt % (C, G), and 30 wt % (D, H). A → D show close-ups of the template spheres where E → H show that the spheres can be isolated and dispersed on a glass slide.....57

Figure 3.8 SEM images of a collection of 1500/110 nm raspberry (A) and strawberry templates (using 0.05 wt% (B), 1 wt% (C) and 10 wt% (D) triton X-100).....	58
Figure 3.9 SEM images for the 450/110 nm strawberry templates under high (A) and low (B) magnification	59
Figure 3.10 Overview of the different template packing approaches. (1) evaporate-induced self organization, (2) filtering by Buchner funnel, (3) slow speed spin coating (4) dip coating at an angle (5) self-assembly via electrostatics or chemical bonding (6) drop evaporation at an angle	63
Figure 3.11 Template packing mechanism: (a) evaporation approach, (b) slow speed spin coating approach, and (c) sedimentation approach.....	64
Figure 3.12 SEM images of template packing by different method (a) dip coating with an angle and (b) self-assembly by charge effect.	65
Figure 3.13 (A) (B) SEM images of 340/29 nm on glass slide by evaporation induced packing at an angle and (C) (D)1500/110 nm hierarchical spheres on polycarbonate membrane packed by Buchner funnel packing at two different magnifications..	68
Figure 3.14 Illustration of the type of 3D, 2D and 0D hierarchical porous structures that can be fabricated using hierarchical templates	69

Chapter 4

Figure 4.1 Simplified diagram of the cross-section of multimodal silica along with relevant parameters.	74
---	----

Figure 4.2 SEM image of the silica gel/hierarchical template (1500/110 nm) composite made by using TEOS/DETEOS silanes. The templates and the cavities are both present at the interface of a large crack made on purpose 75

Figure 4.3 SEM images for hierarchical porous silica prepared from the 1500/110 nm hierarchical spheres. Different magnifications are shown. 76

Figure 4.4 TEM images for hierarchical porous silica prepared from the 1500/110 nm hierarchical spheres. A, B are identical images showing neighboring pores. Dashed white circles have added to the image shown in B to aid in the visualization of the pores that resided in the upper layer. C) Single pore with windows (bright spots) clearly visible. D) Small macropores/windows at higher magnification. 77

Figure 4.5 N₂ adsorption-desorption isotherm for hierarchical porous silica prepared from the 1500/110 nm hierarchical spheres. Open circles are the adsorption branch; closed circles are the desorption branch. Inset: Pore size distribution obtained from the desorption branch. The lines have been added to guide the eye. 79

Figure 4.6 Mercury intrusion porosimetry data for hierarchical porous silica prepared from the 1500/110 nm hierarchical spheres. 80

Figure 4.7 Multimodal porous silica generated by using a stronger mechanical vacuum pump. (A) Top view, (B) side view, and (C) blowup of the porous silica surface. (D) Multimodal porous silica generated without calcination. 82

Chapter 5

Figure 5.1 Fabrication of bimodal porous gold film (A) clean gold slide, (B) templates packed on the gold slide, (C) gold deposited around the templates by electrodeposition, (D) is ½ layer porous gold film after the template removal, and (E) is 1½ layer porous gold film after template removal 87

Figure 5.2 Schematic illustration of the formation processes of (a) ordered porous gold film and (b) ordered bimodal porous gold film by electrodeposition. The metal complexes in the solution are reduced on the exposed conductive substrate 88

Figure 5.3 SEM images of hierarchical porous films fabricated using different plating solution (A) H_{AuCl₄} solution, (B) Recipe 1 solution, (C) Recipe 2 solution and (D) Commercial plating solution 89

Figure 5.4 CV of hierarchical templates coated gold electrode (A) in 0.3 M H_{AuCl₄} gold plating solution at 0.1 V/s; (B) Potentiostatic deposition curve of the gold slide at – 0.9 V. 91

Figure 5.5 SEM images for a bimodal macroporous gold film prepared from 1500/110 nm hierarchical templates at two different magnifications. (A) low magnification, (B) high magnification..... 92

Figure 5.6 Potential-time trace at the hierarchical sphere (1200/60 nm) modified gold electrode in the gold plating solution following the application of 0.1 microamps. 95

Figure 5.7 SEM images of porous gold electrodes prepared from (A, B) PS latex sphere, diameter 1200 nm, half-layer, (C, D) PS hierarchal latex sphere, 1200/60 nm, half-layer, and (F) PS hierarchal latex sphere, 1200/60 nm, one and one half-layer. (E): cartoon

depicting multilayer formation and the resultant windows that form.....	97
Figure 5.8 XPS survey spectra for (A) electrodeposited flat gold (B) macroporous gold (1/2 layer; dia = 1200 nm) and (C) hierarchical porous gold (1/2 layer; 1200/60 nm)	99
Figure 5.9 XPS spectra for electrodeposited flat gold, macroporous and hierarchical porous gold.	100
Figure 5.10 Cyclic voltammetric curves of UV cleaned hierarchical (1200/60 nm), macroporous (1200 nm), and bare gold electrode in 0.5 M H ₂ SO ₄ . Scan rate: 100 mV/s. Electrode area = 0.32 cm ²	103
Figure 5.11 Experimental setup for the multichannel electrochemistry studies. The reference electrode (Ag/AgCl) and auxiliary electrode (Pt gauze) are indicated by the arrows in the figure	105
Figure 5.12 CVs of 1 mM FcCH ₂ OH in 0.1 M KCl at bare flat gold, macroporous gold, hierarchical porous gold, and 1 ½ layer macroporous gold electrodes at different scan rates. (a) 0.01 V/s, (b) 0.1 V/s and (c) 1 V/s.....	107
Figure 5.13 Cyclic voltammograms of 1 mM ferrocene methanol in 0.1 M KCl at different scan rates. Bare flat gold (A), macroporous gold (B), hierarchical porous gold (C) and 1 ½ layer macroporous gold electrode (D) are shown.....	108
Figure 5.14 Plot of peak current (anodic) obtained versus square root of the scan rate. for 1 mM ferrocene methanol in 0.1 M KCl (CVs shown in Figure 5.15) The solid lines: linear regression lines. Only data acquired at slow scan rates (0.01 V/s to 0.1 V/s) were fit	109

Figure 5.15 CVs of FcCH ₂ OH on bare flat gold, macroporous gold, hierarchical porous gold, and 1 ½ layer macroporous gold electrodes in 0.1 M KCl at different scan rates (a) 0.01 V/s, (b) 0.1 V/s and (c) 1 V/s.	111
Figure 5.16 (A) Plot of charging current measured at E = 0.05 V versus scan rate for four different electrodes, bare flat gold (black), macroporous gold (red), hierarchical porous gold (blue), and 1 ½ layered macroporus gold (green). The solid lines are linear regression lines. (B) Simplified view of how charging current was measured: by measuring i and dividing by 2.	112
Figure 5.17 CVs of FcSH self-assembled gold electrodes in 1 M HClO ₄ at different scan rates. (A) Bare flat gold (B) Macroporous gold and (C) Hierarchical porous gold. Arrows show the direction of the scan	114
Figure 5.18 Plot of peak current vs. scan rate for FcSH assembled gold electrodes in 1M HClO ₄ . (A) Bare flat gold (B) Macroporous gold and (C) Hierarchical porous gold. The solid lines are linear regression lines.....	115
Figure 5.19 (a) CVs of 2 mM K ₃ Fe(CN) ₆ , 0.1 M KCl, PBS, 25 mM, pH 6.3 before and after the addition of BSA (final concentration 2 mg/mL) for (A) electrodeposited flat gold, (B) macroporous gold, and (C) hierarchical porous gold electrodes. Scan rate: 0.1 V/s	121
Figure 5.20 Plot of normalized CV current at the peak potential (0.18 V) before and after the addition of 2 mg/mL of BSA to solution. The current ratio was obtained by dividing the peak Faradaic current at t > 0 by the peak Faradaic current at t = 0.	122

Figure 5.21 Plot of ΔE_p before and after the addition of BSA (final concentration: 2 mg /mL). The cyclic voltammetric data is shown in Figure 5.18. 123

Figure 5.22 (a) CVs of 2 mM $K_3Fe(CN)_6$, 0.1 M KCl, PBS, 25 mM, pH 6.3 at 0.1 V/s before and after the addition of 2 mg/mL BSA at a large electrodeposited flat gold with the same surface area as bimodal porous gold electrodes ($\sim 0.32cm^2$). (b) Current change at the peak potential of the “before” CV versus time..... 124

Figure 5.23 CVs of 2 mM $K_3Fe(CN)_6$, 0.1 M KCl, and PBS, 25 mM, pH 6.3 at 0.1 V/s for gold electrodes soaked in BSA (2 mM concentration) solution for 48 h. (a) electrodeposited flat gold (b) macroporous gold (c) bimodal porous gold125

Figure 5.24 SEM images of (a) As-received bare flat gold (b) electrodeposited flat gold (c) macroporous gold, and (d) Hierarchical porous gold. 126

Figure 5.25 CV scans of bare flat and hierarchical porous gold in 1 mM cytochrome c in 25 mM PBS buffer (pH=7) at 0.1 V/s.127

Figure 5.26 XPS survey spectra of bare flat gold, deposited flat gold, macroporous gold and hierarchical porous gold after soaking in the $Fe(CN)_6^{3-}/KCl/PBS/BSA$ solution for (A) 0 min, (B) 10 min and (C) 60 min. XPS parameters were 150 eV pass energy, 3 scans, and 0.100 eV step size 129

Figure 5.27 Nitrogen (1s) peaks from XPS data of (A) bare flat gold, (B) deposited flat gold, (C) macroporous gold and (D) hierarchical porous gold after soaking in the $Fe(CN)_6^{3-}/KCl/PBS/BSA$ solution before and after addition of BSA XPS parameters were 50 eV pass energy, 10 scans, and 0.100 eV step size.130

Figure 5.28 Normalized N (1s) XPS before and after exposure to BSA. Solution:

Fe(CN)₆³⁻/ KCl/BSA/PBS for electrodeposited flat gold, macromorous gold, and hierarchical porous gold. Error bar corresponds to standard deviation N = 3..... 132

Figure 5.29 Possible mechanisms for the longer passivation process of bimodal porous gold electrode. 133

Chapter 6

Figure 6.1 (a) overview of the fabrication process. (b) simplified 2D images of the fabrication strategy 138

Figure 6.2 Schematic images for possible encapsulation styles (a) encasing the entire template, (b) encasing both the core and satellite spheres, and (c) coating only on the inner sphere 139

Figure 6.3 Silica sol coated 1500 nm/ 110 nm hierarchical templates dispersed on the PS-coated glass slide. (A), (B), and (C) are different magnifications. (D) a cartoon of the side view of the slide. 141

Figure 6.4 (A) SEM image for the porous capsule obtained by direct calcination after spin coating on a glass slide B) SEM image of porous capsules after releasing them back to solution and calcining..... 142

Figure 6.5 STEM images of hollow capsules at a large (A) and small (B) magnification. The arrows show the locations of the “buttons”..... 143

Figure 6.6 STEM images of broken porous capsules formed by redispersed in more acetic acid. (A) secondary electron image; (B) transmission electron image..... 143

Figure 6.7 (A) 3D scheme of the fabrication strategy; SEM images of (B) hierarchical

template (C) porous capsule (D) inner opening of the pores on the shell (E) TEM image of a broken shell. Inset is a blowup of the outer surface of the capsule. Scale bar is 100 nm.....	145
Figure 6.8 AFM images ($1.5 \times 1.5 \mu\text{m}^2$) of the 1500/110 nm COOH-NH ₂ hierarchical templates.	147
Figure 6.9 AFM images of the silica capsules fixed on a glass slide fabricated by spin coating on a glass slide without PS layer. (a) 10 μm scale range, (b) 20 μm scale range, (c) zoomed in image, and (d) AFM image of one window and its corresponding sectional.	148
Figure 6.10 Example of capsules that have different void sizes, window sizes and shell thicknesses.....	149
Figure 6.11 Asymmetric pore (left) versus cylindrical pores (right) in the shell wall.	151
Figure 6.12 SEM images of capsules fabricated by using a silica sol containing 300 μL DMDEOS/ 1000 μL TEOS instead of 1300 μL TEOS. (A), (B), and (C) are different magnifications of the hollow capsules.	153

Chapter 7

Figure 7.1 Functions that might be realized based on the hollow sphere structure (a) reaction container and encapsulated catalyst (b) size exclusive separation	158
--	-----

List of Tables

Table 3.1 Table of various hierarchical templates that have been fabricated and their features.	47
Table 5.1 Table of four types of gold plating solutions used for electrodeposition and deposited surfaces features.	88
Table 5.2 Table of surface area data obtained from CVs of flat gold, half-layer porous gold films made from 1200 nm amine PS templates and half-layer hierarchical porous gold film made from the 1200/60 nm hierarchical template.	103
Table 5.3 Peak Splitting for bare flat gold, macroporous gold, hierarchical porous gold and 1.5 layer macroporous gold at three scan rates for CVs in Figure 5.13.....	107
Table 5.4 Results from the regression analysis of anodic peak current vs. square root of scan rate for CVs of FcCH ₂ OH on bare flat gold, macroporous gold and hierarchical porous gold in KCl.....	110
Table 5.5 Results from the regression analysis of charging current vs. scan rate for FcCH ₂ OH on bare flat gold, macroporous gold and hierarchical porous gold in KCl	113
Table 5.6 Results from the regression analysis of peak current vs. scan rate for FcSH adsorbed on bare flat gold, macroporous gold and hierarchical porous gold in 1M HClO ₄	116
Table 5.7 Peak splitting (ΔE_p) for bare flat gold, macroporous gold and hierarchical porous gold at different scan rates.	117

Table 5.8 FWHM of the voltammetric curves obtained at 20 mV/s for FcSH assembled electrodes: bare flat gold, macroporous gold and hierarchical porous gold..... 117

Table 5.9 The integrated area under the anodic voltammetric peaks acquired at 20 mV/s for bare flat gold, macroporous gold and hierarchical porous gold in 1.0 M HClO₄. 118

List of Abbreviation

0D	Zero dimensional
2D	Two dimensional
3D	Three dimensional
AAO	Anodic Aluminum Oxide
AFM	Atomic force microscopy
AE	Auxiliary electrode
Ag/AgCl	Silver chloride coated silver wire
BET	Brunauer-Emmett-Teller surface area measurement
BSA	Bovine serum albumin
cmc	Critical micelle concentration
CP MAS	Cross polarization magic angle spinning
CV	Cyclic voltammetry or cyclic voltammogram
COOH-PS	Carboxyl group functionalized polystyrene sphere
DMTEOS	Dimethyldiethoxysilane
EDC	1-Ethyl-3-(3-dimethylaminopropyl) carbodiimide
EISA	Evaporation induced self assembly
ET	Electron transfer
Epoxy-PS	Epoxy group functionalized polystyrene sphere
F	Faraday constant

FcCH ₂ OH	Ferrocene methanol
GA	Geometric area
HPGE	Hierarchical porous gold electrode
I	Current
IUPAC	International Union of Pure and Applied Chemistry
LBL	Layer by layer
LC	Liquid crystalline
MC%	Mobil composition of matter
MCM-41	Mobil Crystalline Materials
MMS	Mesoporous molecular sieve
MOF	Metal-organic framework
MOPS	3-(N-morpholino)propanesulfonic acid
NH ₂ -PS	Amine functionalized polystyrene sphere
NHS	N-Hydroxy-succinimide
[Ru(NH ₃) ₆] ³⁺	Hexaammineruthenium (III) ion
PMMA	Poly(methyl methacrylate)
PBS	Phosphate buffered saline
PS	Polystyrene
Q	Coulomb
RE	Reference electrode
rpm	Rotation per minute
SA	Surface area

SAM	Self assembled monolayer
SBA-n	Santa Barbara USA
SEM	Scanning electron microscopy
STEM	Scanning transmission electron microscopy
-SH	Thiol group
TEM	Transmission electron microscopy
TEOS	Tetraethoxysilane
TMOS	Tetramethoxysilane
Triton X-100	$C_{14}H_{22}O(C_2H_4O)_n$
UV	Ultra-violet
UV-Vis	Ultraviolet visible spectrometry
v	Scan rate
WE	Working electrode
XPS	X-ray photoelectron spectroscopy

Abstract

**HIERARCHICAL TEMPLATES AND THEIR APPLICATION TO MAKING
MULTIMODAL POROUS STRUCTURES FOR DIFFERENT APPLICATIONS**

By Bo Zhao, PhD

A Dissertation submitted in partial fulfillment of the requirements for the degree of
Doctor in Philosophy at Virginia Commonwealth University.

Virginia Commonwealth University, 2011

Major Director: Maryanne M. Collinson,

Professor, Department of Chemistry

Hierarchical materials offer great promise for high-performance sensors and catalysis carriers. Well-defined hierarchically porous materials are promising candidates for a wide range of applications relating to biosensors, separations, drug delivery, surface-enhanced Raman scattering (SERS), etc. Research on synthetic methodologies is expanding. However, fabrication of hierarchical porous structures with tunable pore dimension and shape, controllable pore distribution and interconnectivity is still a challenging task in materials science. One of the main tasks of this work is to establish a facile and reliable approach of making well-defined hierarchically porous materials. Then, based on those multimodal porous structures, different functions and applications can be realized.

This work utilizes a direct hard templating method to obtain hierarchical porous structures with a well-defined bimodal distribution of the pores based on hierarchical templates. The hierarchical templates were prepared by synthetically joining appropriately functionalized commercially available polystyrene (PS) latex spheres together. Two different coupling reactions were used to form the hierarchical templates: carbodiimide-assisted coupling of COOH groups with NH₂ groups and base-assisted coupling of epoxy groups with NH₂ groups. Two different morphologies of templates, "raspberry-like" and "strawberry-like" were made. The template can be defined by the sizes of both the "core" and the "satellite" spheres, and altering the coverage of "satellites" on the "core". The main advantage of this strategy is the tailorability of the size and shape of the hierarchical templates, which allows an easy and independent adjustment to the multiporosity of the material structure design. Also, the monodispersed hierarchical templates are constructed of only one material, can be isolated, and can be assembled using standard template packing procedures that have been used for unimodal porous material fabrication described in published literature.

Based on the predefined monodispersed hierarchical templates, multimodal porous silica, bimodal porous gold film and porous capsules were fabricated in this work as representative 3D, 2D, and 0D hierarchical porous structures, respectively. Because the template was predefined as one whole body, the connectivity between the big pores and small pores is guaranteed. The way the templates are packed together on a surface also ensures connections between each "template-shaped pore cluster". The uniform interconnectivity and ordered arrangement among the pores allows the different modals

of pores to communicate with each other. The different hierarchical porous materials made in this work were characterized with SEM, TEM, AFM, XPS, STEM, gas adsorption, and mercury intrusion porosity. The results indicate that the multimodal porous materials can be successfully fabricated using predefined hierarchical templates. The different arrangement (3D, 2D, 0D) of those templates and the independent tailorability of the pore sizes provide more flexibility and control on the hierarchical porous material fabrication.

The main parts of this work are as follows: (1) Fabrication and characterization of morphology controllable hierarchical templates (2) Fabrication and characterization of various multimodal porous structures of different materials based on the obtained templates (3) Study of the application of hierarchical porous gold electrode obtained and (4) The comparison between conventional porous structures and hierarchical porous structures.

Chapter 1 Introduction

1.1 Introduction

This dissertation work aims to establish a facile and flexible approach to prepare well-defined hierarchical porous materials based on hard templating. New preparation methods are essential for the utilization of various hierarchical porous materials for a range of applications that include sensors, catalysts, and renewable energy and storage devices. In this chapter, an overview of the history of porous materials, their properties and different approaches to make porous materials will be discussed. This overview is followed by the recent advances in the fabrication and applications of hierarchical porous materials.

1.2 Overview of inorganic porous materials

The field of porous inorganic materials has a long history in both natural and man-made materials. Porous materials are ubiquitous in our daily life due to their porous structure and properties such as low density, permeability, thermal insulation, separation, adsorption, and sound absorption.¹ Originally porous materials were those that had random pore sizes and shape distributions. As people's knowledge of porous materials expanded, porous materials with a tunable pore size and a narrow pore size distribution (called unimodal pores) or an ordered porous structure were developed to better meet application requirements.^{2,3} Unimodal pores, for example, can exclude some molecules due to the differences in molecule size and shape or can help to distinguish molecules based on size differences as they will result in a different diffusion rate (size selectivity⁴/selective permeability^{5,6}). Materials containing ordered interconnected pores with a

narrow pore size distribution are needed for applications that require uniform diffusion such as shape-selective catalysis or the separation of gas and liquid mixtures based on molecular size. In addition, the high specific surface areas and rich surface chemistry provided by porous materials can result in the development of high efficiency catalysts and their supporting structures for catalysis applications.⁷

There are three classes of porous materials as defined by IUPAC: microporous ($d < 2$ nm), mesoporous ($2 \text{ nm} < d < 50 \text{ nm}$), and macroporous ($d > 50 \text{ nm}$).⁸ Each type of pore has a characteristic diffusion profile.

(1) Microporous materials: the small size of the micropores is defined by molecular structures or macromolecular templates. Typical examples are zeolites and molecular sieves. These materials are mostly used for gas phase applications, such as gas storage^{9,10}, purification^{11,12}, separation¹², or gas phase catalysis¹³. For a liquid-phase application, the transport of molecules and ions in the micropore network is driven by activated diffusion (molecules and ions move against the concentration gradient due to the interaction between the molecules and the pore wall materials). The high surface area that results from the microporosity is compromised by slow diffusion, which limits the fast and full exposure of the inner surface area to the liquid phase. Metal-organic framework (MOF) materials, also designed on molecular level, consist of a framework supporting a regular, porous structure.¹⁴ Most MOF materials belong under the ‘microporous’ category, while some extend into the ‘mesoporous’ material range. MOF materials possess unique physical and chemical characteristics and their high surface area can provide a greater storage volume compared to other porous materials.^{15,16} A molecular imprinted matrix is

another type of microporous material according to the definition of microporous material. Due to the molecule (biomolecules or other macromolecules) size, the materials composed of imprinted molecule cavities fall under the microporous material category.^{17,18} Based on the conformation, functional groups and size of the analyte molecule, the cavities formed by molecular imprinting can be used for molecule recognition, which is an important strategy in sensor design.¹⁹

(2) Mesoporous materials: the mesopores can be fabricated based on soft templating strategies like using micelles, or by templating mesoporous materials like SBA-series, MCM-series, Anodic aluminum oxide (AAO), etc. that have mesopores.²⁰⁻²³ Typical mesoporous materials include some forms of silica and alumina that have similarly-sized fine mesopores. Applications of mesoporous materials include catalysis, sorption, drug delivery, gas sensing, imaging and ion exchange.^{3,24} The diffusion style through mesopores is described by Knudsen diffusion, a means of diffusion that occurs in a narrow pore (2–50 nm) because molecules frequently collide with the pore wall.²⁵ Surface diffusion may contribute to the flow when a concentration gradient exists.²⁶ Ordered mesoporous materials, which have an open pore structure, uniform pore size, and large pore volume, high surface areas and shape-selectivity for guest molecules, are promising in many applications.^{27,28} Compared with microporous materials, mesoporous materials have bigger pores and more accessible inner pores. However, due to pore size limitations they still exhibit considerable resistance to diffusion, especially over long distances.

(3) Macroporous materials: Macroporous materials are made based on hard templating

strategies, like using particle templates or bulk templates.^{29,30} Hard templating is the method most often used to prepare uniform macroporous materials due to the rigid support and uniform size distribution provided by the hard template. The microemulsion method has also been reported for fabricating macroporous materials.^{31,32} Three-dimensional (3D) macroporous materials made via colloidal crystal template packing (the so-called inverse opals) are a typical example.³³ Polymer beads and other colloidal latexes are the mostly widely used hard templates to make a 3D close-packed structure for opal and inverse opal porous material fabrication.³⁴ Bulk templates like biomaterials^{35,36} and porous matrices³⁷ can also be employed as templates for macroporous material fabrication. Diffusion through macropores is bulk diffusion, and when a gradient exists, the flow in the macropores is viscous flow.²⁶ Compared with mesoporous and microporous materials, macroporous materials have relatively low surface area, but significantly improved diffusion rate. Macropores are also used as storage reservoirs.³⁸

The transport mechanism and characteristic features are summarized in Figure 1.1 and Figure 1.2.

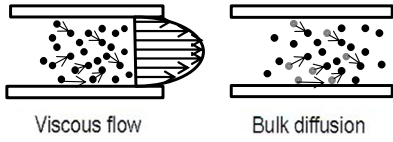
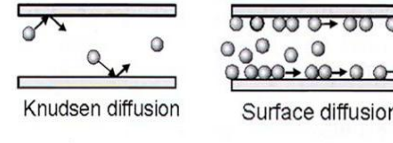
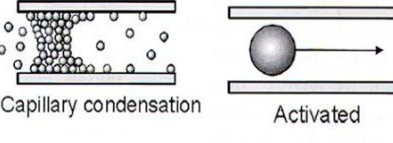
Diffusion in macropore	 <p>Viscous flow Bulk diffusion</p>	<p>Fick's Law</p> $J = -D \frac{\partial \phi}{\partial x}$ <p>J is the "diffusion flux" per unit area per unit time; D is the diffusion coefficient; Φ is concentration; x is the position.</p>
Diffusion in mesopore	 <p>Knudsen diffusion Surface diffusion</p>	<p>Knudsen diffusion</p> $D_s(c) = \lim_{t \rightarrow \infty} \frac{1}{6Nt} \left\langle \sum_{i=1}^N \mathbf{r}_i(t) - \mathbf{r}_i(0) ^2 \right\rangle$ <p>D_s is the self-diffusion coefficient, which depends on the concentration c, t is time, N is the total number of particles in the system, and \mathbf{r}_i is the position vector of particle i.</p>
Diffusion in micropore	 <p>Capillary condensation Activated</p>	<p>Capillary condensation</p> $\ln \frac{P_v}{P_{sat}} = -\frac{2H\gamma V_l}{RT}$ <p>P_v is equilibrium vapor pressure; P_{sat} is saturation vapor pressure; H is mean curvature of meniscus; γ is liquid/vapor surface tension; V_l is liquid molar volume; R is ideal gas constant; T is temperature.</p>

Figure 1.1 Transport mechanisms through pores (Reprinted from ref 26 with kind permission from Wiley-VCH. Copyright 2005).²⁶

Microporous d < 2 nm	Pore size comparable to the molecules. Activated transport dominates.
Mesoporous 2 < d < 50 nm	Same order or smaller than the mean free path length. Knudsen diffusion and surface diffusion. Multilayer adsorption and capillary condensation may contribute.
Macroporous d > 50 nm	Larger than typical mean free path length of typical fluid. Bulk diffusion and viscous flow.

Figure 1.2 Three categories of porous materials and their transport mechanisms.²⁶

1.3 Introduction of templating methods

Numerous approaches for the synthesis of porous materials have been explored in the past decades. Porous inorganic materials can be made using methods like templating, dealloying, spray drying, and sol-gel processing etc. Among those, template based synthesis strategies are the most popular due to their flexibility and ability to precisely control pore size and shape.³⁹

The templating method uses templates to direct reactions to a certain region.^{34,40,41} Templates are used to control, influence and modify material morphology and pore size to tune the properties of the porous material accordingly. A brief overview of the diverse set of porous materials developed using the templating method is shown in Figure 1.3. Different structures can be obtained by changing the templates and/or assembly, while chemically different materials can be fabricated by changing the components.³⁴ The flexibility provided by templating methodology provides a means to improve material performance for different applications.

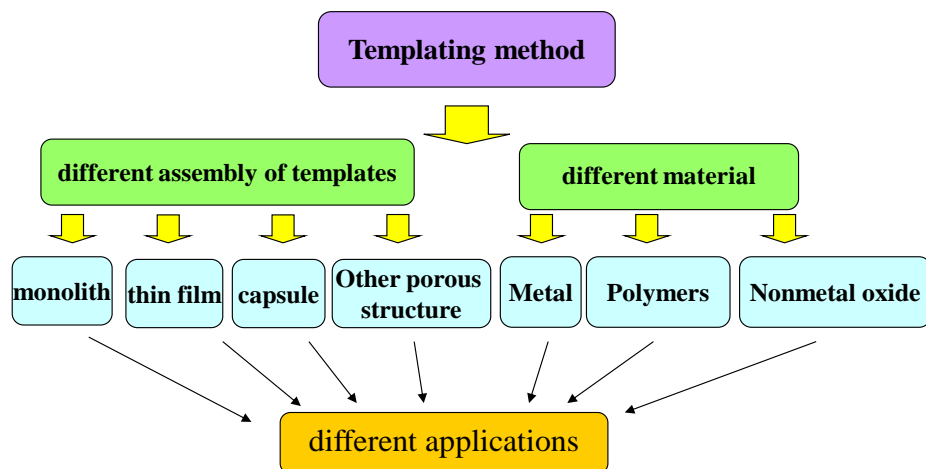


Figure 1.3 Overview of the templating process used to prepare porous materials in various forms for different applications.

The templating method can be subdivided into four categories: hard templating, soft templating, sacrificial templating, and others based on the type of template.

1.3.1 Hard templating

Hard templating methods are suitable for the synthesis of a broad range of materials, including porous structures, quantum dots, wires, rods, and tubes, etc. This method can also be used to make various novel porous structures that are difficult to fabricate by the soft template method. Literally anything solid could be used as a hard template.⁴² In general, the individual templates are first assembled in a certain arrangement on a surface, like close packing into a 2D or 3D structure. The template packing is then impregnated with the desired precursor, e.g., a silica or titania sol. Upon template removal, an array of pores that are exactly the inverse structure of the template packing is produced.^{43,44} An example of the hard templating process is shown in Figure 1.4. For porous structures that have long-range order, the template can be a porous material itself such as anodic aluminum oxide (AAO) or Zeolite, membranes, MCM (Mobil Crystalline Materials), SBA-n (Santa Barbara USA).³⁷ For example, microporous zeolites and ordered mesoporous silicas (*e.g.*, MCM-48, SBA-15, and SBA-16) have been used to fabricate microporous and mesoporous carbons, respectively.^{27,28,45-48} Considerable efforts have also been focused on employing uniform templates and creating the complementary structure for accurate control over the composition, pore size, volume, surface area and connectivity.⁴⁹⁻⁵² Examples of hard templates that are routinely used to form porous materials include colloidal spheres,^{34,53,54} opals and an assortment of biostructures including diatoms, bacteria, viruses, and parts of insects.⁵⁵ The template removal schemes

are versatile, for instance, by acid leaching, base leaching, calcination, plasma etching, etc. depending on the nature of the hard template.

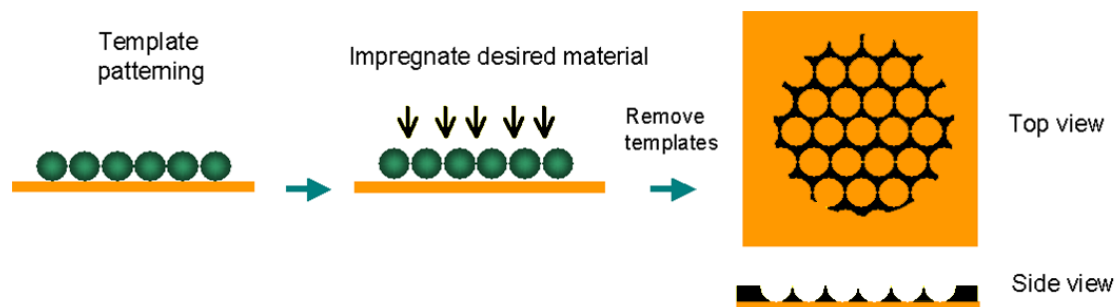


Figure 1.4 Schematic process of porous thin film fabrication via the hard templating method. First, pack the templates on a surface, and then impregnate the desired material into the empty spaces in the template packing. After template removal by post treatment, the structure that remains on the surface is a porous thin film.

1.3.2 Soft templating

Soft templating primarily uses “soft templates” to restrict and direct the growth of the desired material. These “soft templates” include reverse micelles, micro-emulsions, block copolymers, surfactants, biomacromolecules, organic-based molecules, vesicles, lyotropic liquid crystals (LLCs), ionic liquids etc.^{22,56,57} The templating structures include lamellar, hexagonal, cubic, etc.. Soft templating is widely employed to fabricate mesoporous materials. The size of the pores can be tuned by changing the concentration of the surfactant. Compared with other templating methods, soft templating has many advantages in the preparation of hollow nanostructures.⁵⁸ The drawback is that most of these fabrication procedures require calcination to completely remove the templates, which limits applications to those materials that cannot stand high temperatures. In many cases, it is also difficult to use soft templating to control the pore size uniformity and to scale up soft templating methods.

1.3.3 Sacrificial templating

Sacrificial templates are templates that are removed during which the porous matrix forms. Examples include inorganic salts, ice crystals⁵⁹, etc. Those templates are either consumed by the interaction between the template and desired material, or dissolved during the formation of the desired porous material. Galvanic replacement reaction is one effective strategy for sacrificial templating. It has been used to produce hollow nanostructures of noble metals.⁶⁰ A replacement reaction happens between the template metal and the desired metal and is driven by the electrical potential between those two metals. The template metal primarily acts as the reducing agent (anode) and is oxidized by the cations of the other metal acting as the oxidizing agent (cathode). After the reaction, the sacrificial template is consumed and the desired metal is formed based on the original shape of the template. This method is normally used to fabricate hollow capsules, tubes or other individual hollow structures.⁶¹ The size and shape of the interior void are mainly determined by the size and shape of the sacrificial template. Due to the sacrificial growth mechanism, this method is not very effective for the preparation of porous monoliths or thin films.

1.3.4 Other templating methods

Air bubbles produced by sonication, surfactants in the solution or gas bubbles generated during a reaction have also be used as “templates” to prepare porous materials.⁶² Recently, Ostwald ripening has been employed to fabricate hollow structures by a one-step self-templating method.⁶³ Basically, nanoparticles are introduced into a hollow composite structure composed of nanoparticles and templates, and then Ostwald

ripening in confined microspace will result in a shell structure along the original hollow structure. According to IUPAC's definition, Ostwald ripening is “Dissolution of small crystals or sol particles and the redeposition of the dissolved species on the surfaces of larger crystals or sol particles.”⁶³ This process is driven by chemical potential differences among different sized particles. The average radius of the particles $\langle R \rangle$, grows as follows:

$$\langle R \rangle^3 - \langle R \rangle_0^3 = \frac{8\gamma c_\infty v^2 D}{9R_g T} t$$

Where $\langle R \rangle$ = average radius of all the particles; γ = particle surface tension or surface energy; c_∞ = solubility of the particle material; v = molar volume of the particle material; D = diffusion coefficient of the particle material; R_g = ideal gas constant; T = absolute temperature and t = time.⁶⁵

In summary, it can be seen that for all the different templating methods used, it is crucial that monodispersed, uniform templates be used and good packing (assembly, or distribution) of the templates are employed to control the porosity and morphology of the final porous structure. This is the most important foundation for the fabrication of high quality porous materials.

1.4 Introduction to hierarchical porous materials

Hierarchical porous materials³⁹ are defined as materials that contain a porous structure that consists of interconnected pores on different length scales (i.e., macropore and mesopore). Most of the “hierarchical porous structures” found in natural environments consist of randomly distributed pores of various size and shape, and sponge-like morphologies. There is no clear distinction of each level of multiporosity; neither does

each level of porosity necessarily and effectively communicate with the other levels. Strictly speaking, this type of material doesn't have controlled function based on multimodal porosity and morphology of the material; thus, it is not exactly a hierarchical porous material, but more of a natural porous material.

Porous materials that have been developed range from those with randomly distributed pore size and shape to unimodal ordered porous material and most recently to hierarchically structured porous materials. Conventional porous materials frequently have disordered and randomly distributed pores, including such examples as alumina, silica, and activated carbon which have been used as catalysts, catalyst supports, and adsorbents. During the evolution from traditional porous materials to unimodal porous materials, many unique properties and functions were realized as scientists obtained more control over porous material design. For example, the inverse opals made based on the colloidal templates have special optical properties relevant to their pore sizes.⁶⁶ Highly ordered mesoporous carbon has been used for supercapacitors and in fuel cell and sensing applications.⁶⁷⁻⁶⁹ Based on recent knowledge and new synthesis techniques, the hierarchical combination of the three types of porous materials has begun to get people's attention. Many researchers have been interested in the synthesis of hierarchically porous materials,^{70,71} while others on the application of such materials. Developments in this hierarchical porous material field have lead to improved material function and new applications.⁷²⁻⁷⁹

Multimodal porous material (hierarchical porous material) can ideally have more than one function by effectively arranging different porosities in one material. Studies on

hierarchical meso/macroporous materials have been investigated the most.⁸⁰⁻⁸² The prime aim has been to couple in a single material the different features associated with micropores and/or mesopores, specifically high surface area provided by the micropores and the improved access and transport resulting from the macropores. The multi-level architectures can provide unique properties or features to the structure, such as wettability and increased surface area, molecule or ion diffusion ability, etc. Previous research in this field designed and utilized these materials for superhydrophobicity and catalysis.⁸³⁻⁸⁵ Hierarchically porous materials have many special applications in other fields as well. For example, in catalysis, strategies to enhance catalyst effectiveness involve the synthesis of materials with high surface area and short diffusion length.⁷⁹ To maximize permeated flux through the porous structure without losing the critically needed interfacial area, two different sized pores can be combined hierarchically; big pores to improve diffusion and small pores to increase surface area. In this way, ideally more catalyst surface area will be available to the reactants in a relatively shorter time, which can help increase the catalytic efficiency. Another example is the application of stationary phases materials in chromatography, big pores facilitate fast diffusion to achieve short retention time, while smaller pores improve the separation. Different applications can be expected, depending on how the pores of different length scales can be arranged and how they communicate with each other.

1.5 Strategies for hierarchical porous material fabrication

Hierarchical porous materials can be prepared via "bottom-up" self-assembly techniques, "top-down" methods, or a combination of both. "Bottom-up" methods are

often combined with templating methods in order to define the sizes of the multimodal pores, while “top-down” methods are more physical processes, such as lithography, or involve chemical treatments, such as etching. Soft lithography and other lithographic methods (e-beam lithography, AFM lithography, photolithography, etc.) are additional ways to make those materials, but they are mostly limited by the 2D design (not 3D). Some are also expensive and require high quality synthesis conditions.⁸⁶⁻⁸⁸ As a result, the “bottom-up” method combined with templating is still the most widely used strategy to make hierarchical porous materials. Recent studies carried out on the fabrication, characterization, and applications of the hierarchically hollow structures with designed size, shape, composition and function are discussed below in different categories.

1.5.1 Dual templates

Hierarchically bi-modal and tri-modal porous structures can be fabricated by combining two different templating methods or by using a secondary template of the same type, i.e., combining a hard template with soft template,⁸⁹ a soft template with a sacrificial template, two different hard templates,⁹⁰ or two different soft templates of different length scales, etc. .^{71,91} Figure 1.5 (A) is an example of a dual hard templating approach that has been used to form bimodal porous carbon. The macropores are generated by templating polystyrene spheres, while the mesopores are generated by the spaces among the small silica beads that were used to fill in the gaps between the polystyrene spheres. After that, the carbon precursor was introduced into the spaces generated by silica beads, and then silica was removed to form the carbon matrix as shown in the lower images. Figure 1.5 (B) is an example of a combined hard templating and soft templating method that has

been used to form porous silica bead arrays. A polymer-based inverse opal produced spherical cavities in which the cooperative assembly of silica precursors and the triblock copolymer mesophase takes place. After template removal, a porous silica array was obtained. Figure 1.5 (C) is an example of dual soft templating method. The highly organized mesoporous silica monoliths were prepared by two soft templates: fluorinated nonionic surfactants and micelles of two hydrocarbon block copolymers. The two soft templates did not influence each other, but template individually to form bimodal pores. In the dual templating method, the distribution in size, shape, and organization of the pores is directly related to the templates and their assembly. The key issues for the synthesis of hierarchical porous materials are how to template the pores and order and shape them to realize their interconnectivity and multiporosity as needed to further carry out the desired function. The complex template, for example, can be a surfactant template in combination with a colloidal-crystal template. It can also be a surfactant template combined with polymer foam, bio-cellulose, emulsion, inorganic salt, or ice crystal templates.⁷¹ Various bimodal meso–macroporous materials with interconnected pore channels have been prepared using this strategy including carbon, zirconia, and titania, as well as silica monolith with interconnected channels. Most of the hierarchical porous materials fabricated by templating methods reported up to now involved soft template methods, for example, micelle, vesicle, liquid drops by Layer by layer (LBL), emulsion-assisted technology or self-assembly.⁹²⁻⁹⁸ These methods are a good way to prepare particles or hollow spheres, but not necessarily porous monoliths, thin films or other large-dimension structures due to the difficulty of ordered assembly of templates

over a long range.

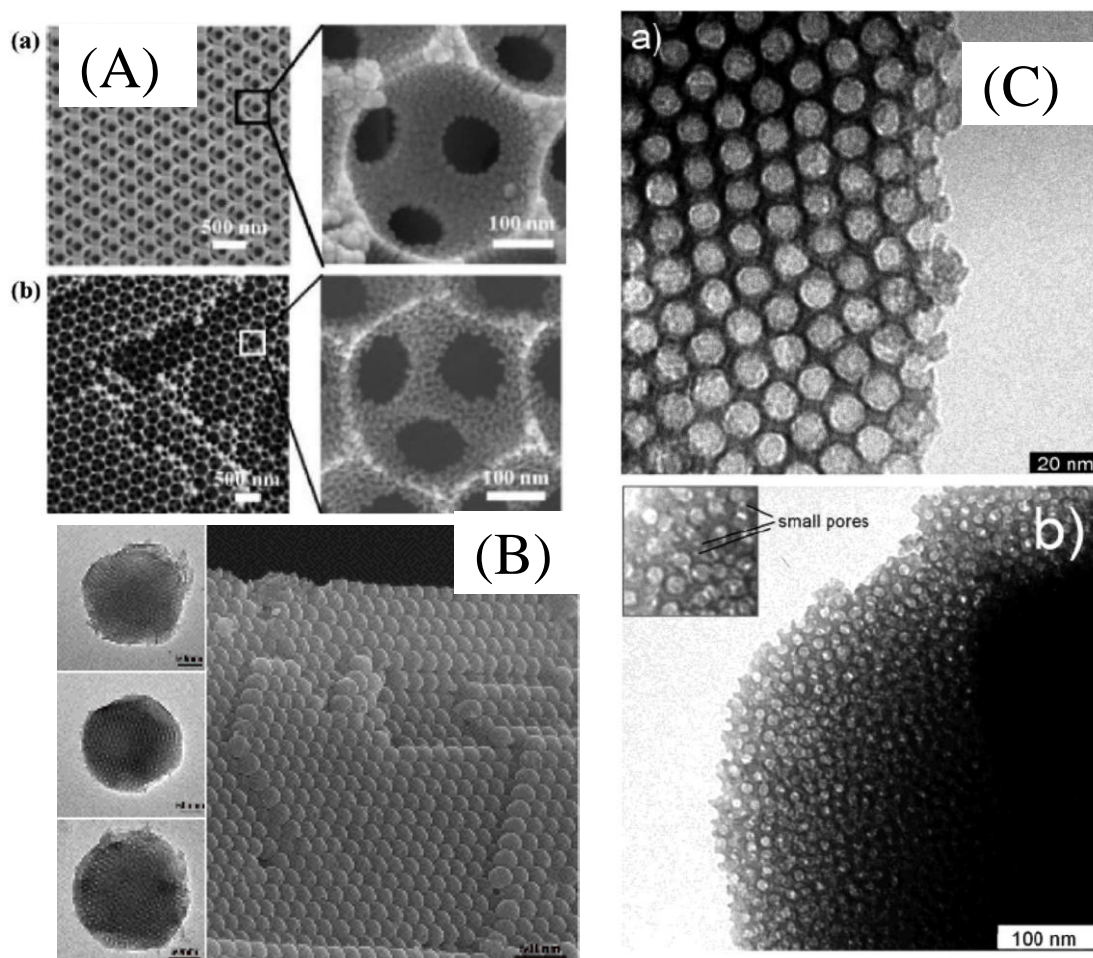


Figure 1.5 (A) An example of dual templating with polystyrene and silica beads,⁸⁸ (B) 3D-assembled mesoporous silica colloids and their different internal structures,⁹⁹ and (C) Mixed micellar phases of nonmiscible surfactants: mesoporous silica with bimodal pore size distribution via the nanocasting process.¹⁰⁰ Reprinted from ref 88, 99, 100 with kind permission from Wiley and American Chemical Society. Copyright 2004, copyright 2004 and copyright 2007.

A drawback of the dual templating strategy is that it is hard to control the interconnectivity between the different levels of porosity. Most of the methods result in two or more modals of pores in the structure that don't interact with each other, an

example of which is shown in Figure 1.6. In this figure, three modal of pores in a silica material are shown: large spherical pores generated by polymer colloid templates, small spherical pores and wire-shaped pores generated by two types of micelles, block copolymer and ionic liquid, respectively. The three types of pores are randomly distributed in the silica matrix; they are not interconnected, which limits the effective communication among each level of porosity.

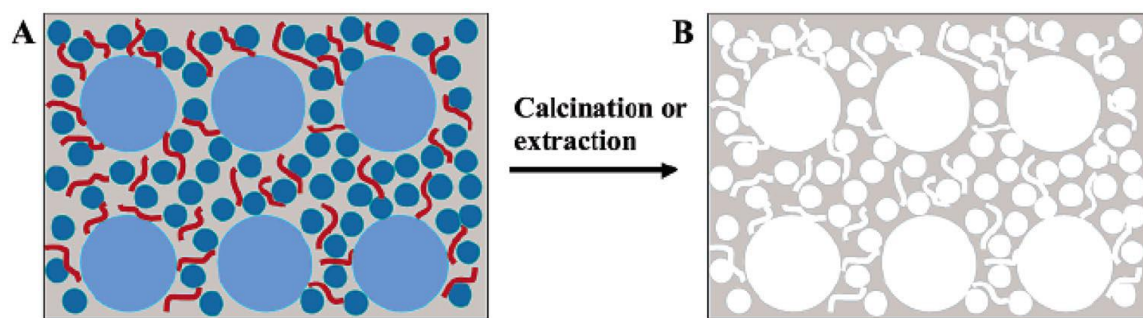


Figure 1.6 A dual templating approach to obtain trimodal hierarchical porous materials, (A) Hybrid material (silica: gray; polymer colloid: blue; BC micelle: dark blue; LC micelle: red). (B) Corresponding silica material after calcination or extraction of the three templates (Reprinted from ref 101 with kind permission from American Chemical Society. Copyright 2006.)¹⁰¹

1.5.2 Porous material employment

This strategy is to use existing unimodal porous material as building blocks to assemble multimodal porous materials as shown in Figure 1.5 (B). Mesoporous particles have the mesoporosity in themselves, and their particle size can be used to generate secondary pores.^{99,102}

1.5.3 Templating method combined with other chemical or physical methods

Sol-Gel method combined with templating

One commonly used method to prepare porous materials (typically micro- and mesopore) in forms such as films, powders, and monoliths utilizes the sol-gel process.¹⁰³ When merged with templating, materials with tailorable multimodal pore sizes and specific morphologies and characteristics can be easily prepared.¹⁰⁴ The sol-gel process can be used to synthesize metal- and semimetal oxides using metal- or semi-metal alkoxides as precursors, with silica being the most extensively studied material.¹⁰⁵ The sol-gel method starts with the hydrolysis of precursors catalyzed by acid or base, and leads to the formation of Si-O-Si through polycondensation to gradually form a 3D network. The method is based on the sol-gel phase transformation. A sol will gradually polymerize (condense) to form a wet gel. Further condensation will result in an inorganic metal oxide material such as glass, polycrystals or a dry gel.¹⁰⁵

Sol-gel methods are advantageous in their versatility, cheapness and the fine control of the product's chemical composition.^{106,107} Various dopants, such as dyes, molecules and rare earth elements, can be introduced into the sol and dispersed uniformly throughout the whole material.¹⁰⁸⁻¹¹⁰ Organically modified silanes with various functional groups can be used to modify the sol-gel framework and provide binding sites for molecules, proteins,^{110,111} etc. The porosity of the material depends on the size and shape of the particles formed by condensation, the organization of these particles to form a gel, and the gelation process.¹¹² When using an organoalkoxysilane, phase separation might also lead to the formation of pores of controlled size.^{113,114}

Lithography combined with templating

Lithography includes photolithography, E-beam lithography, Extreme-UV lithography, dip pen nanolithography, soft lithography, etc. The basic principal is a sculpture based on a certain pattern defined by masks or predefined shapes. Figure 1.7 is an example of templating combined with soft lithography. Porous silica with three-dimensional patterns over multiple length scales were prepared by combining micromolding, polystyrene sphere templating, and cooperative assembly of silica sol with triblock copolymers.⁹¹

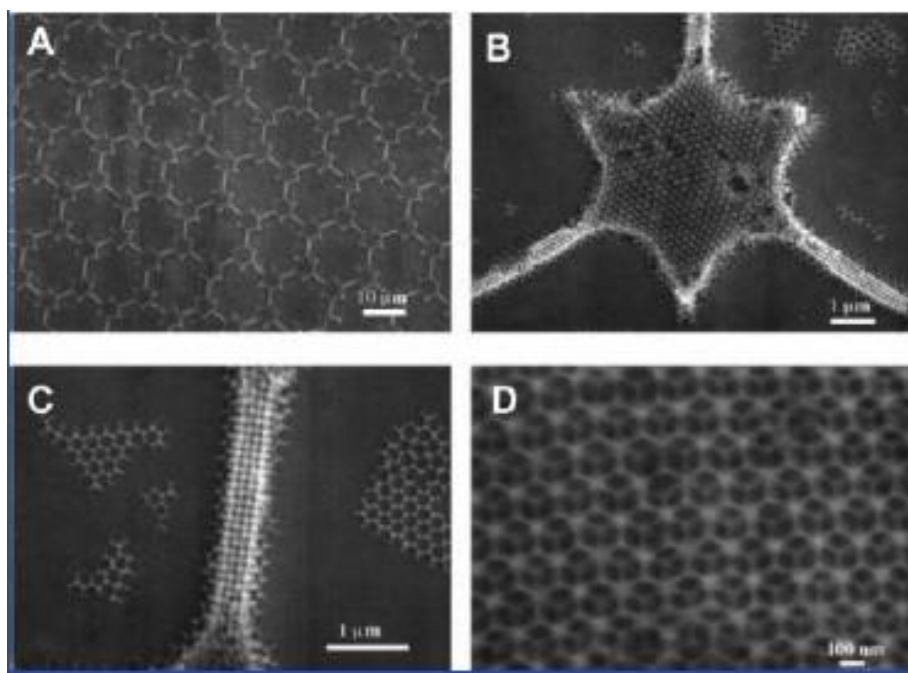


Figure 1.7 Example of lithography combined with templating (Reprinted from ref 91 with kind permission from The American Association for the Advancement of Science. Copyright 1998.⁹¹) (A to D) SEM images at different magnifications of hierarchically ordered mesoporous silica. A lattice of the macroporous framework skeleton is visible in (B) and (D). Pluronic F127 block copolymer was used as the structure-directing agent.

Other methods combined with templating

Dealloying, nanocasting, and electrodeposition have been combined with templating to

generate multimodal porous structures.^{100,115,116}

1.5.4 Other strategies

Phase separation Phase separation is a process in which a mixture separates into more than two phases. The phase separation strategy can be applied to liquids or solids. One example is polymerization induced phase separation copolymer. Sol-gel chemistry sometimes also includes phase separation.^{113,114,117} After the separation, one or more phases are then selectively removed to generate pores through the matrix. The way of phase removal, also called post treatment, includes chemical etching, physical etching etc.

1.6 Potential applications of hierarchical porous material

Different pore sizes coupled in a single material are supposed to perform different functions in a hierarchically porous structure. The communication between the various levels of pores is through the interconnected windows, which is vital to optimize the benefits of hierarchy and material functions. Transport of active species to the internal surface can be enhanced by hierarchically assembling the pores, which is supposed to provide a more efficient performance than traditional porous structures.

1.6.1 Catalysts and sensors. Hollow structures have shown improved performance as catalysts and sensors.^{79,118,119} High surface areas and large surface-to-volume ratio contribute to high catalytic and sensing activity. Porous metal electrodes with a very high active surface area show current up to three orders-of-magnitude higher than those of flat electrodes for some redox active species.¹²⁰ However, an increase in surface area does not necessarily lead to current amplification if the molecules cannot explore the inner surface of the electrode.¹²¹ Thus, it is important that the material have a high surface area but also

open paths for a molecule in solution to access the inner surface. Hierarchically porous structures have both of these features and, as a result, have the potential to amplify the current, enhance the sensitivity and lower the limit of detection (LOD) of such. Another potential advantage of such hierarchical structures is that multistep catalysis, or catalysis and separation can be done in one material by combining several functions together. This greatly improves efficiency and reduces cost.

1.6.2 Separation. Multimodal porous materials have been shown to exhibit excellent size selectivity for the adsorption of proteins in a solution of bovine serum albumin (BSA) and cytochrome c. As shown in Figure 1.8, the width of band 2 in area c is reduced compared with that observed in areas a and b, indicating a large adsorption capacity of the hierarchically ordered porous silica with macropore entrance for BSA. For cytochrome c, however, there is no clear difference. Another example is the application of hierarchical porous materials as a high performance liquid chromatography stationary phase. For example, a C-18-grafted silica monolith was investigated for the separation of aromatic molecules.^{113,122} These hierarchical porous structures are potentially useful in selective adsorption and separation of biomolecules.

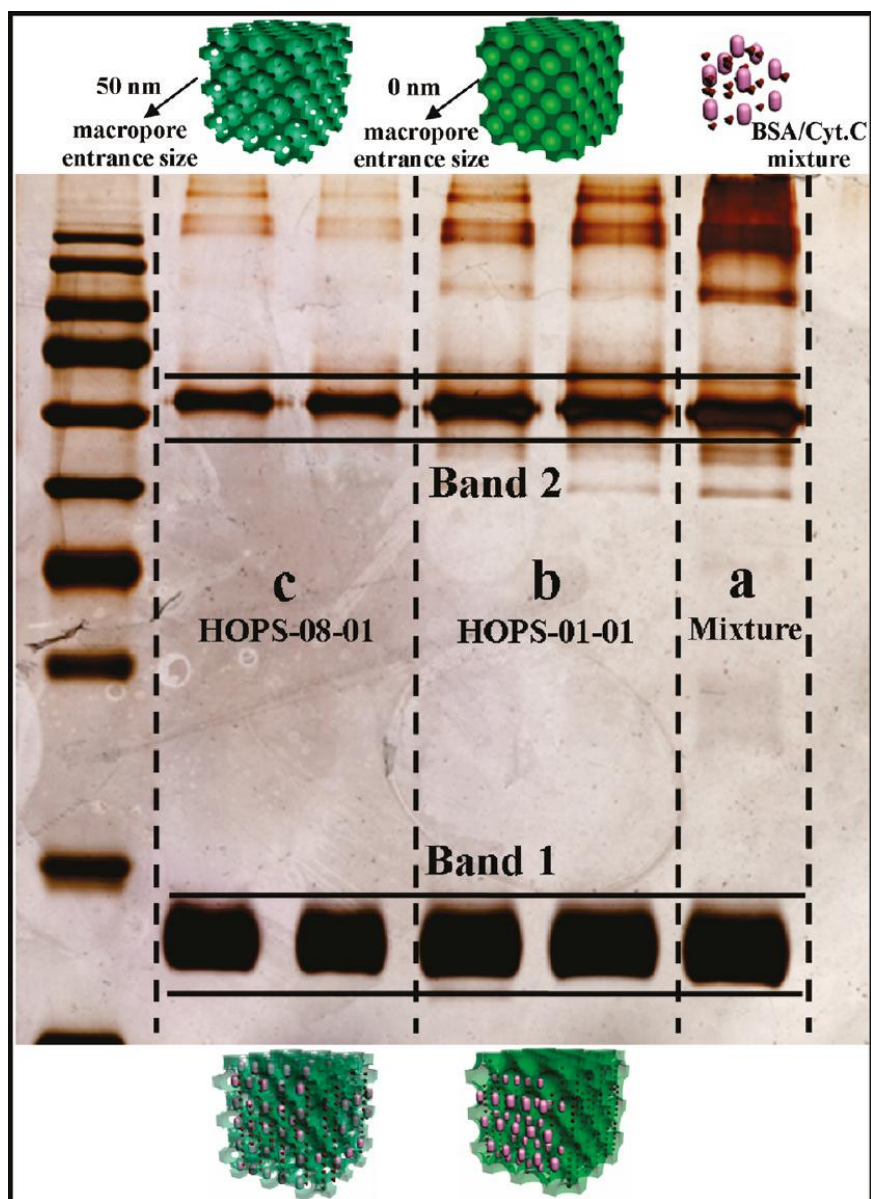


Figure 1.8 Hierarchically ordered macro-/mesoporous silica monolith for size-selective adsorption of proteins (Reprinted from ref 123 with kind permission from American Chemical Society. Copyright 2011.¹²³) SDS-polyacrylamide gel electrophoresis analysis results of (a) the mixture solution containing BSA and cytochrome c before the adsorption, (b) the mixed solution after the adsorption by the sample hierarchically ordered porous silica monoliths without macropore entrance, and (c) hierarchically ordered porous silica monoliths with 50 nm size macropore entrance.

1.6.3 Drug delivery. Hierarchical porous materials are attractive vehicles for drug delivery not only because of their high surface area, but also their intrinsic structures and facile surface functionalization.¹²⁴ Generally, there are two means for drug release: burst release and sustained release. Burst release can be achieved by degradation of the carrier triggered by an external stimulus.¹²⁵ Sustained release can be achieved by either slow diffusion of the therapeutic molecules through an increasingly permeable wall.¹²⁶⁻¹²⁸ A hierarchical porous structure can use macropores for drug storage and mesoporous or microporous walls to control the drug release. Porous capsules are an ideal example. Hierarchically porous hollow spheres are very promising for applications in drug delivery.

1.6.4 Superhydrophobic surfaces and biomimetic. Structures with hierarchical features have been shown to be superhydrophobic in many studies.¹²⁹ Hydrophobic surfaces with bimodal roughness that mimics the lotus leaf structure are a well-known superhydrophobic example. Hierarchical micro/nanoparticle arrays made by lithography have also been shown to exhibit superhydrophobicity.^{130,131} There are also applications on the transition from superhydrophobic to superhydrophilic on hierarchical porous structured surfaces. Hierarchical porous materials are also fabricated for biomimic or for artificial products, such as bone tissue engineering.¹³²

1.6.5 Other potential applications. The applications are not limited within those applications mentioned above. There is more research on energy storage^{38,133}, surface enhanced Raman scattering¹³⁴, photoelectrochemical properties¹³⁵, etc. More applications of conventional porous material applications might be improved with the enhanced diffusion into the porous structure.

1.7 Summary of Objectives:

Research on hierarchical hollow structures is still in its infancy and considerably more work still needs to be done. To systematically study the relationship between structure and performance as well as to broaden the applications of those structures, it is important to develop general strategies with fewer synthetic steps to obtain high quality and high yield products. To obtain high quality hierarchically porous structures, it is important to precisely control the size and shape of the pores, interconnected areas, and composition uniformity throughout the material. With control over the synthesis of these structures, it will be possible to thoroughly study their use in applications that require minimal diffusion resistance and improved accessibility to interior surfaces.

The overall goal of this dissertation work is to develop general synthetic approaches to prepare multimodal porous materials with well-defined architectures for various applications. It is a general strategy to use self-assembled colloidal crystals as templates to prepare various porous materials. In this project, we will develop hierarchical templates which can be assembled and packed into 2D and 3D structures in a similar fashion as conventional colloidal (latex) beads. Many of the existing strategies that employ latex spheres to prepare high surface area, porous materials can be easily adapted to make hierarchical porous materials. The materials synthesized in this dissertation include multimodal porous silica, bimodal porous thin films and silica porous capsules. Some key objectives of this dissertation work are:

- (a) Fabricate well-defined size tunable hierarchical templates
- (b) Pack the hierarchical templates into 2D and 3D structures.

- (c) Create the porous framework around these hierarchical templates
- (d) Fully characterize all the multimodal porous materials fabricated in this work

Chapter 2 Characterization techniques

2.1 Introduction

Characterization of the porous materials fabricated in this work includes both morphology and porosity. In this chapter, scanning electron microscopy and atomic force microscopy were used to evaluate surface morphology. Transmission electron microscopy and scanning transmission microscopy were employed to study the hollow architectures. Gas adsorption and mercury intrusion were used to characterize the porosity of the silica monoliths prepared in this investigation. In addition, x-ray photoelectron spectroscopy and electrochemical methods were used in the characterization of the gold electrodes made in this investigation.

2.2 Transmission Electron Microscopy (TEM)

Transmission electron microscopy (TEM)¹³⁶ was used in this work to study the hollow structures, specifically the porous silica monolith fractures reported in chapter 4 and the hollow capsules described in chapter 6. Electron microscopy techniques employ a high energy electron beam, which requires the entire system to be under high vacuum to prevent beam scattering that will result in noise and a loss in resolution. The beam is accelerated by a high voltage and focused by several mechanical and electromagnetic lenses before being directed onto the sample surface. The high energy electron beam focused on the samples will be blocked or adsorbed when sample particles or solid structures are in the way. In typical TEM images, the hollow structures thus appear bright in color while the solid structures appear dark, depending on the extent that the electrons penetrate the structure and are detected by the detector located beneath the

sample. The imaging mechanism is similar to optical microscopy. Instead of using a light source, an electron beam is used as the source.¹³⁷ In this work, transmission electron microscopy (TEM) images were acquired with a JEOL Model 2010 transmission electron microscope with an accelerating voltage of 200 kV and a charge-coupled device (CCD) camera for image display. For TEM sample preparation, it is critical to make really thin samples, or small pieces, but there is no requirement for sample conductivity. For bulk sample or fragile sample preparation, a microtome is normally used to obtain a really thin specimen buried in a polymer resin. In this work, the samples were prepared via sonication in methanol for few minutes after which they were cast onto carbon-coated Cu TEM grids and evaporated naturally.

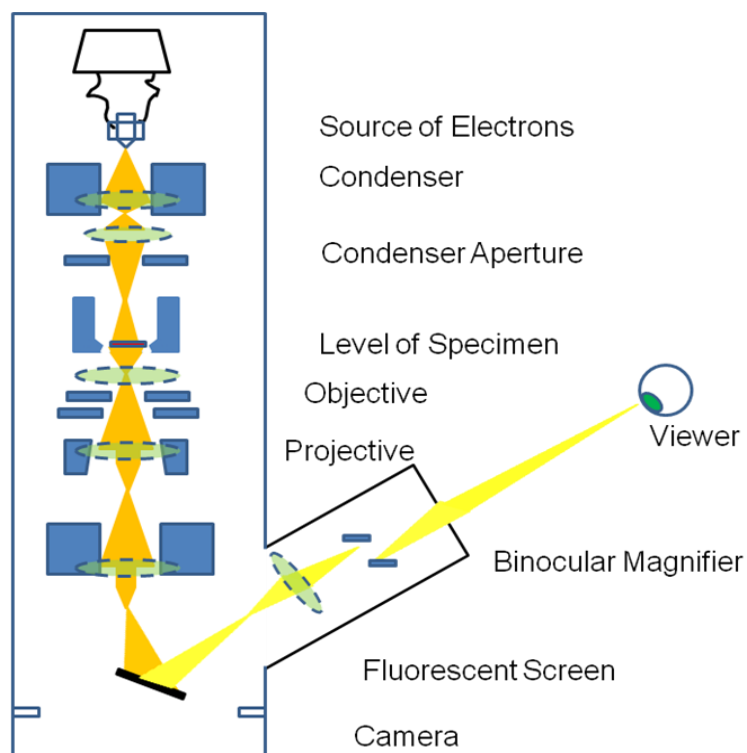


Figure 2.1 Schematic image of the components of a transmission electron microscope. (<http://universe-review.ca/R11-13-microscopes.htm>)

2.3 X-ray Photoelectron Spectroscopy (XPS)

X-ray photoelectron spectroscopy (XPS) was used in this work to determine the elemental composition on the surface of the gold electrodes made in this work in chapter 5. In XPS, incoming X-ray photons can remove an inner shell electron from an atom and the kinetic energy of the leaving electron measured. The binding energy (E_{binding}) is calculated using the following equation where the binding energy equals the incoming photon energy minus the kinetic energy of the leaving electron.¹³⁸

$$E_{\text{binding}} = E_{\text{photon}} - E_{\text{kinetic}} \quad (1)$$

Because the binding energy for different elements are characteristic of that element, information about the elemental composition of the top 7-10 nm of a surface can be determined using this technique. XPS can measure the elemental composition, empirical formula, chemical state and electronic state of elements located on the surface of the material.¹³⁸ Binding energy in the energy range of 0 - 1400 eV can be measured. By using a database of binding energies, it is possible to identify the composition of a sample. All XPS analysis done for this work was performed at the VCU Nanomaterials Characterization Center (NCC). X-ray photoelectron spectroscopy (XPS) was performed on a Thermo Scientific ESCALAB 250 microprobe with a focused monochromatic Al $K\alpha$ x-ray (1486.6 eV) source and a 180° hemispherical analyzer with a 6-element multichannel detector. The main parts of the XPS instrument are X-ray source, electron collection lens, electron energy analyzer, electron detector, and high vacuum system. The aliphatic hydrocarbon C 1s peak at 284.6 eV was used to calibrate the spectra. For survey

scans, a pass energy of 150 eV was used while for element specific individual scans a pass energy of 50 eV was used. In both cases, a step size of 0.100 eV was used. The advantage of this technique is its sensitivity and the ability to obtain both quantitative and qualitative data.¹³⁹ Because of that, XPS has been widely used to estimate chemical formulas. The drawbacks of XPS are that it is relatively expensive, utilizes a high energy beam, and requires a high vacuum. Also, XPS analysis works better with uniform and flat surfaces. For rough surfaces, the information collected can be partially missing because parts of the surface can be inaccessible by the X-rays. There have been many studies on how to adjust the data for regular shaped surfaces,¹⁴⁰ but for real analysis, rough surfaces rarely have ordered regular shapes.

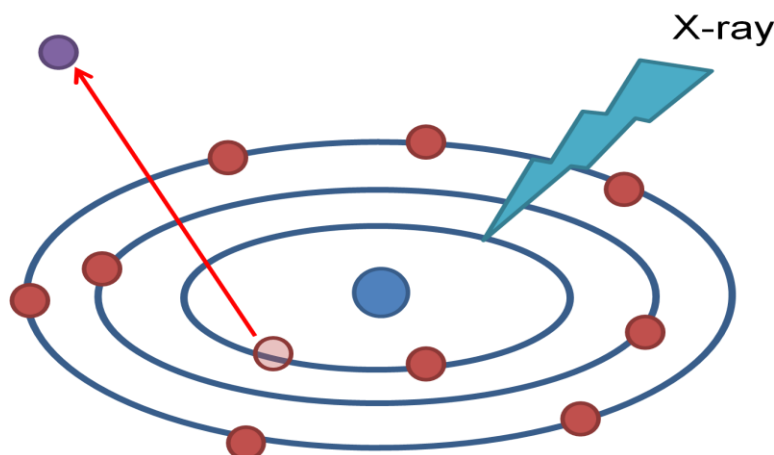


Figure 2.2 X-ray photoelectron spectroscopy theoretical background. The incoming X-ray knocks out an inner layer electron; the kinetic energy of the leaving electron equals the X-ray energy minus the binding energy.

2.4 Scanning Electron Microscopy (SEM)

Scanning Electron Microscopy (SEM)¹⁴¹ was used to characterize all the template and hierarchical porous structure morphologies made in this work. SEM images are acquired

by bombarding a focused high energy electron beam on a sample and collecting the secondary electrons emitted from the surface of the sample. There are two types of SEM emitters that are typically used, field emission guns that use single crystal tungsten as the emitter, and those using lanthanum hexaboride cathodes. The beam is focused by mechanical and electromagnetic lenses just like the TEM beam. The SEM analysis done for this work was performed with two instruments, a Hitach SU 70 and a Zeiss EVO 50 XVP. To acquire SEM images of sufficient quality, the samples must be electrically conductive to prevent the surface charging. In some environmental SEM instruments, the sample does not necessarily have to be conductive or imaged under a high vacuum, but resolution is sacrificed. Nonconductive samples were made conductive by sputtering a thin layer of metal, alloy or carbon on the surface prior to use.

When the electron beam bombards the sample surface, most of the electrons penetrate within a certain depth into the sample surface and interact with the sample atoms and become scattered.¹⁴¹ These electrons gradually lose their energy as the interaction keeps going between the electrons and different sample atoms. Secondary electrons (SE), backscattered electrons (BSE), cathodoluminescence (CL), continuum x-ray radiation (bremsstrahlung), characteristic x-ray radiation, and phonons (heat) are generated from the surface.¹⁴¹ Secondary electron collection by detectors provides the SEM images. Backscattered electron can provide information on different phases, so in a typical backscattered image, the color difference results from different phases. X-ray radiation generated can be used for element analysis by energy–dispersive X-ray spectroscopy (EDS) which is normally a part of an SEM instrument. Principally, the background

theory is similar to XPS, where the binding energy equals the energy of the incoming electron minus the energy of the X-ray radiated.

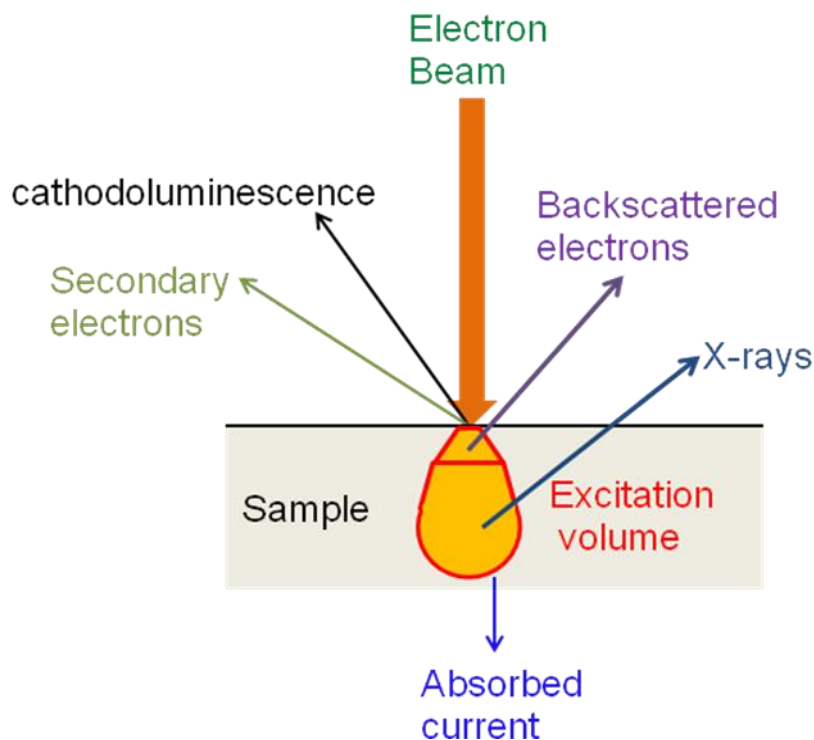


Figure 2.3 Illustration of radiation and electrons generated when the electron beam bombards the sample surface.¹⁴¹

The scanning transmission electron microscope (STEM) images were also collected by the Hitachi SEM at a 30V voltage with the detector below the sample. The sample powder was dispersed on a copper grid just like was done for the TEM samples. STEM images are composed of both SEM and TEM images. The SEM image is generated by the secondary electrons ejected from the sample surface, while the TEM image is obtained by electrons transmitted through the sample. STEM can provide information on the surface morphology of a sample (from SEM image) and information about the inner hollow structure of the same area from the TEM image.¹⁴² STEM thus provides more

information about the whole sample architecture. Compared with TEM, STEM uses a much lower accelerating voltage (about 30KV in our instrument), thus the images obtained are not as clear as TEM images collected on a TEM instrument.

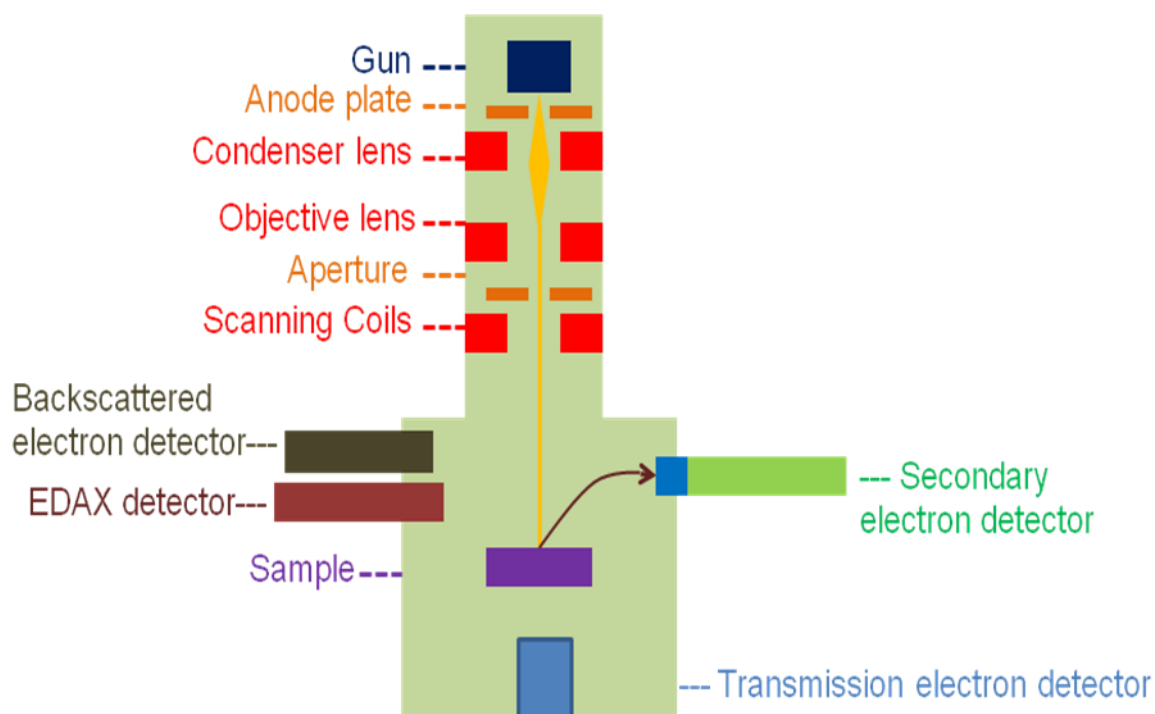


Figure 2.4 Illustration of the components of a scanning electron microscope.¹⁴¹

2.5 Atomic Force Microscopy (AFM)

Atomic Force Microscopy (AFM) provides information about the surface topography. In this technique, a constant force or wave amplitude is maintained by adjusting the distance between the AFM tip and sample surface. The movement of the tip/sample can then be recorded by a laser reflection onto a detector screen to generate a topographical image.¹⁴³ In this work, the AFM was used to image the top surface of the hierarchical template and the pore size in the silica capsules described in chapter 6. The resolution of

an AFM image depends on the sharpness of the AFM tip. The advantages of AFM are that it can provide information about the height or depth of a structure, surface roughness, it can generate 3D images and does not require a vacuum. Its disadvantages relative to SEM are that AFM scans can be time consuming and it can be challenging to obtain large area images of very rough surfaces. The two most often used AFM modes are tapping mode and contact mode. For contact mode, a constant force between the tip and the sample surface is kept while the position of the tip relative to the sample surface adjusted by the piezoelectric actuator stage. As a result, the cantilever bends which will result in the change of laser reflection direction.¹⁴⁴ From the position of the reflected laser light on the detector screen, the morphology of the surface can be obtained. For tapping mode, the cantilever is oscillating at a certain frequency. As the cantilever is scanned over the sample and the tip comes close to the surface, the amplitude of this oscillation decreases due to the intermolecular forces acting on the cantilever. The piezo stage adjusts the relative height to maintain the cantilever oscillation amplitude. Thus a tapping mode image can be recorded. For soft materials, or biomaterials, tapping mode should be used because the tip might damage the sample surface in contact mode. In this work, the templates and capsule samples were imaged using an atomic force microscope (AFM, Digital Instruments, Nanoscope IIIa) in the tapping mode with silicon nitride tips (Nanoscience Instruments). The data are shown in chapter 6.

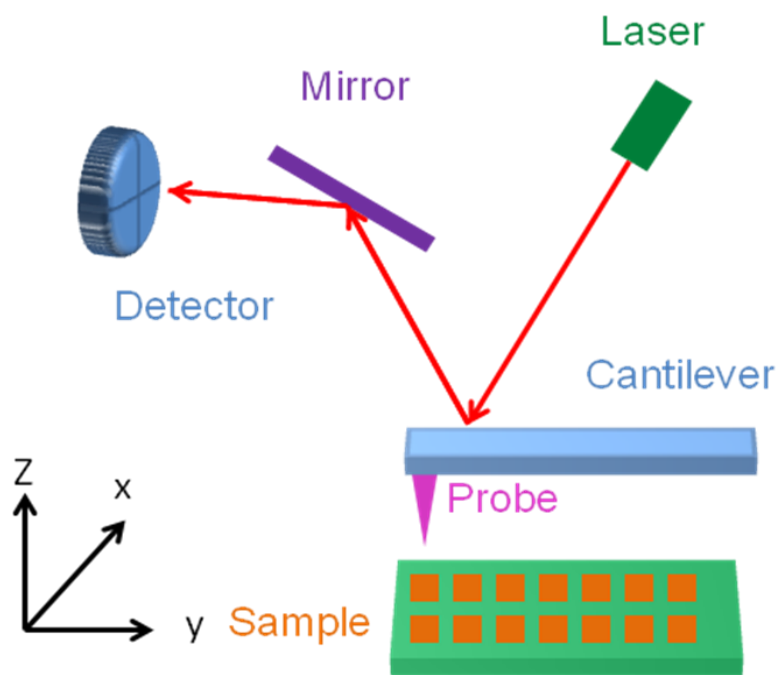


Figure 2.5 Illustration of the components of an atomic force microscope.

2.6 Gas Adsorption analysis

Gas adsorption analysis is customarily used to measure the surface area and porosity of high surface area materials. An adsorption isotherm obtained from the analysis is a plot of surface coverage of adsorbate versus relative gas pressure at a constant temperature. This technique is most often used for mesoporous and microporous materials, but it can also be used for macroporous materials. Normally the analyzing temperature is 77 K by liquid nitrogen and the adsorbate is nitrogen. The nitrogen will be adsorbed along the entire surface first, and then physical adsorption of multiple layers of gas molecules will form as the nitrogen pressure increases. A langmuir isotherm is used to describe monolayer adsorption (chemical adsorption) of gas on a solid surface while BET is for multilayer adsorption (physical adsorption).¹⁴⁵ Each category of porous materials has a characteristic

isotherm curve. Microporous material will show a significant increase at very low pressure. Mesoporous material will have a characteristic hysteresis between adsorption and desorption branches. Macroporous materials only show significant increase at high relative pressure.¹⁴⁵ In this work, to evaluate the porosity and pore interconnectivity, particularly mesoporosity, N₂ sorption experiments were conducted with a Quantachrome Autosorb 1 MP analyzer with an equilibration time of 3 min. Samples were outgassed at 120° C overnight. The data is shown in chapter 4. In a typical nitrogen adsorption isotherm curve, the desorption branch is used to calculate the internal surface area per unit mass. Pore size distribution can be calculated from the isotherm.

2.7 Mercury intrusion porosimetry

Mercury intrusion porosimetry provides information of the distribution of pore sizes in cement-based materials.¹⁴⁶ Mercury is a non-wetting liquid with a contact angle greater than 90°. So unlike other wettable liquids that will be sucked into the pores by capillary force, it will only intrude pores under pressure. Mercury is forced into the porous structure under a gradually increasing pressure.¹⁴⁶ The relationship between the pressure and capillary diameter is described as:

$$P = -4 \gamma \cos\theta/d \quad (2),$$

where P is pressure, γ is the surface tension of the liquid, θ is the contact angle of the liquid, and d is the diameter of the capillary.¹⁴⁷

Based on the pressure change, the pore size distribution and interconnectivity can be obtained. The intrusion of mercury can give information about the interconnected windows between the pores. But it has limitations when applied to materials that have

irregular pore geometry. For these systems that have large internal pores accessed by very narrow “bottlenecks”, the MIP technique take the size of these bottlenecks as the diameter of the internal pores, which is considered an unavoidable limitation referred to as the "ink bottle" effect.¹⁴⁸

Another drawback of this technique is the toxicity of mercury, and that is why this technique is not widely used. However, this method is more ideally suited for the study of macroporous materials providing the porous material being studied has enough mechanical strength to survive the high pressure of mercury during analysis. After the analysis, the sample is not reusable due to the mercury residual contamination. In this work, the samples of hierarchical porous silica monolith powders were sent out to PMI Company (Porous Materials, Inc.) for analysis. The original purpose of collecting this data was to study the interconnected part between the pores and obtain the pore size distribution of the sample. The data are shown in chapter 4.

2.8 Electrochemical studies

Electrochemical measurements were performed with a BAS 100 potentiostat using a Ag/AgCl (3.5 M KCl) reference electrode and a Pt auxiliary electrode in a one-chamber three arm electrochemical cell. For electrochemical comparison, some of the experiments were performed using a 1001A multichannel CH instrument. In a multichannel instrument, six working electrodes, one reference electrode, and one auxiliary electrode are placed in an electrochemical cell containing the solution of interest (e.g. supporting electrolyte or redox couple in supporting electrolyte). By having all the electrodes in the

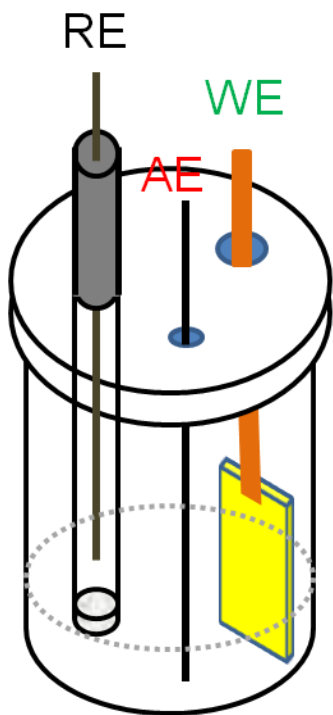


Figure 2.6 A typical three electrode cell setup

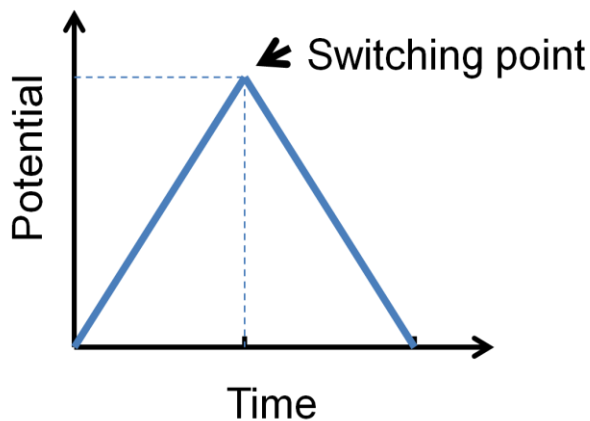


Figure 2.7 Cyclic potential sweep

same solution simultaneously, comparisons between different electrodes become more straightforward. In addition, the experiments take a lot less time.

2.8.1 Cyclic Voltammetry

Cyclic voltammetry is one of the mostly used methods for electrochemical characterization. CV is traditionally undertaken in a three-electrode cell with a working electrode, a counter electrode (auxiliary electrode), and a reference

electrode. The potential is defined based on the potential difference between working electrode and reference electrode, while current is measured between the working electrode and the counter electrode. Reference electrodes normally have very stable potential, such as Ag/AgCl, or saturated calomel electrode (SCE). Counter electrodes are inert electrodes, such as Pt and carbon.

In a typical cyclic voltammetry study, a cyclic potential scan, Figure 2.7, is applied between the working electrode and the reference electrode. The scan rate (V/s) of the cyclic voltammetry experiment is the slope of the potential-time curve.¹⁴⁹ The current produced during this potential scan is measured and a cyclic voltammogram curve similar to the one shown in Figure 2.8 is obtained. During a CV cycle, a redox couple goes through an oxidation and reduction process. Electrolyte in the solution serves to lower the resistance of the solution and eliminate migration. Normally it is an inert salt, which doesn't show any Faradaic current during the CV scan; neither does it react with other redox species in the solution.

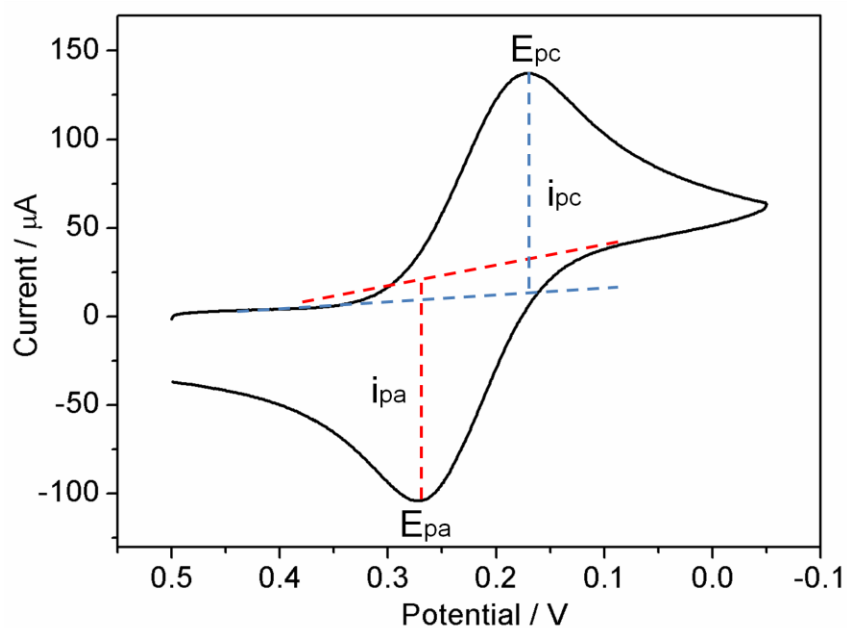


Figure 2.8 A typical cyclic voltammogram of a gold working electrode in 1 mM FcCH₂OH/ 0.1 M KCl solution at 0.1 V/s scan rate.

Important information can be obtained from a CV, such as the electrode capacitance (which is related to the area of the electrode), electron transfer kinetics, concentration of the redox molecules in solution and diffusion coefficients.¹⁵⁰⁻¹⁵² When the redox reaction is electrochemically reversible, the peak splitting ideally is 59/n mV, and the cathodic current (i_{pc}) and anodic current (i_{pa}) are the same. The peak current can be calculated by the following equation

$$i_p = (2.69 \times 10^5)n^{3/2}AD^{1/2}Cv^{1/2} \quad (3)$$

where the peak current is directly related to the concentration of the redox species (C), square root of scan rate (v) and electrode area (A), the number of electrons transferred (n) and the diffusion coefficient (D) of the redox species.¹⁴⁹

For a redox species that is adsorbed on the electrode and not present in solution, the cathodic and anodic peak position for an electrochemically reversible redox species should be at the same potential and the cathodic peak current and anodic peak current should be the same.¹⁴⁹ The current can be calculated by the equation

$$i_p = (n^2F^2/4RT)vA\Gamma^* \quad (4)$$

where the peak current is directly related to the concentration of the total adsorbed redox species (Γ^*), scan rate (v), electrode area (A), and the number of electrons transferred (n). The total width at half-height of the cathodic or anodic peak should theoretically be

$$\Delta E_{p,1/2} = 3.53 RT/nF = 90.6/n \quad (5)$$

But the ideal shape rarely is experimentally seen. When there are lateral interactions between the adsorbed species, the half-height width of the cathodic or anodic peak will not be $90.6/n$ mV.

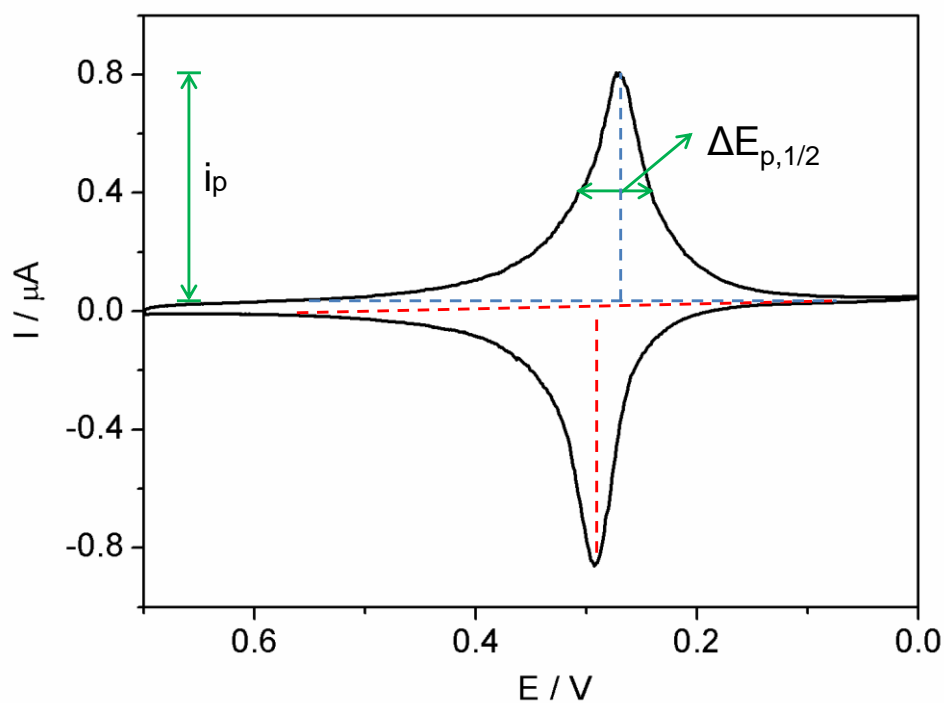


Figure 2.9 Cyclic voltammogram for the reduction and subsequent reoxidation of an electrochemically reversible adsorbed redox couple.

2.8.2 Chronoamperometry and Chronopotentiometry

Chronoamperometry and chronopotentiometry are two other examples of commonly used electrochemical techniques. In chronoamperometry, the potential is held at a certain value and the current measured as a function of time. In chronopotentiometry, a constant current is applied and the potential measured as a function of time.¹⁴⁹ In this study, the

gold plating (electrodeposition) is performed using both techniques. The electrochemical instrument is operated in either the Galvanostat mode to perform chronopotentiometry or in a potentiostatic mode when used for chronoamperometry. For metal plating applications, galvanostatic deposition is better in generating a fine and smooth deposition.

Chapter 3 Hierarchical templates

3.1 Introduction

The major objective of this study is to make a monodisperse bimodal hard template (e.g., a hierarchical template) that is constructed of only one material, can be isolated, and ultimately used to construct ordered multimodal porous materials with well-defined architecture and interconnected pores using standard template packing procedures.^{33,153} Part of the material shown in this chapter has been published.¹⁵⁴

3.2 Background

In general, the use of a one-step hard templating method to make hierarchical porous materials involves four major steps: (1) preparation of the hierarchical templates; (2) packing these templates into 2D or 3D structures; (3) impregnating the array of packed templates with the desired precursors; and (4) selective removal of the templates to yield hollow multimodal structures for different applications (Fig. 3.1).

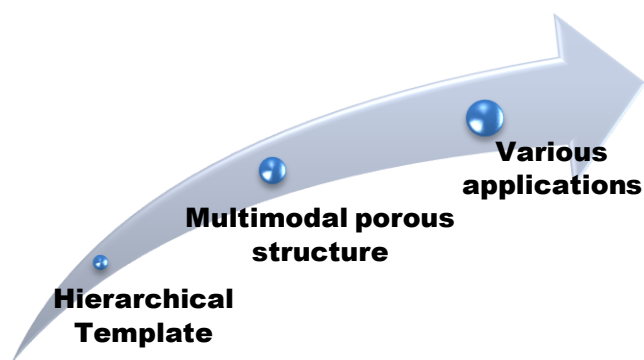


Figure 3.1 The development process of multimodal porous material.

The use of a single, bimodal template constructed of one material will simplify this fabrication process. The advantage of this method is as follows: predefined hierarchical

templates, which can be packed into a certain arrangement, can yield a material with well-defined bimodal porosity with pore interconnectivity and exquisite control over pore size and pore size distribution. The hard templating method is also a well-established methodology; various template packing and space filling methods have been reported.¹⁵⁵ These methods can be easily adapted and provide many choices for porous material fabrication.

As summarized above, monodispersed hierarchical templates are the first step to the preparation of well-defined multimodal porous structure by the hard templating method. In this chapter, the fabrication of various hierarchical templates will be discussed. Commercially available, uniform polystyrene spheres and silica beads are commonly used to make ordered porous structures.⁵³ Polystyrene latex spheres with a size range that runs from ~ 20 nm to tens of microns with a wide variety of surface functional groups can be purchased from Interfacial Dynamics Corporation (<http://www.invitrogen.com>). The individual spheres can be strategically coupled together to form a hierarchical template by reacting surface-bound functionalities located on the different spheres.

In this work, two types of hierarchical templates were fabricated: bimodal spheres with (1) raspberry-like and (2) strawberry-like morphologies, as shown in Figure 3.2. This terminology comes about because in both cases the structures are “aggregates” or compound structures just like the raspberry and strawberry are considered to be examples of aggregate fruits composed of appendages that are either fruit (in the case of a raspberry) or seeds *partially* coating and dispersed around the fruit (in the case of a strawberry). Raspberry-like particles reported in the literature have been prepared via emulsion

polymerization, heterocoagulation, templating, layer-by-layer assembly, and chemical bonding.^{98,156-166} In addition, particles with more exotic shapes such as daisy-like, snowman-like, and currant-bun-like have also been reported.¹⁶⁷⁻¹⁷³ In most examples, the composite particles were constructed from two different materials, typically a polymer core with silica particles forming the secondary (satellite) spheres. There have also been examples where the core/shell have been polymer/polymer, inorganic/polymer, and polymer/biological.^{174,175} Because of their rough surface morphology, these organic-inorganic composite particles have been particularly successful in the construction of superhydrophobic/superhydrophilic surfaces.^{156,160,165,166} Likewise, capsules (hollow spheres) have also been formed from such composite particles.^{96,98,176}

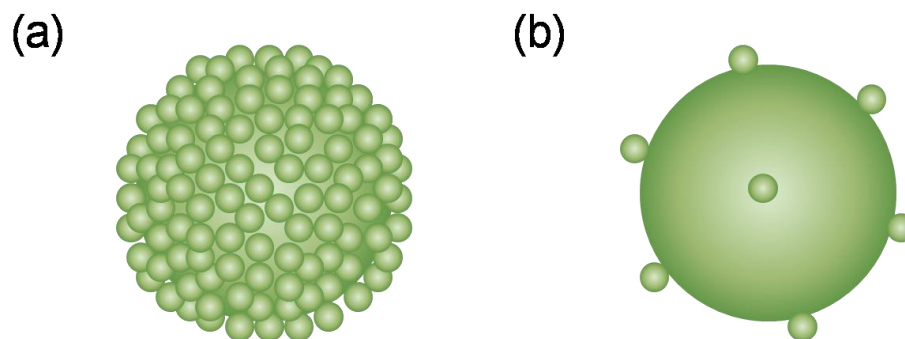


Figure 3.2 Schematic images of hierarchical templates. (a) raspberry-like template and (b) strawberry-like template.

In this work, the raspberry-like and strawberry-like templates were prepared by synthetically joining appropriately functionalized commercially available polystyrene (PS) latex spheres together. Two different coupling reactions were used to form the hierarchical templates: carbodiimide-assisted coupling of COOH groups with NH₂ groups and base-assisted coupling of epoxy groups with NH₂ groups. The size and

morphology of the hierarchical template is defined by varying the sizes of both the "core" and the "satellite" spheres, as well as altering the coverage of "satellites" on the "core". Because the hierarchical template is composed of only one material (e.g., polystyrene), it can be easily removed from the matrix in one step leaving its imprint in the material host.

3.3 Coupling mechanisms

Three coupling reactions can be considered as a means to make the hierarchical latex sphere: the coupling reaction between NH_2 and COOH , NH_2 and COH , and epoxy and NH_2 (Figure 3.3). The mechanisms are as follows:

For the NH_2 coupling reaction with COOH (Fig 3.3 a), the carboxyl is first activated by EDC to form an unstable reactive o-acylisourea intermediate, then the intermediate reacts with amine to form a stable amide bond.^{177,178} When NHS is present in the solution, it further interacts with the intermediate to form a semi-stable amine-reactive NHS-ester. Since the stability of intermediate is improved, the coupling efficiency can be significantly increased (up to 90 % efficiency has been reported).^{179,180}

For the NH_2 coupling reaction with COH (Figure 3.3 b), H^+ works as a catalyst. In the first step, H^+ forms a bond with the carbonyl oxygen, which leaves a positive charge on the carbonyl carbon. The NH_2 acts as a nucleophile and will attack the positively charged carbon to form a bond between N and C. By losing H^+ , the whole structure becomes neutral again.¹⁸¹ The structure might be rearranged into an $\text{N}=\text{C}$ double bond after H^+ removed the OH group.

For the NH_2 , the coupling reaction with epoxy under basic conditions (Figure 3.3 c), a ring opening nucleophilic attack happens to form a secondary amine bond.¹⁸¹ Other

coupling reactions could also be considered, but these three types are the easiest considering the commercial availability of the PS spheres with either COH, NH₂ or COOH functional groups.

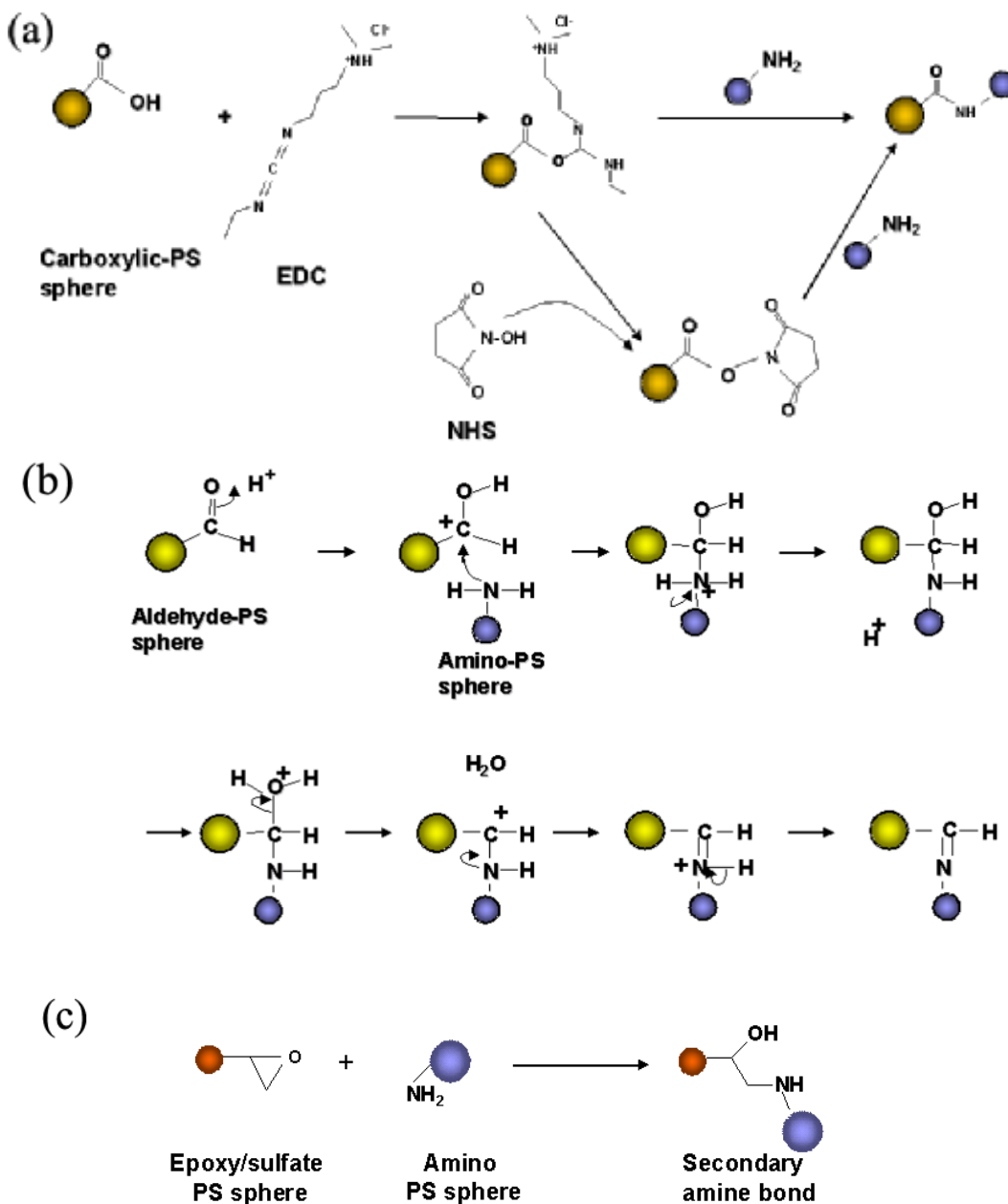


Figure 3.3 Reaction mechanisms (a) Carbodiimide-Amine (EDC) (b) Aldehyde-Amine (c) Epoxy-Amine.

The size ratio of the core sphere to the satellite spheres influences the stability of the template suspension. A larger size ratio will result in a better coverage of satellites on the core giving a hierarchical template that will be either positively or negatively charged. When the satellite spheres are large, the satellites will not completely cover the core, which will result in the presence of both positive and negative charges on the template surface leading to aggregation. Also, a large size difference between the core and the satellite can make the separation of template from the original mixture easier. For all the different types of coupling used to make hierarchical templates, it is important that the satellites are in excess and the overall surface charge on the core and the satellites opposite.

For the coupling of NH_2 with epoxy, it is easier to obtain complete coverage of satellites on the core since this reaction has higher yield because it is a one-step reaction and the steric effect for NH_2 to attack a β carbon is lower (see Figure 3.3). In the COOH-NH_2 reaction, EDC is not very stable and needs to be used right after the solution preparation. The coupling between the core and the satellites has to be one way. For example, the 340 nm NH_2 spheres contain both NH_2 and a small amount of COOH groups on their surfaces. When the coupling begins, aggregation takes place between the core and the satellites, but also among satellites. Ionic strength also influences the extent of aggregation. If the salt concentration in the reaction solution is too high, it will reduce the interaction of charges, thus affecting the uniform distribution of cores and satellites in the solution. The different types and sizes hierarchical templates that have been prepared

and characterized are listed in Table 3.1. The coverage and dispersity of those templates are directly related to the size ratio of the core and satellite spheres, and the number of surface functional groups.

Table 3.1 Table of various hierarchical templates that have been fabricated and their features.

Hierarchical templates (core-satellites)	Features
1500 / 110 nm COOH-NH ₂	Good coverage, dispersed well in acetic acid not in water.
450 / 80 nm COOH-NH ₂	Poor coverage, dispersed well in acetic acid not in water, dimers, and trimers happens.
1500 / 340 nm COOH- NH ₂	Severe aggregation, polymers
1200 / 450 nm NH ₂ -COOH	Very poor coverage, pretty bad aggregation, polymers.
1200 / 60 nm NH ₂ - epoxy	Good coverage, dispersed well in water. Monodispersed.
1200 / 29 nm NH ₂ - epoxy	Good coverage, dispersed well in water. Monodispersed.
710 / 60 nm NH ₂ - epoxy	Good coverage, dispersed well in water. Monodispersed.
710 / 29 nm NH ₂ - epoxy	Good coverage, dispersed well in water. Monodispersed.
340 / 29 nm NH ₂ - epoxy	Good coverage, dispersed well in water. Aggregation happens.

3.4 Template fabrication

Reagents and chemicals. N-(3-Dimethylaminopropyl)-N'-ethyl-carbodiimide hydrochloride (EDC, protein seq. grade), N-Hydroxy-succinimide (NHS, 98 %) and

Triton X-100 were purchased from Aldrich. Aqueous suspensions of polystyrene microspheres functionalized by either carboxylates or amines or epoxy/sulfate with diameters ranging from 20 nm to 1.5 μm were obtained from Invitrogen (formally Interfacial Dynamics Corporation (IDC), 4.1 wt/v% for COOH-PS, 2.1 wt/v% for NH₂-PS, and 4.1 wt/v% for PS-Epoxy/Sulfate). The PS-NH₂ latex spheres contained no COOH groups. Water was purified with a Millipore water purification system.

Instrumentation. Scanning electron microscopy (SEM) was conducted on a ZEISS/LEO under high vacuum condition. Atomic force microscopy (AFM) was performed at a Veeco Multi-mode AFM in the tapping mode with conventional tips.

Hierarchical templates were prepared by synthetically joining appropriately functionalized commercially available polystyrene latex spheres together using two different coupling reactions: carbodiimide assisted coupling of COOH groups with NH₂ groups and the base-assisted coupling of epoxy groups with NH₂ groups. These hierarchical latex spheres are referred to as being “raspberry”-like or “strawberry”-like depending on the number density of the “satellite” spheres surrounding the central “core”.

3.4.1 Raspberry-like hierarchical template synthesis. Two different sized “raspberry-like” templates were prepared by coupling NH₂ groups with COOH groups: one with a 450 nm core and 80 nm satellites and another with a 1500 nm core and 110 nm satellites. Polystyrene microspheres (80 or 110 nm diameter of PS-NH₂; 450 or 1500 nm diameter of PS-COOH) were sonicated 10 min before use. An excess amount of PS-NH₂ spheres (1.2 mL for 1500/110 nm template; 0.5 mL for 450/80 nm template) were dispersed in

MOPS buffer (3-[N-Morpholino]propanesulfonic acid, pH = 6, 0.025 M) and then the PS-COOH spheres (1.0 mL for 1500/110 nm template; 0.15 mL for 450/80 nm template) were added to the solution. This suspension was sonicated for ~ 10 min to completely mix the spheres. Because of the electrostatic force and the presence of excess PS-NH₂ spheres, each negatively charged PS-COOH was surrounded by positively charged PS-NH₂ spheres. EDC/NHS (0.1 g EDC/0.03 g NHS in 10 mL of MOPS buffer (pH = 6.4, 0.025 M) for the 1500/110 nm template; 0.03 g EDC/0.01 g NHS in 2 mL of MOPS buffer for the 450/80 nm template) was added to the mixture followed by slow rotation for 24 h. The colloidal solutions were centrifuged and washed with diluted acetic acid (1:1) several times to remove the excess small spheres. In this work, hierarchical spheres with core/satellite diameters of 1500/110 nm, 450/80 nm for COOH-NH₂ type, 340/29 nm, 710/29 nm, 710/60nm, 1200/29 nm and 1200/60 nm for NH₂-epoxy type were made. These templates were isolated by centrifugation and later used to prepare hierarchical porous structure.

3.4.2 Strawberry-like hierarchical template synthesis

“Strawberry-like” templates were also prepared using a similar coupling strategy but with a different solvent system. In this case, the PS-NH₂ (110 nm) and PS-COOH (1500 nm) spheres were dispersed in a mixture of Triton X-100 in ethanol (0.05%, 1%, 10%, or 30% by weight). Triton X-100 is a nonionic viscous surfactant. The different amounts of Triton X-100 in ethanol change the viscosity of the coupling solution and thus influence the reaction rate. Hence the coupling efficiency was indirectly slowed down. After washing/centrifugation, the templates were re-dispersed and incubated for 1 h in the

Sulfo-NHS-acetate/phosphate buffer (pH = 7.5, 0.1 M) solution to block the remaining reactive amines and help prevent aggregation. For the epoxy-amine coupling reaction, an excess amount of satellite spheres (29 nm PS-Epoxy/Sulfate, 500 μ L) was diluted with deionized water (500 μ L). The core spheres (PS-NH₂, 340 or 1200 nm, 200 μ L) were then added and the resulting solution was sonicated for 10 min. The pH of the solution was increased to 10 via the addition of Na₂CO₃ buffer solution (pH = 10, 0.1 M) and the coupling reaction allowed to proceed for 24 hours. The reaction was terminated by the addition of HCl drop wise until the pH = 7. The templates were separated from the reaction solution by centrifugation and washed thoroughly with water several times.

Figure 3.4 shows simplified reactions schemes for the preparation of raspberry-like and strawberry-like hierarchical templates using these two coupling methods. The carbodiimide assisted coupling of PS-COOH with PS-NH₂ requires that the PS-NH₂ latex spheres not contain surface COOH groups as these residual groups are still reactive and could couple with other PS-NH₂ resulting in agglomeration/aggregation. For the base-assisted coupling of epoxy groups, it is not critical that the PS-NH₂ spheres be free from COOH groups and thus it provides more flexibility in the size of the core because most commercially available batches of PS-NH₂ latex spheres contain COOH groups. (Lack of NH₂-PS spheres may result in particle aggregation, because a single NH₂-PS sphere can react with more than one COOH-PS sphere). One of the advantages that this approach provides is simplicity in that only one template is needed in contrast to combining two or more different templates.¹⁸² The different post-treatments (chemical etching or thermal heat-treatment) must then be used to render the multimodal porosities in the final

products in those materials, which can complicate the chemistry. Having one hierarchical template that is made completely out of polystyrene allows flexibility in removal via calcination or solvent exchange.

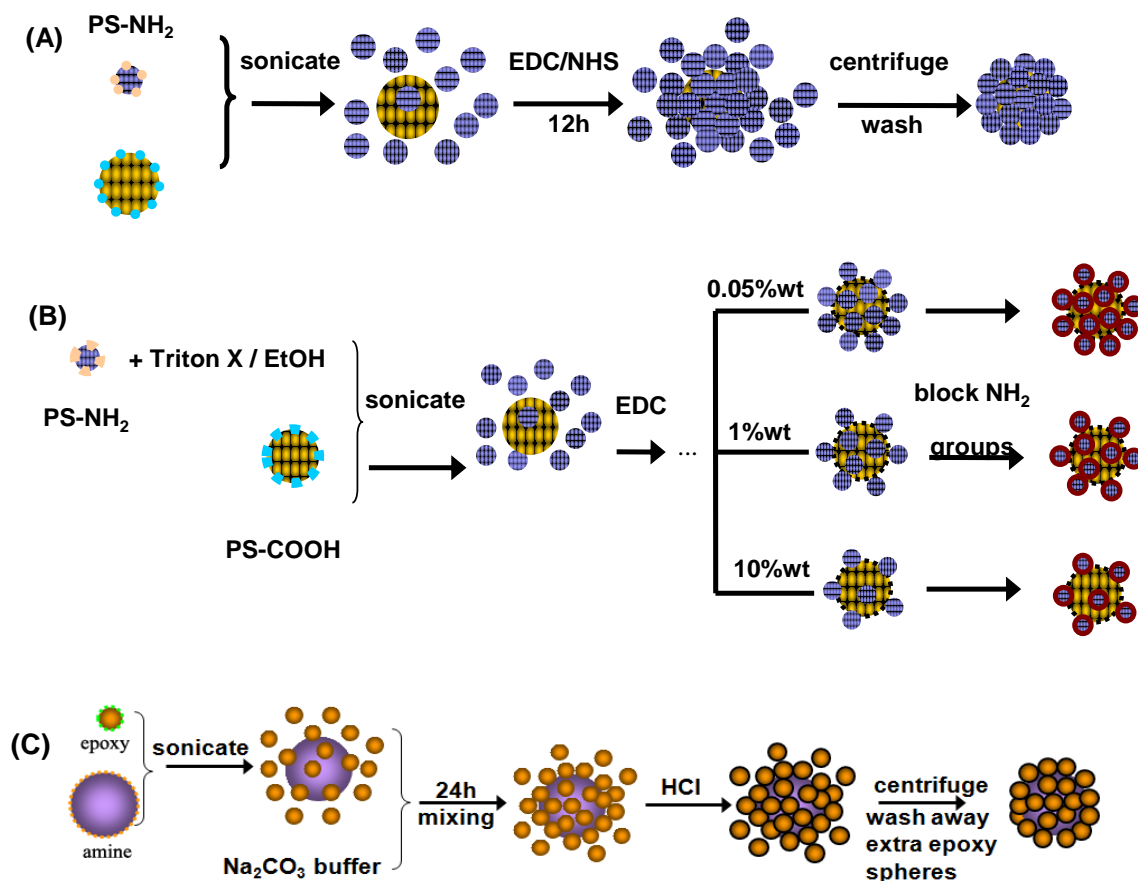


Figure 3.4 Simplified reaction schemes for the preparation of (A) raspberry-like hierarchical spheres and (B) strawberry-like hierarchical spheres via carbodiimide chemistry and (C) raspberry-like hierarchical spheres via epoxy chemistry.

3.5 Separation of hierarchical templates.

The separation of the as-formed composite particles from the excess satellite spheres is very important for their later utilization as templates to make hierarchical porous materials (thin films, monoliths, powders, capsules). This required multiple

centrifugation/washing steps. For the carboxyl-amine coupled templates, we found that dilute acetic acid worked well as the solvent. The reasons why diluted acetic acid (1:1 ratio) was used in the preparation of carboxyl-amine coupling templates is as follows: First, acetic acid can protonate the amine groups on the surface of the raspberry-like template. Because the templates have positive charges on their surface, they repel each other to prevent agglomeration. Thus, the extra satellite spheres can be separated from the templates. Second, acetic acid is a good solvent for both organic and inorganic materials, and it wets the hydrophobic polystyrene surfaces well. When other acidic solvents were used, the dispersion was bad (e.g. HCl of the same concentration or pH value), which indicates that it is not due to the pH value or salt effect alone. Third, the density of pure acetic acid is 1.049 g/mL (Fisher Scientific MSDS), which is pretty close to the density of polystyrene 1.055 g/mL (Invitrogen MSDS of the polystyrene spheres). When concentrated acetic acid was used, long centrifuge times were needed for the templates to settle; so a dilute solution was used. In later work, concentrated acetic acid was used to pack the template. In this case, a relatively stable colloidal template solution (templates won't settle by gravity before the evaporation due to the close densities) is required. For the epoxy-amine coupled templates, water can be used in the washing/centrifugation steps as the spheres are stabilized with surface sulfate groups present on the PS-Epoxy/Sulfate satellite surface.

3.6 Characterization

Figures 3.5 and Figure 3.6 show SEM images of several different sizes of the

hierarchical templates prepared using the coupling reactions depicted in Figure 3.3. Since the templates are made by chemically bonding PS spheres together, both the "core" and "satellite" spheres can be different sizes. We can very easily change the core and satellite sizes as needed for the design of that optimal hierarchical material with the correct balance of macroporosity (defined by core sphere) and sub-macroporosity or mesoporosity (defined by the size of the satellites). In Fig. 3.5, hierarchical templates with 340/29 nm, 710/29 nm, 710/60 nm, 1200/29 nm and 1200/60 nm core/satellite by epoxy/NH₂ coupling are shown whereas in Fig. 3.6, hierarchical templates with 1500/110 nm and 450/80 nm core/satellite prepared by COOH/NH₂ coupling are shown. When the hierarchical templates are properly washed/centrifuged, monodispersity is good (estimated to better than ~ 90% from SEM images).

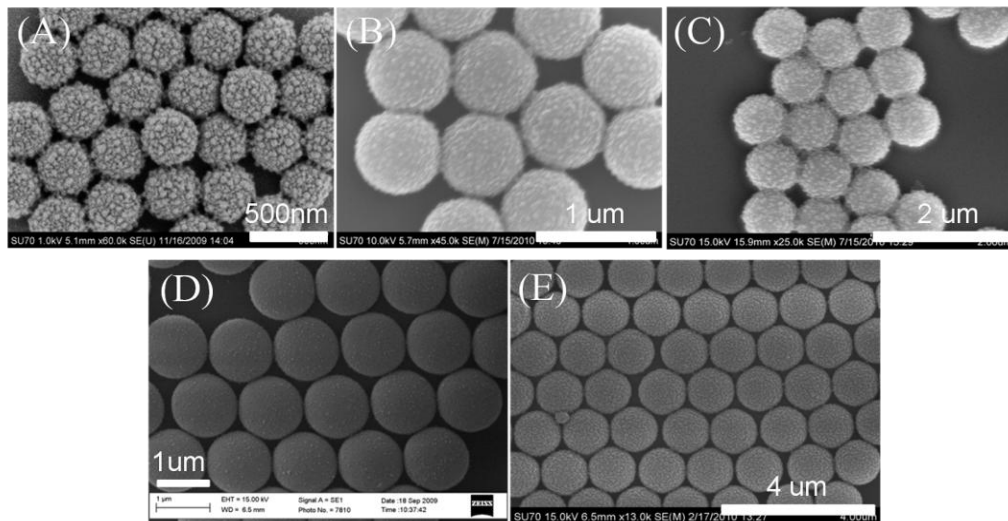


Figure 3.5 SEM images of raspberry-like hierarchical templates (A) 340 nm/29 nm templates, (B) 710 nm/29 nm templates (C) 710 nm/60 nm (D) 1200 nm/29 nm (E) 1200 nm/60 nm prepared by coupling PS-NH₂ spheres with PS-Epoxy/Sulfate spheres.

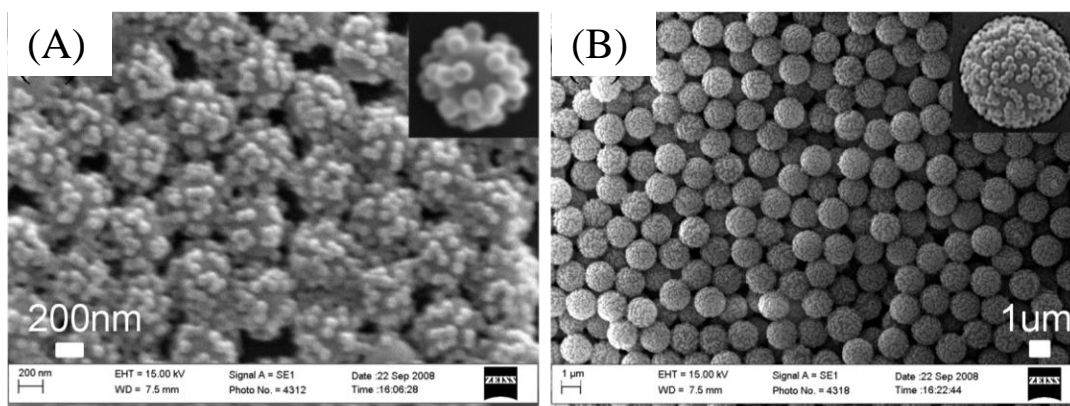


Figure 3.6 SEM images of raspberry-like hierarchical templates (A) 450 nm/80 nm templates, (B) 1500 nm/110 nm templates prepared by coupling PS-COOH spheres with PS-NH₂ spheres. Insets are the blowups of each template.

For the epoxy-amine coupling, an excess amount of satellite spheres was dispersed in deionized water followed by the addition of the core spheres. The epoxy spheres used here have many SO₄²⁻ groups on its surface, thus they disperse well in aqueous solution. In a pH = 7 solution, each of the positively charged NH₂-PS spheres are surrounded by the negatively charged epoxy-PS spheres due to electrostatics. After the spheres are well dispersed in solution, the pH of the solution is increased to pH=10 via the addition of Na₂CO₃ to the system. After mixing and coupling for 24 h, the raspberry templates were obtained. By slowing down the coupling process via pH, control over the coverage can be achieved. As described above for the raspberry-shaped templates, the hierarchical templates were then separated from the extra NH₂-PS spheres via successive washing/centrifuge steps. The templates were redispersed and incubated for 3-4 h in the Sulfo-NHS-acetate/ PBS solution to block the amines. This step is not necessary when the satellites can totally cover the core sphere, otherwise it is needed to remove the positive charge on the templates to make them more stable in the solution.

Since the templates are made by chemically bonding PS spheres together, both the "core" and "satellite" spheres can be of different sizes. We can change the core and satellite sizes as needed. Compared with other templates, 450 nm/80 nm in Fig.3.6 (A) are less uniform and show lower coverage. This can be explained by the relative size between the core and satellite. The ratio of core size to satellite size for 450 nm/80 nm is smaller than all the other three sizes. Thus, for 450 nm/80 nm template, the steric hindrance and repulsive charge effect become significant between the satellite spheres, and it is harder to obtain high coverage.

In addition to varying the sizes of the core/satellites, it is also possible to modify the number density of the satellites to form particles that are raspberry-like vs. strawberry-like. This feature was demonstrated using the 1500/110 nm hierarchical spheres, Figure 3.7. To vary the number of satellite spheres on the central core and form what are called "strawberry-like" hierarchical templates, either the amount of carbodiimide, the reaction time, or the reaction rate could be changed. The most success was found by modifying the solvent to slow down the coupling reaction between the PS-COOH and PS-NH₂. In this work, the concentration of Triton X-100 in ethanol was changed to alter the viscosities of the coupling solution and hence the rate of diffusion and reaction. The net result was a change in the coupling efficiency and a subsequent change in the number of satellites that attach to the center core.

Fig. 3.7 shows SEM images of 1500/110 nm hierarchical spheres obtained using different concentrations of Triton X. As the concentration of Triton X increases, the number of satellites that attach to the core decreases from (A) to (D). The uniformity is

also lost, which is consistent with our assumption that the viscosity influences the coupling efficiency. In general, these strawberry-like hierarchical spheres were less stable and more prone to aggregation relative to the raspberry-like spheres. Because the core sphere is only partially coated with satellite spheres, the unreacted COOH groups are exposed to solution and can also influence the overall surface charge of the hierarchical particle. Stability was improved by capping the NH₂ groups on the satellite spheres with NHS-acetate making them less attractive to each other. The raspberry-like spheres, being fully coated with satellite spheres, have barely any exposed COOH groups to influence the surface charge and react with PS-NH₂ and are thus less likely to aggregate. The long-term stability of these raspberry-like hierarchical templates was very good.

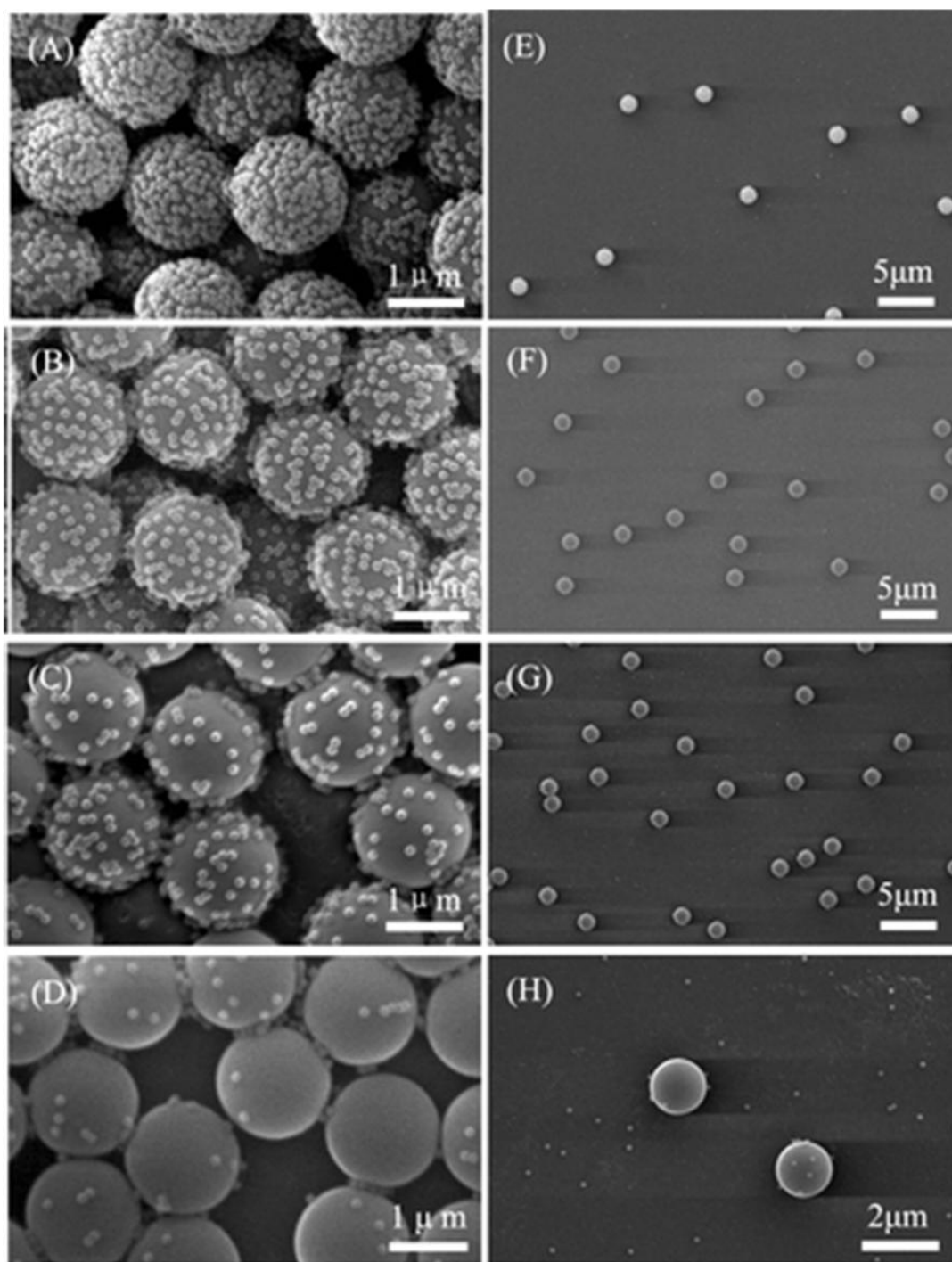


Figure 3.7 SEM images of 1500/110 nm “raspberry-like” templates (A, E), and “strawberry-like” templates synthesized at a Triton X-100 concentration of 0.05 wt % (B, F), 1 wt % (C, G), and 30 wt % (D, H). A → D show close-ups of the template spheres where E → H show that the spheres can be isolated and dispersed on a glass slide.

The SEM images in Fig. 3.8 show packed ensembles of the "raspberry" and "strawberry" templates of 1500 nm/110 nm made by COOH-NH₂ coupling using 0.05 wt% (B), 1 wt% (C) and 10 wt% (D) Triton X-100. Those monodispersed templates can be fabricated in a relatively large amount, and uniformity is relatively good through the whole batch, which provides an advantage in structure design. Figure 3.9 shows the images of 450nm/80nm strawberry templates under two different magnifications. This 450/80 nm strawberry template is hard to control compared with the 1500/110 nm strawberry template because of the similarity in the size of the core and the satellites makes it hard to distribute those two type of spheres well making sure each core is surrounded by satellites. Aggregation is a problem.

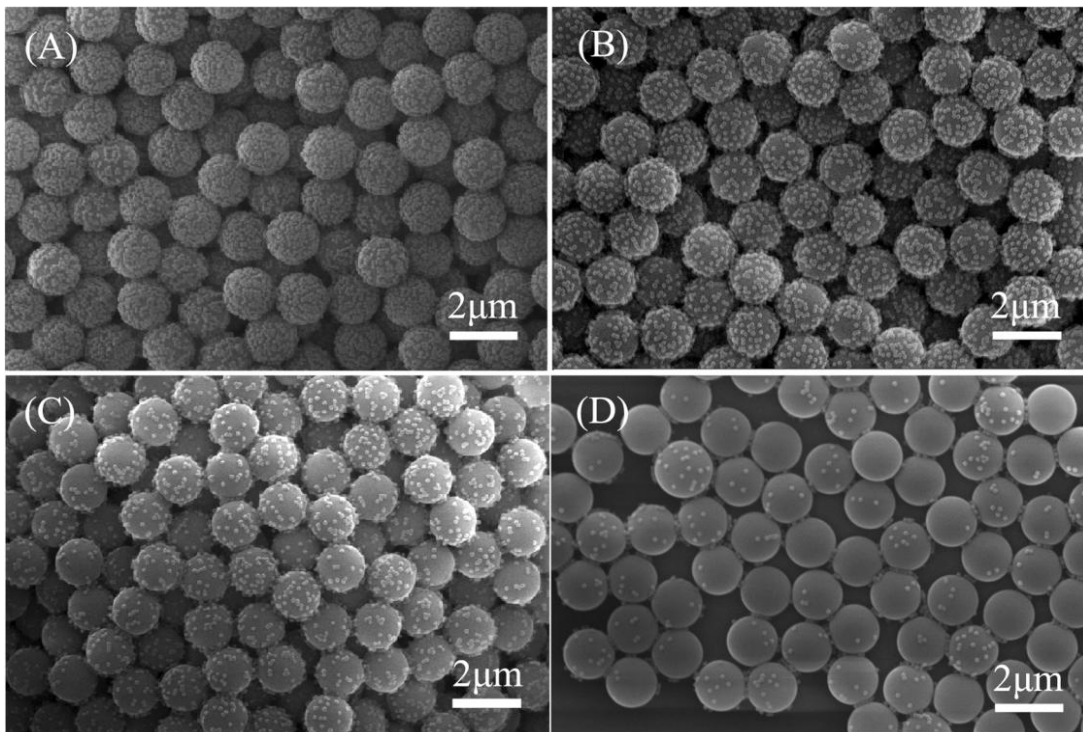


Figure 3.8 SEM images of a collection of 1500/110 nm raspberry (A) and strawberry templates (using 0.05 wt% (B), 1 wt% (C) and 10 wt% (D) triton X-100).

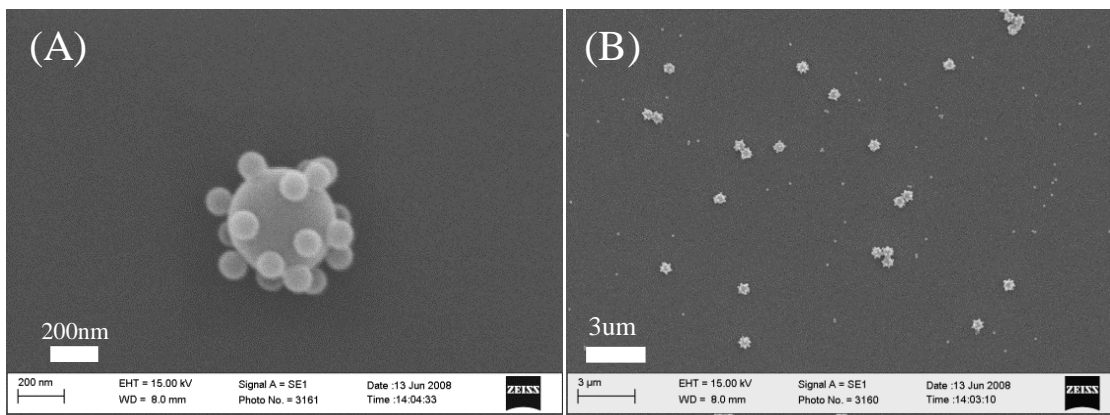


Figure 3.9 SEM images for the 450/110 nm strawberry templates under high (A) and low (B) magnification.

3.7 Packing of spheres

Latex spheres can be packed on a surface in a close-packed arrangement using a number of different procedures reported in the literature that include sediment, capillary force induced packing, electrophoretic deposition, etc.^{39,183,184, 185,186}

(1) Evaporation induced self assembly. One of the most effective and convenient ways to form a large area with good packing is via the evaporation induced self-assembly method.^{187,188} In this method, 50 μL of the template suspension is placed on a clean gold slide and slowly evaporated under a 40-50% humidity atmosphere. The assembly of the setup is shown in Figure 3.10 (1). The template suspension dries from the center of the confined area, and gradually expands to the edge, which results in a thin center with very thick edge. In our case, the surface of gold is first self assembled with a layer of cysteamine to improve the wettability of the gold slide. During the slow evaporation process, the templates assemble in a close-packed arrangement by capillary forces.^{53,189} This approach usually produces multilayers of spheres, the thickness of which depends

on the concentration and the amount of spheres in the colloidal suspension.^{66,190} To obtain close packing, slow evaporation is crucial. By evaporating under a saturated atmosphere, good packing can be obtained. According to a previous study¹⁹¹, the attractive capillary force and mobility of templates during solvent evaporation are the two governing factors for ordering. The interaction between charged templates and the substrate affects the mobility of the spheres on the surface. When the templates and the substrate have the same surface charge, ordered self-assembly can be achieved. However, when they have opposite charges, strong coulombic attraction between the spheres and the substrate takes place and the net result is disordered packing due to strong adhesion and low mobility of templates.¹⁹² To avoid the templates from settling before the solvent evaporates, the solvent needs to have a density close to the PS material to sustain the colloidal suspension state. In this work, we use this well-established procedure for uni-modal templates to pack our raspberry-shaped hierarchical template (COOH-NH₂) in a close-packed arrangement under an acetic acid atmosphere.

(2) Buchner funnel packing under weak vacuum. In this procedure, the templates are packed on a polycarbonate membrane (pore size 1 μm) in the Buchner funnel using a weak water faucet vacuum (Figure 3.10 (2)). As the liquid phase gradually passes through the filter (membrane), the templates pack on the PC membrane as shown in Figure 3.11 (c). This method was used to fabricate a multimodal porous silica monolith. Experimental details will be discussed in chapter 4.

(3) Self-assembly method is based on electrostatic force or chemical bonding between the template and the substrate. By exposing the gold slide to the amine terminated

templates, the template will be assembled on the gold slide as shown in Figure 3.10 (3) due to the interaction between gold and amine groups. This method produces a very low packing density of templates particles on the surface, due to the electrostatic attraction between the template and the substrate, which will restrict the mobility and hence the packing of the templates. In Figure 3.12 (B), the 450/80 nm COOH-NH₂ templates were self assembled on a clean gold surface. As can be seen, there is no order to the packing. Hence, this method is not a good way to make ordered arrays of templates.

(4) Dip coating with an angle. In this method, a cysteamine modified gold slide is placed on a stationary plastic slide and pulled by a thread attached to it as shown in Figure 3.10 (4). During the slow movement at the pulling direction, the gold slide will be pulled out of the template suspension at an angle, during which the templates pack on the gold slide. The key is to minimize the friction between the stationary slide and the moving slide to manage a smooth and uniform motion. It is difficult to completely remove the friction just by a consistent pulling force in this experiment, thus the packing is not good. As shown in Figure 3.12 (A), the packing is only good over a small range, and several areas of bare substrate are exposed.

(5) Slow speed spin coating. In this procedure, a drop of the template suspension is placed on a cysteamine modified gold slide, and then the slide spin coated at a slow speed (400-600 rpm). The mechanism is shown in Figure 3.11 (b). By slow speed spinning, a balance between the suspension surface tension contraction from the water solvent and the centrifuge force can be achieved. The centrifugal force will push the suspension to the edges, leaving a very thin layer of suspension in the center exposed to the air. Thus,

evaporation happens from the center, and then gradually to the edge. Similar to evaporation induced packing, this packing also takes advantage of capillary forces between the template particles, but is faster. The packing is thin at the center and thick on the edge.

(6) Drop evaporation with an angle. In this method a drop of the template suspension is placed on a cysteamine modified gold slide and then the gold slide tilted at a certain angle (~30 degree) where the solvent gradually evaporates without disturbance or vibrations. Like that shown in Figure 3.11 (a), the meniscus of the suspension will push the templates up along the substrate, and the capillary force among the template particles will pull the particles together into close packed arrangement as it dries.

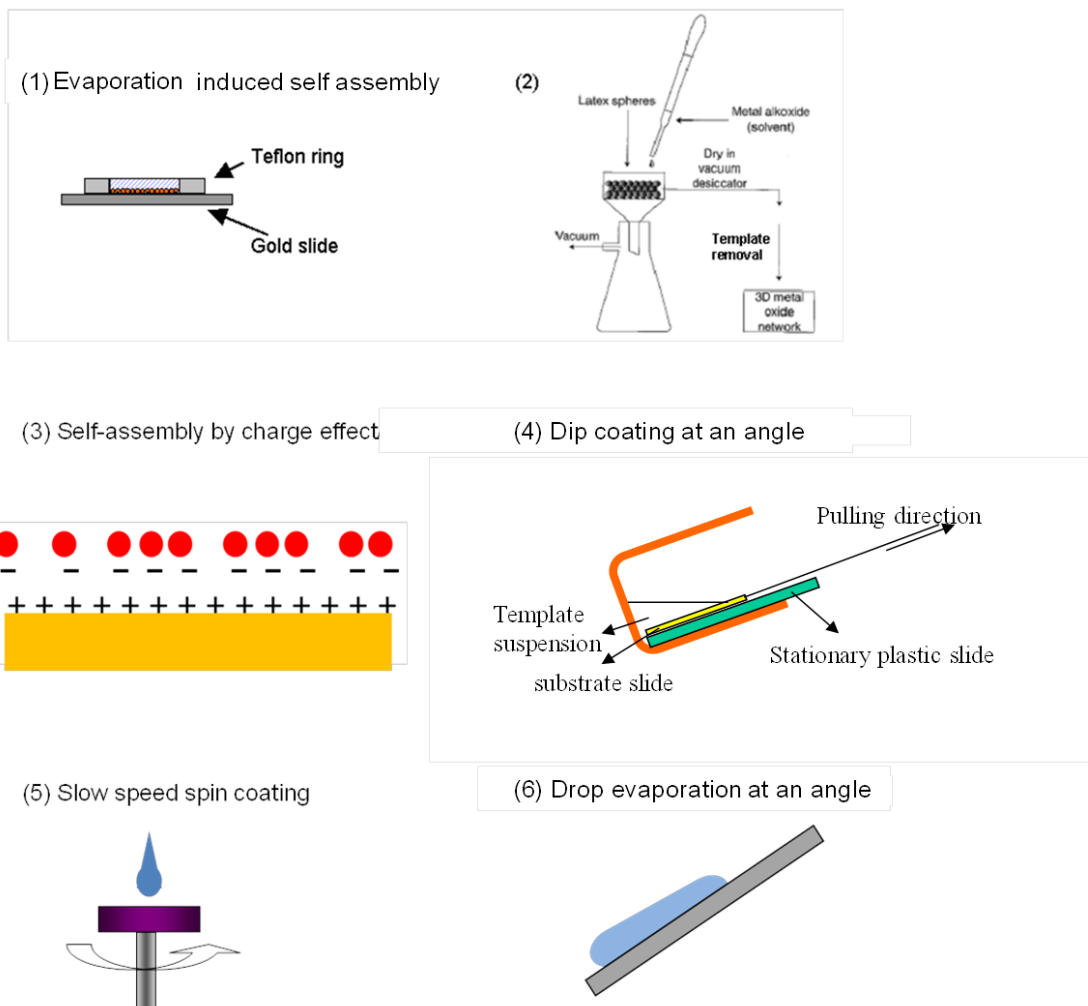


Figure 3.10 Overview of the different template packing approaches. (1) Evaporation-induced self organization, (2) Filtering by Buchner funnel, (3) Slow speed spin coating (4) Dip coating at an angle (5) Self-assembly via electrostatics or chemical bonding and (6) Drop evaporation at an angle.

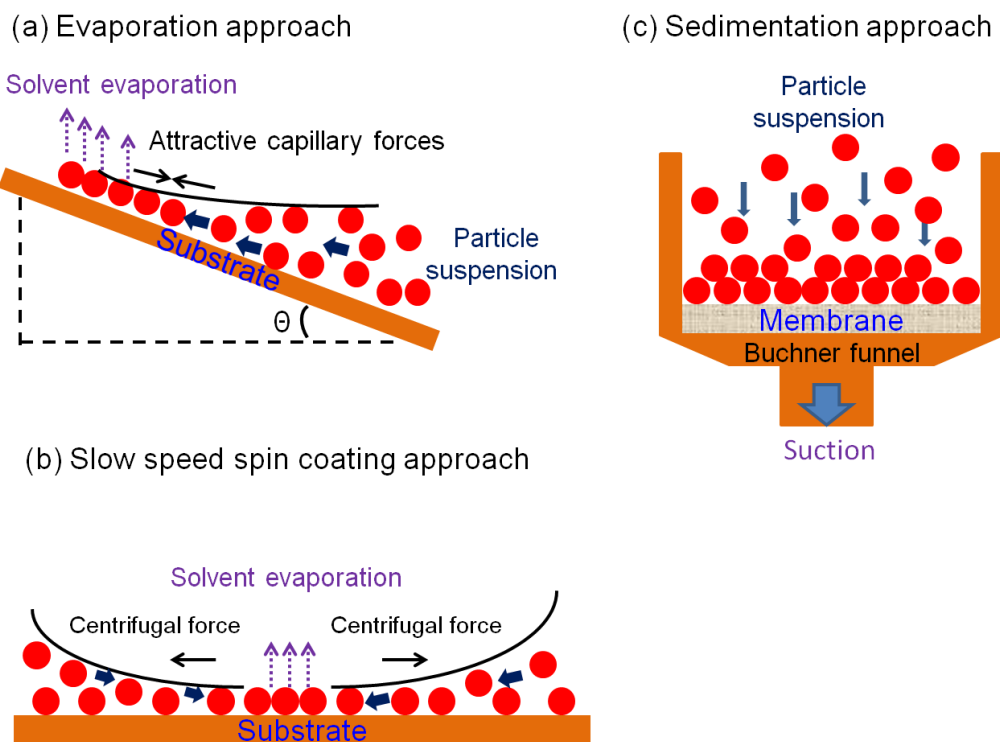


Figure 3.11 Template packing mechanism: (a) evaporation approach, (b) slow speed spin coating approach,^{53,193} and (c) sedimentation approach.

Compared with unimodal polystyrene spheres, the hierarchical templates have rough surfaces, which to a certain degree can limit template mobility on the surface of the substrate. Acetic acid was used to help disperse the COOH-NH₂ templates in solution and monodispersed templates were used to form the packing. A certain percentage of the PS sphere surface is occupied by well-separated, monovalent functional groups. The remaining surface is made up of the stacked benzene rings of the polystyrene, which are hydrophobic (<http://www.invitrogen.com>). Acetic acid is a good solvent for both aqueous and organic solutions. So here, as we see from the SEM, the templates are perfectly monodispersed. Neither HCl or H₂SO₄ was as effective as acetic acid in dispersing and wetting the hierarchical spheres. Using concentrated acetic acid as the solvent, however,

does cause many problems because it is so corrosive. But there are still many methods that can be used to pack the hierarchical templates. For NH_2 -epoxy templates, the dispersion can be carried out in aqueous solution since the satellite sulfate/epoxy spheres can be easily dispersed in water. It is easier to pack these hierarchical templates without concern with contaminations resulting from the caustic acetic acid. Packing methods (5) and (6) in Figure 3.1.0 were used for the NH_2 -Epoxy hierarchical template while for the COOH-NH_2 templates, the evaporation induced packing method and Buchner funnel packing were used.

The packed hierarchical templates can then be used to prepare porous materials with well-defined architecture. Multimodal porous silica was fabricated using the 1500/110 nm hierarchical template packing while the bimodal macroporous gold electrodes were fabricated using the 1200/60 nm hierarchical template as described in chapter 4 and chapter 5. The 1500/110 hierarchical template was also used to prepare hollow capsules as described in chapter 6.

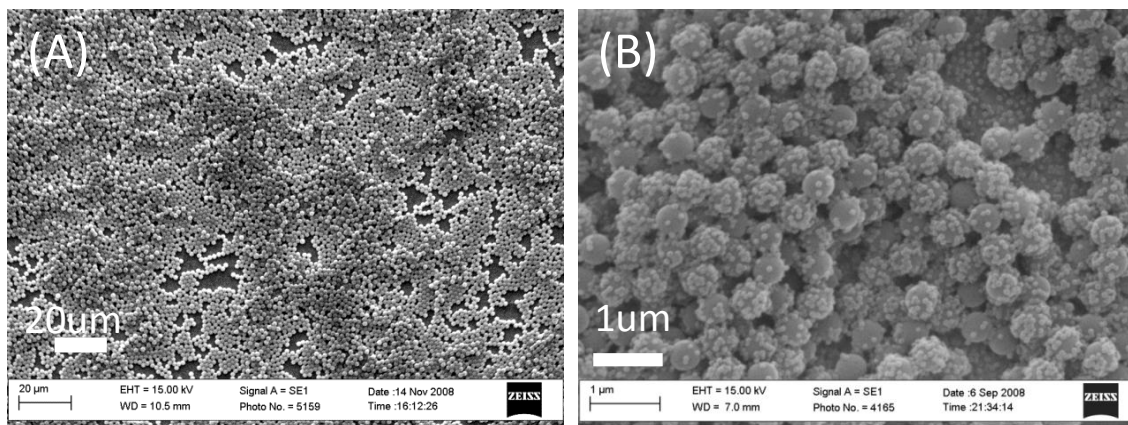


Figure 3.12 SEM images of template packing by different method (a) dip coating with an angle and (b) self-assembly by charge effect.

3.8 Advantages of the hierarchical templates.

Materials with well-defined pore sizes and long-range order can be prepared straightforwardly by coupling sol-gel chemistry with templating or by electrodepositing metals around templates pre-organized on a conducting surface. For example, macroporous gold, platinum, and copper electrodes with well-defined macropores have been made by electrodepositing suitable metal salts around a colloidal crystal template.^{66,190} Ordered mesoporous silica materials (powders, films) have been prepared using surfactant assemblies as a template (or site-directing agent)¹⁹⁴ while ordered macroporous materials (powders, films, monoliths) have been made using colloidal crystals as templates.^{33,153} More recently, silica with bimodal (or hierarchical) pore structure has been made by dual templating procedures as well as via layer-by-layer assembly and self assembly methods that utilize particles/templates of differing length scales/composition (nano to micron).^{84,91,93,195-198} These approaches can be quite complicated because of the multiple templates involved and the interplay that is often needed to successfully produce the desired material.

The advantage of utilizing a hierarchical template to create two vastly different types of hierarchical porous materials (multimodal silica and a bimodal metallic thin film) is demonstrated in this work. This approach has three noteworthy features worth mentioning: (1) the template itself is hierarchical thus ensuring an interconnected pore structure with the larger pores connected through smaller pores, a necessary requirement in many applications, (2) the templates can be easily captured in a pellet form via centrifugation, dispersed in an appropriate solvent, and then assembled on a surface in a

2D (for film formation) or 3D (for monolith/powder formation) architecture, thus maximizing flexibility in material fabrication, and (3) the template is prepared from only one material thus allowing it to be easily removed from the matrix in a one-step procedure under mild conditions minimizing sample/substrate destruction to yield the bimodal porous material with pores of well-defined sizes that corresponded to the size of the template.

The isolated hierarchical spheres can be assembled on a suitable surface in a quasi-close-packed arrangement using methods previously reported in the literature¹⁵³ and described above. Figure 3.13 shows SEM images of a single layer packing of 340/29 nm NH₂-epoxy raspberry-like templates and the top surface of 1500/110 nm diameter COOH-NH₂ raspberry-like spheres packed in an organized fashion prepared using the drop evaporation with an angle induced self organization and the Buchner funnel sedimentation packing method. As can be seen, the presence of the smaller satellite spheres on the central core does not significantly influence the way the spheres are able to pack. The packing obtained is similar to that obtained when using traditional monodisperse unimodal latex spheres of similar size. After the hierarchical colloidal crystal is encapsulated into a suitable host framework, the individual templates can then be removed via calcination or chemical treatment. Because the hierarchical sphere is composed of one material (e.g., polystyrene), it can be easily removed from the matrix using a single solvent.

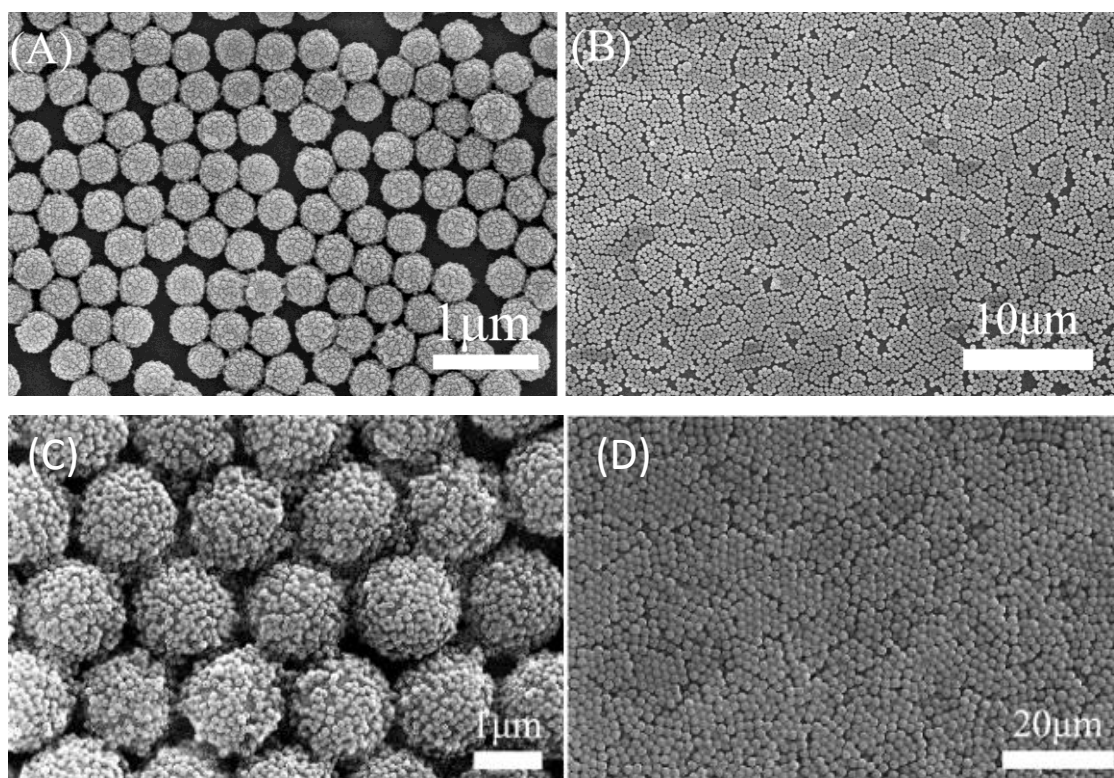


Figure 3.13 (A) (B) SEM images of 340/29 nm on glass slide by evaporation induced packing at an angle and (C) (D) 1500/110 nm hierarchical spheres on polycarbonate membrane packed by Buchner funnel packing at two different magnifications.

3.9 Introduction of the applications of those hierarchical templates

By using the as-formed hierarchical templates, a variety of different multimodal porous materials can be designed and made including multimodal porous monoliths, thin films, or hollow spheres as shown in Figure 3.14. In the following three chapters, the fabrication and characterization of multimodal porous monoliths, thin films and capsules using the hierarchical templates are presented as examples for 3D, 2D and 0D multiporous materials.

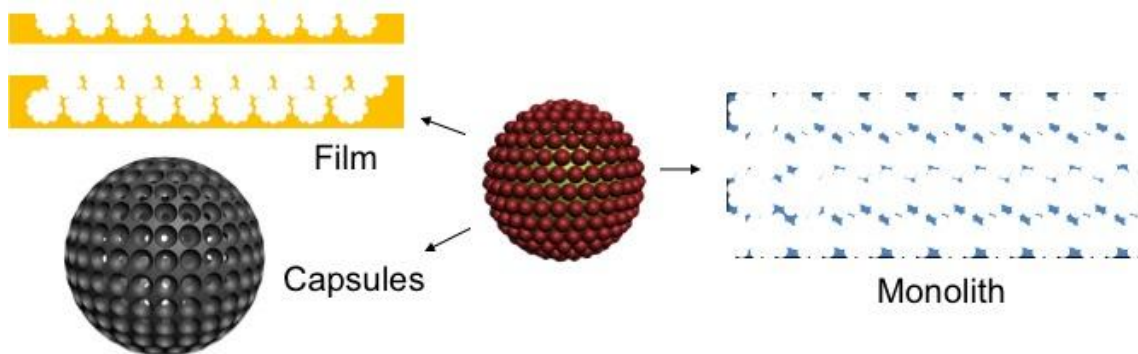


Figure 3.14 Illustration of the type of 3D, 2D and 0D hierarchical porous structures that can be fabricated using hierarchical templates.

3.10 Conclusion

Hierarchical templates with raspberry and strawberry morphologies were fabricated by chemically binding two types of polystyrene spheres together and packed in a close-packed arrangement. The templates are size tailorable in both core and satellite sizes. Strawberry-like templates were obtained with different coverage by slowing down the coupling efficiency. The controllable design of the templates provides us more possibilities and control in porous materials design. Hierarchical templates of a predefined size and shape can be used to prepare multimodal porous materials with a well-defined large macropore surrounded by much smaller pores. The large macropore can provide easy access to the inner pores, which help to increase the overall surface area of the porous material. The advantages that this approach provides are simplicity and versatility: (a) the template is size-tailorable through alterations in the size of the central core and/or satellites and by changing the number density of the satellites; (b) only one template is needed in contrast to combining two or more templates, which can complicate

the chemistry; (c) both 2D (films) or 3D (monoliths, powders) can be made, (d) having a hierarchical template that is made completely out of polystyrene allows flexibility in removal via mild solvent dissolution (e) the materials produced have well-defined pore sizes that are interconnected. The one current drawback is access to the “micropore” ($d < 2 \text{ nm}$) and to some extent the “mesopore” ($2 \text{ nm} < d < 50 \text{ nm}$) regions is limited by the smallest size of the latex sphere that can be purchased commercially. However, this limitation can likely be circumvented by in-house synthesis or utilization of another type of appropriately functionalized colloid. It is envisioned that these hierarchical porous materials will be useful as platforms for chemical sensing, chromatography, and catalysis.

Chapter 4 Multimodal porous silica

4.1 Introduction

In this chapter, well-defined multimodal porous silica is fabricated by the hard templating method using the 1500/110 nm COOH-NH₂ hierarchical raspberry-like template prepared as described in Chapter 3. The major objective of this study is to demonstrate the feasibility of using the hierarchical template to obtain 3D structured multimodal porous using silica as an example. The materials produced can be easily modified and functionalized for further applications.

4.2 Background and purpose

Porous silica materials prepared by the sol-gel process have been extensively studied.^{111,199} The properties of the material can be tuned by varying the sol-gel synthesis conditions such as pH, temperature, and additives. The ability to dope various molecules, particles, etc. into the silica network makes silica very useful for different applications.²⁰⁰⁻²⁰³ Furthermore, another reason silica supports have gained so much attention is because the surface of silica can be easily modified and functionalized.²⁰⁴

Significant interest has recently been directed toward the fabrication of hierarchical porous supports. Such hierarchical structures are particularly useful for applications that require fast and efficient transport in, out, or within a high surface area porous framework such as in separations, energy storage, drug delivery, catalysis, sorption, tissues engineering and chemical sensing.^{37,39,205-208} These supports, with a desired acceptor or special molecule assembled on its surface, can provide a effective platform for generating sensitive sensors, highly efficient catalysis supports, high volume dosimeter, etc.

Multimodal porous silica structures have been made using a dual templating method, such as combining polystyrene spheres with an ionic liquid²⁰⁹ or combining polystyrene with microporous zeolite.²¹⁰ Phase separation¹²² and self assembly²¹¹ have also been used for this type of material fabrication. In this work, a vastly different approach was used to prepare hierarchical porous structures. This approach starts with a hierarchical template, which is defined as a template with morphology on different length scales. The hierarchical template is combined with conventional one-step hard templating methods to form the multimodal porous structure. The main advantage of this strategy is the tailorability of the pores, which provides more control over structure design.

4.3 Fabrication process

Reagents and chemicals. Tetramethoxysilane (TMOS, 98%) and dimethyldiethoxysilane (DMDEOS) were purchased from Aldrich. All reagents were used as received. Polycarbonate filters (1 μm) were purchased from SPI supplies. Water was purified with a Millipore water purification system.

Instrumentation. N_2 sorption experiments were conducted with a Quantachrome Autosorb 1 MP analyzer with an equilibration time of 3 minutes. Samples were outgassed at 120 $^{\circ}\text{C}$ overnight.

Synthesis of multimodal porous silica. The original silica sol was prepared by mixing 1000 μL TMOS, 300 μL of DMDEOS, 2000 μL of ethanol, and 300 μL of 0.1 M HCl followed by stirring for 30 min and aging for two days at room temperature. The hierarchical raspberry-like templates (1500/110 nm) were deposited on a polycarbon filter in a Buchner funnel under vacuum as described in chapter 3.²¹² The sol was then

added drop wise to infiltrate the latex templates while suction was applied. The silica coated colloidal crystal was dried for several hours and then peeled off the filter and further dried for 2 days at ca. 40~45 % humidity at room temperature. When completely dry, the hierarchical template was removed via calcination. The temperature was held at 70 °C for 30 min, and then the temperature was increased to 540 °C at 4 °C/min and maintained at 540 °C for 3 h to yield multimodal porous silica.

To prepare hierarchical porous silica with well-defined macropores, the hierarchical spheres (1500/110 nm) were packed via filtration in Buchner funnel followed by infiltration with a silica sol.²¹² Briefly, the templates were deposited on polycarbonate filter in a Buchner funnel under a weak vacuum. The 3D arrangement of latex spheres was infiltrated with a silica sol prepared by hydrolyzing and condensing TMOS/DMDEOS while suction was applied. When completely dry, the hierarchical templates were removed from the silica framework by calcination to leave porous silica with *innate* mesoporosity along with well-defined *bimodal* macroporosity created from the core/satellite spheres. The innate mesoporosity stems from the nature of sol-gel polymerization which takes place between the individual templates.²¹²

4.4 Characterizations and discussion

A highly simplified diagram of the cross-section of the resultant multimodal silica is shown in Figure 4.1. The textured area represents the mesoporous silica that forms when the silica sol is infiltrated through the network of spheres and subsequently polymerized. Macropore C represents the pore formed from the core sphere and macropore S represents that formed from the satellite sphere. Windows are formed in the location

where two spheres make contact such as at the core-satellite interface and the interface between adjacent hierarchical templates. These are the regions where there will be significant size disparity as the silica framework will be thin and fragile.

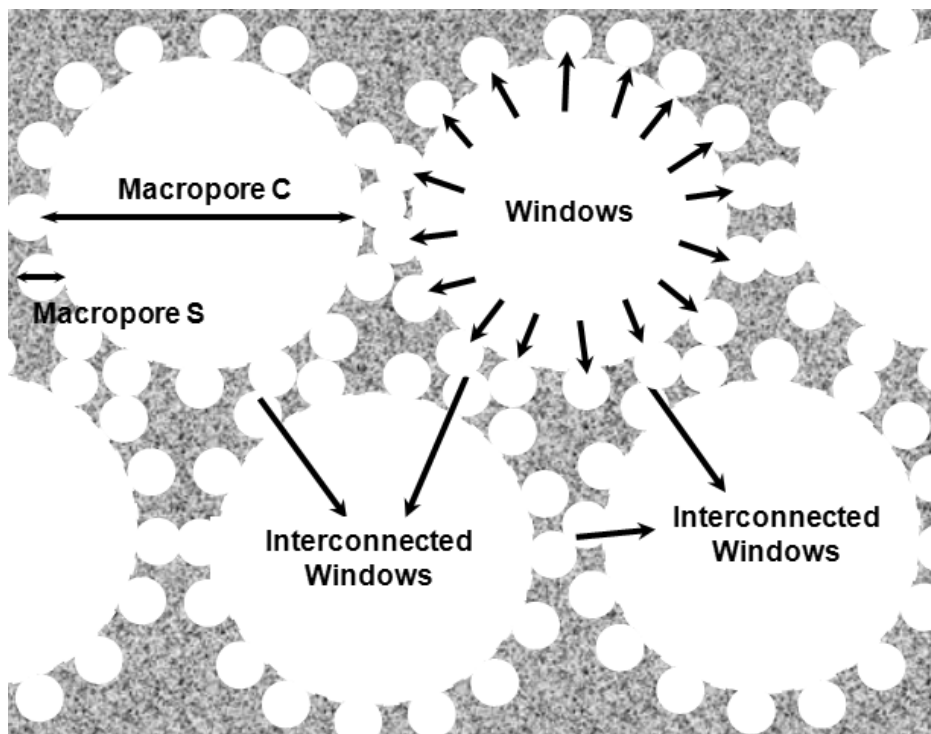


Figure 4.1 Simplified diagram of the cross-section of multimodal silica along with relevant parameters.

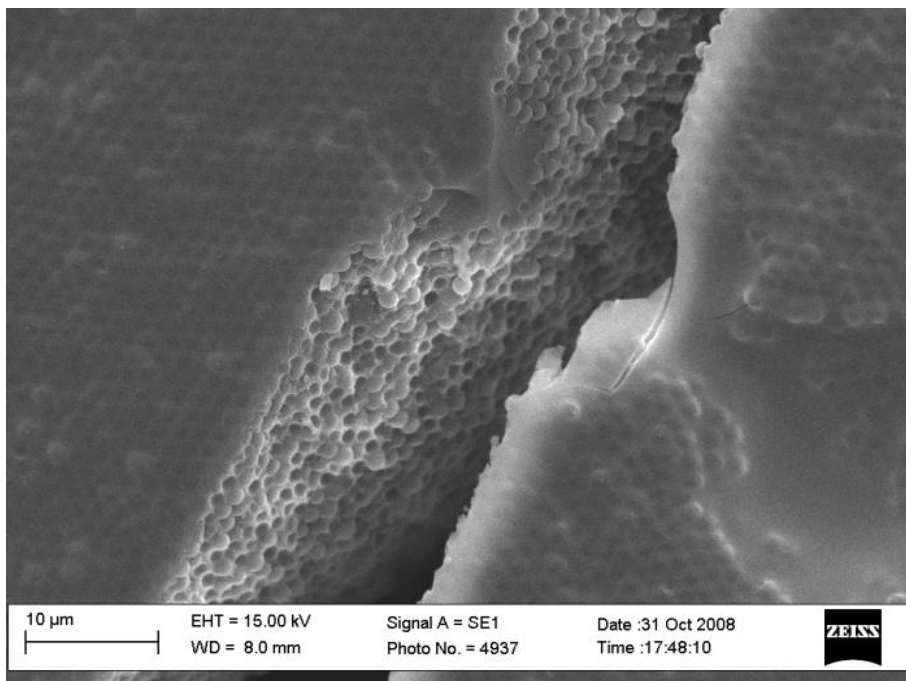


Figure 4.2 SEM image of the silica gel/hierarchical template (1500/110 nm) composite made by using TEOS/DMTEOS silanes. The templates and the cavities are both present at the interface of a large crack made on purpose.

Figure 4.2 shows an SEM image of the silica/hierarchical template (1500/110 nm) composite formed after the infiltration of silica sol into the packed multi-layer of spheres. From the SEM image, a close packed template framework can be seen beneath the silica. On the interface of the crack, the pores generated by the hierarchical templates and the hierarchical templates themselves can be clearly seen. Because of the way the silica cracks, most of the satellites spheres are unplugged by the surrounding silica. The polystyrene spheres can be removed either via dissolution in an organic solvent or via calcination. Even though porous silica shrinks during calcination, calcination strengthens the silica structure and completely removes the template and any organic groups (such as from the silane precursor) to generate three levels of porosity. Compared to calcination,

organic solvent dissolution is not as effective in the complete removal of the polystyrene, particularly for this type of complicated porous structure. The advantage of organic solvent dissolution, however, is that organic functional groups bound to the silica framework are not removed by washing with an appropriate solvent.

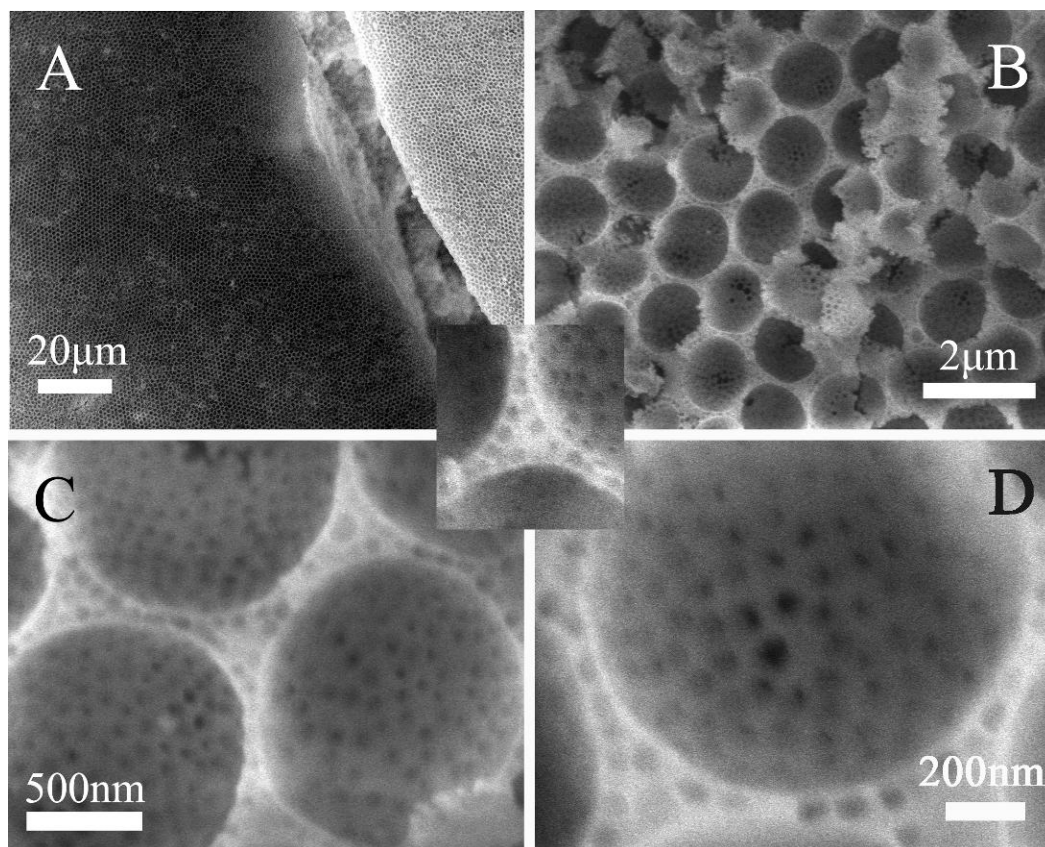


Figure 4.3 SEM images for hierarchical porous silica prepared from the 1500/110 nm hierarchical spheres. Different magnifications are shown.

SEM and TEM were undertaken to obtain a visual image of pore interconnectivity. Figure 4.3 shows SEM images of the hierarchical porous silica prepared using the 1500/110 nm hierarchical templates. In the zoomed SEM images (Fig. 4.3 C,D), the small pores produced from the satellite spheres can clearly be seen on the exterior of the

large macropore formed from the core sphere. In addition, the windows of varying size that lead into the small macropores formed from the satellite spheres located just underneath the large macropore can also be seen.

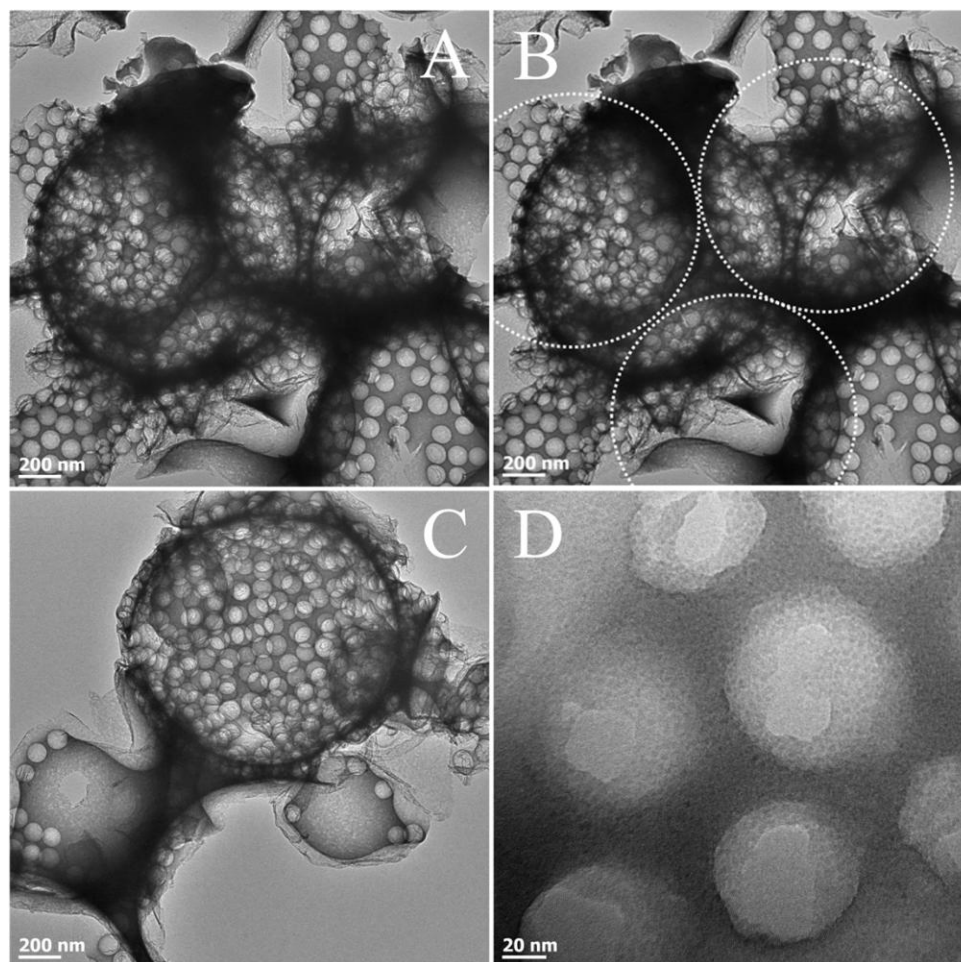


Figure 4.4 TEM images for hierarchical porous silica prepared from the 1500/110 nm hierarchical spheres. A, B are identical images showing neighboring pores. Dashed white circles have added to the image shown in B to aid in the visualization of the pores that resided in the upper layer. C) Single pore with windows (bright spots) clearly visible. D) Small macropores/windows at higher magnification.

The TEM images shown in Figure 4.4 are consistent with SEM images. Figure 4.4A and 4.4B are the same image. In Fig. 4.4A, two large macropores and their

associated windows can be observed adjacent to each other. Also evident in this image but more clearly shown in Fig. 4.4B with the addition of the dashed white circles is remnants from three pores that likely resided one layer above that which was fractured upon sonication. Figure 4.4C shows a TEM image a single pore with smaller pores showing up as bright white spots. A higher magnification image of the small pores (windows) is shown in Fig. 4.4D. As can be seen, the regularity and uniformity of the windows that lead into the smaller macropore is not great as the silica is thin and likely easily fractures in this area. The pore sizes are about 1300 nm and 85 nm by TEM, which is smaller than the nominal size of the templates but can be attributed to shrinkage associated with calcination. It is not uncommon to have some shrinkage in the area of 10-30% in such materials.³⁹ While demonstrated herein with silica, this approach can be easily adaptable to other inorganic precursors such as titanium ethoxide or zirconium propoxide to form bimodal TiO₂ or ZrO₂.²¹²

To evaluate the porosity and pore interconnectivity, particularly mesoporosity, nitrogen sorption experiments were conducted. Figure 4.5 show N₂ adsorption-desorption isotherms for the silica material prepared from the 1500/110 nm hierarchical spheres. In this experiment, the silica material was calcined to ensure complete removal of the polystyrene hierarchical template. As can be seen in Fig. 4.5, the isotherm is Type II and characteristic of a macroporous material showing a significant rise at high P/P₀ range.²¹³ The BET surface area is not particularly large, 74 m²/g, because the material is predominately macroporous with thin walls and little to no microporosity. The presence of hysteresis in the adsorption/desorption branch is indicative of mesoporosity. A plot of

the pore size distribution, calculated using the BJH from the desorption branch, shows a broad peak centered at 12 nm and a small narrow peak at ~ 4 nm. This type of pores arises from the innate porous structure of silica generated by sol gel process. Besides, during calcination, some shrinkage will take place and the methyl groups (which arise from the dimethyldiethoxysilane precursor used) will also be removed thus leading to mesoporosity.

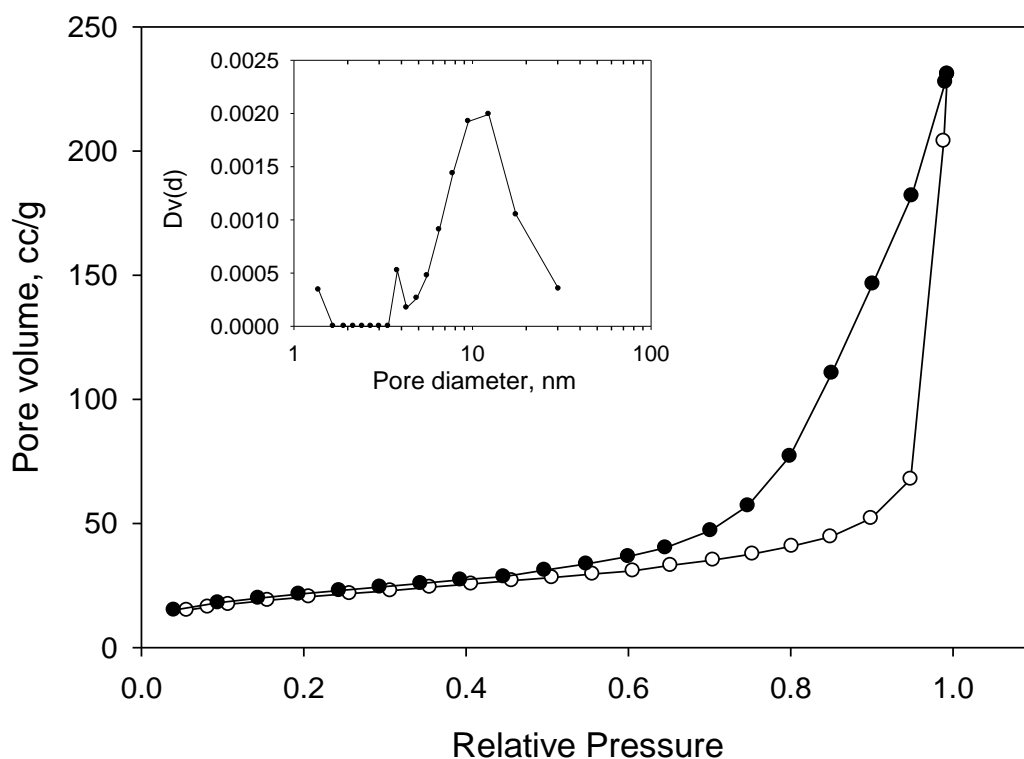


Figure 4.5 N_2 adsorption-desorption isotherm for hierarchical porous silica prepared from the 1500/110 nm hierarchical spheres. Open circles are the adsorption branch; closed circles are the desorption branch. Inset: Pore size distribution obtained from the desorption branch. The lines have been added to guide the eye.

Mercury intrusion porosimetry was also undertaken to more fully characterize the

macroporosity of the multi-modal material produced.²¹⁴ However, the results were less conclusive with the pore size distribution plot showing a very broad peak centered at 500 nm with small shoulders near ~ 150 and ~1500 nm as shown in Figure 4.6. It is clear from the results that the silica material can not withstand the very high pressure required to intrude mercury through the small pores/windows that lead into the large macropore, which has been previously observed for 3D macroporous silica.²¹⁵ The wall thickness is very thin especially in the window regions and it is likely that the small pores fracture because of the pressure needed to intrude mercury through this bimodal pore structure.

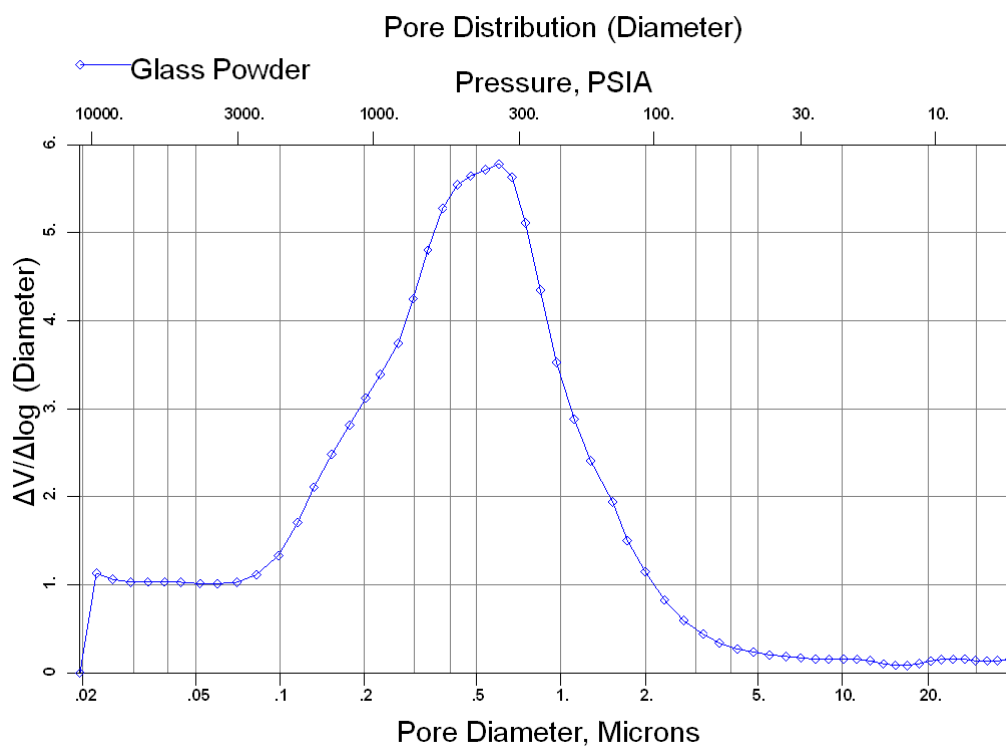


Figure 4.6 Mercury intrusion porosimetry data for hierarchical porous silica prepared from the 1500/110 nm hierarchical spheres.

In related work, we also examined the effect of vacuum and calcination on the material produced. Figure 4.7 shows SEM images of the silica material obtained after a strong vacuum was applied to infiltrate the silica sol into the multi-layer of packed templates using a mechanical pump. The strong force quickly removes extra silica sol to generate a silica structure, which is a thin layer closely attached to the hierarchical templates, as the satellites sphere can still hold some of the silica sol around the template surfaces during the suction. This material is more fragile since the porosity is higher compared with inverse opal structure generated by use of a weak vacuum. With regard to calcination, when the hierarchical template was removed by dissolving in chloroform to form the porous matrix, there was no obvious shrinkage of the silica framework. The pore sizes were similar to the template spheres, as shown in Figure 4.7. The porous matrix can form without calcination, but the interconnected windows are too small to be clearly seen since the silica sol wets the template surfaces pretty well. After calcination, the silica network structure shrinks, and the interconnecting necks become more obvious. A similar effect was also observed in porous capsule fabrication as described in Chapter 6.

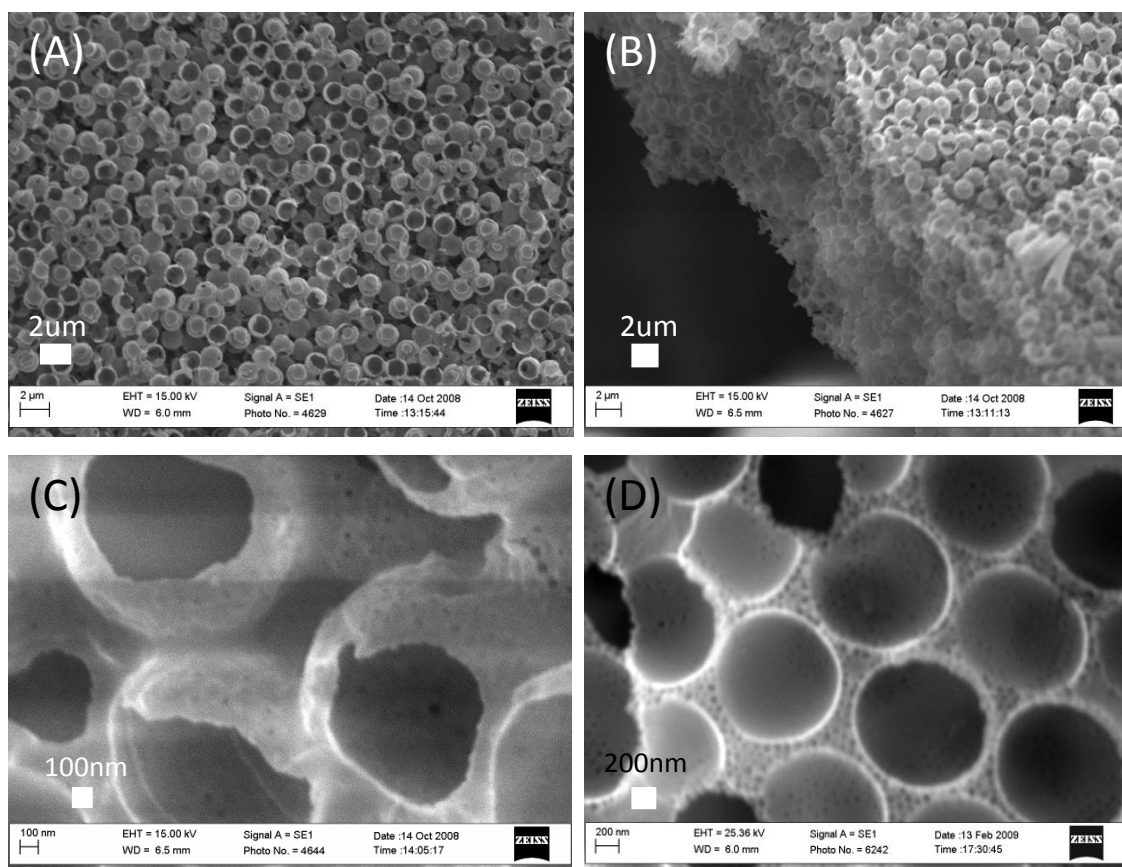


Figure 4.7 Multimodal porous silica generated by using a stronger mechanical vacuum pump. (A) Top view, (B) side view, and (C) blowup of the porous silica surface. (D) Multimodal porous silica generated without calcination.

4.5 Conclusion

A three-dimensional interconnected, highly porous silica material with porosity on different scales, that is, macropores (1.4 μm , 100 nm) and mesopores (12 nm, 4 nm), was successfully fabricated by a hard templating method using well-defined hierarchical templates. The surface area of this porous silica structure was 74 m^2/g by N_2 adsorption measurements at 77 K. A 3D arrangement of well-defined pores of different sizes was obtained, with the bigger pores open to the smaller ones. Thereby the connectivity is

established, which assures the easy removal of the template without disrupting the host material. The silica network itself is porous, thus the resulting material can be considered to have hierarchical multi-modal porosity. Such materials will be useful in separations, purifications, as catalysis carriers, and in the adsorption of gases.

Chapter 5 Bimodal porous gold electrode

5.1 Introduction

In this chapter, well-defined bimodal porous gold electrodes were fabricated by the electrodeposition of gold around preassembled hierarchical raspberry-like templates. The hierarchical templates were made by coupling the functional groups on the surface of two different sizes of PS latex spheres as described in chapter 3. After electrodeposition of gold around the template-packed gold slide and subsequent removal of the template, hierarchical porous gold films with well-defined architecture were obtained.

The major objective of this study was to demonstrate the feasibility of using hierarchical templates to obtain 2D structured bimodal porous thin films and to study their electrochemical properties using both a diffusing and an adsorbed redox couple. Comparisons of surface area and electrochemical response of the hierarchical porous gold electrode and a macroporous gold electrode prepared from 1200 nm diameter NH₂-PS latex spheres and either electrodeposited flat gold or an as-received flat gold electrode were made.

5.2 Specific aim for bimodal porous gold film

High surface area electrodes have received considerable attention in recent years. These electrodes provide an effective way to increase the real surface area of an electrode without compromising its physical size. This attribute is especially important for miniaturized devices that require electrodes to be geometrically small but also to have a high surface area to improve sensitivity and lower detection limits. Rough or porous

electrodes have a higher faradaic current and enhanced sensitivity and low LOD (limit of detection) for certain analytes.²¹⁶ In addition to chemical sensing, high surface area electrodes are also important in the design of catalytic supports, batteries, and fuel cells⁶⁹. High surface area noble metal electrodes have been fabricated using a number of different approaches that include hard templating of latex spheres or SiO₂ spheres, chemical dealloying,²¹⁷ electrochemical dealloying,^{218,219} electrodeposition in the pores of nanopore membranes²²⁰ as well as from ensembles of gold nanoparticles, gold microparticles,²²¹ and electrospun gold nanofibers.²²² The electrochemical properties of such macroporous and nanoporous Au electrodes have been described in the literature.⁶⁶ Advantages include size selectivity in sensing,²²³ more active sites for catalysis,²²⁴ high surface area for signal generating,²²⁵ and high capacitance for energy storage and other electronic device applications.²²⁶

Equally important to the need for high surface area is the need for this area to be accessible. However, pore size limitations hinder the diffusion of analytes deep into the inner surface. For a redox couple with fast electron transfer kinetics, the electron transfer between the electrode and the solution only happens on the top layer of the electrode, thus the inner structure is not used.²²⁷ One means to enhance the accessibility is to design a hierarchical electrode, one that will have well-defined pores on more than one length scale. A large pore, for example, will facilitate transport to the smaller pores, which act to increase the electrode area and provide additional places for electron exchange to take place. However, there have been very few examples of hierarchical porous electrodes with well-defined pores on more than one length scale reported in the literature. In

chapter 3, we described the fabrication of a hierarchical template formed by coupling two different sized polystyrene latex spheres together. The size and morphology of the hierarchical template was defined by varying the sizes of both the “core” and the “satellite” spheres, as well as altering the coverage of “satellites” on the “core”. When these hierarchical latex spheres are used as hard templates, hierarchical, high surface area materials can be easily prepared. The main advantage of such a strategy is that it provides a means to form a hierarchical material with an interconnected pore structure.

5.3 Fabrication process

Reagents and Chemicals

Ferrocene methanol, 97% was purchased from Acros Organics. 2-aminoethanethiol (also known as cysteamine) and HClO₄ were purchased from Fisher Scientific. 6-Ferrocenyl-1-hexanethiol was purchased from Dojindo Molecular Technologies, Inc. All reagents were used as received. Aqueous suspensions of polystyrene (PS) microspheres functionalized with either amine or epoxy/sulfate groups with diameters ranging from 29 nm to 1.2 μm were obtained from Invitrogen (formally Interfacial Dynamics Corporation (IDC), 2.1 wt/v% for PS-NH₂, and 4.1 wt/v% for PS-Epoxy/Sulfate). Gold mirror electrodes (100 nm Au, 10 nm Ti) were purchased from EMF Corporation. The gold plating solution, Gold 25, was purchased from Technic Inc. Water was purified with a Millipore water purification system.

Synthesis of bimodal porous gold films

Highly ordered macroporous electrodes with an increased surface area obtained by electrodeposition of gold around colloidal crystals have been reported in the literature.^{66,190,228,229} This strategy was employed in this chapter to obtain a hierarchical porous gold film with the exception that a hierarchical template was used. Hierarchical gold electrodes with well-defined pores of more than one size were prepared by electrodepositing gold around a packed ensemble of hierarchical PS latex spheres followed by their removal. The schematic process is shown in Figure 5.1.

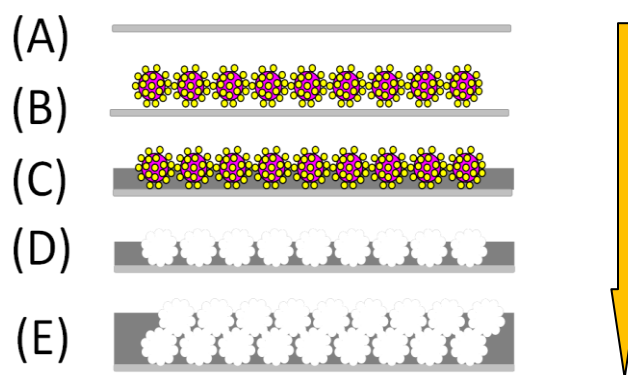


Figure 5.1 Fabrication of bimodal porous gold film (A) clean gold slide, (B) templates packed on the gold slide, (C) gold deposited around the templates by electrodeposition, (D) is ½ layer porous gold film after the template removal, and (E) is 1½ layer porous gold film after template removal.

For templates packed on a gold slide (substrate), the gold surface that is not blocked by the templates is directly exposed to the plating solution (Figure 5.2). Thus the deposition proceeds uniformly within the templates packing. After the deposition, different spots along the gold surface should have the same thickness. Each time, when the quantity of electricity is the same, the same mass of gold will be reduced. Assuming that the depositing area is the same and the packing of templates is uniform and close packed, the

film thickness should be similar for each sample given the same deposition conditions. Thus, we can control the thickness by controlling the quantity of electricity passing through the electrode surface Q .

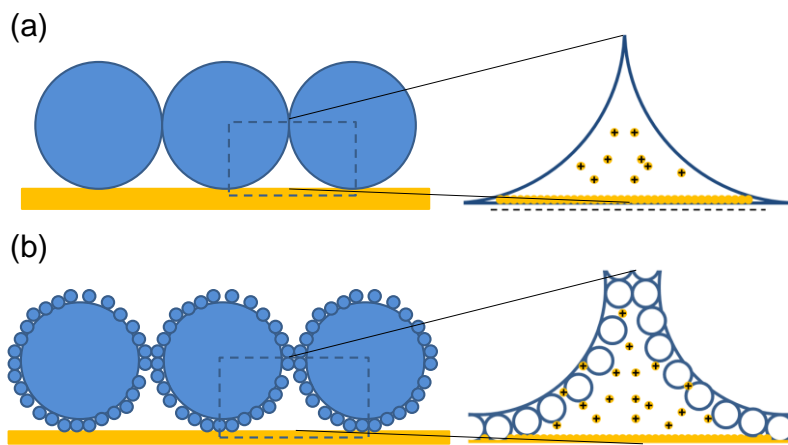


Figure 5.2 Schematic illustration of the formation processes of (a) ordered porous gold film²³⁰ and (b) ordered bimodal porous gold film by electrodeposition. The metal complexes in the solution are reduced on the exposed conductive substrate.

Four different gold plating solutions, their ingredients and the features of the deposited surfaces are summarized in Table 5.1. The corresponding SEM images of the surfaces are also shown in Figure 5.3. Clearly, the commercial plating solution shows the best stability and flat, mirror-like surfaces.

Table 5.1 Four types of gold plating solutions used for electrodeposition and electrode surface feature.

Plating solution	Composition	Deposited surface and stability of the solution
H ₂ AuCl ₄ solution	0.03 M H ₂ AuCl ₄ in water	Rough, stable
Recipe 1 solution	100 g/L Triammonium citrate 25 g/L KAuCl ₄ , 68.5 g/L Na ₂ SO ₃	Relatively smooth, not very stable
Recipe 2 solution	12 g/L H ₂ AuCl ₄ , 5 g/L EDTA, 160 g/L Na ₂ SO ₃ , 30g/L K ₂ HPO ₄	Relatively smooth, unstable
Commercial plating solution	Gold Tech 25	Mirror like plating, very stable

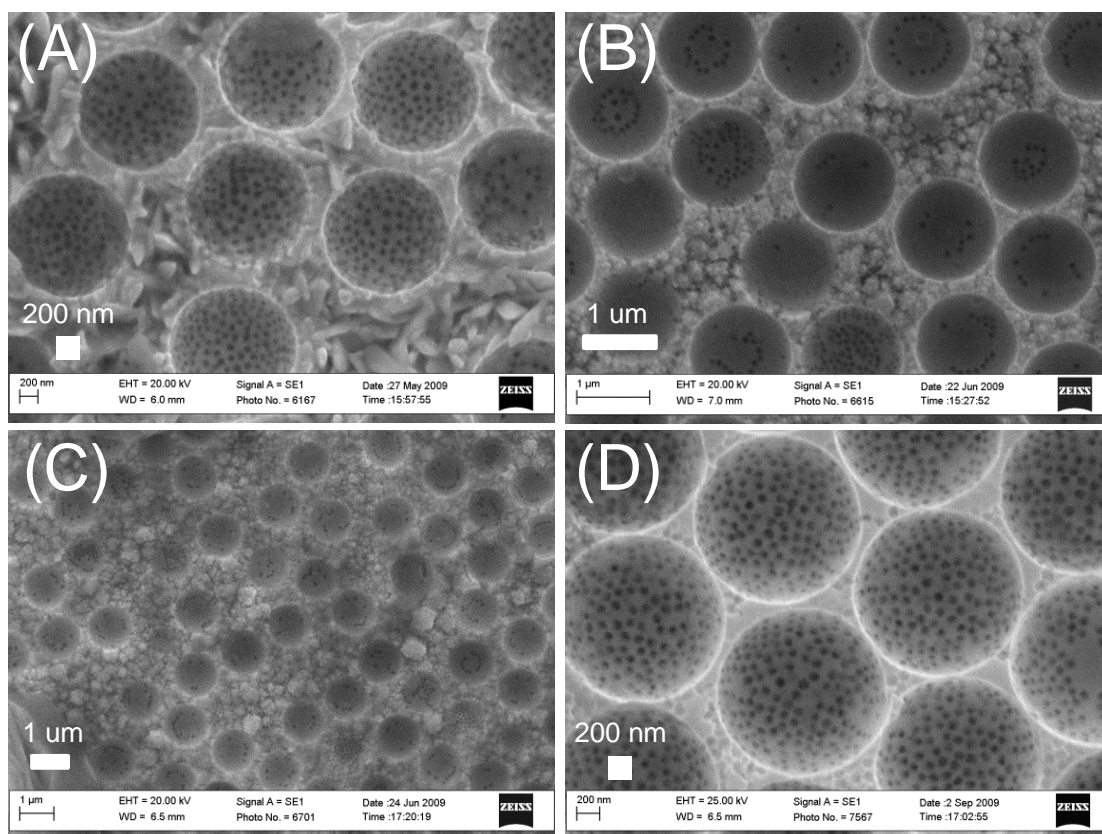


Figure 5.3 SEM images of hierarchical porous films fabricated using different plating solution (A) HAuCl_4 solution, (B) Recipe 1 solution, (C) Recipe 2 solution and (D) Commercial plating solution.

Hierarchical porous gold electrodes were successfully prepared using both potentiostatic deposition and galvanostatic deposition. Similar procedures were also used to prepare macroporous gold electrodes from a 1200 nm diameter NH_2 PS sphere and electrodeposited flat gold electrodes.

5.3.1 Synthesis of Hierarchical Porous Gold Electrodes by Potentiostatic Deposition

Hierarchical gold electrodes were prepared potentiostatically in a manner similar to that described in the literature.⁶⁶ Gold slides were cleaned by soaking in 95°C Piranha

solution (CAUTION: Piranha is dangerous and must be handled carefully and disposed of appropriately) for 5 min, then immersed in a 10 mM 2-aminoethanethiol hydrochloride/ ethanol solution to self assemble a layer of positively charged amine groups on the gold surface. Because cysteamine (2-aminoethanethiol) is a small molecule, it will not impede electron transfer, which is required for electrodeposition. Approximately 150 μL of a suspension of the monodisperse hierarchical templates (1500/110 nm) in acetic acid was spread over the area of the gold electrode defined by a hole punched into a piece of Teflon tape (geometric area $\approx 0.079 \text{ cm}^2$). The sample was slowly dried under an acetic acid environment. The sphere packed gold slide was then exposed to an oxygen plasma (10 V for 2 s) to make the surface of the templates more hydrophilic. The multilayered material was soaked in the gold plating solution for 5-10 min and then the gold ions reduced to metallic gold as outlined in procedures pioneered by the Bartlett group.⁶⁶

Electrodeposition was carried out in a three-electrode electrochemical cell that contains a "working electrode" (PS template modified gold slide), a "reference electrode" (Ag/AgCl), and a "counter electrode" (platinum gauze). A CV of the template modified gold slide in a 0.3 M HAuCl_4 gold plating solution is shown in Fig 5.4 (A). The current change during the electrodeposition of gold is shown in Fig 5.4 (B). The electrodeposition was done potentiostatically via application of -0.9 V for about 8 minutes. This in turn results in gold formation around the templates. According to the literature, for high quality template packed electrodes, oscillations in the current should be observed as the gold film grows thicker due to changes in the electrode surface area.²²⁷ The deposition

can be stopped at the point where the gold is at the $\frac{1}{2}$ layer point or the $1\frac{1}{2}$ layer point. Thus this method allows for control over the bimodal pore sizes and the thickness of the porous material with high precision. In the data shown in Figure 5.4 (A), current oscillations are not observed because the deposition is too thin compared to the size of the hierarchical templates used. The hierarchical templates can be removed in one step via washing the electrode with chloroform.

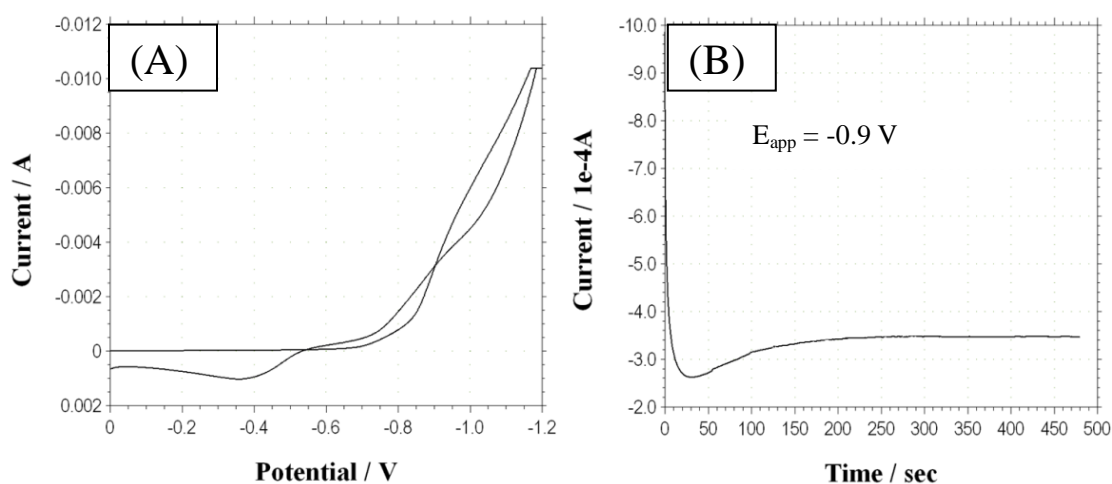


Figure 5.4 (A) CV of a hierarchical template coated gold electrode in 0.3 M HAuCl_4 gold plating solution at 0.1 V/s; (B) Potentiostatic deposition curve of the gold slide at -0.9 V .

Figure 5.5 shows SEM images of the surface of a bimodal macroporous gold film after template removal. Because the whole material is conducting, very clear SEM images can be obtained of the windows located inside the large macropore that lead into the small pore formed from the satellite spheres. As can be seen from such images, the packing of the spheres is quite good in some areas, and the interconnections between the small pores can be seen in high magnification SEM images. In other areas, the spheres do not pack as well and there are more dead spaces between spheres. How well-ordered the spheres

pack on the surface is highly dependent on the procedure used to assemble the spheres as well as the surface chemistry and cleanliness of the substrate. In this particular example, numerous small pores formed from residual small (satellite) spheres that were not completely removed during template preparation are also evident.

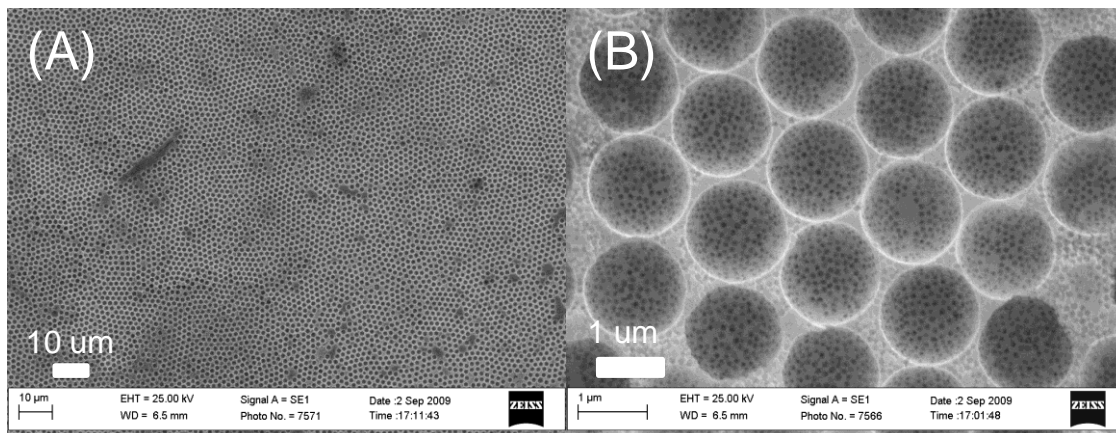


Figure 5.5 SEM images for a bimodal macroporous gold film prepared from 1500/110 nm hierarchical templates at two different magnifications. (A) low magnification, (B) high magnification.

5.3.2. Synthesis of Hierarchical Porous Gold Electrodes by Galvanostatic Deposition

Hierarchical gold electrodes were also prepared galvanostatically. Galvanostatic deposition is more often used in plating because the low constant current can result in a smoother deposited surface compared with potentiostatic deposition. In this part, a different type of hierarchical template, NH_2 -epoxy raspberry template, and a different packing method was used. Hierarchical templates were made via the base-assisted coupling of epoxy groups with NH_2 groups as described in chapter 3. Briefly, the amino-spheres latex (1.2 μm) and epoxy-spheres latex (60 nm) were mixed uniformly together with excessive epoxy-spheres by sonication for several minutes, and then a Na_2CO_3

buffer (pH = 10, 0.1 M) was added into the colloidal solution to start the coupling between amine and epoxy groups. After 24 h, the hierarchical templates were separated from the original solution by centrifugation.

To prepare the hierarchical gold electrodes, the gold slides were first sonicated in soap solution and ethanol for 10 min, respectively, followed by plasma cleaning at 10 W for 2 min and immersion in a 10 mM 2-aminoethanethiol hydrochloride/ ethanol solution for 2 days. The templates were then packed on the modified gold slides by slow speed spin coating. Specifically, $\sim 50 \mu\text{L}$ of an aqueous suspension of the templates ($\sim 2 \text{ wt } \%$) was spread in a circular area of $\sim 1 \text{ cm}^2$. After sitting for about 1 min, the sample was then allowed to dry by slowly rotating the electrode at a spin speed of 450 rpm for about 30-45 min. Under these conditions, a very thick layer of spheres covered the electrode with the bottom few layers being relatively ordered compared to the top few layers. Since electrodeposition of gold begins from the bottom up, this method works well for making gold electrodes that have an ordered arrangement of pores. The disordered top layers of the PS spheres are just simply washed away upon template removal.

To fabricate the hierarchical gold electrodes, gold was electrodeposited around the template in a manner similar to what has been described in the literature for the formation of a macroporous gold electrode with the exception that deposition proceeded galvanostatically vs. potentiostatically. For comparison purposes, a macroporous gold electrode with pore size of 1200 nm was also made in a similar fashion. The electrode area ($\sim 0.3 \text{ cm}^2$) was defined by a $\frac{1}{4}$ inch circle hand punched in a piece of Teflon tape (HYDE model) placed over the surface of the densely packed spheres. Electrodeposition

was carried out galvanostatically with a current of 0.1 mA in a three-electrode electrochemical cell. Figure 5.6 illustrates how the potential changes with time following the application of a constant current to the electrode surface. The observed oscillation in the potential that takes place during deposition is related to the oscillation in electrode area that inevitably happens during electrodeposition. It is very similar to that observed when deposition proceeded potentiostatically; in that case, the current oscillated with time.²²⁷ At the start of electrodeposition, the latex sphere only touches the surface at a small point and the electrode area is relatively large. As deposition proceeds, the gold film grows thicker and the surface area decreases. In order to maintain the applied current, a more negative potential must be applied. At the half way point, the electrode area is at its smallest point, and the potential at its most negative potential. Once the half-way point is past, the potential must drop to a less negative number to maintain the applied current as the electrode area begins to increase again. The amplitude gradually decreases as the layer number increases because the packing is less uniform for the upper layers, which balances off the effect. As previously described, these deposition curves provide an accurate means to control the thickness of the gold film.²²⁷ It also provides a means to indirectly evaluate the order of the templates (yields sharper oscillations) and partially control the surface area upon template removal (via variations in film thickness).²³¹ Each point is supported by SEM images. Current density is another important parameter in deposition. Smoother films result from lower current density.²³²

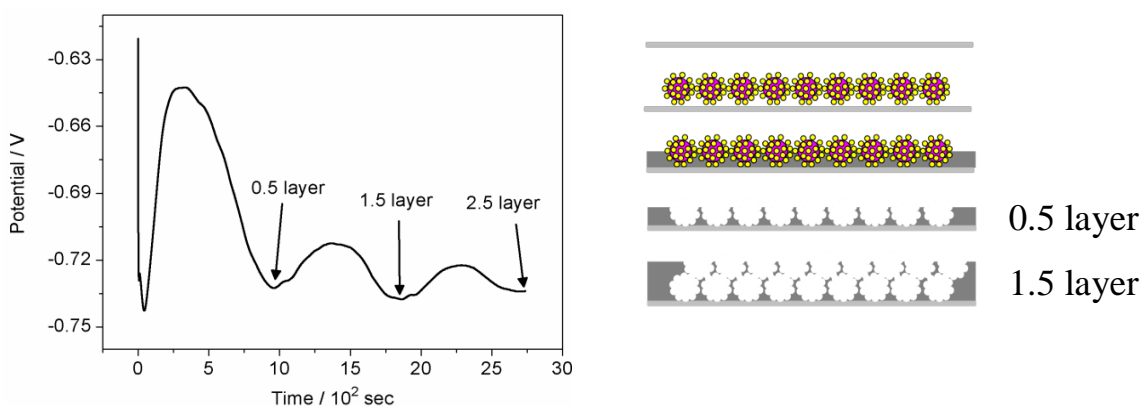


Figure 5.6 Potential-time trace at the hierarchical sphere (1200/60 nm) modified gold electrode in the gold plating solution following the application of 0.1 microamps.

After electrodeposition, the Teflon tape was removed and the sphere-coated gold slide was rinsed with water and air dried. To remove the polystyrene templates, the sphere-coated gold slide was soaked in a 2:1 ratio chloroform/acetone mixture for several minutes prior to sonication for 5 min. As described in the text, the electrodes were then either cleaned by KOH + H₂O₂ (50 mM KOH and 25% H₂O₂ for 2h), or by irradiation with UV light (254 nm, 20 W) for at least 18 hrs. A hole punched piece of Teflon tape (dia = 1/4 or 1/8 inch) defined the electrode area. The tape was pressed hard against the gold substrate with an exposed deposited area so that it seals the undesired area tightly. The 1/8 inch puncher size can ensure the defined electrode area is smaller and located entirely with the 1/4 inch diameter circle that defines the electrodeposited area. Flat electrodeposited gold was made by electrodepositing on a 2-aminoethanethiol hydrochloride modified gold slide for 10 min. Current was kept the same at 0.1 mA.

SEM images of half-layer and 1½ layer of hierarchical porous gold films are shown in Figure 5.7 along with a SEM of a macroporous electrode prepared using 1200 nm

diameter PS spheres for comparison. What can be clearly seen in the SEM images of the gold films prepared from the hierarchical PS spheres is the presence of very small pores at the bottom of each of the significantly larger macropores. The neck of the smaller pores are approximately 20 nm in diameter, where big sphere touches smaller sphere. For the multilayer images, three interconnected porous windows can be observed between the two neighboring layers. These windows are composed of small pores formed where the satellites touched. Similar windows have been observed in macroporous materials in other's work.⁹⁰ Those porous windows were not observed in the hierarchical porous silica monolith in our previous work (chapter 4), which is probably because the big, uniform and smooth amino satellites of the template used for making silica monolith resulted in less touching among the satellites. In addition, the silica sol wets the polystyrene spheres better, which can form very small interconnected pores after template removal. Therefore no porous windows were observed.

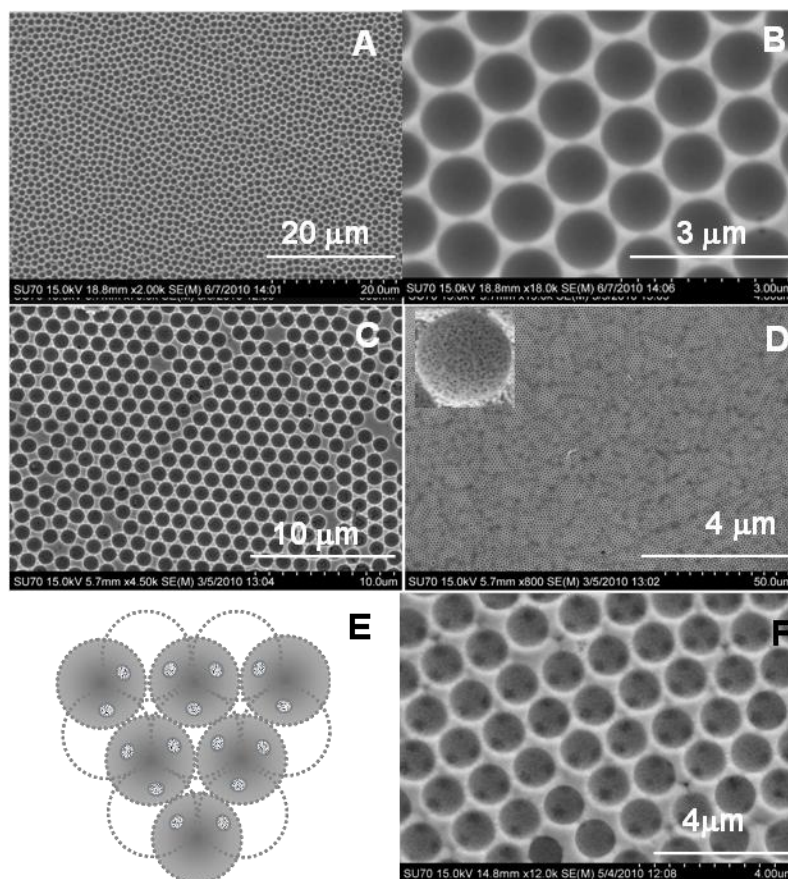


Figure 5.7 SEM images of porous gold electrodes prepared from (A, B) PS latex sphere, diameter 1200 nm, half-layer, (C, D) PS hierarchical latex sphere, 1200/60 nm, half-layer, and (F) PS hierarchical latex sphere, 1200/60 nm, one and one half-layer. (E) Cartoon depicting multilayer formation and the resultant windows that form.

5.4 Characterization of Hierarchical Porous Gold Electrodes

5.4.1 Surface Characterization

Surface chemistry plays an important role in electroanalytical chemistry. Therefore it is very important to make sure the electrode surfaces being used are clean and free from contaminants. To evaluate the presence of surface contaminants on the top ~ 5 nanometers of the surface of the electrodes after cleaning, x-ray photoelectron spectroscopy (XPS) was used. In Figure 5.8, XPS survey scans of three gold electrodes

(an electrodeposited gold electrode, macroporous gold, and hierarchical gold) cleaned either by thoroughly rinsing in chloroform, treatment with KOH/H₂O₂, and/or exposure to UV radiation are shown. In addition to gold, peaks were observed for carbon, oxygen, and nitrogen, the heights of which were strongly dependent on the cleaning method, Figure 5.9. Nitrogen, observed on all the gold electrodes, likely arises from the gold plating solution as a bare, as-received gold electrode showed no nitrogen peak. A small oxygen peak was observed only on the gold electrodes after the chloroform followed by either KOH/H₂O₂ cleaning and UV treatment. Of the cleaning methods investigated, washing with chloroform/acetone followed by UV radiation proved best. When the electrodes were only cleaned with chloroform, which dissolves the PS, a large carbon peak and very small gold peaks were observed indicative that the outermost layer of the electrodes are contaminated. Some remnants of the polystyrene likely remain on the surface. After KOH/H₂O₂ cleaning, the gold peaks become larger and the carbon peak smaller. After UV cleaning, however, the carbon peak becomes even smaller, the gold peaks even larger, and their peak ratios similar to that observed at the bare electrodeposited electrodes. Irradiation with UV light for a day or two generates ozone, which oxidizes organic contaminants without disrupting the hierarchical framework. Since XPS is only sensitive to the outermost surface, this technique will not be able to integrate the satellite pores or the inner surface of the electrode. Due to the nature of UV cleaning, however, it is believed that residual PS has also been removed from the small satellite pores as well.

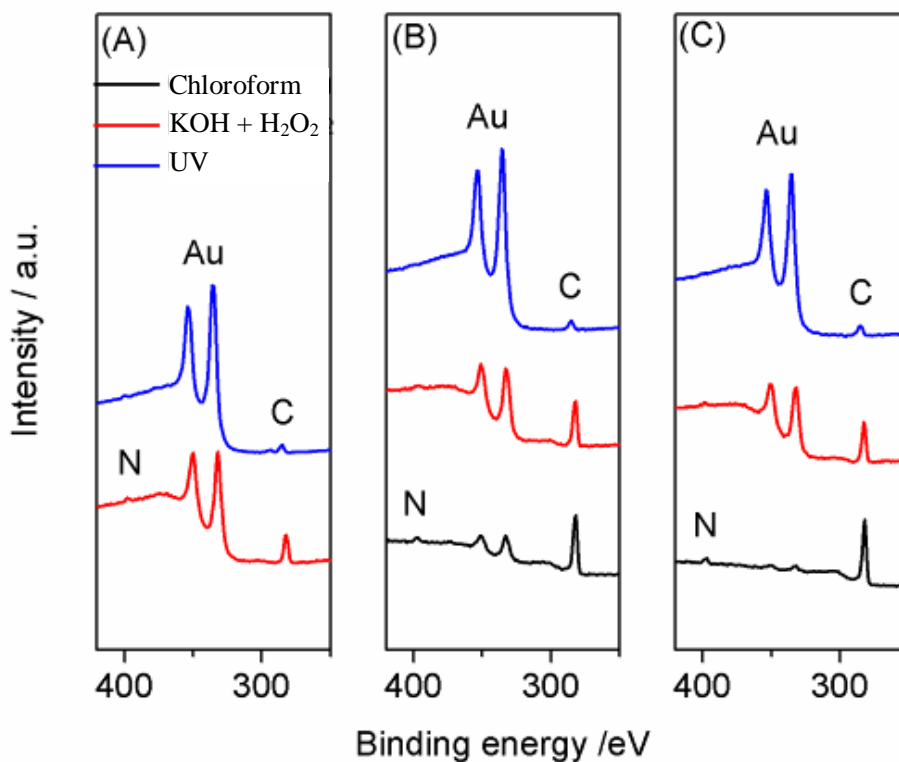


Figure 5.8 XPS survey spectra for (A) electrodeposited flat gold (B) macroporous gold (1/2 layer; dia = 1200 nm) and (C) hierarchical porous gold (1/2 layer; 1200/60 nm).

Different gold surface cleaning methods have been studied and compared in Fischer's work.²³³ Among all the cleaning methods, piranha solution, oxygen plasma cleaning, and electrochemical cleaning are not ideal for cleaning bimodal porous gold because these methods roughen the electrode surfaces and result in the loss of the fine structure of the bimodal porous gold. KOH+H₂O₂ alone is not effective in removing the polystyrene left after the electrode is soaked in an organic solvent. High intensity UV radiation is another method tried in this study, because UV can generate ozone, which will decompose the polymer into CO₂ without etching away gold structure. UV, however, is not an effective

way to remove bulk organic material, so combining organic solvent dissolution followed by UV cleaning was shown to be best.

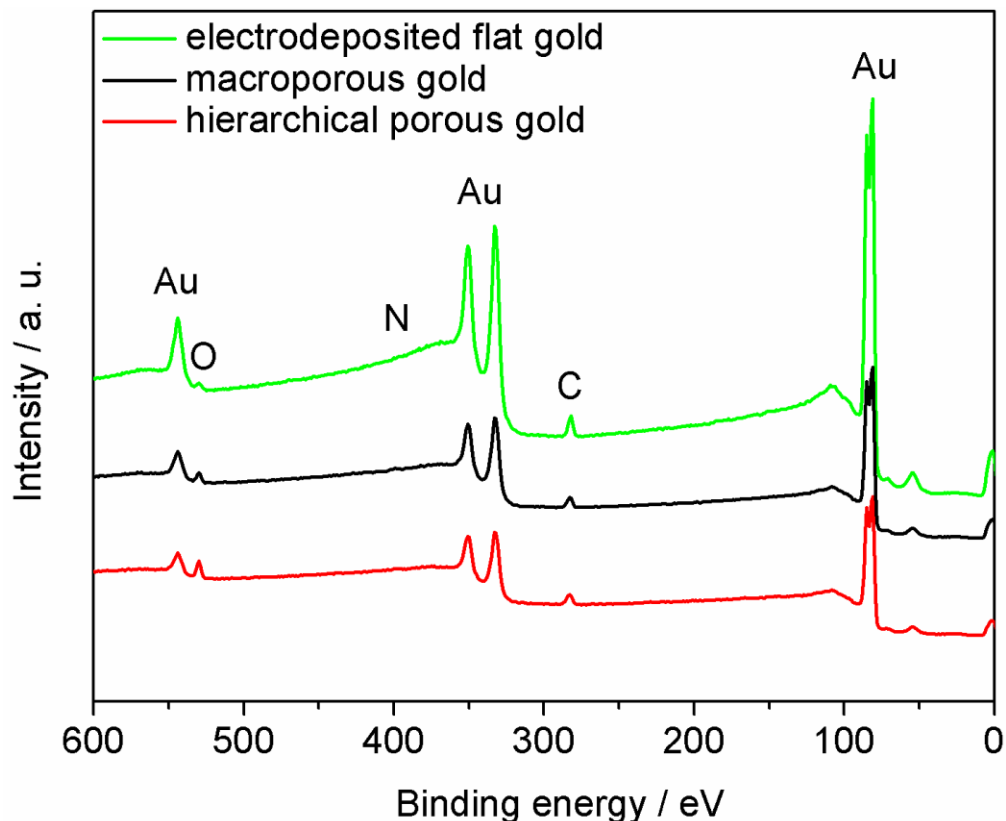


Figure 5.9 XPS survey spectra for electrodeposited flat gold, macroporous and hierarchical porous gold.

The comparison among three different types of gold slides was made. XPS surveys of three samples (deposited flat gold, macroporous gold, and hierarchical porous gold) after UV cleaning are shown in Figure 5.9. Besides gold peaks, carbon and oxygen peaks are clearly shown in all three samples. Also, there are small bumps at about 395 eV, which is at the nitrogen peak position, for all samples. The similar amount of nitrogen observed on the electrodeposited sample indicates that it does not entirely originate from the amino polystyrene sphere in the template, but from the gold plating solution. Thus,

electrodeposited flat gold is a better control comparing with bare gold. With peak comparison, the ratio of carbon versus gold is 0.07 for hierarchical porous gold, 0.08 for macroporous gold, and 0.05 for electrodeposited flat gold, which are comparable to each other. We also compared other cleaning methods; so far, UV cleaning is the best, and we can consistently get similar result based on the same treatment.

5.4.2 Surface Area Measurement

Two relevant areas of an electrode are (1) the geometric area measured with a ruler and (2) the real surface area as measured via cyclic voltammetry by integrating the charge required to reduce the gold oxide formed upon oxidation of the gold electrode immersed in 0.5 M H₂SO₄. The real surface area can be calculated using the following formula,

$$S_r = Q_m / e d_m$$

where: S_r = real surface area, e = electron charge, d_m = surface metal atom density, and Q_m is

$$Q_m = \int_x^y (1/v) I dE - Q_{dl}$$

and $x = (E_o - E_i)/v$, $y = (E_o - E_f)/v$ Q_m = charge due to monolayer formation, v = scan rate, I = current, V = voltage, Q_{dl} = charge due to the double layer capacitance.

From the CV data, the real surface area can be obtained by integrating the area under the reduction peak and then dividing by the scan rate and a constant 0.386 mC/cm^2 .¹²⁰

To determine how much the surface area increases, the CVs were obtained in 0.5 M H₂SO₄, and the charge required to reduce the gold oxide peak was measured. As expected, the area under the gold oxide stripping peak appearing at $\sim 0.9 \text{ V}$ increases upon going

from a flat gold electrode, to a macroporous gold electrode, to a hierarchical gold electrode. Using a conversion factor of 0.386 mC/cm^2 ,^{234,235} the surface area of the electrodes were calculated to be $0.70 (\pm 0.02) \text{ cm}^2$, $N = 3$; $1.24 (\pm 0.18) \text{ cm}^2$, $N = 6$ for the macroporous and $\frac{1}{2}$ layer hierarchical gold electrode, respectively. N is the number of samples and the number in parenthesis is the standard deviation. The higher relative standard deviation ($\sim 3\%$ vs 14%) for the hierarchical electrode is due to variations in the packing and the number density of the satellite nanowells inside the core nanowell. Compared to a bare gold electrode (geometric area = 0.32 cm^2 ; real area = 0.34 cm^2), the surface area of the macroporous electrodes were $\sim 2\text{x}$ larger with a relative standard deviation of 2.85% while the hierarchical electrodes were $\sim 3.9\text{x}$ larger with a $\sim 14\%$ relative standard deviation. These numbers agree with theoretical calculations that indicate that the macroporous electrode should have an area 1.8x larger than a bare gold and the hierarchical 4.4x larger. These calculations assume that the nanowells are hemispherical (Area = $2\pi r^2$) and they pack in a close-packed arrangement either on the flat surface for the macroporous electrode or around the $1.2 \mu\text{m}$ core sphere in the case of the hierarchical electrode. This assumption likely overestimates the area a small amount given that the packing is not perfect and the satellite nanowells are not all hemispherical as some are deeper than others as judged from the diameter of the openings as observed via SEM. The calculation, however, does not take into account the surface roughness of the electrodeposited gold, which will increase the electrode area by a factor of ~ 1.1 to 1.3 .

For the hierarchical gold electrodes, the agreement between theory and experiment

supports the statement that almost all of the pores are interconnected and consequently contribute to the active surface area. The approximate doubling of the electrode area is due to the hundreds of small satellite pores located in the large hemispherical well formed from the core sphere.

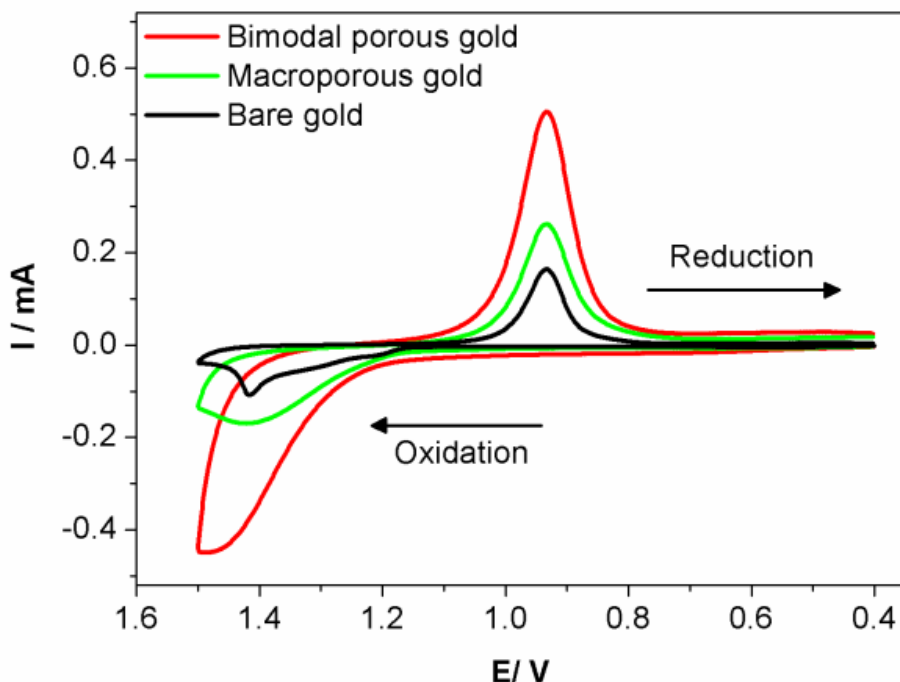


Figure 5.10 Cyclic voltammetric curves of UV cleaned hierarchical (1200/60 nm), macroporous (1200 nm), and bare gold electrode in 0.5 M H₂SO₄. Scan rate: 100 mV/s. Electrode area = 0.32 cm².

Table 5.2 Surface area data obtained from CVs of flat gold, half-layer porous gold films made from 1200 nm amine PS templates and half-layer hierarchical porous gold film made from the 1200/60 nm hierarchical template.

Sample	Average surface area (cm ²)	STDEV	STDEV/AVG	Ratio to geometric area
Flat gold	0.345 (n=2)			1.1
½ NH ₂	0.703 (n=3)	0.020	2.85%	2.22
½ Hierarchical	1.24 (n=6)	0.179	14.5%	3.92

5.5 Electrochemical studies

Macroporous electrodes are particularly important in electrochemistry applications where they have been shown to be attractive supports for investigating the direct electrochemistry of small molecules, proteins, and enzymes either immobilized on their surface and/or in solution. The higher surface area allows for a greater amount of an enzyme/protein to be immobilized.¹²⁰ In addition, they have been shown to significantly increase signals, lower detection limits and improve sensitivity of biosensors because of their high surface areas.^{227,236} It is envisioned that the current “hierarchical macroporous electrodes” will have similar advantages but an even higher surface area due to the presence of the smaller pores formed from the satellite spheres.

Electrochemistry at high surface area electrodes has been studied. For redox species that exchange electrons rapidly with the electrode surface, current does not scale linearly with electrode area. For these redox species, the inner surface is not utilized because the redox species are completely depleted at the outer electrode surface. When the redox specie exchanges electrons slowly with the electrode surface, depletion does not take place as extensively as it does for a kinetically fast redox species. Under these conditions, the inner surface area is used and Faradaic current can be significantly higher than that observed for a kinetically reversible redox couple.²²⁵

In this section, a multi-potentiostat was used to collect the electrochemical data. A multi-potentiostat can work with eight independent cells or eight working electrodes in the same solution with a common reference and counter electrode. Figure 5.11 shows the experimental set up. In this set-up, six working electrodes share one reference electrode

and one counter electrode, both of which are located in the center of the electrochemical cell. By setting it up this way, all the working electrodes will be same distance from the reference and counter (auxiliary) electrodes. Since the electrodes are all immersed in the same solution, the individual errors can be reduced.

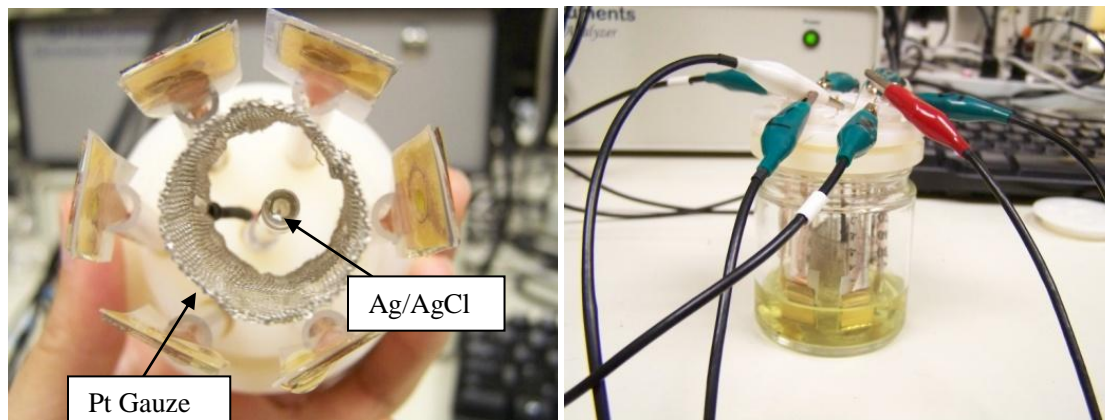


Figure 5.11 Experimental setup for the multichannel electrochemistry studies. The reference electrode (Ag/AgCl) and auxiliary electrode (Pt gauze) are indicated by the arrows in the figure.

5.5.1 FcCH₂OH in KCl (reversible redox system)

The clean hierarchical porous gold electrodes made with 1200/60 nm NH₂/epoxy templates were used as working electrodes to acquire CVs in 1 mM ferrocene methanol / 0.1 M KCl solution at scan rates of 0.1, 0.25, 0.5, 1, 5, 10, 20 V/s, respectively. Ferrocene is a reversible redox couple and exchanges electron quickly with an electrode surface. Comparisons were made to bare flat gold and to macroporous gold electrodes (½ layer and 1 ½ layers) made from 1200 nm diameter NH₂ polystyrene spheres. The data are shown in Figure 5.12. As can be seen, bare flat gold, macroporous gold, hierarchical porous gold and 1 ½ layer macroporous gold have very similar CVs at 0.01 V/s. The peak current for all the electrodes overlap except for the 1 ½ layer macroporous electrode.

When the scan rate was increased from 0.01 V/s to 0.1 V/s and 1 V/s, the differences in the voltammograms become more obvious, with an increase in Faradaic peak current and a greater peak splitting being observed. This result can be attributed to the hidden inner surfaces of those porous structures becoming more useful as the time scale of the experiment gets shorter. As the scan rate increases, the time the potential is applied to the electrode becomes shorter and less redox species are depleted at the electrode surface relative to that taking place under slow scan rates. This allows some of the redox species to diffuse further into the inner porous structure and exchange electrons with the inner structure surface. Hence, an increase in current is observed. Simultaneously, the peak splitting of the CVs for all four electrodes increases as the scan rate increases (shown in Table 5.3). At low scan rates, the peak splitting for all four electrodes is 59 mV, which means that there is barely any Ohmic drop at slow scan rate and it is a kinetically reversible electrochemical process. The 1 ½ layer macroporous gold electrode shows both the highest current increases and the largest peak splitting.

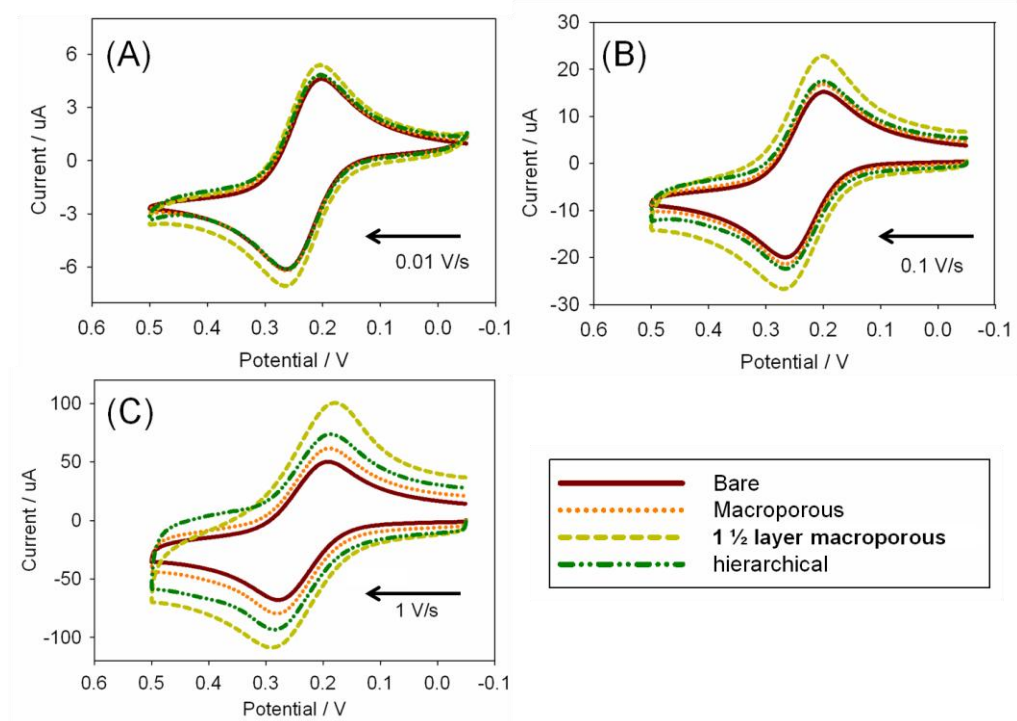


Figure 5.12 CVs of 1 mM FcCH₂OH in 0.1 M KCl at bare flat gold, macroporous gold, hierarchical porous gold, and 1 ½ layer macroporous gold electrodes at different scan rates. (A) 0.01 V/s, (B) 0.1 V/s and (C) 1 V/s.

Table 5.3 Peak Splitting for bare flat gold, macroporous gold, hierarchical porous gold and 1 ½ layer macroporous gold at three scan rates from CVs in Figure 5.13.

Scan rate \ Sample		Bare flat gold	Macroporous gold	Hierarchical porous gold	1 ½ layer macroporous gold
0.01 (V/s)	E _{pc} (V)	0.204	0.204	0.204	0.204
	E _{pa} (V)	0.263	0.263	0.263	0.263
ΔE_p (mV)		59	59	59	59
0.1 (V/s)	E _{pc} (V)	0.265	0.265	0.265	0.271
	E _{pa} (V)	0.200	0.200	0.200	0.200
ΔE_p (mV)		65	65	65	71
1 (V/s)	E _{pc} (V)	0.276	0.28	0.283	0.289
	E _{pa} (V)	0.192	0.191	0.186	0.18
ΔE_p (mV)		84	89	97	109

In Figure 5.13, cyclic voltammograms of ferrocene methanol at sweep rates ranging from 0.01 V/s to 1 V/s are shown for each electrode. The current obtained at each electrode increases with scan rate.

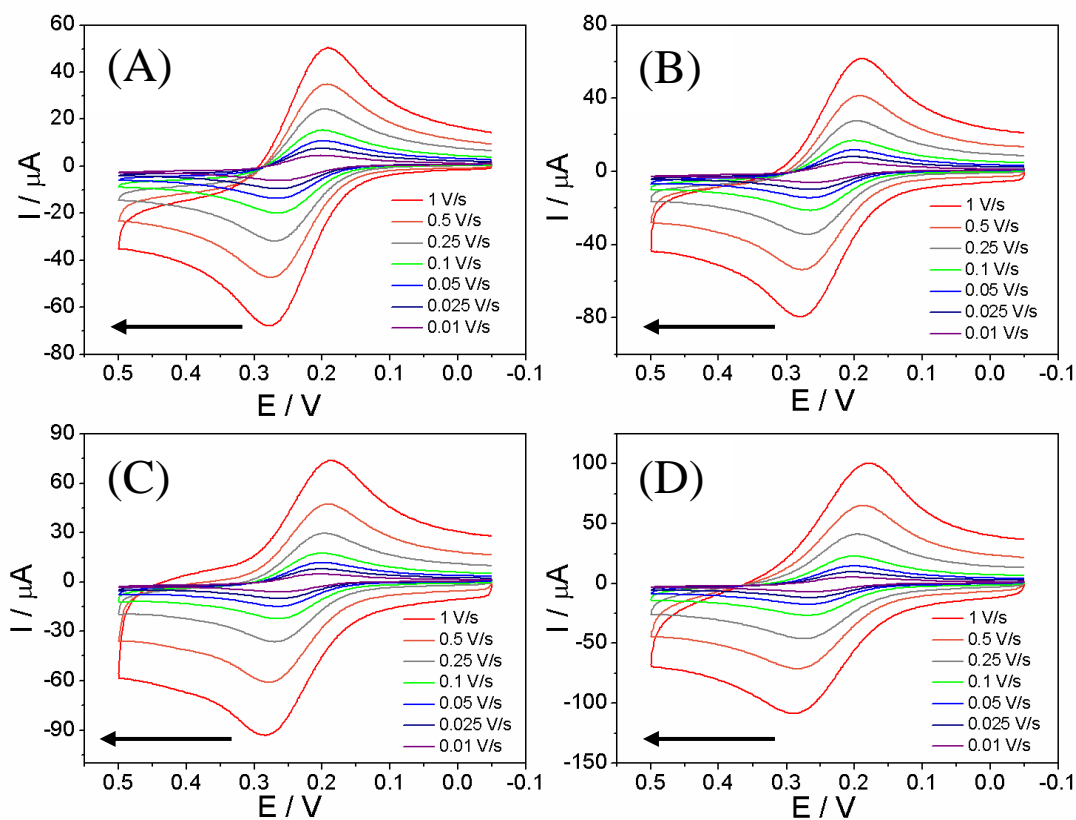


Figure 5.13 Cyclic voltammograms of 1 mM ferrocene methanol in 0.1 M KCl at different scan rates. Bare flat gold (A), macroporous gold (B), hierarchical porous gold (C) and 1 ½ layer macroporous gold electrode (D) are shown.

A plot of the peak (anodic) faradic current versus the square root of scan rate is shown in Figure 5.14. As expected for a diffusion controlled redox process, a linear fit is obtained at relatively low scan rates. The results from the regression analysis are shown in Table 5.4. At higher scan rates, a positive deviation is observed for 1 ½ layer macroporous gold

electrode because more of the electrode area is utilized as described earlier. Theoretically, the slope of the curve should be linearly dependent on electrode area. In this case, it can be seen that all three electrodes have the same or nearly the same slope, regardless of their electrode area. As described above, this is consistent with that previously observed for high surface area nanostructured electrodes for a redox species that exchanges electrons quickly with an electrode surface. To fully utilize the entire area, an electrochemically slow kinetic redox species should be used as described in the literature.²²⁵

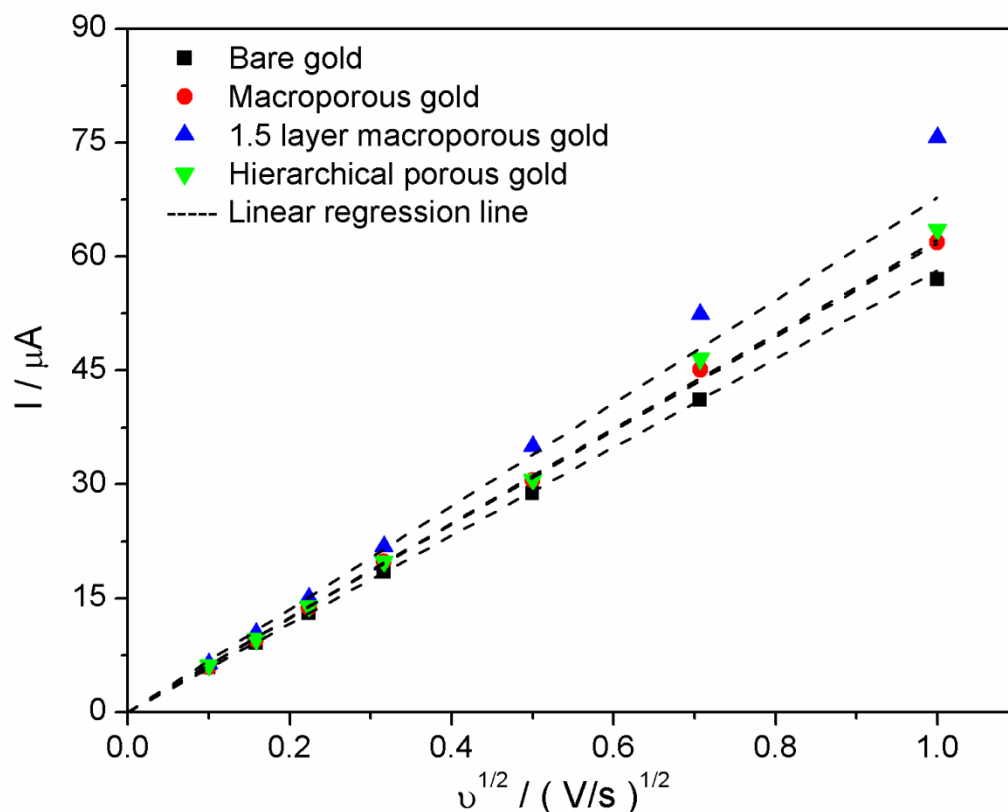


Figure 5.14 Plot of peak current (anodic) obtained versus square root of the scan rate, for 1 mM ferrocene methanol in 0.1 M KCl (CVs shown in Figure 5.15) The solid lines: linear regression lines. Only data acquired at slow scan rates (0.01 V/s to 0.1 V/s) were fit.

Table 5.4 Results from the regression analysis of anodic peak current vs. square root of scan rate for CVs of FcCH₂OH on bare flat gold, macroporous gold and hierarchical porous gold in KCl.

Sample	Intercept (μA)	Slope ($\mu\text{As}^{1/2}\text{V}^{(-1/2)}$)	R ²
Bare flat gold (black)	0	58.19	0.9997
Macroporous gold (red)	0	61.75	0.9996
Hierarchical porous gold (green)	0	62.19	0.9987
1 ½ layered macroporous gold (blue)	0	67.79	0.9907

In Figure 5.15, cyclic voltammograms at sweep rates ranging from 0.01 V/s to 1 V/s are shown for each electrode in 0.1 M KCl solution. The current observed is non Faradaic current and arises from the charging of the electrical double layer on electrode surface. It can be described by the following equation,

$$I_c = \nu C_d,$$

where ν is the scan rate, and C_d is the capacitance representing the electrical double layer on the electrode surface. Typical values for metal electrodes are from 10 $\mu\text{F}/\text{cm}^2$ to 40 $\mu\text{F}/\text{cm}^2$.²³⁷ From this equation, it can be seen that the charging current is proportional to the scan rate and the capacitance of the double layer, which is directly proportional to the electrode surface area. It can be described by the following equation,

$$C_{dl} = A\epsilon_{dl}/d,$$

where ϵ_{dl} is the dielectric permittivity at the electrically charged double layer; A is the electrode area, and d is the thickness of the double layer.²³⁸

In Figure 5.16, charging current measured from the CVs at 0.05 V (see Figure 5.16B) is

plotted against the scan rate for all four electrodes. As expected, a linear relationship was obtained for all electrodes except for the 1 ½ layer macroporous gold which is only linear at slow scan rates. Results from the regression analysis are given in Table 5.5. As can be seen, the slope increases by a factor of 3, 5 and 7 times relative to a bare flat electrode, for macroporous gold, hierarchical porous gold and 1 ½ layer macroporous gold, respectively.

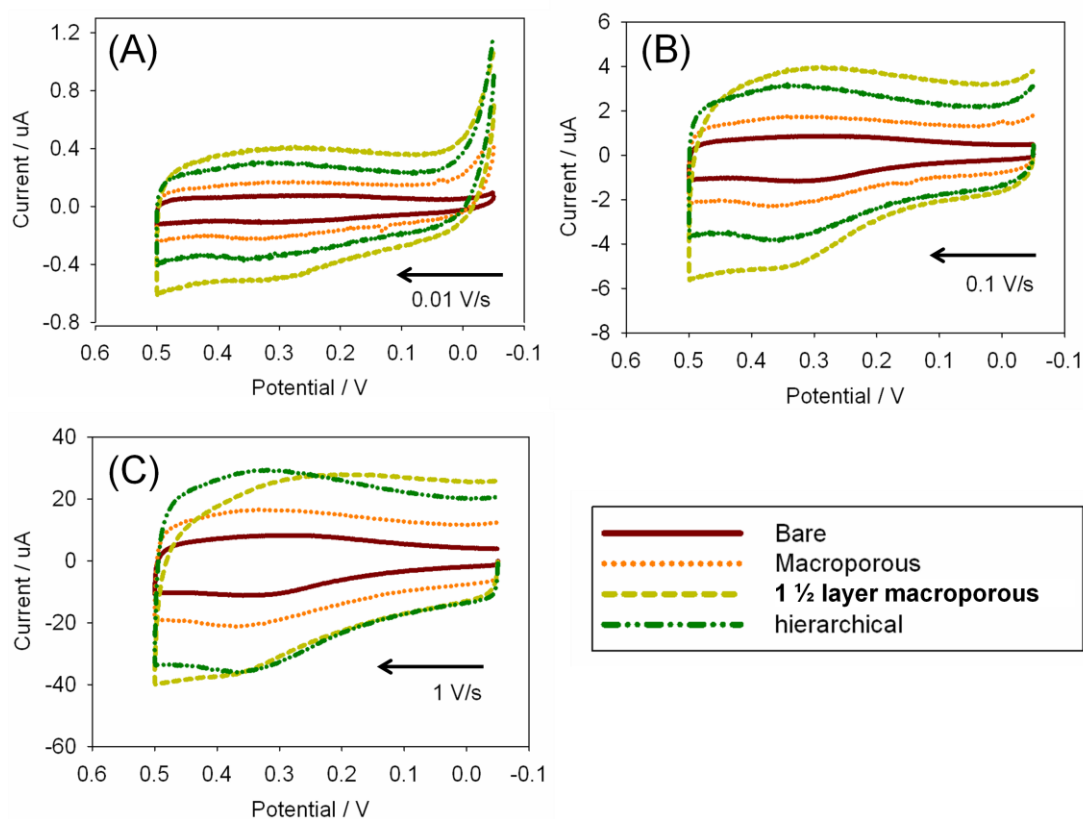
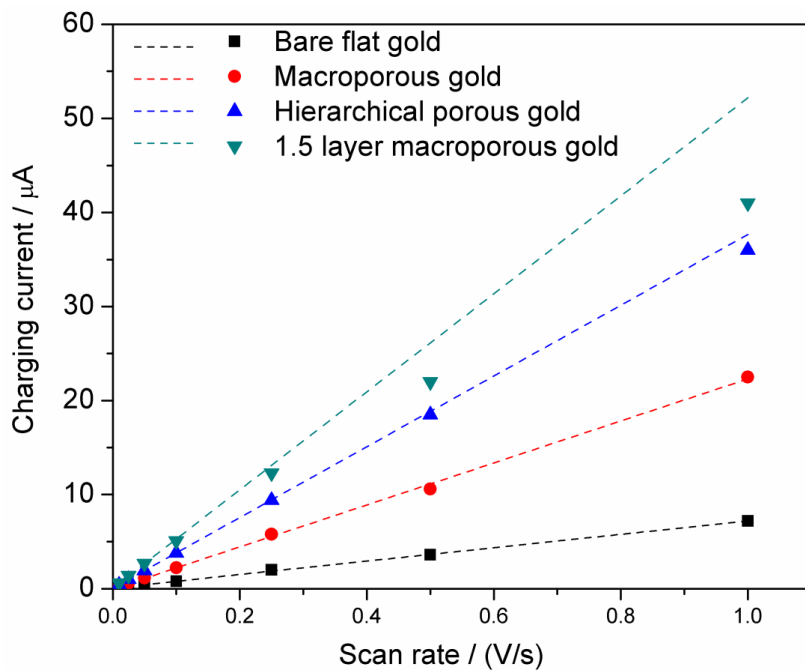


Figure 5.15 CVs at bare flat gold, macroporous gold, hierarchical porous gold, and 1 ½ layer macroporous gold electrodes in 0.1 M KCl at different scan rates (A) 0.01 V/s, (B) 0.1 V/s and (C) 1 V/s.

(A)



(B)

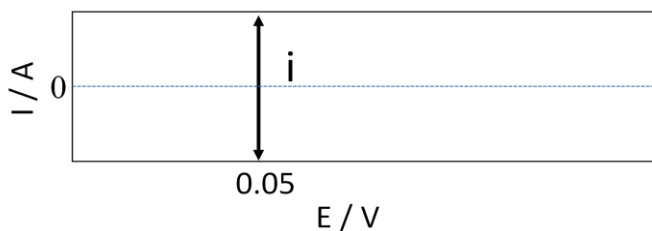


Figure 5.16 (A) Plot of charging current measured at $E = 0.05 \text{ V}$ versus scan rate for four different electrodes, bare flat gold (black), macroporous gold (red), hierarchical porous gold (blue), and 1 $\frac{1}{2}$ layered macroporous gold (green). The solid lines are linear regression lines. (B) Simplified view of how the charging current was measured: by measuring i at 0.05 V and dividing by 2.

Table 5.5 Results from the regression analysis of charging current vs. scan rate for FcCH₂OH on bare flat gold, macroporous gold and hierarchical porous gold in KCl.

Sample	Intercept (μA)	Slope (μAs/V)	R ²
Bare flat gold (dark red)	0	7.246	0.9990
Macroporous gold (orange)	-0.0298	22.3300	0.9988
Hierarchical porous gold (dark yellow)	0.0373	37.63	0.9966
1 ½ layered macroporous gold (green)	0.0838	52.10	0.8699

5.5.2 FcSH adsorbed redox system

In addition to studying the electrochemistry at these electrodes with a diffusing redox probe in solution, we also examined the electrochemistry of a redox probe adsorbed on the electrode surface. In this experiment, the electrodes were immersed in a 1 mM FcSH/ethanol solution for 24 h right after the UV cleaning to self assemble a monolayer of ferrocene-thiol molecules on the gold surface. The gold slides were rinsed with ethanol, deionized water and dried with N₂ prior to use. In this case, 1 M HClO₄ was used as the supporting electrolyte because of the ion pairing between Fc⁺ and ClO₄⁻, which can help the electron transfer.²³⁹ Figure 5.17 shows the CV obtained for FcSH self-assembled on bare flat gold, macroporous gold and hierarchical porous gold.

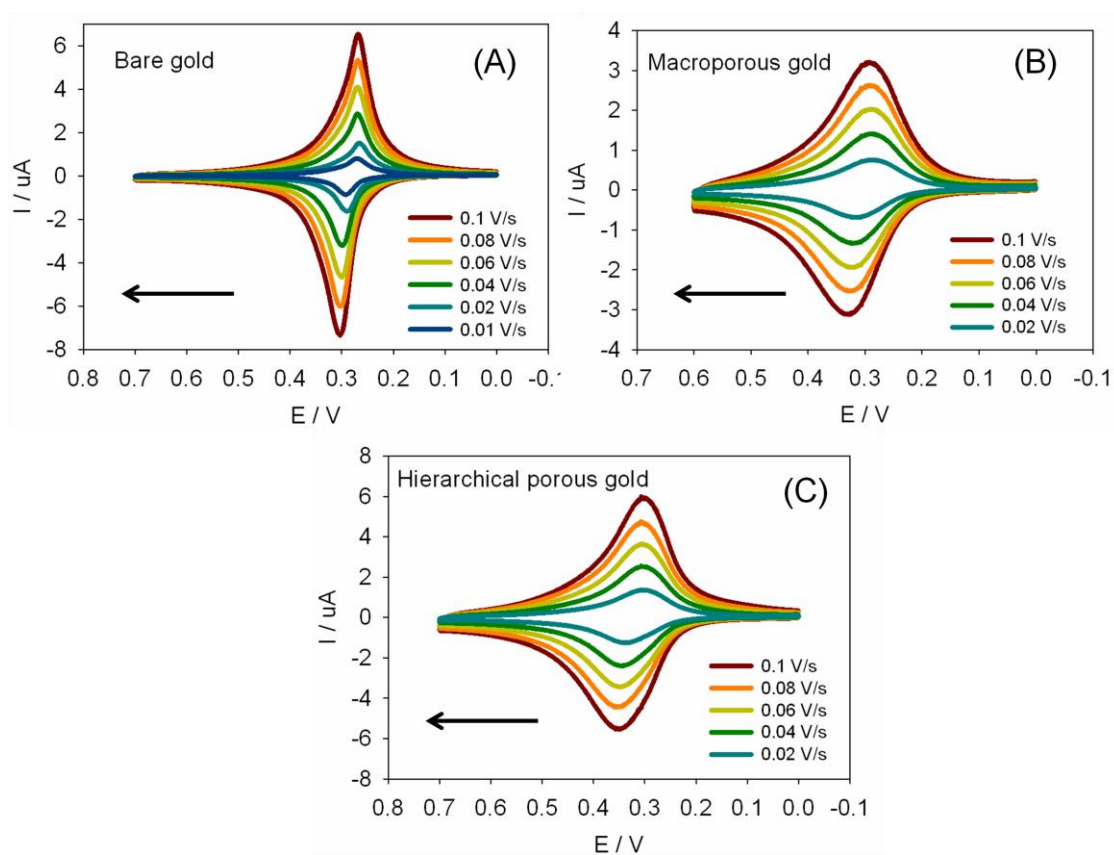


Figure 5.17 CVs of FcSH self-assembled gold electrodes in 1 M HClO₄ at different scan rates. (A) Bare flat gold (B) Macroporous gold and (C) Hierarchical porous gold. Arrows show the direction of the scan.

For an adsorbed redox couple exhibiting reversible electron transfer kinetics, the peak current is given by the following equation,

$$i_p = (n^2 F^2 / 4RT) \nu A \Gamma^*$$

where the peak current (i_p) is directly related to the concentration of the total adsorbed redox species (Γ^*), scan rate (ν) and electrode area (A) and the number of electrons transferred (n). For an adsorbed redox couple, the peak current should be directly proportional to the scan rate. Figure 5.18 shows the plot of peak Faradaic current vs. scan

rate for the bare flat gold, macroporous gold, and hierarchical porous gold. As expected for a surface adsorbed redox couple at slow scan rates, peak current (both anodic and cathodic) is directly proportional to scan rate. Results from the regression analysis are shown in Table 5.6. The R^2 numbers of the linear regressions are very close to 1.

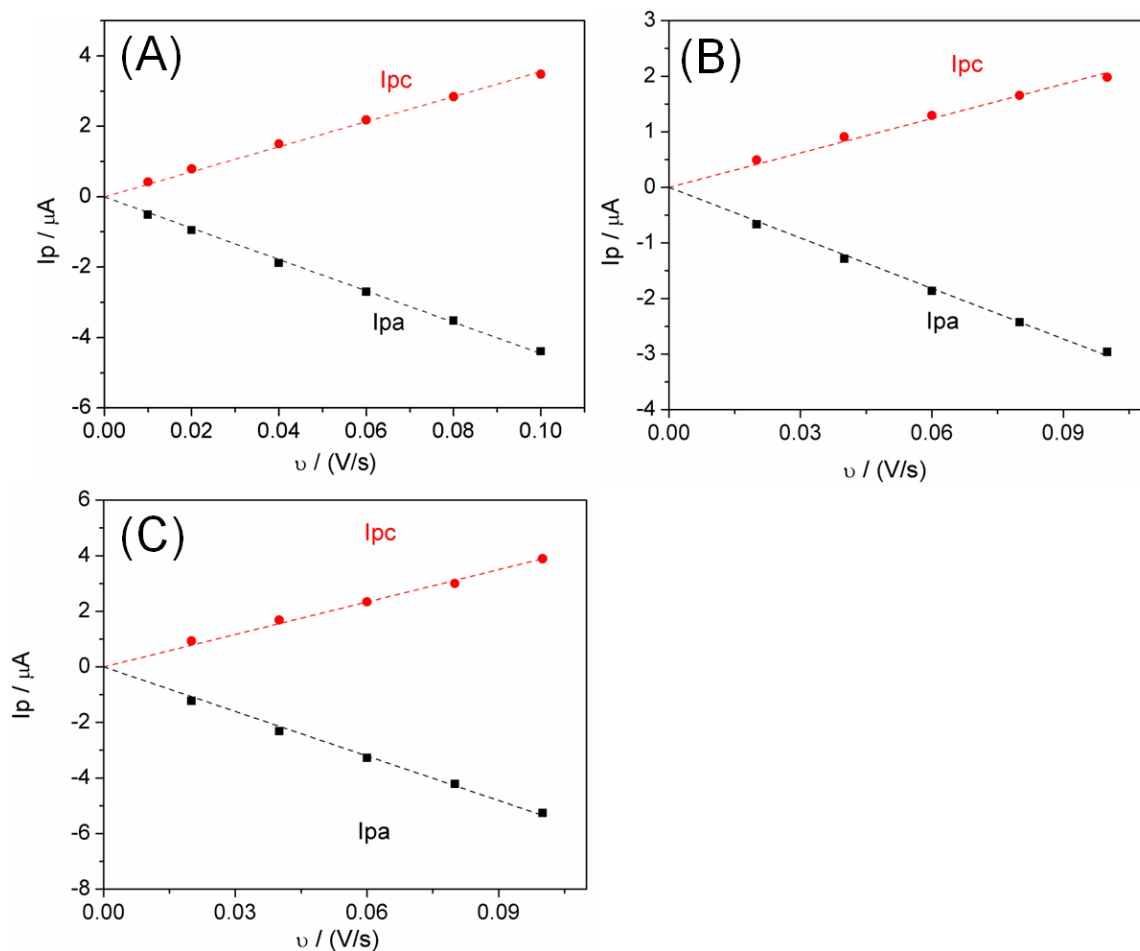


Figure 5.18 Plot of peak current vs. scan rate for FcSH assembled gold electrodes in 1 M HClO_4 . (A) Bare flat gold (B) Macroporous gold and (C) Hierarchical porous gold. The solid lines are linear regression lines.

Table 5.6 Results from the regression analysis of peak current vs. scan rate for FcSH adsorbed on bare flat gold, macroporous gold and hierarchical porous gold in 1M HClO₄.

Sample (anodic current)	Intercept (μA)	Slope ($\mu\text{As/V}$)	R ²
Bare flat gold	0	-44.52	0.9993
Macroporous	0	-30.30	0.9991
Hierarchical porous gold	0	-53.45	0.9986

For an ideal system that is kinetically reversible, $E_{pa} = E_{pc}$, $\Delta E_p = 0$, and $\Delta E_{p,1/2} = 3.53RT/nF = 90.6/n$ (mV). However, this situation is rarely obtained. As discussed in chapter 2, the FWHM (full width at half max) and the shape of the CV shape are influenced by the interactions among the molecules assembled on the electrode surface.¹⁴⁹ Previous work on electrochemistry of assembled redox species showed that the peaks are often sharper and have a FWHM less than 90.6 mV when the assembled layer is densely packed electroactive SAMs.²⁴⁰ And broad peaks are caused by a distribution of formal potentials.²⁴¹ On bare flat gold, the CV peaks are sharper than those obtained for macroporous and hierarchical porous gold. It is likely the ferrocene molecules are located closer to each other on flat gold compared to nanostructured gold, giving rise to narrow distribution of formal potentials. On macroporous and hierarchical gold electrodes, the peaks are much broader likely due to the curvature present on the nanostructured electrodes. On the FcSH assembled gold electrode, neighboring HSFc⁺ molecules will repel each other at positive potentials after ferrocene is oxidized.

In addition, the difference between the cathodic and anodic peak positions (ΔE_p) is often greater than 0 mV. ΔE_p also depends on electron transfer kinetics. We see similar results on bare, flat gold, Table 5.7 and Table 5.8. The shift of the peak position relative

to formal potential of the redox couple depends on the adsorption of Fc^+ and Fc . In our system, the 1 M HClO_4 solution is a strong acid media with very low pH value, in which the repulse of the molecules assembled are stronger in Fc^+ form. Thus the adsorption strength of Fc is stronger than that of Fc^+ . As a result, the anodic wave occurs at a more positive potential than the formal potential. As the curvature of the surface becomes bigger from bare flat gold to macroporous gold to hierarchical porous gold, the repulsion among the molecules become larger, thus the peak splitting ΔE_p is increasing.

Table 5.7 Peak splitting (ΔE_p in mV) for bare flat gold, macroporous gold and hierarchical porous gold at different scan rates.

scan rate (V/s)	0.1	0.08	0.06	0.04	0.02
ΔE_p (mV), Bare flat gold	34	34	32	29	23
ΔE_p (mV), Macroporous gold	35	35	32	36	22
ΔE_p (mV), Hierarchical porous gold	43	50	43	37	31

Table 5.8 Anodic FWHM and cathodic FWHM of the voltammetric curves obtained at 20 mV/s for FcSH assembled electrodes: bare flat gold, macroporous gold and hierarchical porous gold.

Sample\ Full width at half max	Cathodic FWHM (mV)	Anodic FWHM (mV)
Bare flat gold	60	50
Macroporous gold	125	119
Hierarchical porous gold	123	124

The amount of ferrocene adsorbed on the electrodes can be determined by measuring the area underneath the voltammetric peak. The results from such an analysis are given in Table 5.9. The area under the anodic peak is larger for macroporous and hierarchical porous gold compared to bare flat gold due to their higher surface areas. For the hierarchical gold electrode, the area underneath the anodic peak is ca. 2 times bigger than

the macroporous electrode consistent with its 2 times larger electrode area. When the area underneath the voltammetric curve is divided by the electrode area, surface coverage in terms of moles/cm² can be obtained. For both the hierarchical and macroporous gold electrodes, similar values were obtained. For the bare, flat electrode, a significantly higher surface coverage was obtained. The ferrocene molecules can assemble significantly closer on a flat gold electrode than they can on a nanostructured gold electrode with significant curvature giving rise to a larger surface coverage.

Table 5.9 The integrated area under the anodic voltammetric peaks acquired at 20 mV/s for bare flat gold, macroporous gold and hierarchical porous gold in 1.0 M HClO₄.

Sample	Bare flat gold	Macroporous gold	Hierarchical porous gold
Area under the anodic peak (μC)	6.16	4.51	8.45
Surface coverage (mole/cm ²)	1.85x10 ⁻¹⁰	6.65x10 ⁻¹¹	7.06x10 ⁻¹¹

5.5.3 Protein biofouling study

Nanostructured surfaces have been shown to be more biocompatible relative to “flat” surfaces. They have been shown to be attractive supports for investigating the direct electrochemistry of small molecules, proteins,²⁴² and enzymes²⁴³ either immobilized on their surface and/or in solution. The direct electrochemistry of various biomolecules including cytochrome c,²⁴⁴ myoglobin, hemoglobin,²⁴⁵ horseradish peroxidase,²⁴⁶ glucose oxidase,²⁴⁷ acetylcholine esterase,²⁴⁸ has been made possible without the use of mediators or surface promoters. Attributes of nanostructured electrodes include a significantly higher surface area (greater number of sites for electron transfer (ET) and ideal surface

topography designed to decrease the effective distance for ET between the electrode and redox active group in a protein, to allow adsorption to take place without passivation of the electrode surface (i.e., biocompatibility). Hierarchical electrodes have an additional attribute that is particularly important in this line of research: pores on more than one length scale. Such electrodes are needed for this application because nanopores can increase the effective surface area, while macropores can enhance the diffusion and provide a more direct electron transfer pathway. In this work, we examine the electroactivity of a redox probe (potassium ferricyanide, $\text{Fe}(\text{CN})_6^{3-}$) in the presence and absence of common biofouling agents (bovine serum albumin, BSA) and the ability of a biological redox probe (cytochrome c) to exchange electrons with nanostructured electrodes.

The premise behind these experiments is that if albumin adsorbs on the electrode surface, it will impede the electron transfer of ferricyanide. In a CV experiment, this will be manifested by an increase in ΔE_p and a decrease in peak Faradaic current. The presence of albumin on the surface of the electrode can be independently evaluated using XPS, where the presence of nitrogen and/or sulfur confirms that albumin has adsorbed on the electrode surface.

In these experiments, the UV-cleaned Au electrode was placed in a solution of potassium ferricyanide (2 mM, 0.1 M KCl PBS, pH 6.3) and a cyclic voltammogram was acquired at 100 mV/s. Bovine serum albumin (BSA) was added to the solution and CVs were acquired over the course of an hour. The data shown were collected at different time intervals of 1, 2, 5, 8, 12, 16, 20, 30, 40 and 60 min after addition of BSA.

Figure 5.19a shows representative results. Initially, before addition of BSA, the voltammetric peak shape of $\text{Fe}(\text{CN})_6^{3-}$ observed at all three electrodes is consistent with a diffusion controlled, reversible redox probe freely exchanging electrons with the electrode surface, with $\Delta E_p \sim 80$ mV. After addition of BSA, the current decreases, ΔE_p increases, and the shape of the voltammetric curve becomes less peaked shaped and more ‘flat’ indicative that BSA is adsorbing on the electrode surfaces and impeding electron transfer. The extent at which the current drops and the shape of the voltammetric curve change depends on the electrode. At a bare, flat electrode, the current drops significantly faster than at the nanostructured electrodes. In addition, the shape of the CV changes more dramatically for the bare electrode compared to the hierarchical electrode. Qualitatively, the hierarchical electrodes perform better.

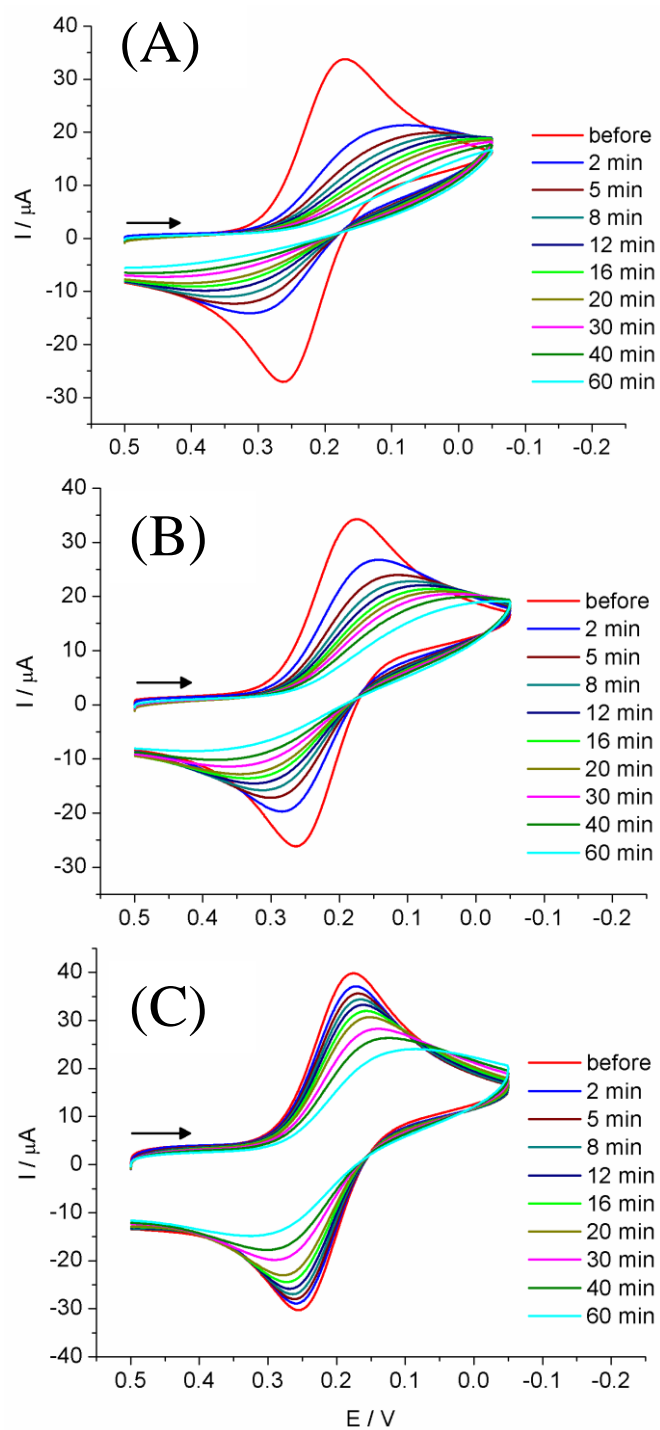


Figure 5.19 CVs of 2 mM $K_3Fe(CN)_6$, 0.1 M KCl, PBS, 25 mM, pH 6.3 before and after the addition of BSA (final concentration 2 mg/mL) for (A) electrodeposited flat gold, (B) macroporous gold, and (C) hierarchical porous gold electrodes. Scan rate: 0.1 V/s.

To more quantitatively evaluate the three electrodes, the normalized current at 0.18 V was plotted as a function of the length of time after the addition of BSA to the solution of potassium ferricyanide. The data has been normalized by dividing the current at 0.18 V by the current measured before the addition of BSA. For all three electrodes, the normalized peak current decreased. However, for the structured electrodes, the drop was significantly smaller than that observed at a bare flat electrode. Of the three electrodes, hierarchical porous gold showed the smallest drop. In this case, significant Faradaic current can still be observed one hour after the addition the BSA.

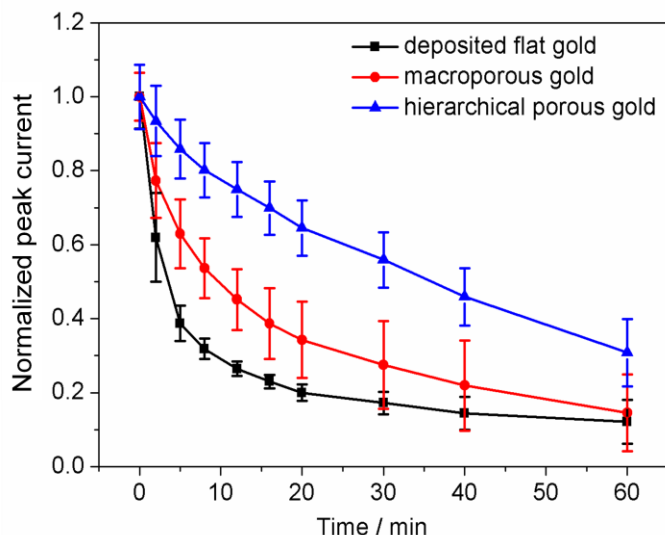


Figure 5.20 Plot of normalized CV current at the peak potential (0.18 V) before and after the addition of 2 mg/mL of BSA to solution. The current ratio was obtained by dividing the peak Faradaic current at $t > 0$ by the peak Faradaic current at $t = 0$.

Another parameter that can be measured is ΔE_p . Peak splitting is related to the kinetics of the electron transfer. A blocked (fouled) surface will slow down the rate of electron transfer, which will evident by increase in ΔE_p . Figure 5.21 shows how ΔE_p for potassium ferricyanide changes after the addition of BSA to the solution for the two

structured electrodes. As can be seen, ΔE_p increases quickly for the macroporous electrode and much more slowly for the hierarchical porous gold electrode. These results indicate that the hierarchical electrode was significantly more successful in being able to study the electrochemistry of a diffusing redox probe in a solution containing albumin compared to “flat” gold, which showed complete passivation in a very short time.

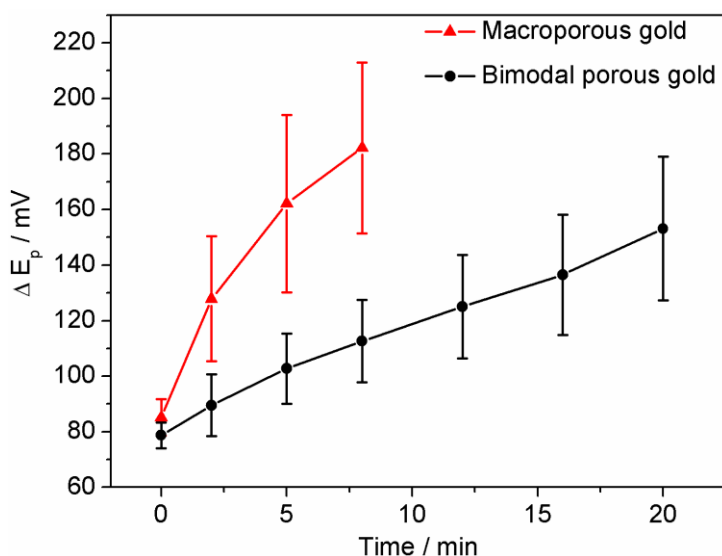


Figure 5.21 Plot of ΔE_p before and after the addition of BSA (final concentration: 2 mg/mL). The cyclic voltammetric data is shown in Figure 5.18.

It is believed that porous, structured gold electrodes are better than flat, bare gold for doing electrochemistry in the presence of possible biofouling agents for two main reasons: (1) Compared with flat gold, porous gold of the same geometric area will have a real surface area increase of about 2 times for macroporous gold, and 3.5 times for hierarchical porous gold. As a result, it will take longer for BSA to completely cover the entire electrode surface. (2) The “roughness” of the macroporous and hierarchical porous gold electrodes make the blocking of the surface by protein adsorption less effective, which means that there are still many active sites available for the electron transfer to

take place. To evaluate if the increased surface area contributes, an electrodeposited flat gold electrode with the same surface area as the real surface area of the hierarchical porous gold was used. The results are shown in Figure 5.22. As can be seen, the current drop and the change in the shape of the CV is very fast similar to that observed for the small electrodeposited flat gold shown in Figure 5.18. This indicates that the increased surface area of hierarchical porous gold is not the reason why it takes longer to passivate compared to bare, flat gold. Thus, surface morphology appears to be the main cause.

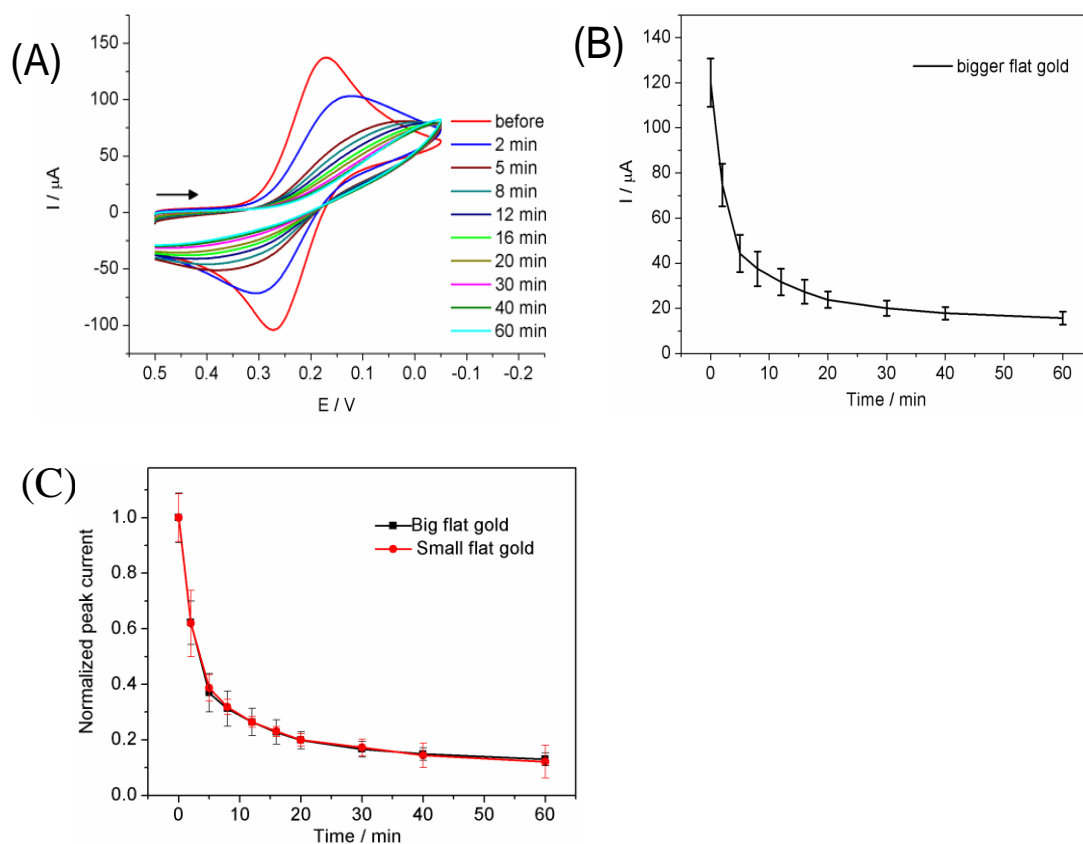


Figure 5.22 (A) CVs of 2 mM $\text{K}_3\text{Fe}(\text{CN})_6$, 0.1 M KCl, PBS, 25 mM, pH 6.3 at 0.1 V/s before and after the addition of 2 mg/ml BSA at a large electrodeposited flat gold with the same surface area as bimodal porous gold electrodes ($\sim 0.32\text{cm}^2$). (B) Current change at the peak potential of the initial CV versus time. (C) Normalized current change (by dividing by the peak current in the initial CV) in (B) versus the current change of the small flat gold.

To examine the electroactivity of potassium ferricyanide at a surface that was fully coated with BSA, the electrodes were soaked in the BSA solution for about 4 days. From the CVs shown in Figure 5.23, no Faradaic current can be observed for potassium ferricyanide because the surface of all three electrodes are completely covered with BSA. It can also be seen that the charging current is consistent with the real surface area ratio, hierarchical porous gold > macroporous gold > deposited flat gold with the ratio of about 3.5: 2:1. These results indicate that those electrodes are saturated with BSA and the structured surface morphology does not completely prevent protein adsorption.

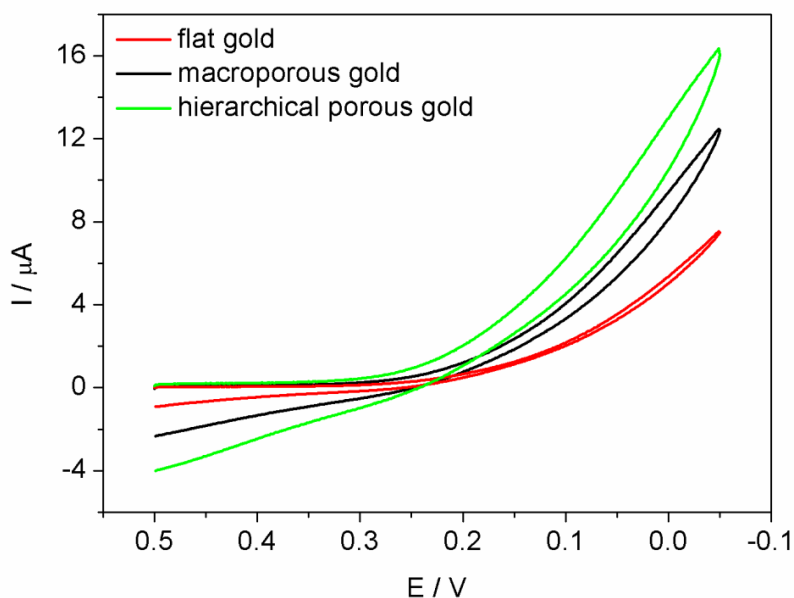


Figure 5.23 CVs of 2 mM $\text{K}_3\text{Fe}(\text{CN})_6$, 0.1 M KCl, and PBS, 25 mM, pH 6.3 at 0.1 V/s for gold electrodes soaked in BSA (2 mM concentration) solution for 48 h.

The surface of all the electrodes were examined before exposure to BSA using SEM. Figure 5.24 shows the SEM images of the four different electrodes before exposure

to BSA. As can be seen, the bare flat gold has a very different surface morphology compared with electrodeposited flat gold. A smoother surface will result in a faster biofouling process. Since both macroporous gold electrodes and hierarchical porous gold electrodes are made by electrodeposition using the same plating solution as the electrodeposited flat gold, electrodeposited flat gold is a better control than bare flat gold. The reason of the prolonged adsorption process is probably because the rough and irregular surface of biomodal porous gold makes complete blocking difficult.

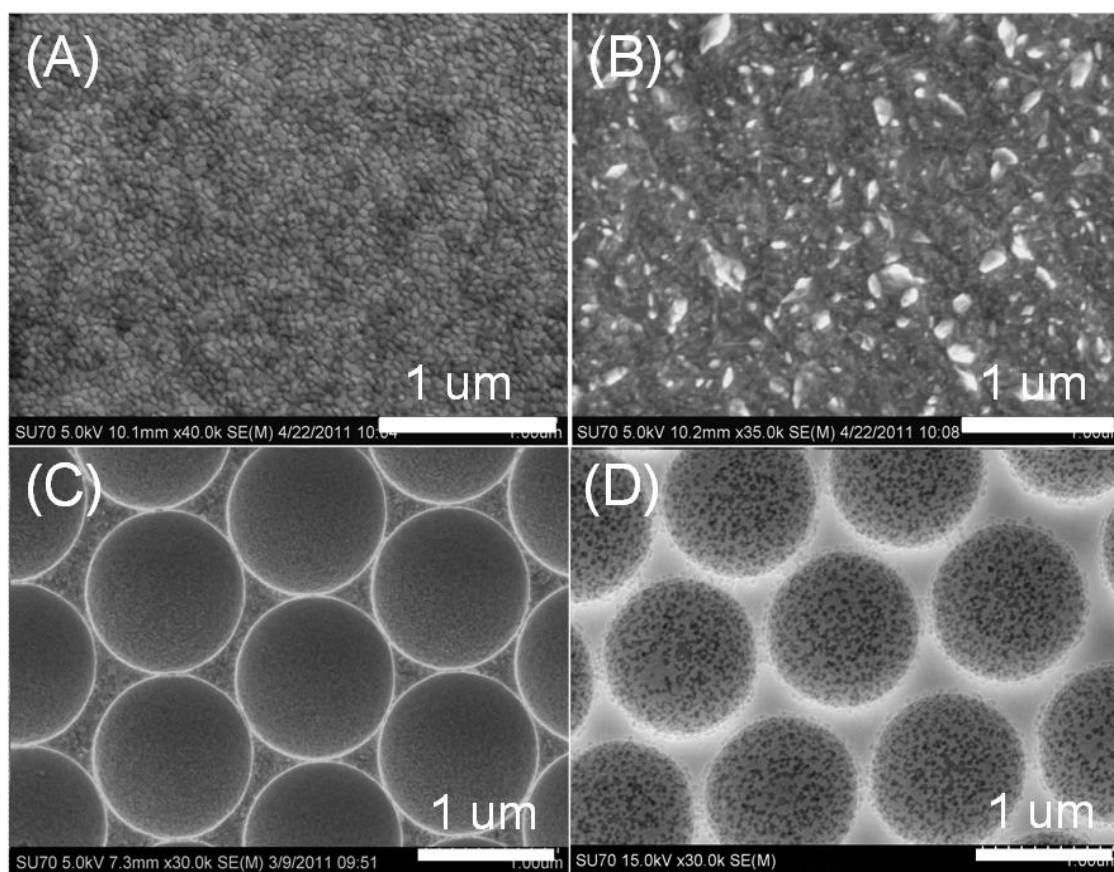


Figure 5.24 SEM images of (a) as-received bare flat gold (b) electrodeposited flat gold (c) macroporous gold, and (d) hierarchical porous gold.

Figure 5.25 shows the CV of bare flat gold and hierarchical porous gold in 0.1 mM

cytochrome c in PBS buffer (25 mM, pH = 7) at 0.1 V/s. At a bare electrode, no current was observed because cytochrome c (pigeon heart) adsorbs and denatures on the electrode surface as noted in the published literature.^{249,250} For the hierarchical porous electrodes, however, direct electrochemistry can be observed as evident from the peak centered near 0.06 V. Direct electrochemistry has also been observed on gold particle electrodes.^{251,252} Consistent with the results shown earlier using potassium ferricyanide as a redox probe, this result also indicates that hierarchical porous gold is less prone to blocking and/or denaturation or otherwise peak would not be observed. A similar drop in current was observed as the electrode remained in the solution of cytochrome c for longer periods of time.

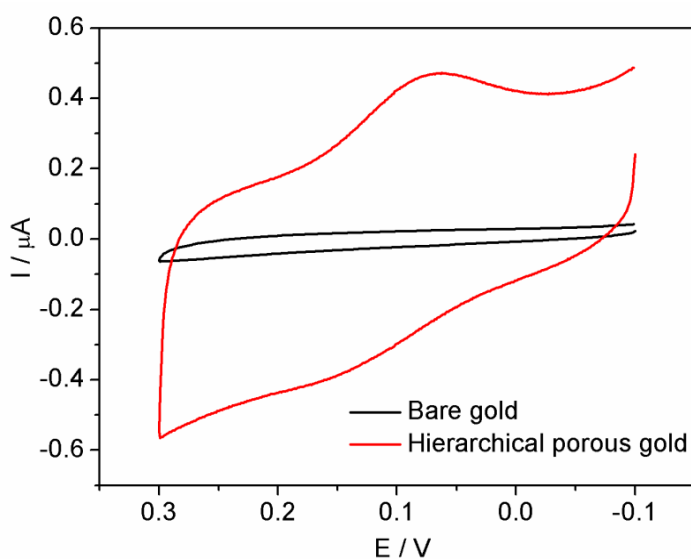


Figure 5.25 CV at bare flat and hierarchical porous gold in 1 mM cytochrome c (pigeon heart) in 25 mM PBS buffer (pH=7) at 0.1 V/s.

XPS was used to confirm the electrochemistry findings. XPS samples were prepared by soaking a bare flat electrode, a flat electrodeposited electrode, a macroporous

electrode and a hierarchical porous electrode in 1 mM $\text{Fe}(\text{CN})_6^{3-}$ / 0.1 M KCl/ 0.025 M PBS(pH=7)/ 2 mM BSA solution for different times. XPS spectra are shown in Figure 5.26. As can be seen, both N and C peaks increase and Au peak decreases after a 10 min and 60 min exposure to BSA. The S peak can not be clearly distinguished in these spectra. This result indicates that BSA is adsorbing on the electrode surface. To more quantitatively evaluate the data, the area under the nitrogen peak was analyzed. In this experiment, a 50 eV pass energy and a step size of 0.100 eV were used. Average values of 10 scans at three different positions for each sample were taken. From the results shown in figure 5.27, it can be seen that the nitrogen content increased after the electrode was soaked in BSA for 10 minutes, indicative of protein adsorption.

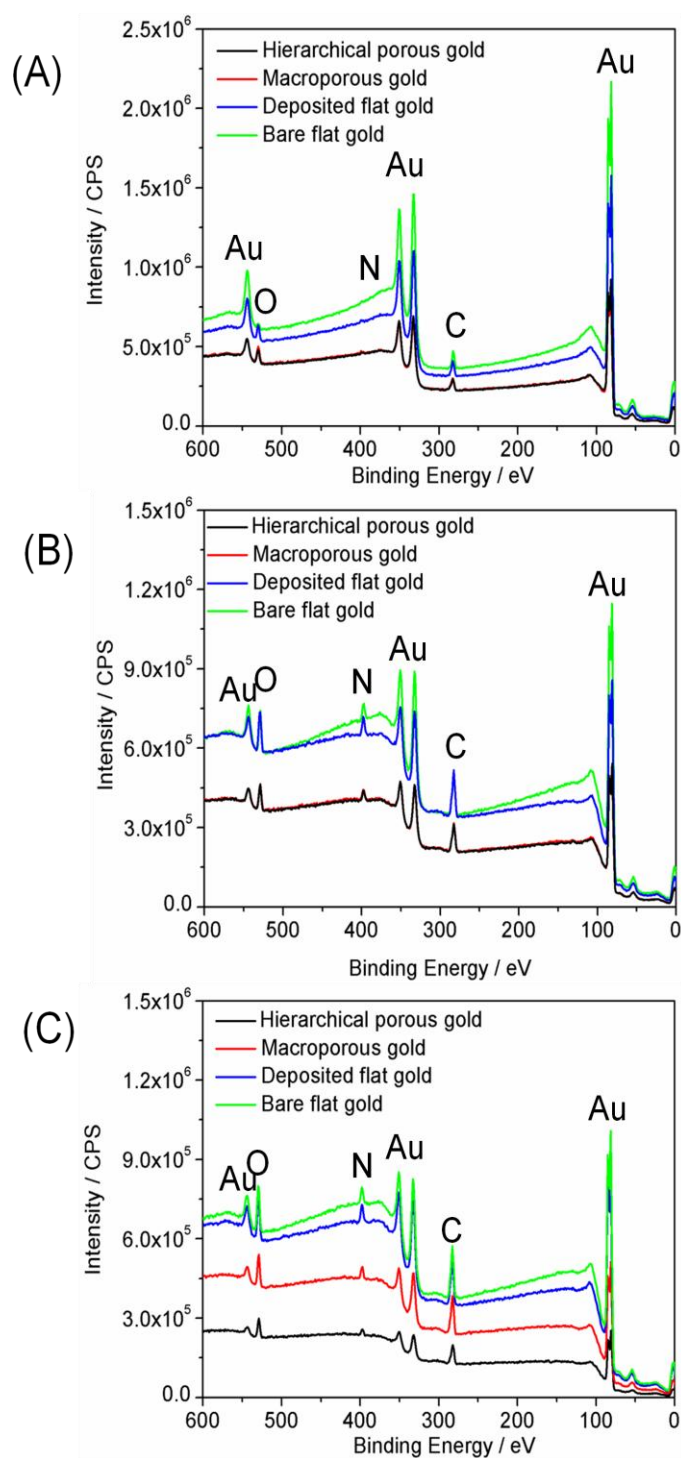


Figure 5.26 XPS survey spectra of bare flat gold, deposited flat gold, macroporous gold and hierarchical porous gold after soaking in the $\text{Fe}(\text{CN})_6^{3-}/\text{KCl}/\text{PBS}/\text{BSA}$ solution for (A) 0 min, (B) 10 min and (C) 60 min. XPS survey parameters were 150 eV pass energy, 3 scans, and 0.100 eV step size

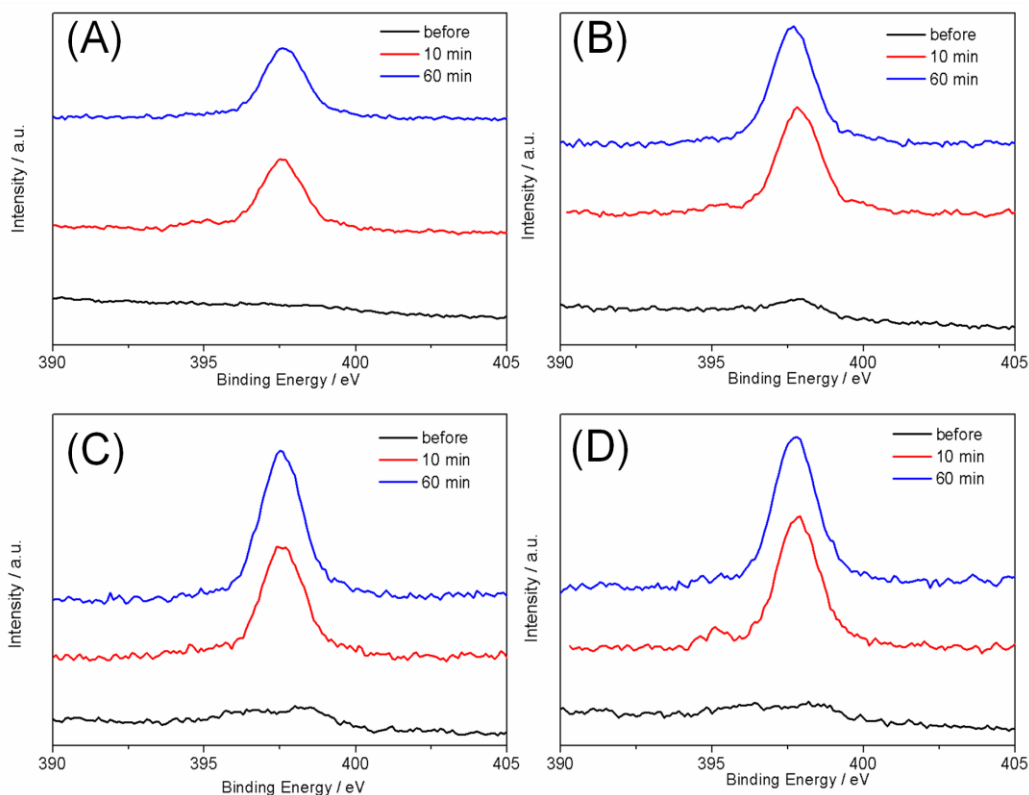


Figure 5.27 Nitrogen (1s) peaks from XPS data of (A) bare flat gold, (B) deposited flat gold, (C) macroporous gold and (D) hierarchical porous gold after soaking in the $\text{Fe}(\text{CN})_6^{3-}/\text{KCl}/\text{PBS}/\text{BSA}$ solution before and after addition of BSA. XPS parameters were 50 eV pass energy, 10 scans, and 0.100 eV step size.

Peak comparison can be a little tricky there in XPS as there are many factors that influence the XPS signals. One important variable is the collection efficiency of the instrument. The increased surface area for porous gold will result in more signal collection than the flat gold for the same XPS beam size. Also, the roughness of the surface will result in scattering of the signals, thus lowering the signal collection efficiency. To exclude these influencing factors, a comparison was made by taking the ratio of the N content to the saturated N content. Specifically, for each electrode, the N

data was normalized by taking the area under the N curve at $t > 0$ and dividing it by the area under the nitrogen peak acquired for the saturated BSA. In this manner, direct comparisons can be made because the data has been corrected for changes in the collection efficiency of the instrument. Before exposure to BSA, all three electrodes have small nitrogen content that can be barely noticed in the XPS surveys shown in Fig 5.11. For electrodeposited flat gold, the nitrogen content after a 10 min and 60 min exposure to BSA were not much different, which is consistent with the fact that the passivation (BSA adsorption) takes place very fast. In 10 min, the electrode is fully covered with enough BSA to passivate the surface since the protein likely unravels on flat gold and occupies more of the surface. For the macroporous and hierarchical porous gold, significant N content can be observed after 10 min, with small increases seen at a longer times (60 min, 4 days). This means that there are still a significant amount of active sites available on the surface and the adsorption still happens at a noticeable rate. Similar N content was observed for three electrode surfaces at 10 mins and 60 mins, with some variations. However, it takes longer for hierarchical porous gold electrode to passivate, consistent with the electrochemistry results. Excluding the possibility of having significantly different adsorption processes at the different electrodes, we can conclude at this point that passivation is less effective on the porous surfaces because it is harder to completely block the entire gold surface. Electron transfer can still take place on exposed areas. In addition, for the hierarchical electrodes, diffusion of BSA may be hindered in the small satellite pores relative to significantly smaller $\text{Fe}(\text{CN})_6^{3-}$ molecules. Thus, differences in the transport rates in the small inner pore may also help prolong the

observation time window.

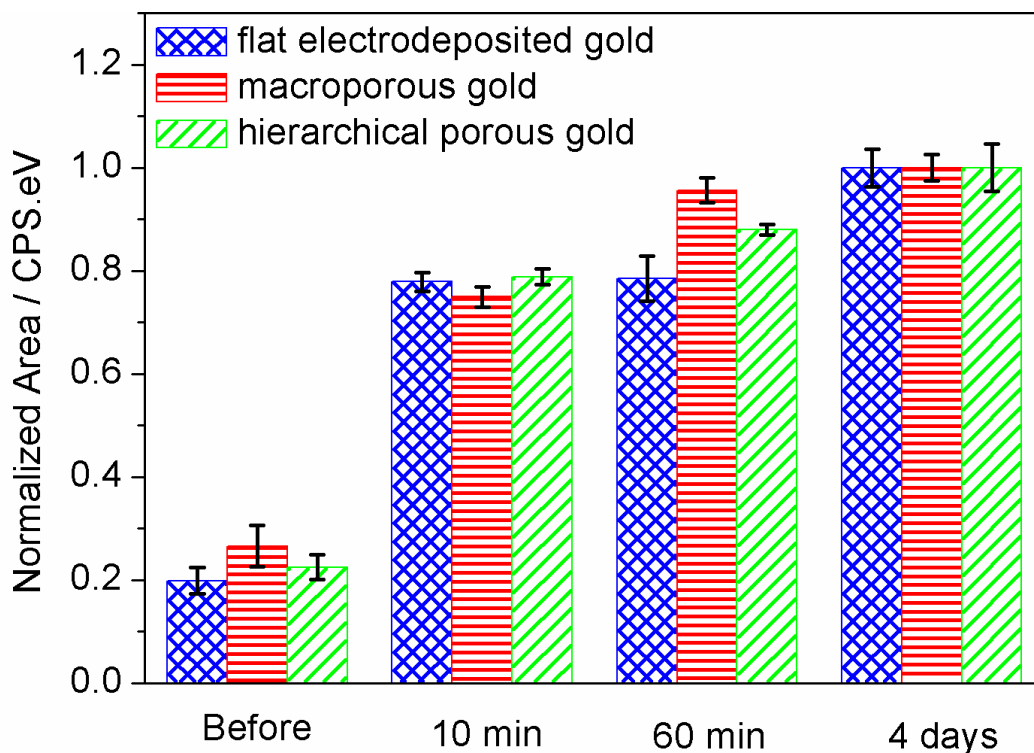


Figure 5.28 Normalized N (1s) XPS before and after exposure to BSA. Solution: $\text{Fe}(\text{CN})_6^{3-}/\text{KCl}/\text{BSA}/\text{PBS}$ for electrodeposited flat gold, macroporous gold, and hierarchical porous gold. Error bar corresponds to relative standard deviation $N = 3$

There are two possible reasons for the longer passivation (1) On the curvy surface of bimodal gold, the complete coverage of the surface is impossible in relative short time. As shown in Figure 5.29(a), There are still quite a few sites available for the electron transfer between the redox couple and the electrode surface, so the signal won't be completely blocked in a fast process. (2) Adsorption in the secondary pore is slower due to the slower diffusion rate. As shown in Fig. 5.29 (b), the satellite pores are of 60 nm size and 20 nm opening, which means that the diffusion into the dead end pores will be

much slower, especially for the relatively big proteins. Thus the inner surface won't be blocked as fast, and provide enough sites for electron transfer there.

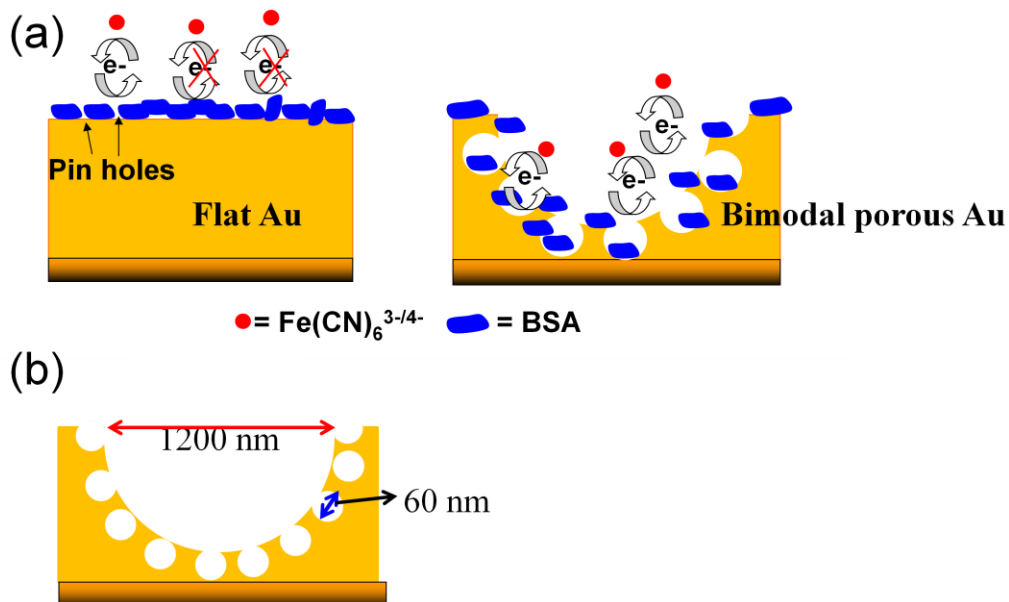


Figure 5.29 Possible mechanisms for the longer passivation process of bimodal porous gold electrode.

5.6 Conclusion

In this work, hierarchical porous gold electrodes were fabricated by a hard templating method using hierarchical templates. The structured electrode obtained showed a higher surface area and retarded the passivation of its surface with BSA. In chapter 3, the advantages of using a single hierarchical template with well-defined sizes in fabricating hierarchical porous materials were clearly addressed. What can be concluded at this point is that adsorption does take place on hierarchical porous surfaces, and it does not scale with increase in surface area. But the process is much slower compared with flat gold thus providing a prolonged observation time window. The reason that the “rough” surface

is not easily electrochemically passivated is likely because of the “antenna” effect, where there are still significant locations for electron transfer to take place even with protein adsorption.

Chapter 6 Hollow sphere with well defined windows on the shell

6.1 Introduction

In this chapter, the fabrication and characterization of a well-defined porous hollow capsule with asymmetric pores in the shell using a hard templating method and the 1500/110 nm COOH-NH₂ hierarchical raspberry-like template is described. The major objective of this study is to show hierarchical templates can be used to create porous capsules with asymmetric windows with potential applications in medicine and pollution treatment.

6.2 Background

A key challenge in material design and fabrication is the ability to control pore architecture, whether it be at the micro-, meso-, or macropore level or a combination of levels as in the case of hierarchical structures. Not only is size important, but also the distribution in size, shape, order of the pores (both long range and short range), interconnectivity, and number density. Such physical characteristics play an important role in the performance of such materials, particularly in applications that require fast and/or efficient transport into and out of the porous structure. Inorganic porous capsules are one such structure.^{124,253-256} These materials have a morphology that consists of an interior void and a porous inorganic shell and have served as microreactors, drug storage containers, and adsorbants for applications ranging from chemical sensing, drug delivery, to separation and filtering.^{124,257} The pore channel(s) in the capsule shell plays an important role in this architecture, as this is the location where loading and releasing of

the desired molecules takes place.

During the past decade, there have been many reports on the preparation and characterization of hollow capsules with a porous shell using various approaches that include layer-by-layer (LBL) assembly, direct chemical deposition or adsorption, soft templating, and nanocasting.^{124,182,257,258} Many of those porous shells contain nonuniform, randomly distributed pores innate to the material itself while others have more directed porosity created via the use of a secondary template such as a surfactant/block copolymer.^{96,97,259} Such secondary pores are typically nanometers in size, which are not necessarily efficient for applications that require fast loading and release characteristics. To address this challenge, more recent work has focused on the introduction of a large, single hole into the polymer capsule structure²⁶⁰⁻²⁶⁵ and/or a collection of holes (windows) of nonuniform size scattered around the surface of the capsule.²⁶⁶⁻²⁷⁰ These nanometer to micron- sized holes are valuable because they provide an efficient pathway for chemical loading and releasing. However, explicit control over the size of the windows, their number density, and how they are connected to interior is needed.

In this work, hollow capsules with well-defined pore architecture have been fabricated by the hard templating route using a raspberry-like hierarchical template formed by chemically coupling a large (1500 nm) polystyrene (PS) core sphere to an ensemble of small (110 nm) satellite spheres.¹⁵⁴ The interconnectivity between pores is guaranteed by the bonding between core and satellite spheres while the size of the windows is controlled by the size of the satellite sphere. The porous silica capsule thus produced has a high density of asymmetric pores (windows) providing a direct path from interior to exterior

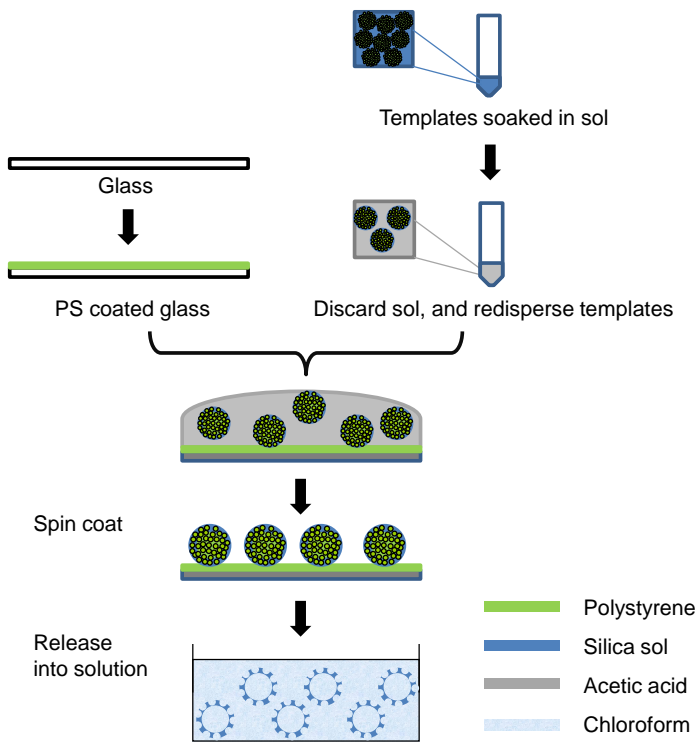
and vice versa. The asymmetric pores thus produced provide a short diffusional pathway from one side to the other, potentially leading to asymmetric diffusion with the ability of ions to more readily pass through in one direction than the other.²⁷¹ Compared with polymeric shells, the rigid nature of silica capsule provides fixed void space and shape, which can be potentially useful when used as storage and/or reaction containers.

6.3 Fabrication process

The fabrication process, depicted in Figure 6.1, is relatively straightforward. The hierarchical template was made by the carbodiimide coupling of COOH groups located on the core polystyrene sphere and NH₂ groups on the satellite polystyrene spheres as previously described.¹⁵⁴ The hierarchical template (1500/110 nm) was mixed with a 2-day old aged sol formed by hydrolyzing tetraethoxysilane (TEOS, 1.3 mL) in the presence of water (0.3 mL), ethanol (2 mL), and HCl (0.1 M, 0.3 mL). After soaking for 5 min, the templates were separated from the solution by centrifugation, re-dispersed in 25 μ L of concentrated acetic acid by quick vortexing and then immediately spin coated onto a polystyrene coated hydrophobic glass slide at 8000 rpm. The spun slides were dried at 40–45% humidity at room temperature for 1-2 days to strengthen the silica framework. Upon immersion in chloroform, the underlying polystyrene layer was removed thus releasing the silica coated templates into solution; the polystyrene template also dissolved at the same time. The silica capsules thus produced were collected and washed via filtration by cellulose membrane in a funnel and calcined at 450 °C for 5 h (ramp of 5 °C/min) to ensure all the polystyrene was removed. Scanning electron microscopy (SEM) and scanning transmission electron microscopy (STEM) were used to characterize the

materials.

(a)



(b)

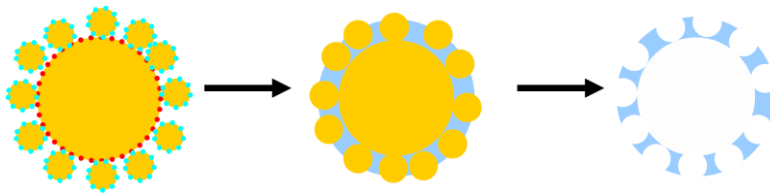


Figure 6.1 (a) Overview of the fabrication process and (b) simplified 2D images of the fabrication strategy.

6.4 Characterizations

To form a porous capsule with a closely packed ensemble of well-defined windows, (as in Figure 6.2 (c)) the silica sol must uniformly coat the inner sphere but, most

importantly, not encase the entire template (as in Figure 6.2 (a) or (b)). If the silica sol polymerizes around the entire structure, the result would be a macroscopically rough silica capsule with a bimodal inner pore structure but without clear openings (windows) to the external environment as shown in Figure 6.2 (a) and (b). The problem is compounded in this work because the satellite spheres have residual NH_2 groups on the surface, which catalyze the condensation of silica that may result in localized deposition of silica. To circumvent this problem, the sol-coated hierarchical latex spheres were dispersed in acetic acid and spin coated on an appropriate substrate. The sheer act of spin coating causes excess sol to be flung off the template/surface creating a thin shell. Most importantly, during spin coating, the residual sol wicks down the sides on the satellite spheres, thus exposing their tops while still producing the silica shell around the core. This process has been noted in prior work as a means to form nanowells that are open on the top and bottom by spin coating latex spheres doped in a silica sol on a planar surface.^{231,272,273} The only difference in the present work is that the surface is not a planar surface but rather a spherical one. The sacrificial polymer layer on the glass slide enables the capsules to then be transferred back into solution, if so desired.

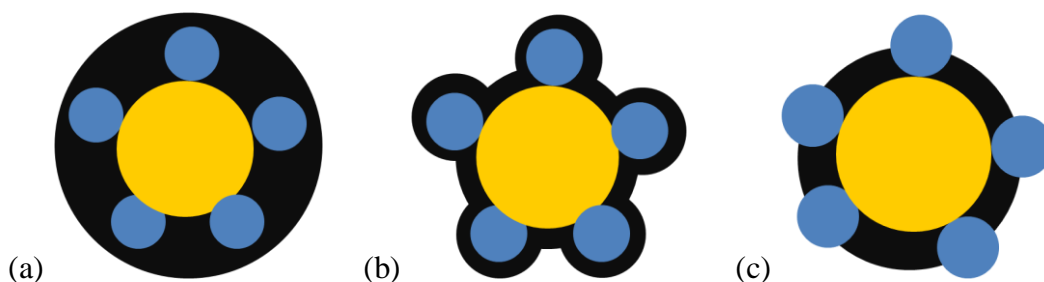


Figure 6.2 Schematic depictions of possible encapsulation styles (a) encasing the entire template, (b) encasing both the core and satellite spheres, and (c) coating only on the inner sphere.

The windows that ultimately form on the capsule upon removal of the templates will be asymmetric as the outside diameter will be larger than the inside diameter.²³¹ The diameter of the window located on the outside of the capsule is primarily determined by the size of the satellite sphere and extent at which the sol wicks down the sphere while the diameter of the pore leading to the interior of the capsule depends on the how much contact the satellite sphere makes with the inner core sphere.²³¹ The size of the inner pore will also be influenced by the calcination process. Capsules without calcination treatment have very tiny inner holes that are hardly observed from SEM images.

The distribution of sol coated templates on the PS-glass slide is shown in Figure 6.3 (A). As can be seen, there are monomers, dimers and polymers, which are inevitably formed by using the spin coating method. In Figure 6.3 (B), silica sol was trapped in the space between the satellite spheres without covering the top of the satellite spheres. This will later transform into the silica shell of the capsule, and the shell windows will form when the satellite spheres are removed. The size of the hierarchical template is 1500 nm/110 nm, so the shell thickness formed should be about 50-60 nm as estimated from Figure 6.3 (B).

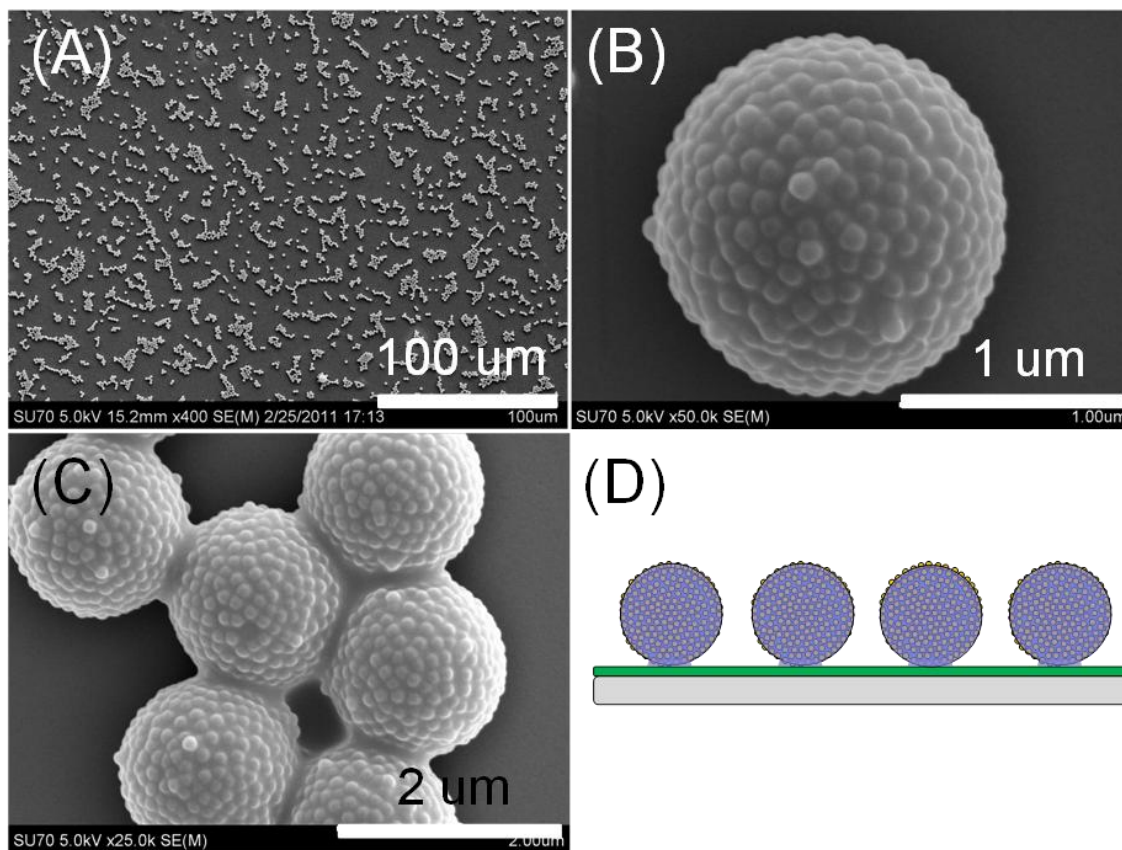


Figure 6.3 SEM images of silica sol coated 1500 nm/ 110 nm hierarchical templates dispersed on the PS-coated glass slide. (A), (B), and (C) are different magnifications. (D) is a cartoon of the side view of the slide.

Figure 6.4 shows SEM images of the porous capsules formed by directly calcining the glass slide/silica coated templates while Figure 6.4 (B) shows the porous capsules released into solution (chloroform) followed by calcination. In both images, the diameters of the capsules are ~ 1400 nm and the outer openings of the windows are ~ 100 nm size. These sizes are slightly smaller than the raspberry templates used for the fabrication (1500/110 nm) due to the shrinkage associated with the calcination. The acetic acid used to redisperse the sol-coated templates is necessary for spreading them evenly on the

polystyrene-coated glass surface. It is inevitable that there will be dimers, trimers, and polymers formed because of the spin coating method employed. Using more acetic acid (50 μL) to disperse the sol-coated templates can help reduce the aggregation.

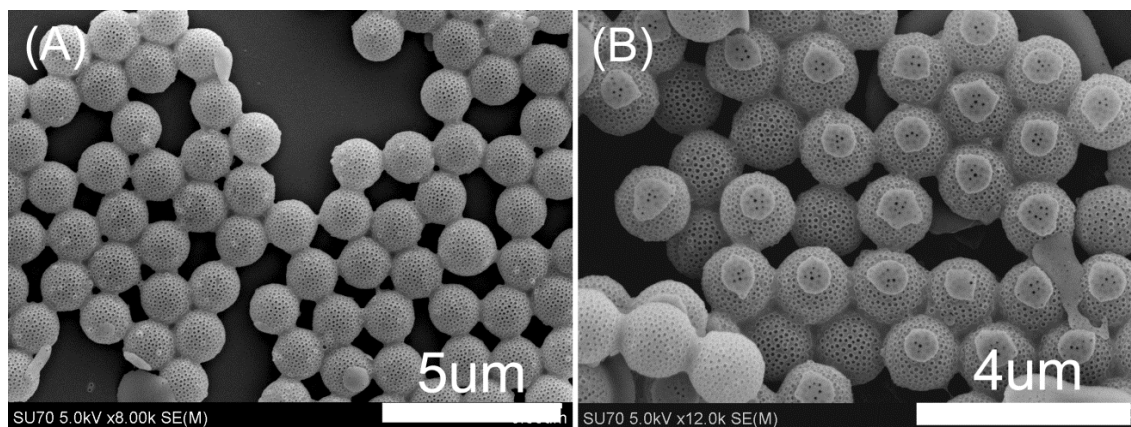


Figure 6.4 (A) SEM image of the porous capsule obtained by direct calcination after spin coating on a glass slide. (B) SEM image of porous capsules after releasing them back into solution and calcination.

In Figure 6.4 (B), what appears to be a ‘button’ (a small circular raised area with several holes in its center) can be seen on many of the capsules. When the silica sol-coated template is spin coated on the polystyrene coated glass slide, it makes contact with the surface resulting in the trapping of sol at this location. The small volume of trapped sol leads to the formation of the “button” upon gelation as shown in Figure 6.3 (D). As long as the capsules remain on the slide, the button can not be easily seen (Figure 6.4 (A)). When the capsules are removed from the surface, redispersed in solution, and then cast on another slide, the button becomes visible (Figure 6.4 (B)) on the capsules with the bottom side facing up. The “buttons” can also be easily distinguishable from the STEM

images shown in Fig. 6.5. The arrow indicates the locations of the “buttons”. The average size of the “buttons” is $\sim 600 - 700$ nm. The size of the button can be reduced by further diluting the sol-coated hierarchical templates in acetic acid and/or increasing the rate of spin coating but often at the expense of shell thickness and integrity, leading to broken capsules. Representative STEM images of broken capsules obtained by the two ways mentioned above are shown in Figure 6.6.

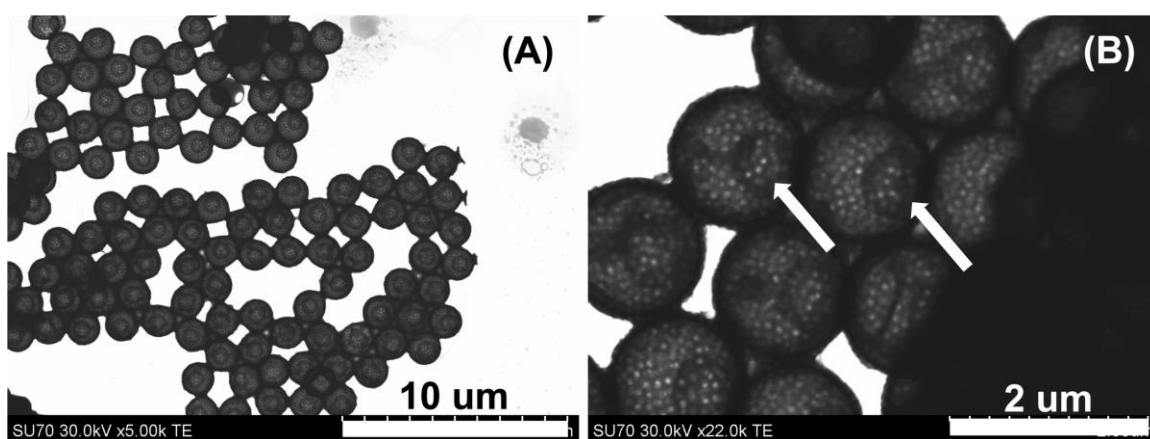


Figure 6.5 STEM images of hollow capsules at a large (A) and small (B) magnification. The arrows show the locations of the “buttons”.

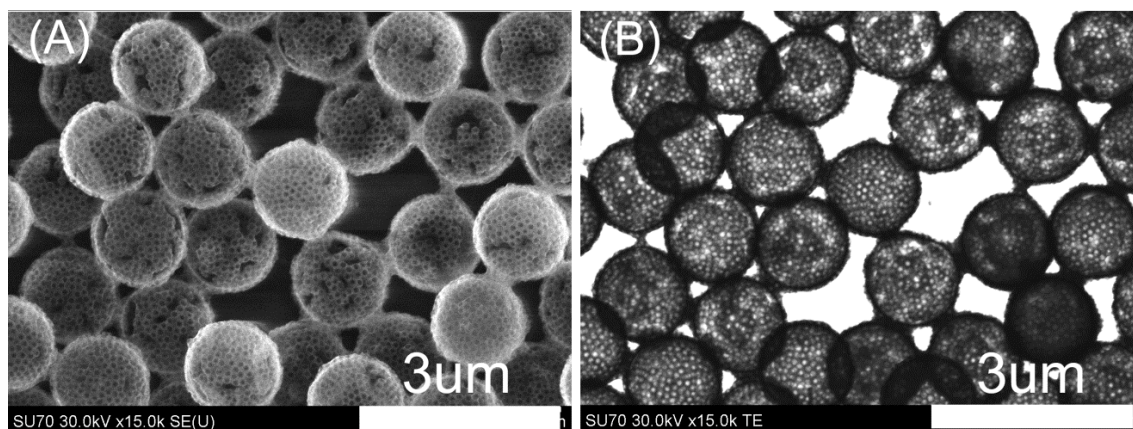


Figure 6.6 STEM images of broken porous capsules formed when they were redispersed in more acetic acid ($50 \mu\text{L}$). (A) secondary electron image; (B) transmission electron image.

To help understand the architecture of the capsule, a 3D model of a hierarchical sphere and its corresponding porous, hollow capsule were created by 3D Max software, Figure 6.7 (A). The SEM image of a hierarchical capsule shown in Figure 6.7 (C) matches what is shown in the model, Figure 6.7 (A): a capsule with a closely packed ensemble of asymmetric pores (windows) through the shell. The number density of pores in the shell is high, because the satellite spheres are closely packed on the surface of the core sphere. The diameters of the windows located on the exterior surface of the capsule are larger than the openings on the inner surface, thus giving rise to an asymmetric pore. A clear depiction of the inner window can be seen in Figure 6.7 (D), which shows the inside of a broken capsule obtained by sonication. The diameters of the inner pores estimated from this SEM image are ~ 30 nm. A magnified image of the outer windows, which are ~ 100 nm in diameter, can be seen in the center inset, which shows the outer diameter to be ~ 100 to 110 nm. Both these images indicate that the pores are asymmetric and transverse through the shell. The asymmetry factor, defined as the diameter of the outer window to the diameter of the inner window, is ~ 3 . The thickness of the shell, estimated from this image, is 75 nm given that the edges of the outer openings are a little thicker than the real shell.

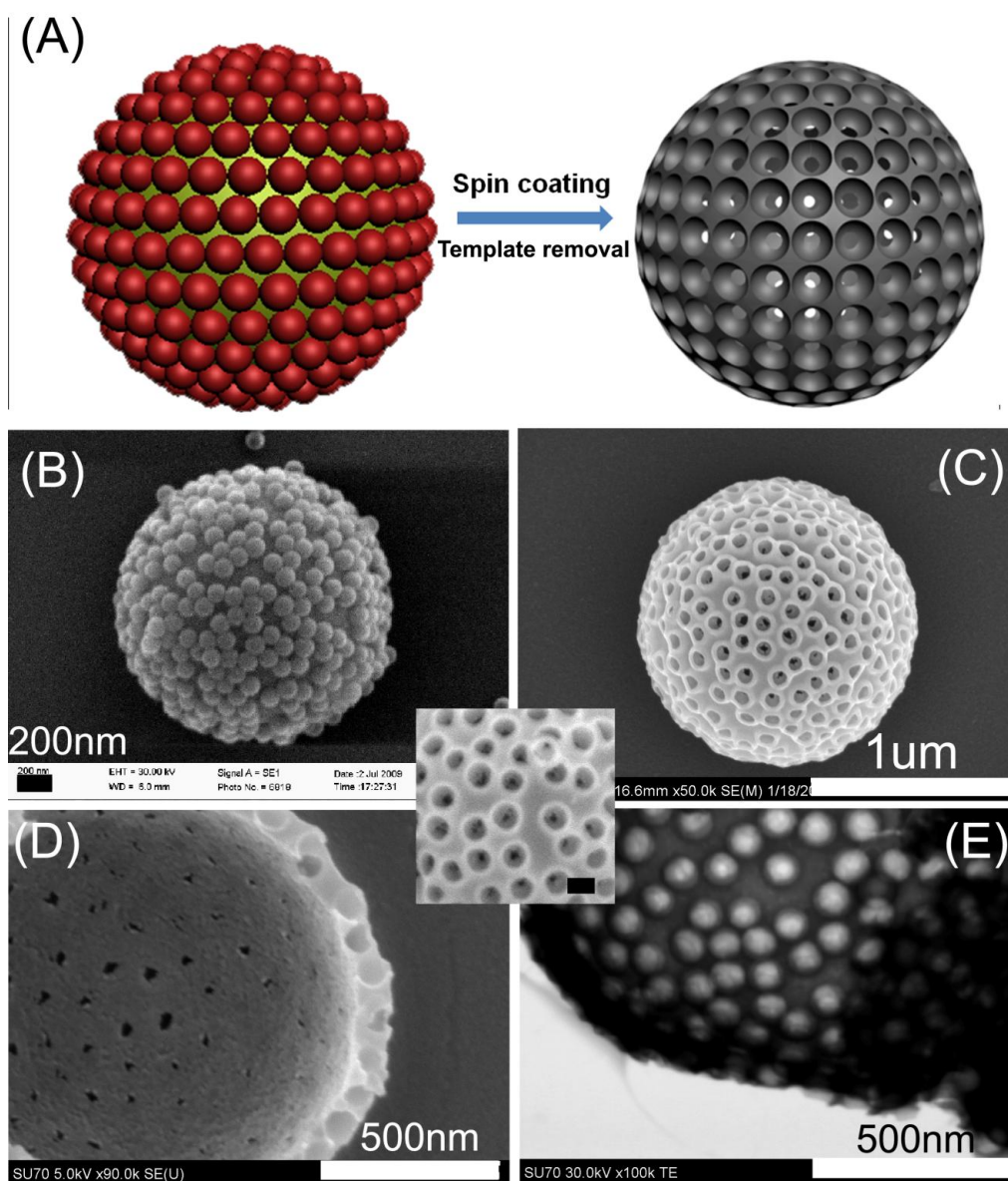


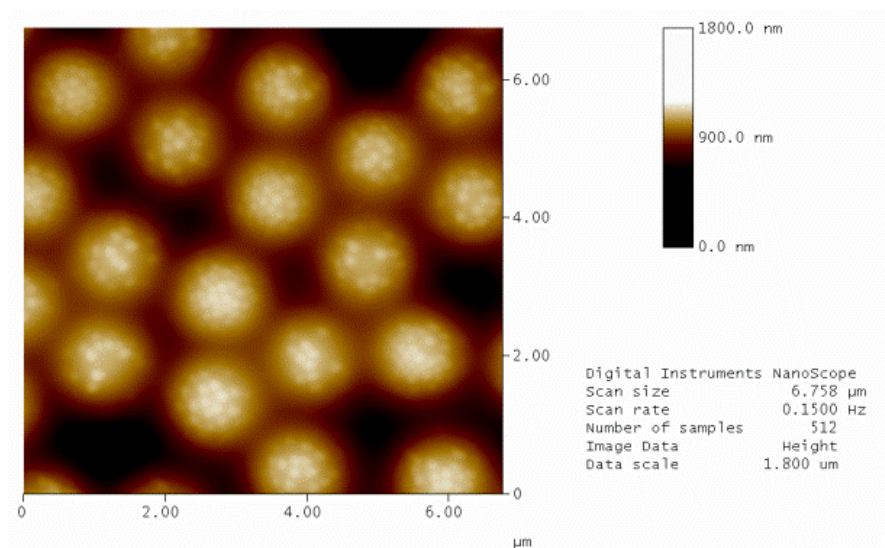
Figure 6.7 (A) 3D scheme of the fabrication strategy; SEM images of (B) hierarchical template (C) porous capsule (D) inner opening of the pores on the shell and (E) TEM image of a broken shell. Inset is a blowup of the outer surface of the capsule. Scale bar is 100 nm.

Similar results are also observed in the STEM images shown in Figure 6.7 (E). The pores (windows) are clearly open from outside to inside as evident from the bright

centers, which are also ~ 30 nm in diameter. In the button area, only the center has several openings. These openings form at the place(s) where the satellite spheres touch the polymer coated substrate.

AFM was also used to characterize the porous capsule shell. Because resolution is defined by the sharpness of the AFM tip, height or depth information obtained by AFM has to be viewed carefully. Figure 6.8 shows the AFM images of the top surface of the 1500/110 nm COOH-NH₂ template. The satellite spheres are clearly observed in these images. Since the AFM tip moves only in vertical direction, the satellite spheres located on the side of the template can not be seen in these images. Figure 6.9 shows the AFM images of the silica capsules fixed on a glass slide. The only difference is this sample was spin coated on a glass slide not a PS-coated slide. When zoomed in, such as that shown in Figure 6.9D, small circles are clearly seen on each big bump, which are the asymmetric windows in the shell. As can be seen from the sectional image, the diameter of the outer windows is about 100 nm, which is in consistent with the size obtained from SEM and STEM images.

(A)



(B)

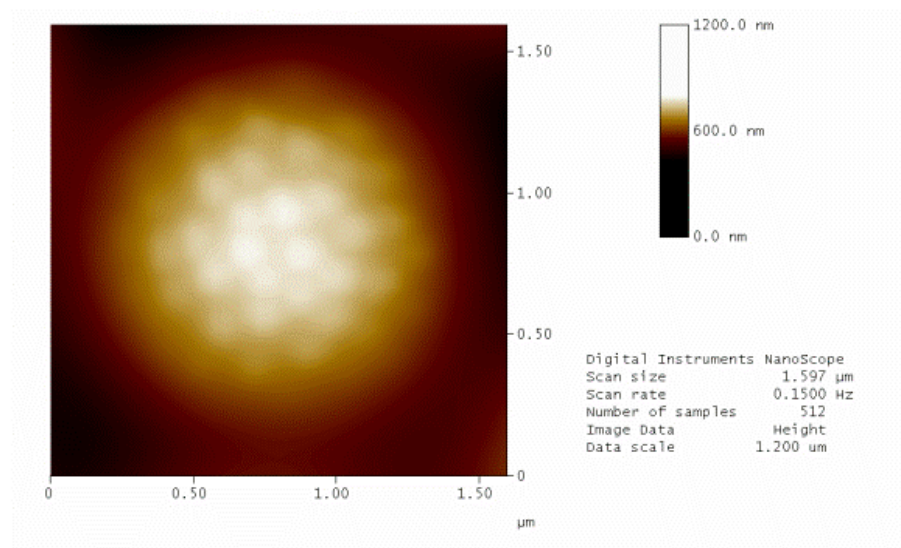


Figure 6.8 AFM images of the 1500/110 nm COOH-NH₂ hierarchical templates. (A) 6.0 x 6.0 μm² and (B) 1.5 x 1.5 μm².

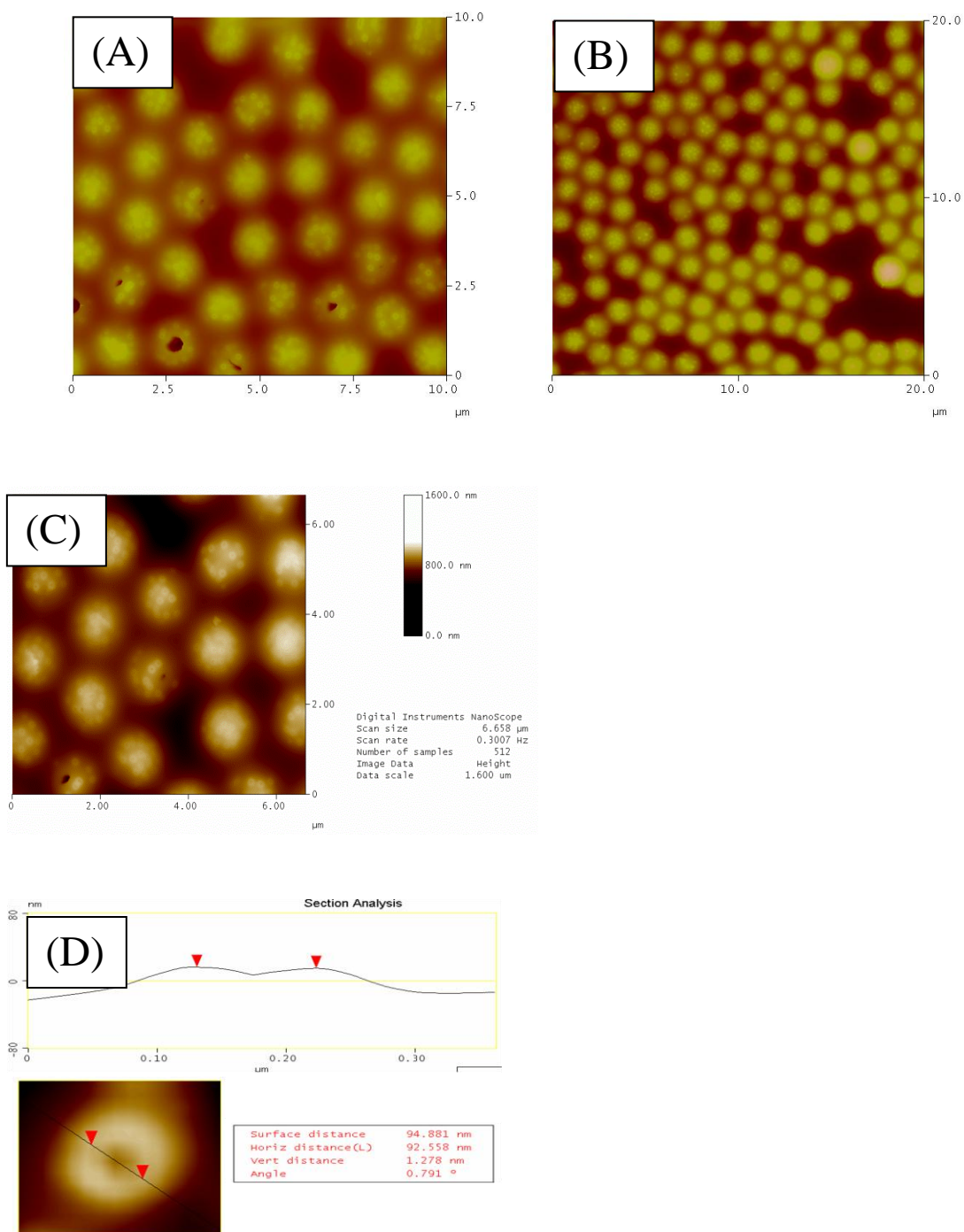


Figure 6.9 AFM images of the silica capsules fixed on a glass side fabricated by spin coating on a glass slide without a PS layer. (A) 10 μm scale range, (B) 20 μm scale range, (C) zoomed in image, and (D) AFM image of one window and its corresponding sectional.

6.5 Discussion

Precise control over the capsule structure is very important. All the parameters influence the performance of the whole structure, like the size of the hollow void, the sizes of the small opening and big opening in the shell, the thickness and porosity of the shell, etc. Several modal examples are shown in Figure 6.10. The window area is determined by both the two sizes of the template PS spheres, specifically the area of the spheres that are in contact with each other. It is also determined by the wettability of the shell material (silica sol in this case) on the PS surfaces. The shell thickness is determined by the viscosity of the sol, the spin speed and the washing duration by acetic acid. These parameters are crucial with respect to structure design and its practical applications.

60 nm/450 nm



180 nm/450 nm



800 nm/1.5 μm



Figure 6.10 Example of capsules that have different void sizes, window sizes and shell thicknesses.

The glass slide coated with a thin layer of polystyrene beforehand is the key for transferring the capsules back into solution. A smooth PS layer also helps the templates to distribute evenly on the slide during the spin coating process. This relatively

hydrophobic surface also helps ensure the extra sol will be spun away during spin coating. When immersed in chloroform, both the templates and the polystyrene layer will be simultaneously dissolved, which will release the porous capsules back into solution. The capsules can then be easily collected, and washed with chloroform on a cellulose membrane via a Buchner funnel.

The washing step before the spin coating is very important to this whole fabrication process. Different solution and solvents have been used and compared for this step. Concentrated acetic acid doesn't hydrolyze the sol much over short times, and it can mix well with the sol, so it was found to be the best candidate for the washing step. Other solvents were also tried in this step, including water, ethanol, water/ethanol mixture, hexane, and dilute acetic acid. Water resulted in a complete coverage of the whole template due to the hydrolysis during the washing, and it also had trouble spreading the sol-coated templates on the relatively hydrophobic PS-coated glass slide; so nothing will be left on the surface. Ethanol, water/ethanol and dilute acetic acid had similar results where the satellite spheres on the template were covered by a thin layer of silica. Hexane didn't disperse the sol/template well.

Compared with cylindrical pores, the asymmetric pores have many advantages, such as enhanced transport and preferential diffusion direction. For cylindrical shaped pores in the shell, ions or particles have to pass through the whole shell thickness in a very narrow channel. For asymmetric shaped pores, however, this narrow part is substantially reduced, since only the inner opening has the smallest size. Transport into the capsule can be greatly enhanced in this way. Furthermore, asymmetric pores have been shown to exhibit

geometric-induced asymmetric diffusion when the diffusing particles are of a similar size to the pore.²⁷⁴ Thus, asymmetric pores in a capsule may introduce more interesting diffusion phenomenon to the capsule structure compared with cylindrical pores.

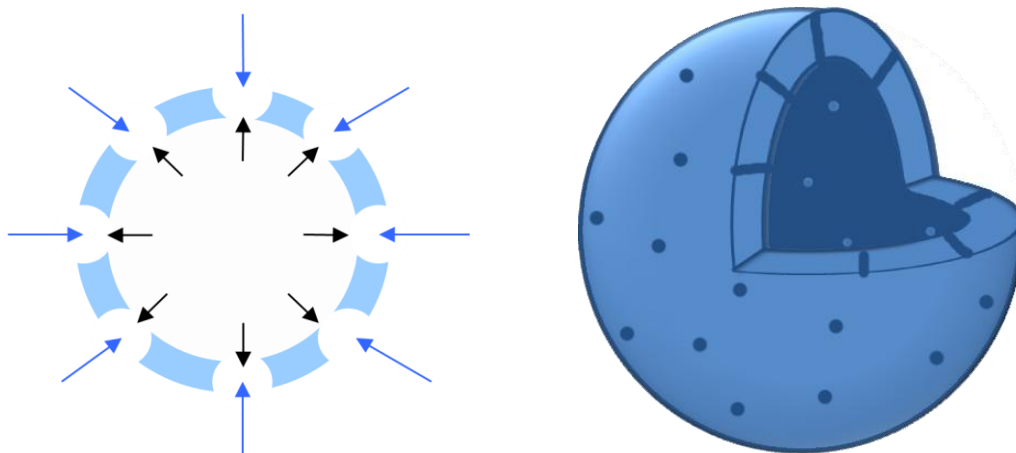


Figure 6.11 Asymmetric pore (left) versus cylindrical pores (right) in the shell wall.

This is the first time that spin coating has been used to make silica capsules. Spin coating is a facile method normally used for thin film fabrication. Traditional ways to make silica capsules are mostly done homogeneously in solution, via nucleation and growth or the layer-by-layer (LBL) method.^{124,275,276} Nucleation involves the spontaneous formation of a new phase in a supersaturated solution.²⁷⁷ First is the generation of nuclei of atoms or ions, then the structure grows based on those nuclei. The problem with this method is that it is very hard to selectively grow on certain areas on the sphere surface. Also, the slow nucleation process makes the surfaces very porous and rough.

Layer-by-layer assembly is another way to form the shell of a capsule. Layer-by-layer assembly involves the construction of coatings by the adsorption of alternately charged

polyions.²⁷⁸ There are many steps to the fabrication process, and aggregation may be problematical during the "positive"- "negative"- "positive"..... layer-by-layer process.

Spin coating, however, is very easy, and the capsules produced using this method would have a more condensed, uniform shell that gives rise to well-defined pores. For capsules with more porous shells, the hollow structure would be much more fragile than those that have more condensed shells. Spin coated sol-gel has a more condensed structure compared with the one obtained by nucleation and growth in solution, since the silica sol has been partially hydrolyzed and condensed.

In a related experiment, another silica sol recipe was also evaluated for porous silica capsule fabrication. This particular sol contained a difunctional organosilane, specifically dimethyldiethoxysilane. The sol contained 1000 μL TEOS, 300 μL of DMDEOS, 2000 μL of ethanol, and 300 μL of 0.1 M HCl. It was stirred for 30 min and aged for two days at room temperature. SEM images of the capsules produced from this sol are shown in Figure 6.12. As can be seen most clearly in Fig. 6.12 (C), the outer openings of the windows on the shell of the porous capsules are almost closed. Organosilanes coat the polystyrene surface better than TEOS during spin coating, which ultimately resulted in a smaller opening on the outer shell of the capsule. Thus, a different morphology of the capsules can be obtained by changing the components of the sol.

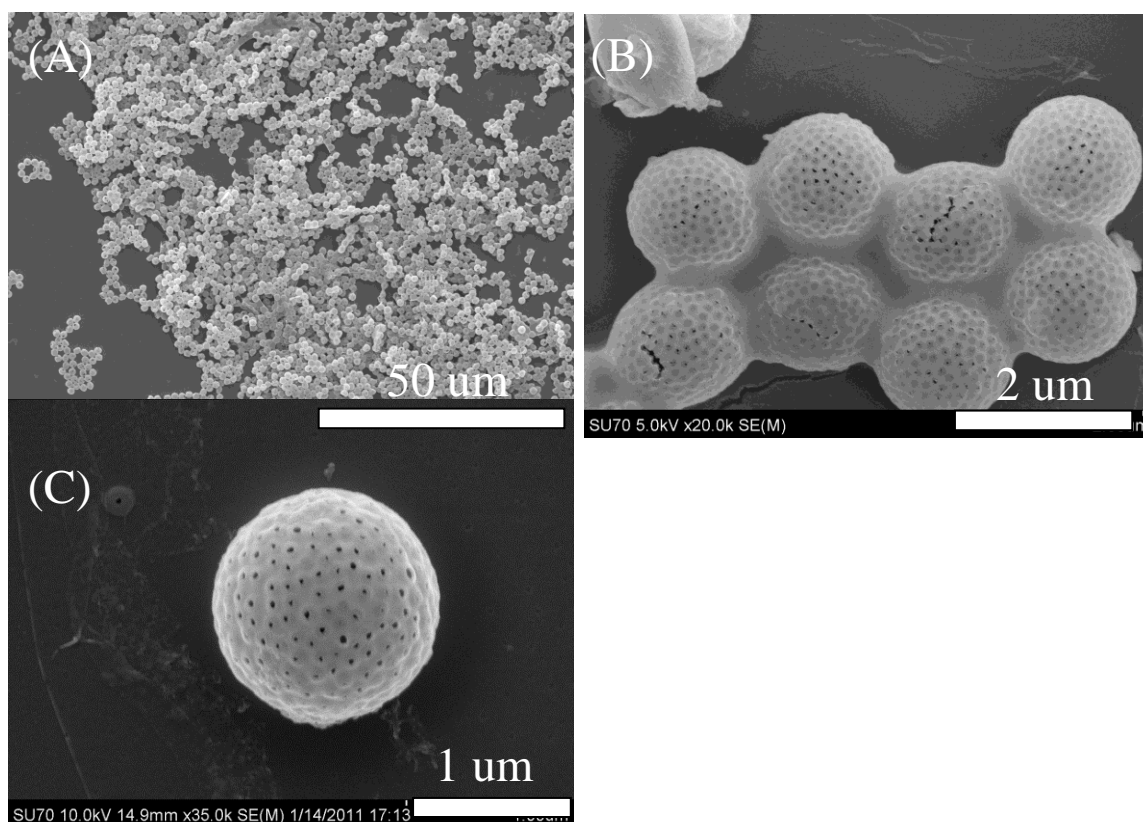


Figure 6.12 SEM images of capsules fabricated by using a silica sol containing 300 μL DMDEOS/ 1000 μL TEOS instead of 1300 μL TEOS. (A), (B), and (C) are different magnifications of the hollow capsules.

6.6 Summary

In this work, a novel, well-defined hollow capsule with asymmetric pores that transverse through the shell has been fabricated by spin coating. In our approach, the core of the hierarchical template controls the size of the interior void while the size of the asymmetric pores in the shell is defined by the satellite spheres. The interconnectivity is guaranteed by the bonding between core and satellites on the hierarchical template. The hollow capsules are very uniform due to the hard templating method employed.

Compared with polymer capsules, the rigid nature of silica helps provide a fixed void space and shape, which can be potentially useful when they are used as reaction containers. This is the first report where the “windows” in the shell of porous capsules are finely tailored and near uniformly distributed over the entire shell of the capsule. Both the inner pore and the outer pores have a relatively narrow pore size distribution due to the monodispersivity of the PS particles used to make the hierarchical templates (Coefficient of variation between 2-5%). Two important attributes of this structure are: (1) the numerous direct channels with short diffusional passageways and (2) asymmetric windows. All together these direct channels potentially provide efficient pathways to connect the inside of the capsule to the outside. The asymmetric windows offer the potential for facilitated diffusion and rectification, particularly when the diffusing particles are similar in size to the inner hole.²⁷¹ By rectifying motion in a given direction, the option for separation/ concentration of a given species in solution exists, such as that shown for microorganisms²⁷⁹ and particles.²⁷¹ It is envisioned that these capsules can be potentially useful for a number of applications including pollution treatment and drug delivery applications.

Chapter 7 Conclusion and Future work

7.1 Conclusion

A facile and reliable method of making multimodal porous materials based on hierarchical templates has been established in this work. Hierarchical templates of a predefined size and shape can be used to prepare multimodal porous materials with a well-defined large macropore surrounded by much smaller pores. The large macropore can provide easy access to the inner pores, which help to increase the overall surface area of the porous material. The templates can be easily prepared by chemically joining commercially available functionalized polystyrene latex spheres. Multimodal porous silica, bimodal porous gold and porous silica capsules have been successfully fabricated based on the 1500/110 nm and 1200/60 nm raspberry-like templates as examples for 3D, 2D and 0D multimodal porous materials fabrication. SEM, TEM, and nitrogen adsorption were employed to characterize the multimodal porous silica monoliths. The surface area and electrochemical properties were studied for the bimodal porous gold. A thorough morphology characterization was carried out for porous capsules. The single polystyrene hierarchical template simplified the fabrication and template removal step. The colloidal crystal packing strategies previously reported in the literature are applicable to hierarchical templates, which makes this methodology of making multimodal porous materials more general and flexible. Hard templating methods compared with other templating methods provides more control over uniformity.

The advantages that this approach provides are simplicity and versatility: (a) the

template is size-tailorable through alterations in the size of the central core and/or satellites and by changing the number density of the satellites; (b) only one template is needed in contrast to combining two or more templates, which can complicate the chemistry; (c) both 2D (films) or 3D (monoliths, powders) can be made, (d) having a hierarchical template that is made completely out of polystyrene allows flexibility in removal via mild solvent dissolution (e) the materials produced have well-defined pore sizes that are interconnected. The one current drawback is access to the “micropore” ($d < 2$ nm) and to some extent the “mesopore” ($2 \text{ nm} < d < 50 \text{ nm}$) regions are limited by the smallest size of the latex sphere that can be purchased commercially- which is about 20 nm. However, this limitation can likely be circumvented by in-house synthesis or utilization of another type of appropriately functionalized colloid. It is envisioned that these hierarchical porous materials will be useful as platforms for chemical sensing, chromatography, and catalysis.

The limitation for this method is the sizes scale of the pores due to the limitation of the PS sphere size. Commercially available uniform PS spheres are relatively big (> 20 nm). By using spheres of other materials that can go down to smaller sizes, like PMMA, quantum dots, we might be able to extend the size range a little wider. But a template composed of two or more materials might complicate the chemistry.

7.2 Future work

Future work can focus on improving the desired properties of a specific material application. By controlling the size and the shape of the hierarchical templates made by

joining PS spheres, multimodal porous structures can be fabricated with more artificial design. It provides us a way to further study the physical/chemical properties improved by this structure, and optimize the parameters of the structure to obtain a better performance in various applications. Also, this size tunable ability provides researcher a possibility of systematical study of some of the size dependent properties, like surface roughness vs. superhydrophobicity, porous size vs. separation efficiency, etc.

For the porous silica capsule project, the structure has an interior void as a storage space or a reaction chamber that can encapsulate various substances, and the shell structure contains asymmetric pores for mass transport and release outlet. The pore channels all over the shell could be useful for many applications that requires fast diffusion in and out of the structure, such as the protection of biologically active species, removal of pollutants, catalysis, and sensing.^{257,280,281} In catalysis applications, it is essential to maximize permeate flux through the shell, while maintain enough thickness to maintain a stable structure under liquid pressure and mass transport. Membranes with asymmetricly shaped pores can have dramatically higher rates of transport than analogous cylindrical pore membranes due to their shorter diffusion pathway. Examples of the hollow spheres used as micro-sized reaction containers or size exclusive separation capsules for uploading drugs/catalyst are shown in Figure 7.1. In (a) the red particles are one of the reactants, and the green particles are the other reactant. After loading them one by one, a blue colored big particle is formed in the cavity, thus it provide a way to uploading catalyst or drugs that needs to be protected from attaching to other surfaces. In (b), a size exclusive uploading/separation is shown.

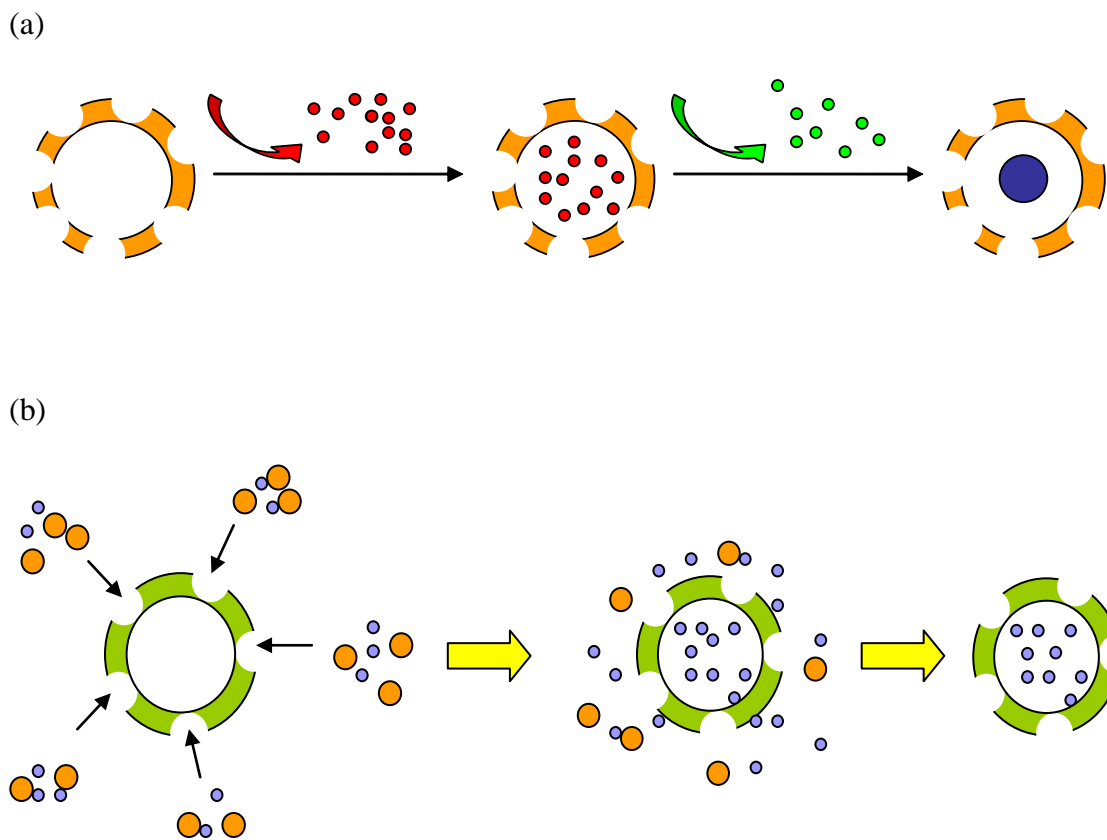


Figure 7.1 Functions based on the hollow sphere structure (a) reaction container and encapsulated catalyst (b) size exclusive separation.

References

- (1) Brinker, C. J. Porous inorganic materials. *Current Opinion in Solid State & Materials Science* **1996**, *1*, 798.
- (2) Gulians, V. V.; Carreon, M. A.; Lin, Y. S. Ordered mesoporous and macroporous inorganic films and membranes. *Journal of Membrane Science* **2004**, *235*, 53.
- (3) Shi, Y.; Wan, Y.; Zhao, D. Ordered mesoporous non-oxide materials. *Chemical Society Reviews* **2011**, *40*, 3854.
- (4) Buschatz, H.; Dageforde, B.; Jakoby, K.; Peinemann, K. V.; Paul, D. Highly selective separations with carrier membranes-State of the art and future prospects. *Chemie Ingenieur Technik* **2001**, *73*, 297.
- (5) Jiang, D. E.; Cooper, V. R.; Dai, S. Porous graphene as the ultimate membrane for gas separation. *Nano Letters* **2009**, *9*, 4019.
- (6) Saufi, S. M.; Ismail, A. F. Fabrication of carbon membranes for gas separation-a review. *Carbon* **2004**, *42*, 241.
- (7) Xie, Z. K.; Liu, Z. C.; Wang, Y. D.; Yang, Q. H.; Xu, L. Y.; Ding, W. P. An overview of recent development in composite catalysts from porous materials for various reactions and processes. *International Journal of Molecular Sciences* **2010**, *11*, 2152.
- (8) J., R. Recommendations for the characterization of porous solids. *Pure and Applied Chemistry* **1994**, *66*.
- (9) Samsonenko, D. G.; Kim, H.; Sun, Y. Y.; Kim, G. H.; Lee, H. S.; Kim, K. Microporous magnesium and manganese formates for acetylene storage and separation. *Chemistry-an Asian Journal* **2007**, *2*, 484.
- (10) Zhang, F.; Ma, H.; Chen, J.; Li, G. D.; Zhang, Y.; Chen, J. S. Preparation and gas storage of high surface area microporous carbon derived from biomass source cornstalks. *Bioresource Technology* **2008**, *99*, 4803.
- (11) Reij, M. W.; Keurentjes, J. T. F.; Hartmans, S. Membrane bioreactors for waste gas treatment. *Journal of Biotechnology* **1998**, *59*, 155.
- (12) Dong, J.; Lin, Y. S.; Kanezashi, M.; Tang, Z. Microporous inorganic membranes for high temperature hydrogen purification. *Journal of Applied Physics* **2008**, *104*.
- (13) Julbe, A.; Guizard, C.; Larbot, A.; Cot, L.; Giroirfendler, A. The sol-gel approach to prepare candidate microporous inorganic membranes for membrane reactors. *Journal of Membrane Science* **1993**, *77*, 137.
- (14) Meek, S. T.; Greathouse, J. A.; Allendorf, M. D. Metal-organic frameworks: A rapidly growing class of versatile nanoporous materials. *Advanced Materials* **2011**, *23*, 249.
- (15) Shekhah, O.; Liu, J.; Fischer, R. A.; Woll, C. MOF thin films: existing and future applications. *Chemical Society Reviews* **2011**, *40*, 1081.
- (16) Guo, M.; Cai, H. L.; Xiong, R. G. Ferroelectric metal organic framework (MOF). *Inorganic Chemistry Communications* **2010**, *13*, 1590.

- (17) Katz, A.; Davis, M. E. Molecular imprinting of bulk, microporous silica *Nature* **2000**, *403*, 286.
- (18) Wulff, G. Molecular imprinting in cross-linked materials with the aid of molecular templates-A way towards artificial antibodies *Angewandte Chemie-International Edition in English* **1995**, *34*, 1812.
- (19) Hillberg, A. L.; Tabrizian, M. Biomolecule imprinting: Developments in mimicking dynamic natural recognition systems *Irbm* **2008**, *29*, 89.
- (20) Fryxell, G. E. The synthesis of functional mesoporous materials *Inorganic Chemistry Communications* **2006**, *9*, 1141.
- (21) Ciesla, U.; Schuth, F. Ordered mesoporous materials *Microporous and Mesoporous Materials* **1999**, *27*, 131.
- (22) Shi, Y. F.; Wan, Y.; Zhao, D. Y. Ordered mesoporous non-oxide materials *Chemical Society Reviews* **2011**, *40*, 3854.
- (23) Yang, Z. L.; Lu, Y. F.; Yang, Z. Z. Mesoporous materials: tunable structure, morphology and composition *Chemical Communications* **2009**, 2270.
- (24) Kumar, P.; Gulians, V. V. Periodic mesoporous organic-inorganic hybrid materials: Applications in membrane separations and adsorption *Microporous and Mesoporous Materials* **2010**, *132*, 1.
- (25) Transport in small pores.
http://sinnott.mse.ufl.edu/Backgrounds/theo02_diff.html **2009**.
- (26) Ulrich Schubert, N. H. *Synthesis of inorganic materials*; 2nd ed.; WILEY-VCH Verlag GmbH & Co. KGaA, Weinheim, 2005.
- (27) Rodriguez-Mirasol, J.; Cordero, T.; Radovic, L. R.; Rodriguez, J. J. Structural and textural properties of pyrolytic carbon formed within a microporous zeolite template *Chemistry of Materials* **1998**, *10*, 550.
- (28) Kim, T. W.; Ryoo, R.; Gierszal, K. P.; Jaroniec, M.; Solovyov, L. A.; Sakamoto, Y.; Terasaki, O. Characterization of mesoporous carbons synthesized with SBA-16 silica template *Journal of Materials Chemistry* **2005**, *15*, 1560.
- (29) Holland, B. T.; Blanford, C. F.; Stein, A. Synthesis of macroporous minerals with highly ordered three-dimensional arrays of spheroidal voids *Science* **1998**, *281*, 538.
- (30) Yang, D.; Qi, L. M.; Ma, J. M. Eggshell membrane templating of hierarchically ordered macroporous networks composed of TiO₂ tubes *Advanced Materials* **2002**, *14*, 1543.
- (31) Imhof, A.; Pine, D. J. Ordered macroporous materials by emulsion templating *Nature* **1997**, *389*, 948.
- (32) Imhof, A.; Pine, D. J. In *Recent Advances in Catalytic Materials*; Rodriguez, N. M., Soled, S. L., Hrbek, J., Eds. 1998; Vol. 497, p 167.
- (33) Velev, O. D.; Kaler, E. W. Structured porous materials via colloidal crystal templating: From inorganic oxides to metals *Advanced Materials* **2000**, *12*, 531.
- (34) Li, Q.; Retsch, M.; Wang, J. J.; Knoll, W. G.; Jonas, U. In *Templates in Chemistry Iii*; Broekmann, P., Dotz, K. H., Schalley, C. A., Eds. 2009; Vol. 287, p 135.
- (35) Towata, A.; Sivakumar, M.; Yasui, K.; Tuziuti, T.; Kozuka, T.; Iida, Y. Synthesis of alumina macroporous materials using yeast cells as bio-templates *Journal of*

the Ceramic Society of Japan **2005**, *113*, 696.

(36) Li, X. F.; Jiang, J. J.; Wang, Y.; Nie, X.; Qu, F. Y. Preparation of multilevel macroporous materials using natural plants as templates. *Journal of Sol-Gel Science and Technology* **2010**, *56*, 75.

(37) Tiemann, M. Repeated templating. *Chemistry of Materials* **2008**, *20*, 961.

(38) Wang, D. W.; Li, F.; Liu, M.; Lu, G. Q.; Cheng, H. M. 3D aperiodic hierarchical porous graphitic carbon material for high-rate electrochemical capacitive energy storage. *Angewandte Chemie-International Edition* **2008**, *47*, 373.

(39) Stein, A.; Li, F.; Denny, N. R. Morphological control in colloidal crystal templating of inverse opals, hierarchical structures, and shaped particles. *Chemistry of Materials* **2008**, *20*, 649.

(40) Zhao, X. S.; Su, F. B.; Yan, Q. F.; Guo, W. P.; Bao, X. Y.; Lv, L.; Zhou, Z. C. Templating methods for preparation of porous structures. *Journal of Materials Chemistry* **2006**, *16*, 637.

(41) Piao, Y. Z.; Kim, H. Fabrication of nanostructured materials using porous alumina template and their applications for sensing and electrocatalysis. *Journal of Nanoscience and Nanotechnology* **2009**, *9*, 2215.

(42) Zhang, D.; Zhang, W.; Gu, J. J.; Zhu, S. M.; Su, H. L.; Liu, Q. L.; Fan, T. X.; Ding, J. A.; Guo, Q. X. Bio-inspired functional materials templated from nature materials. *Kona Powder and Particle Journal* **2010**, 116.

(43) Li, H. N.; Dai, H. X.; He, H.; Au, C. T.; Facile route using highly arrayed PMMA spheres as hard template for the fabrication of 3D ordered nanoporous MgO. *Chinese Journal of Chemical Physics*: **2007**, p 697.

(44) Tang, J. W.; Zhou, X. F.; Zhao, D. Y.; Lu, G. Q.; Zou, J.; Yu, C. Z. Hard-sphere packing and icosahedral assembly in the formation of mesoporous materials. *Journal of the American Chemical Society* **2007**, *129*, 9044.

(45) Ania, C. O.; Khomenko, V.; Raymundo-Pinero, E.; Parra, J. B.; Beguin, F. The large electrochemical capacitance of microporous doped carbon obtained by using a zeolite template. *Advanced Functional Materials* **2007**, *17*, 1828.

(46) Lazaro, M. J.; Calvillo, L.; Bordeje, E. G.; Moliner, R.; Juan, R.; Ruiz, C. R. Functionalization of ordered mesoporous carbons synthesized with SBA-15 silica as template. *Microporous and Mesoporous Materials* **2007**, *103*, 158.

(47) Gundiah, G.; Govindaraj, A.; Rao, C. N. R. Macroporous carbons prepared by templating silica spheres. *Materials Research Bulletin* **2001**, *36*, 1751.

(48) Zhou, Z. C.; Yan, Q. F.; Su, F. B.; Zhao, X. S. Replicating novel carbon nanostructures with 3D macroporous silica template. *Journal of Materials Chemistry* **2005**, *15*, 2569.

(49) Barton, T. J.; Bull, L. M.; Klemperer, W. G.; Loy, D. A.; McEnaney, B.; Misono, M.; Monson, P. A.; Pez, G.; Scherer, G. W.; Vartuli, J. C.; Yaghi, O. M. Tailored porous materials. *Chemistry of Materials* **1999**, *11*, 2633.

(50) Davis, M. E. Ordered porous materials for emerging applications. *Nature* **2002**, *417*, 813.

(51) Forster, S.; Konrad, M. From self-organizing polymers to nano- and biomaterials. *Journal of materials chemistry*, **2003**, *13*(11), 2671.

- (52) Soler-illia, G. J. D.; Sanchez, C.; Lebeau, B.; Patarin, J. Chemical strategies to design textured materials: From microporous and mesoporous oxides to nanonetworks and hierarchical structures. *Chemical Reviews* **2002**, *102*, 4093.
- (53) Xia, Y. N.; Gates, B.; Yin, Y. D.; Lu, Y. Monodispersed colloidal spheres: Old materials with new applications. *Advanced Materials* **2000**, *12*, 693.
- (54) Caruso, F.; Caruso, R. A.; Mohwald, H. Nanoengineering of inorganic and hybrid hollow spheres by colloidal templating. *Science* **1998**, *282*, 1111.
- (55) Sotiropoulou, S.; Sierra-Sastre, Y.; Mark, S. S.; Batt, C. A. Biotemplated nanostructured materials. *Chemistry of Materials* **2008**, *20*, 821.
- (56) Yamauchi, Y.; Kuroda, K. Rational design of mesoporous metals and related nanomaterials by a soft-template approach. *Chemistry-an Asian Journal* **2008**, *3*, 664.
- (57) Wan, Y.; Zhao, D. Y. On the controllable soft-templating approach to mesoporous silicates. *Chemical Reviews* **2007**, *107*, 2821.
- (58) Li, N.; Wang, J. G.; Zhou, H. J.; Sun, P. C.; Chen, T. H. Synthesis of single-crystal-like, hierarchically nanoporous silica and periodic mesoporous organosilica, using polyelectrolyte-surfactant mesomorphous complexes as a template. *Chemistry of Materials* **2011**, *23*, 4241.
- (59) Mukai, S. R. Synthesis of monolithic microhoneycombs equipped with unique hierarchical pore systems using ice templating. *Journal of the Japan Petroleum Institute* **2011**, *54*, 127.
- (60) Cobley, C. M.; Xia, Y. N. Engineering the properties of metal nanostructures via galvanic replacement reactions. *Materials Science & Engineering R-Reports* **2010**, *70*, 44.
- (61) Sun, Y. G.; Mayers, B. T.; Xia, Y. N. Template-engaged replacement reaction: A one-step approach to the large-scale synthesis of metal nanostructures with hollow interiors. *Nano Letters* **2002**, *2*, 481.
- (62) Suzuki, K.; Ikari, K.; Imai, H. Synthesis of mesoporous silica foams with hierarchical trimodal pore structures. *Journal of Materials Chemistry* **2003**, *13*, 1812.
- (63) Lou, X. W.; Yuan, C. L.; Rhoades, E.; Zhang, Q.; Archer, L. A. Encapsulation and ostwald ripening of Au and Au-Cl complex nanostructures in silica shells. *Advanced Functional Materials* **2006**, *16*, 1679.
- (64) IUPAC. Compendium of Chemical Terminology, 2nd ed. (the "Gold Book"). Compiled by A. D. McNaught and A. Wilkinson. Blackwell Scientific Publications, Oxford (1997). created by M. Nic, J. Jirat, B. Kosata; updates compiled by A. Jenkins. ISBN 0-9678550-9-8. doi:10.1351/goldbook. .
- (65) V.V., L. I. M. S. The kinetics of precipitation from supersaturated solid solutions. *Journal of Physics and Chemistry of Solids* **1961**, *19*, 35.
- (66) Bartlett, P. N.; Baumberg, J. J.; Birkin, P. R.; Ghanem, M. A.; Netti, M. C. Highly ordered macroporous gold and platinum films formed by electrochemical deposition through templates assembled from submicron diameter monodisperse polystyrene spheres. *Chemistry of Materials* **2002**, *14*, 2199.
- (67) Yuan, D.; Zeng, J.; Kristian, N.; Wang, Y.; Wang, X. Bi₂O₃ deposited on highly ordered mesoporous carbon for supercapacitors. *Electrochemistry*

Communications **2009**, *11*, 313.

(68) Zhou, M.; Shang, L.; Li, B. L.; Huang, L. J.; Dong, S. J. The characteristics of highly ordered mesoporous carbons as electrode material for electrochemical sensing as compared with carbon nanotubes. *Electrochemistry Communications* **2008**, *10*, 859.

(69) Zhou, M.; Deng, L.; Wen, D.; Shang, L.; Jin, L. H.; Dong, S. J. Highly ordered mesoporous carbons-based glucose/O₂ biofuel cell. *Biosensors & Bioelectronics* **2009**, *24*, 2904.

(70) Innocenzi, P.; Malfatti, L.; Soler-Illia, G. Hierarchical Mesoporous Films: From Self-Assembly to Porosity with Different Length Scales. *Chemistry of Materials* **2011**, *23*, 2501.

(71) Yang, X. Y.; Li, Y.; Lemaire, A.; Yu, J. G.; Su, B. L. Hierarchically structured functional materials: Synthesis strategies for multimodal porous networks. *Pure and Applied Chemistry* **2009**, *81*, 2265.

(72) Ariga, K.; Ji, Q. M.; Hill, J. P.; Vinu, A. Coupling of soft technology (layer-by-layer assembly) with hard materials (mesoporous solids) to give hierarchic functional structures. *Soft Matter* **2009**, *5*, 3562.

(73) Dionigi, C.; Greco, P.; Ruani, G.; Cavallini, M.; Borgatti, F.; Biscarini, F. 3D Hierarchical Porous TiO₂ Films from Colloidal Composite Fluidic Deposition. *Chemistry of Materials* **2008**, *20*, 7130.

(74) Falcaro, P.; Malfatti, L.; Kidchob, T.; Giannini, G.; Falqui, A.; Casula, M. F.; Amenitsch, H.; Marmiroli, B.; Greci, G.; Innocenzi, P. Hierarchical Porous Silica Films with Ultralow Refractive Index. *Chemistry of Materials* **2009**, *21*, 2055.

(75) Liu, Z. T.; Fan, T. X.; Zhang, D.; Gong, X. L.; Xu, J. Q. Hierarchically porous ZnO with high sensitivity and selectivity to H₂S derived from biotemplates. *Sensors and Actuators B-Chemical* **2009**, *136*, 499.

(76) Qiao, H.; Wang, Y. W.; Xiao, L. F.; Zhang, L. Z. High lithium electroactivity of hierarchical porous rutile TiO₂ nanorod microspheres. *Electrochemistry Communications* **2008**, *10*, 1280.

(77) Qiao, Y. P.; Zhao, X. Electrorheological effect of carbonaceous materials with hierarchical porous structures. *Colloids and Surfaces a-Physicochemical and Engineering Aspects* **2009**, *340*, 33.

(78) Yamada, H.; Moriguchi, I.; Kudo, T. Electric double layer capacitance on hierarchical porous carbons in an organic electrolyte. *Journal of Power Sources* **2008**, *175*, 651.

(79) Perez-Ramirez, J.; Christensen, C. H.; Egeblad, K.; Groen, J. C. Hierarchical zeolites: enhanced utilisation of microporous crystals in catalysis by advances in materials design. *Chemical Society Reviews* **2008**, *37*, 2530.

(80) Ma, T. Y.; Zhang, X. J.; Yuan, Z. Y. Hierarchical meso-/macroporous aluminum phosphonate hybrid materials as multifunctional adsorbents. *Journal of Physical Chemistry C* **2009**, *113*, 12854.

(81) Ma, T. Y.; Zhang, X. J.; Yuan, Z. Y. Hierarchically meso-/macroporous titanium tetraphosphonate materials: Synthesis, photocatalytic activity and heavy metal ion adsorption. *Microporous and Mesoporous Materials* **2009**, *123*, 234.

- (82) Yuan, Z. Y.; Su, B. L. Insights into hierarchically meso-macroporous structured materials. *Journal of Materials Chemistry* **2006**, *16*, 663.
- (83) Li, Y.; Li, C. C.; Cho, S. O.; Duan, G. T.; Cai, W. P. Silver hierarchical bowl-like array: Synthesis, superhydrophobicity, and optical properties. *Langmuir* **2007**, *23*, 9802.
- (84) Wang, J. J.; Li, Q.; Knoll, W.; Jonas, U. Preparation of multilayered trimodal colloid crystals and binary inverse opals. *Journal of the American Chemical Society* **2006**, *128*, 15606.
- (85) Vantomme, A.; Leonard, A.; Yuan, Z. Y.; Su, B. L. Self-formation of hierarchical micro-meso-macroporous structures: Generation of the new concept "Hierarchical Catalysis". *Colloid and surfaces-physicochemical and engineering aspects* **2007**, *300(1-2)*, 70.
- (86) Xia, Y. N.; Rogers, J. A.; Paul, K. E.; Whitesides, G. M. Unconventional methods for fabricating and patterning nanostructures. *Chemical Reviews* **1999**, *99*, 1823.
- (87) Xia, Y. N.; Whitesides, G. M. Soft lithography. *Annual Review of Materials Science* **1998**, *28*, 153.
- (88) Xia, Y. N.; Whitesides, G. M. Soft lithography. *Angewandte Chemie-International Edition* **1998**, *37*, 551.
- (89) Holland, B. T.; Abrams, L.; Stein, A. Dual templating of macroporous silicates with zeolitic microporous frameworks. *Journal of the American Chemical Society* **1999**, *121*, 4308.
- (90) Chai, G. S.; Shin, I. S.; Yu, J. S. Synthesis of ordered, uniform, macroporous carbons with mesoporous walls templated by aggregates of polystyrene spheres and silica particles for use as catalyst supports in direct methanol fuel cells. *Advanced Materials* **2004**, *16*, 2057.
- (91) Yang, P. D.; Deng, T.; Zhao, D. Y.; Feng, P. Y.; Pine, D.; Chmelka, B. F.; Whitesides, G. M.; Stucky, G. D. Hierarchically ordered oxides. *Science* **1998**, *282*, 2244.
- (92) Dai, S. Hierarchically imprinted nanoporous sorbents for separation of metal ions. *Abstracts of papers of the American Chemical Society* **2003**, *71*.
- (93) Dai, S.; Burleigh, M. C.; Ju, Y. H.; Gao, H. J.; Lin, J. S.; Pennycook, S. J.; Barnes, C. E.; Xue, Z. L. Hierarchically imprinted sorbents for the separation of metal ions. *Journal of the American Chemical Society* **2000**, *122*, 992.
- (94) Wu, G. H.; Wang, Z. Q.; Wang, J.; He, C. Y. Hierarchically imprinted organic-inorganic hybrid sorbent for selective separation of mercury ion from aqueous solution. *Analytica Chimica Acta* **2007**, *582*, 304.
- (95) Wang, Z. Y.; Stein, A. Morphology control of carbon, silica, and carbon/silica nanocomposites: From 3D ordered Macro-/Mesoporous monoliths to shaped mesoporous particles. *Chemistry of Materials* **2008**, *20*, 1029.
- (96) Wu, X. F.; Tian, Y. J.; Cui, Y. B.; Wei, L. Q.; Wang, Q.; Chen, Y. F. Raspberry-like silica hollow spheres: Hierarchical structures by dual latex-surfactant templating route. *J. Phys. Chem. C* **2007**, *111*, 9704.
- (97) Tan, B.; Rankin, S. E. Dual latex/surfactant templating of hollow spherical silica particles with ordered mesoporous shells. *Langmuir* **2005**, *21*, 8180.
- (98) Cho, Y. S.; Yi, G. R.; Kim, S. H.; Jeon, S. J.; Elsesser, M. T.; Yu, H. K.;

Yang, S. M.; Pine, D. J. Particles with coordinated patches or windows from oil-in-water emulsions. *Chemistry of Materials* **2007**, *19*, 3183.

(99) Chae, W. S.; Braun, P. V. Templated mesoporous silica colloids with controlled internal structures. *Chemistry of Materials* **2007**, *19*, 5593.

(100) Groenewolt, M.; Antonietti, M.; Polarz, S. Mixed micellar phases of nonmiscible surfactants: Mesoporous silica with bimodal pore size distribution via the nanocasting process. *Langmuir* **2004**, *20*, 7811.

(101) Sel, O.; Kuang, D. B.; Thommes, M.; Smarsly, B. Principles of hierarchical meso- and macropore architectures by liquid crystalline and polymer colloid templating. *Langmuir* **2006**, *22*, 2311.

(102) Li, F.; Stein, A. Functional composite membranes based on mesoporous silica spheres in a hierarchically porous matrix. *Chemistry of Materials* **2010**, *22*, 3790.

(103) Frenzer, G.; Maier, W. F. Amorphous porous mixed oxides: Sol-gel ways to a highly versatile class of materials and catalysts. *Annual Review of Materials Research* **2006**, *36*, 281.

(104) Kaune, G.; Memesa, M.; Meier, R.; Ruderer, M. A.; Diethert, A.; Roth, S. V.; D'Acunzi, M.; Gutmann, J. S.; Muller-Buschbaum, P. Hierarchically structured titania films prepared by polymer/colloidal templating. *ACS Applied Materials & Interfaces* **2009**, *1*, 2862.

(105) Brinker, C. J.; Scherer, G. W. *Sol-Gel Science: The Physics and Chemistry of Sol-Gel Processing*; Academic Press Inc.: San Diego, 1990.

(106) Gupta, R.; Chaudhury, N. K. Entrapment of biomolecules in sol-gel matrix for applications in biosensors: Problems and future prospects. *Biosensors & Bioelectronics* **2007**, *22*, 2387.

(107) Mizukami, F. Design of Solid Catalysts by Sol-gel Method Using Organic Polydentate Ligands and Their Catalytic Performance. *Journal of the Japan Petroleum Institute* **2008**, *51*, 332.

(108) Eremenko, A. M.; Smirnova, N. P.; Ogenko, V. M.; Chuiko, A. A. Luminescence of organic-dyes in silica matrices. *Research on Chemical Intermediates* **1993**, *19*, 855.

(109) Yusoff, A. L.; Hugtenburg, R. P.; Bradley, D. A. Review of development of a silica-based thermoluminescence dosimeter. *Radiation Physics and Chemistry* **2005**, *74*, 459.

(110) Avnir, D. Organic-chemistry within ceramic matrices-doped sol-gel materials. *Accounts of Chemical Research* **1995**, *28*, 328.

(111) Chujo, Y.; Saegusa, T. Organic Polymer Hybrids with Silica-gel Formed by Means of the Sol-Gel Method. *Advances in Polymer Science* **1992**, *100*, 11.

(112) Brinker, C. J. S., R.; Hietala S.L.; Deshpande, R.; Smith, D. M.; Loy, D. and Ashley C. S. Sol-gel strategies for controlled porosity inorganic materials. *Journal of Membrane Science* **1994**, *94*, 85.

(113) Nakanishi, K.; Tanaka, N. Sol-gel with phase separation. Hierarchically porous materials optimized for high-performance liquid chromatography separations. *Accounts of Chemical Research* **2007**, *40*, 863.

(114) Kanamori, K.; Nakanishi, K. Controlled pore formation in

organotrialkoxysilane-derived hybrids: from aerogels to hierarchically porous monoliths. *Chemical Society Reviews* **2011**, *40*, 754.

(115) Carvajal, J. J. Combination of templating and dealloying techniques produce multimodal porous gold materials. *MRS Bulletin* **2007**, *32*, 200.

(116) Lu, A. H.; Schuth, F. Nanocasting: A versatile strategy for creating nanostructured porous materials. *Advanced Materials* **2006**, *18*, 1793.

(117) Malfatti, L.; Bellino, M. G.; Innocenzi, P.; Soler-Illia, G. J. A. A. One-pot route to produce hierarchically porous titania thin films by controlled self-assembly, swelling, and phase separation. *Chemistry of Materials* **2009**, *21*, 2763.

(118) Xia, K. S.; Ferguson, D.; Djaoued, Y.; Robichaud, J.; Tchoukanova, N.; Bruning, R.; McCalla, E. Template-free synthesis and photocatalytic activity of hierarchical porous titania with controlled texture and crystalline structure. *Applied Catalysis a-General* **2010**, *387*, 231.

(119) Lee, J. H. Gas sensors using hierarchical and hollow oxide nanostructures: Overview. *Sensors and Actuators B-Chemical* **2009**, *140*, 319.

(120) Wang, C. H.; Yang, C.; Song, Y. Y.; Gao, W.; Xia, X. H. Adsorption and direct electron transfer from hemoglobin into a three-dimensionally ordered, macroporous gold film. *Advanced Functional Materials* **2005**, *15*, 1267.

(121) Walcarius, A.; Kuhn, A. Ordered porous thin films in electrochemical analysis. *Trac-Trends in Analytical Chemistry* **2008**, *27*, 593.

(122) Zhong, H.; Zhu, G. R.; Wang, P. Y.; Liu, J.; Yang, J.; Yang, Q. H. Direct synthesis of hierarchical monolithic silica for high performance liquid chromatography. *Journal of Chromatography A* **2008**, *1190*, 232.

(123) Sun, Z.; Deng, Y.; Wei, J.; Gu, D.; Tu, B.; Zhao, D. Hierarchically ordered macro-/mesoporous silica monolith: Tuning macropore entrance size for size-selective adsorption of proteins. *Chemistry of Materials* **2011**, *23*, 2176.

(124) Liu, J.; Liu, F.; Gao, K.; Wu, J. S.; Xue, D. F. Recent developments in the chemical synthesis of inorganic porous capsules. *Journal of Materials Chemistry* **2009**, *19*, 6073.

(125) Huang, X.; Brazel, C. S. On the importance and mechanisms of burst release in matrix-controlled drug delivery systems. *Journal of Controlled Release* **2001**, *73*, 121.

(126) Muller, R. H.; Mader, K.; Gohla, S. Solid lipid nanoparticles (SLN) for controlled drug delivery - a review of the state of the art. *European Journal of Pharmaceutics and Biopharmaceutics* **2000**, *50*, 161.

(127) Okada, H.; Toguchi, H. Biodegradable microspheres in drug-delivery. *Critical Reviews in Therapeutic Drug Carrier Systems* **1995**, *12*, 1.

(128) Panyam, J.; Labhasetwar, V. Biodegradable nanoparticles for drug and gene delivery to cells and tissue. *Advanced Drug Delivery Reviews* **2003**, *55*, 329.

(129) Li, X.-M.; Reinhoudt, D.; Crego-Calama, M. What do we need for a superhydrophobic surface? A review on the recent progress in the preparation of superhydrophobic surfaces. *Chemical Society Reviews* **2007**, *36*, 1350.

(130) Feng, J.; Tuominen, M. T.; Rothstein, J. P. Hierarchical Superhydrophobic Surfaces Fabricated by Dual-Scale Electron-Beam-Lithography with Well-Ordered

Secondary Nanostructures. *Advanced Functional Materials* **2011**, *21*, 3715.

(131) Jeong, H. E.; Lee, S. H.; Kim, J. K.; Suh, K. Y. Nanoengineered multiscale hierarchical structures with tailored wetting properties. *Langmuir* **2006**, *22*, 1640.

(132) Baino, F.; Vitale-Brovarone, C. Three-dimensional glass-derived scaffolds for bone tissue engineering: Current trends and forecasts for the future. *Journal of Biomedical Materials Research Part A* **2011**, *97A*, 514.

(133) Fu, R.W.; Li, Z. H.; Liang, Y. R.; Li, F.; Xu, F.; Wu, D. C. Hierarchical porous carbons: design, preparation, and performance in energy storage. *New Carbon Materials* **2011**, *26*, 171.

(134) Wu, H.; Lin, D. D.; Pan, W. High performance surface-enhanced raman scattering substrate combining low dimensional and hierarchical nanostructures. *Langmuir* **2010**, *26*, 6865.

(135) Dong, X.; Tao, J.; Li, Y. Y.; Zhu, H. Enhanced photoelectrochemical properties of F-containing TiO₂ sphere thin film induced by its novel hierarchical structure. *Applied Surface Science* **2009**, *255*, 7183.

(136) Williams, D. a. C., C. B. *Transmission electron microscopy. 1-Basics.*; Plenum Press, 1996.

(137) Reimer, L. a. K., H. *Transmission electron microscopy : Physics of image formation*; Springer, 2008.

(138) Watts, J. F. a. W., J. *An Introduction to surface analysis by XPS and AES*; John Wiley & Sons Ltd, The Atrium, Southern Gate, Chichester: West Sussex PO19 8SQ, England, 2003.

(139) Tilinin, I. S.; Jablonski, A.; Werner, W. S. M. Quantitative surface analysis by Auger and x-ray photoelectron spectroscopy. *Progress in Surface Science* **1996**, *52*, 193.

(140) Yehya, M.; Kelly, P. J. Combined AFM and XPS analysis of complex surfaces. *Surface & Coatings Technology* **2003**, *174*, 286.

(141) Zhou, W. L. a. W. Z. L. *Scanning microscopy for nanotechnology techniques and applications*; Springer, 2007.

(142) Muller, S. A.; Engel, A. Structure and mass analysis by scanning transmission electron microscopy. *Micron* **2001**, *32*, 21.

(143) Zavala, G. Atomic force microscopy, a tool for characterization, synthesis and chemical processes. *Colloid and Polymer Science* **2008**, *286*, 85.

(144) Meyer, G.; Amer, N. M. Novel optical approach to atomic force microscopy. *Applied Physics Letters* **1988**, *53*, 1045.

(145) Brunauer, S., Emmett, P. H. and Teller E. Adsorption of Gases in Multimolecular Layers. *Journal of the American Chemical society* **1938**, *60*, 309.

(146) Diamond, S. Mercury porosimetry - An inappropriate method for the measurement of pore size distributions in cement-based materials. *Cement and Concrete Research* **2000**, *30*, 1517.

(147) Washburn, W. E. Note on a method of determining the distribution of pore sizes in a porous material. *Proceedings of the National Academy of Science* **1921**, *7*, 115.

(148) Moro, F.; Bohni, H. Ink-bottle effect in mercury intrusion porosimetry of cement-based materials. *Journal of Colloid and Interface Science* **2002**, *246*, 135.

- (149) Bard, A. J., Faulkner, L. R. *Electrochemical Methods: Fundamentals and Applications*; 2nd ed.; Wiley: New York, 2001.
- (150) Nicholson, R. S. Theory and application of cyclic voltammetry for measurement of electrode reaction kinetics. *Analytical Chemistry* **1965**, *37*, 1351.
- (151) Kissinger, P. T.; Heineman, W. R. Cyclic voltammetry. *Journal of Chemical Education* **1983**, *60*, 702.
- (152) Mabbott, G. A. An introduction to cyclic voltammetry. *Journal of Chemical Education* **1983**, *60*, 697.
- (153) Xia, Y.; Gates, B.; Yin, Y.; Lu, Y. Monodispersed Colloidal Spheres: Old Materials with New Applications. *Adv. Mater.* **2000**, *12*, 693.
- (154) Zhao, B.; Collinson, M. M. Well-defined hierarchical templates for multimodal porous material fabrication. *Chemistry of Materials* **2010**, *22*, 4312.
- (155) Velev, O. D.; Lenhoff, A. M. Colloidal crystals as templates for porous materials. *Current Opinion in Colloid & Interface Science* **2000**, *5*, 56.
- (156) Ming, W.; Wu, D.; van Benthem, R.; de With, G. Superhydrophobic films from raspberry-like particles. *Nano Letters* **2005**, *5*, 2298.
- (157) Barthet, C.; Hickey, A. J.; Cairns, D. B.; Armes, S. P. Synthesis of novel polymer-silica colloidal nanocomposites via free-radical polymerization of vinyl monomers. *Adv. Mater.* **1999**, *11*, 408.
- (158) Fleming, M. S.; Mandal, T. K.; Walt, D. R. Nanosphere-microsphere assembly: Methods for core-shell materials preparation. *Chemistry of Materials* **2001**, *13*, 2210.
- (159) Reculosa, S.; Poncet-Legrand, C.; Ravaine, S.; Mingotaud, C.; Duguet, E.; Bourgeat-Lami, E. Syntheses of raspberry-like silica/polystyrene materials. *Chemistry of Materials* **2002**, *14*, 2354.
- (160) Qian, Z.; Zhang, Z. C.; Song, L. Y.; Liu, H. R. A novel approach to raspberry-like particles for superhydrophobic materials. *Journal of Materials Chemistry* **2009**, *19*, 1297.
- (161) Luna-Xavier, J. L.; Guyot, A.; Bourgeat-Lami, E. Synthesis and characterization of silica/poly (methyl methacrylate) nanocomposite latex particles through emulsion polymerization using a cationic azo initiator. *Journal of Colloid and Interface Science* **2002**, *250*, 82.
- (162) Li, G. L.; Yang, X. L.; Bai, F.; Huang, W. Q. Raspberry-like composite polymer particles by self-assemble heterocoagulation based on a charge compensation process. *Journal of Colloid and Interface Science* **2006**, *297*, 705.
- (163) Chen, M.; Zhou, S. X.; You, B.; Wu, L. M. A novel preparation method of raspberry-like PMMA/SiO₂ hybrid microspheres. *Macromolecules* **2005**, *38*, 6411.
- (164) Chen, M.; Wu, L. M.; Zhou, S. X.; You, B. Synthesis of raspberry-like PMMA/SiO₂ nanocomposite particles via a surfactant-free method. *Macromolecules* **2004**, *37*, 9613.
- (165) Du, X.; Liu, X. M.; Chen, H. M.; He, J. H. Facile Fabrication of Raspberry-like Composite Nanoparticles and Their Application as Building Blocks for Constructing Superhydrophilic Coatings. *Journal of Physical Chemistry C* **2009**, *113*, 9063.

- (166) Li, G. L.; Yang, X. L.; Wang, J. Y. Raspberry-like polymer composite particles via electrostatic heterocoagulation. *Colloids and Surfaces a-Physicochemical and Engineering Aspects* **2008**, *322*, 192.
- (167) Percy, M. J.; Barthet, C.; Lobb, J. C.; Khan, M. A.; Lascelles, S. F.; Vamvakaki, M.; Armes, S. P. Synthesis and characterization of vinyl polymer-silica colloidal nanocomposites. *Langmuir* **2000**, *16*, 6913.
- (168) Reculosa, S.; Mingotaud, C.; Bourgeat-Lami, E.; Duguet, E.; Ravaine, S. Synthesis of daisy-shaped and multipod-like silica/polystyrene nanocomposites. *Nano Letters* **2004**, *4*, 1677.
- (169) Reculosa, S.; Poncet-Legrand, C.; Perro, A.; Duguet, E.; Bourgeat-Lami, E.; Mingotaud, C.; Ravaine, S. Hybrid dissymmetrical colloidal particles. *Chemistry of Materials* **2005**, *17*, 3338.
- (170) Perro, A.; Reculosa, S.; Bourgeat-Lami, E.; Duguet, E.; Ravaine, S. Synthesis of hybrid colloidal particles: From snowman-like to raspberry-like morphologies. *Colloids and Surfaces a-Physicochemical and Engineering Aspects* **2006**, *284*, 78.
- (171) Hu, X.; Liu, H. R.; Ge, X. P.; Yang, S.; Ge, X. W. Preparation of Submicron-sized Snowman-like Polystyrene Particles via Radiation-induced Seeded Emulsion Polymerization. *Chemistry Letters* **2009**, *38*, 854.
- (172) Koo, H. Y.; Yi, D. K.; Yoo, S. J.; Kim, D. Y. A snowman-like array of colloidal dimers for antireflecting surfaces. *Adv. Mater.* **2004**, *16*, 274.
- (173) Xia, Y. N.; Yin, Y. D.; Lu, Y.; McLellan, J. Template-assisted self-assembly of spherical colloids into complex and controllable structures. *Adv. Funct. Mater.* **2003**, *13*, 907.
- (174) Chen, M.; You, B.; Zhou, S. X.; Wu, L. M. Synthesis and characterization of raspberry-like PMMA/SiO₂ organic-inorganic composite particles. *Acta Polymerica Sinica* **2006**, 790.
- (175) Qi, D. M.; Bao, Y. Z.; Huang, Z. M.; Weng, Z. X. Synthesis and characterization of poly(butyl acrylate)/silica and poly(butyl acrylate)/silica/poly(methyl methacrylate) composite particles. *Journal of Applied Polymer Science* **2006**, *99*, 3425.
- (176) Yu, M. H.; Wang, H. N.; Zhou, X. F.; Yuan, P.; Yu, C. Z. One template synthesis of raspberry-like hierarchical siliceous hollow spheres. *Journal of the American Chemical Society* **2007**, *129*, 14576.
- (177) Williams, A.; Ibrahim, I. T. A new mechanism involving cyclic tautomers for the reaction with nucleophiles of the water-soluble peptide coupling reagent 1-ethyl-3-(3-(dimethylamino)propyl)carbodiimide(EDC). *Journal of the American Chemical Society* **1981**, *103*, 7090.
- (178) Gilles, M. A.; Hudson, A. Q.; Borders, C. L. Stability of water-soluble carbodiimides in aqueous-solution. *Analytical Biochemistry* **1990**, *184*, 244.
- (179) Staros, J. V.; Wright, R. W.; Swingle, D. M. Enhancement by N-hydroxysulfosuccinimide of water-soluble carbodiimide-mediated coupling reactions. *Analytical Biochemistry* **1986**, *156*, 220.
- (180) Sehgal, D.; Vijay, I. K. A method for the high-efficiency of water-soluble carbodiimide-mediated amidation. *Analytical Biochemistry* **1994**, *218*, 87.

- (181) Carcy, F. A.; Giuliano, R. M. *Organic Chemistry*; McGraw-Hill, 2011.
- (182) Wang, Y.; Angelatos, A. S.; Caruso, F. Template synthesis of nanostructured materials via layer-by-layer assembly. *Chemistry of Materials* **2008**, *20*, 848.
- (183) Li, Y.; Cai, W.; Duan, G. Ordered micro/nanostructured arrays based on the monolayer colloidal crystals. *Chemistry of Materials* **2008**, *20*, 615.
- (184) Stein, A.; Schroden, R. C. Colloidal crystal templating of three-dimensionally ordered macroporous solids: materials for photonics and beyond. *Current Opinion in Solid State & Materials Science* **2001**, *5*, 553.
- (185) Trau, M.; Saville, D. A.; Aksay, I. A. Assembly of colloidal crystals at electrode interfaces. *Langmuir* **1997**, *13*, 6375.
- (186) Trau, M.; Saville, D. A.; Aksay, I. A. Field-induced layering of colloidal crystals. *Science* **1996**, *272*, 706.
- (187) Jiang, P.; Bertone, J. F.; Hwang, K. S.; Colvin, V. L. Single-crystal colloidal multilayers of controlled thickness. *Chemistry of Materials* **1999**, *11*, 2132.
- (188) Hsiao, S. Y.; Wong, D. S. H.; Lu, S. Y. Evaporation-assisted formation of three-dimensional photonic crystals. *Journal of the American Ceramic Society* **2005**, *88*, 974.
- (189) Walcarius, A. Template-directed porous electrodes in electroanalysis. *Analytical and Bioanalytical Chemistry* **2010**, *396*, 261.
- (190) Bartlett, P. N.; Birkin, P. R.; Ghanem, M. A. Electrochemical deposition of macroporous platinum, palladium and cobalt films using polystyrene latex sphere templates. *Chemical Communications* **2000**, 1671.
- (191) Yan, Q.; Gao, L.; Sharma, V.; Chiang, Y. M.; Wong, C. C. Particle and Substrate Charge Effects on Colloidal Self-Assembly in a Sessile Drop. *Langmuir* **2008**, *24*, 11518.
- (192) Dziomkina, N. V.; Vancso, G. J. Colloidal crystal assembly on topologically patterned templates. *Soft Matter* **2005**, *1*, 265.
- (193) Tull, E. J.; Bartlett, P. N.; Ryan, K. R. Controlled assembly of micrometer-sized spheres: Theory and application. *Langmuir* **2007**, *23*, 7859.
- (194) Ying, J. Y.; Mehnert, C. P.; Wong, M. S. Synthesis and applications of supramolecular-templated mesoporous materials. *Angewandte Chemie-International Edition* **1999**, *38*, 56.
- (195) Rhodes, K. H.; Davis, S. A.; Caruso, F.; Zhang, B. J.; Mann, S. Hierarchical assembly of zeolite nanoparticles into ordered macroporous monoliths using core-shell building blocks. *Chemistry of Materials* **2000**, *12*, 2832.
- (196) Antonietti, M.; Berton, B.; Goltner, C.; Hentze, H. P. Synthesis of mesoporous silica with large pores and bimodal pore size distribution by templating of polymer latices. *Adv. Mater.* **1998**, *10*, 154.
- (197) Li, F.; Wang, Z. Y.; Ergang, N. S.; Fyfe, C. A.; Stein, A. Controlling the shape and alignment of mesopores by confinement in colloidal crystals: Designer pathways to silica monoliths with hierarchical porosity. *Langmuir* **2007**, *23*, 3996.
- (198) Sen, T.; Tiddy, G. J. T.; Casci, J. L.; Anderson, M. W. Synthesis and characterization of hierarchically ordered porous silica materials. *Chemistry of Materials*

2004, 16, 2044.

(199) Raman, N. K.; Anderson, M. T.; Brinker, C. J. Template-based approaches to the preparation of amorphous, nanoporous silicas. *Chemistry of Materials* **1996**, 8, 1682.

(200) Gupta, R.; Kumar, A. Bioactive materials for biomedical applications using sol-gel technology. *Biomedical Materials* **2008**, 3.

(201) Gvishi, R.; Narang, U.; Ruland, G.; Kumar, D. N.; Prasad, P. N. Novel, organically doped, sol-gel-derived materials for photonics: Multiphasic nanostructured composite monoliths and optical fibers. *Applied Organometallic Chemistry* **1997**, 11, 107.

(202) Orignac, X.; Barbier, D.; Du, X. M.; Almeida, R. M.; McCarthy, O.; Yeatman, E. Sol-gel silica/titania-on-silicon Er/Yb-doped waveguides for optical amplification at 1.5 μm . *Optical Materials* **1999**, 12, 1.

(203) Zhou, Y.; Yu, S. H.; Thomas, A.; Han, B. H. In situ cyclodextrin-based homogeneous incorporation of metal (M = Pd, Pt, Ru) nanoparticles into silica with bimodal pore structure. *Chemical Communications* **2003**, 262.

(204) Walcarius, A.; Etienne, M.; Lebeau, B. Rate of access to the binding sites in organically modified silicates. 2. Ordered mesoporous silicas grafted with amine or thiol groups. *Chemistry of Materials* **2003**, 15, 2161.

(205) Walcarius, A.; Collinson, M. M. Analytical Chemistry with Silica Sol-Gels: Traditional Routes to New Materials for Chemical Analysis. *Annual Review of Analytical Chemistry* **2009**, 2, 121.

(206) Yang, S. M.; Kim, S. H.; Lim, J. M.; Yi, G. R. Synthesis and assembly of structured colloidal particles. *Journal of Materials Chemistry* **2008**, 18, 2177.

(207) Thomas, A.; Goettmann, F.; Antonietti, M. Hard templates for soft materials: Creating nanostructured organic materials. *Chemistry of Materials* **2008**, 20, 738.

(208) Fratzl, P.; Weinkamer, R. Nature's hierarchical materials. *Progress in Materials Science* **2007**, 52, 1263.

(209) Zhou, Y.; Antonietti, M. A novel tailored bimodal porous silica with well-defined inverse opal microstructure and super-microporous lamellar nanostructure. *Chemical Communications* **2003**, 2564.

(210) Caruso, R. A.; Antonietti, M. Silica films with bimodal pore structure prepared by using membranes as templates and amphiphiles as porogens. *Advanced Functional Materials* **2002**, 12, 307.

(211) Innocenzi, P.; Malfatti, L.; Kldchob, T.; Falcaro, P. Order-Disorder in Self-Assembled Mesostructured Silica Films: A Concepts Review. *Chemistry of Materials* **2009**, 21, 2555.

(212) Holland, B. T.; Blanford, C. F.; Do, T.; Stein, A. Synthesis of highly ordered, three-dimensional, macroporous structures of amorphous or crystalline inorganic oxides, phosphates, and hybrid composites. *Chemistry of Materials* **1999**, 11, 795.

(213) Sing, K. S. W.; Everett, D. H.; Haul, R. A. W.; Moscou, L.; Pierotti, R. A.; Rouquerol, J.; Siemieniewska, T. Reporting physisorption data for gas solid systems with special reference to the determination of surface-area and porosity. *Pure and Applied Chemistry* **1985**, 57, 603.

- (214) Leon, C. New perspectives in mercury porosimetry. *Advances in Colloid and Interface Science* **1998**, *77*, 341.
- (215) Holland, B. Determination of both mesopores and macropores in three-dimensional ordered porous materials by nitrogen adsorption. *Journal of Porous Materials* **2003**, *10*, 17.
- (216) Evans, S. A. G.; Elliott, J. M.; Andrews, L. M.; Bartlett, P. N.; Doyle, P. J.; Denuault, G. Detection of hydrogen peroxide at mesoporous platinum microelectrodes. *Analytical Chemistry* **2002**, *74*, 1322.
- (217) Jia, F. L.; Yu, C. F.; Deng, K. J.; Zhang, L. Z. Nanoporous metal (Cu, Ag, Au) films with high surface area: General fabrication and preliminary electrochemical performance. *Journal of Physical Chemistry C* **2007**, *111*, 8424.
- (218) Zhang, Q.; Wang, X. G.; Qi, Z.; Wang, Y.; Zhang, Z. H. A benign route to fabricate nanoporous gold through electrochemical dealloying of Al-Au alloys in a neutral solution. *Electrochimica Acta* **2009**, *54*, 6190.
- (219) Zhang, Q.; Zhang, Z. H. On the electrochemical dealloying of Al-based alloys in a NaCl aqueous solution. *Physical Chemistry Chemical Physics* **2010**, *12*, 1453.
- (220) Maas, M. G.; Rodijk, E. J. B.; Maijenburg, A. W.; Blank, D. H. A.; ten Elshof, J. E. Microstructure development in zinc oxide nanowires and iron oxohydroxide nanotubes by cathodic electrodeposition in nanopores. *Journal of Materials Research* **2011**, *26*, 2261.
- (221) Tsai, C. Y.; Chang, T. L.; Chen, C. C.; Ko, F. H.; Chen, P. H. An ultra sensitive DNA detection by using gold nanoparticle multilayer in nano-gap electrodes. *Microelectronic Engineering* **2005**, 78-79, 546.
- (222) Marx, S.; Jose, M. V.; Andersen, J. D.; Russell, A. J. Electrospun gold nanofiber electrodes for biosensors. *Biosensors & Bioelectronics* **2011**, *26*, 2981.
- (223) Chen, L. Y.; Lang, X. Y.; Fujita, T.; Chen, M. W. Nanoporous gold for enzyme-free electrochemical glucose sensors. *Scripta Materialia* **2011**, *65*, 17.
- (224) Jia, F. L.; Yu, C. F.; Gong, J. M.; Zhang, L. Z. Deposition of Prussian blue on nanoporous gold film electrode and its electrocatalytic reduction of H₂O₂. *Journal of Solid State Electrochemistry* **2008**, *12*, 1567.
- (225) Jia, F. L.; Yu, C. F.; Ai, Z. H.; Zhang, L. Z. Fabrication of nanoporous gold film electrodes with ultrahigh surface area and electrochemical activity. *Chemistry of Materials* **2007**, *19*, 3648.
- (226) Nakanishi, H.; Grzybowski, B. A. Supercapacitors based on metal electrodes prepared from nanoparticle mixtures at room temperature. *Journal of Physical Chemistry Letters* **2010**, *1*, 1428.
- (227) Szamocki, R.; Reculosa, S.; Ravaine, S.; Bartlett, P. N.; Kuhn, A.; Hempelmann, R. Tailored mesostructuring and biofunctionalization of gold for increased electroactivity. *Angewandte Chemie-International Edition* **2006**, *45*, 1317.
- (228) Bartlett, P. N.; Dunford, T.; Ghanem, M. A. Templated electrochemical deposition of nanostructured macroporous PbO₂. *Journal of Materials Chemistry* **2002**, *12*, 3130.
- (229) Szamocki, R.; Velichko, A.; Muecklich, F.; Reculosa, S.; Ravaine, S.; Neugebauer, S.; Schuhmann, W.; Hempelmann, R.; Kuhn, A. Improved enzyme

immobilization for enhanced bioelectrocatalytic activity of porous electrodes. *Electrochemistry Communications* **2007**, *9*, 2121.

(230) Sun, F. Q.; Cai, W. P.; Li, Y.; Cao, B. Q.; Lu, F.; Duan, G. T.; Zhang, L. D. Morphology control and transferability of ordered through-pore arrays based on electrodeposition and colloidal monolayers. *Advanced Materials* **2004**, *16*, 1116.

(231) Lu, Z. X.; Namboodiri, A.; Collinson, M. M. Self-supporting nanopore membranes with controlled pore size and shape. *ACS Nano* **2008**, *2*, 993.

(232) He, A.; Liu, Q.; Ivey, D. G. Electroplating of gold from a solution containing tri-ammonium citrate and sodium sulphite. *Journal of Materials Science-Materials in Electronics* **2009**, *20*, 543.

(233) Fischer, L. M.; Tenje, M.; Heiskanen, A. R.; Masuda, N.; Castillo, J.; Bentien, A.; Emneus, J.; Jakobsen, M. H.; Boisen, A. Gold cleaning methods for electrochemical detection applications. *Microelectronic Engineering* **2009**, *86*, 1282.

(234) Trasatti, S.; Petrii, O. A. Real Surface-area Measurements in Electrochemistry. *Pure and Applied Chemistry* **1991**, *63*, 711.

(235) TremiliosiFilho, G.; DallAntonia, L. H.; Jerkiewicz, G. Limit to extent of formation of the quasi-two-dimensional oxide state on Au electrodes. *Journal of Electroanalytical Chemistry* **1997**, *422*, 149.

(236) Szamocki, R.; Velichko, A.; Holzapfel, C.; Mucklich, F.; Ravaine, S.; Garrigue, P.; Sojic, N.; Hempelmann, R.; Kuhn, A. Macroporous ultramicroelectrodes for improved electroanalytical measurements. *Analytical Chemistry* **2007**, *79*, 533.

(237) Wang, J. B.; Luck, L. A.; Suni, II Immobilization of the glucose-galactose receptor protein onto a Au electrode through a genetically engineered cysteine residue. *Electrochemical and Solid State Letters* **2007**, *10*, J33.

(238) Ram íez, N., Regueiro, A., Arias, O, and Contreras R. Electrochemical impedance spectroscopy: An effective tool for a fast microbiological diagnosis. *Bioteconlog í Aplicada* **2009**.

(239) Xiang, D. B.; Gao, G. Y.; Shao, H. B.; Li, H. L.; Zhang, H. L.; Yu, H. Z. Redox Behavior and Ion-Pairing Thermodynamics of Ferrocene and Its Derivatives in the Organic Phase. *Journal of Physical Chemistry C* **2010**, *114*, 617.

(240) Takeda, N.; Stawasz, M. E.; Parkinson, B. A. Electrochemical oxidation and ex-situ STM observations of bis(4-dimethylamino-2-dihydroxyphenyl)squaraine dye layers on HOPG electrodes. *Journal of Electroanalytical Chemistry* **2001**, *498*, 19.

(241) Johannes G. V., R. J. F., T á E. K. *Interfacial supramolecular assemblies*; John Wiley & Sons Ltd: The Atrium, Southern Gate, Chichester, West Sussex PO19 8SQ, England, 2003.

(242) Xiao, C.; Chu, X.; Wu, B.; Pang, H.; Zhang, X.; Chen, J. Polymerized ionic liquid-wrapped carbon nanotubes: The promising composites for direct electrochemistry and biosensing of redox protein. *Talanta* **2010**, *80*, 1719.

(243) Liu, J.; Guo, C.; Li, C. M.; Li, Y.; Chi, Q.; Huang, X.; Liao, L.; Yu, T. Carbon-decorated ZnO nanowire array: A novel platform for direct electrochemistry of enzymes and biosensing applications. *Electrochemistry Communications* **2009**, *11*, 202.

(244) Bianco, P.; Haladjian, J. Recent progress in the Electrochemistry of C-type Cytochromes. *Biochimie* **1994**, *76*, 605.

- (245) Guo, C.; Hu, F.; Li, C. M.; Shen, P. K. Direct electrochemistry of hemoglobin on carbonized titania nanotubes and its application in a sensitive reagentless hydrogen peroxide biosensor. *Biosensors & Bioelectronics* **2008**, *24*, 819.
- (246) Xie, J.; Feng, X.; Hu, J.; Chen, X.; Li, A. Al(3+)-directed self-assembly and their electrochemistry properties of three-dimensional dendriform horseradish peroxidase/polyacrylamide/platinum/single-walled carbon nanotube composite film. *Biosensors & Bioelectronics* **2010**, *25*, 1186.
- (247) Deng, S.; Jian, G.; Lei, J.; Hu, Z.; Ju, H. A glucose biosensor based on direct electrochemistry of glucose oxidase immobilized on nitrogen-doped carbon nanotubes. *Biosensors & Bioelectronics* **2009**, *25*, 373.
- (248) Vamvakaki, V.; Hatzimarinaki, M.; Chaniotakis, N. Bionumetically synthesized silica-carbon nanofiber architectures for the development of highly stable electrochemical biosensor systems. *Analytical Chemistry* **2008**, *80*, 5970.
- (249) Hill, H. A. O.; Page, D. J.; Walton, N. J.; Whitford, D. Direct electrochemistry at modified gold electrodes of redox proteins having negatively-charged binding domains-spinach plastocyanin and a multi-substituted carboxydinitriphenyl derivative of horse heart cytochrome-c. *Journal of Electroanalytical Chemistry* **1985**, *187*, 315.
- (250) Allen, H.; Hill, O.; Hunt, N. I.; Bond, A. M. The transient nature of the diffusion controlled component of the electrochemistry of cytochrome c at 'bare' gold electrodes: an explanation based on a self-blocking mechanism. *Journal of Electroanalytical Chemistry* **1997**, *436*, 17.
- (251) Xu, Q.; Mao, C.; Liu, N. N.; Zhu, J. J.; Sheng, J. Direct electrochemistry of horseradish peroxidase based on biocompatible carboxymethyl chitosan-gold nanoparticle nanocomposite. *Biosensors & Bioelectronics* **2006**, *22*, 768.
- (252) Wang, L.; Wang, E. K. Direct electron transfer between cytochrome c and a gold nanoparticles modified electrode. *Electrochemistry Communications* **2004**, *6*, 49.
- (253) Caruso, F.; Caruso, R. A.; Mohwald, H. Production of hollow microspheres from nanostructured composite particles. *Chem. Mater.* **1999**, *11*, 3309.
- (254) Imhof, A. Preparation and characterization of titania-coated polystyrene spheres and hollow titania shells. *Langmuir* **2001**, *17*, 3579.
- (255) Tissot, I.; Reymond, J. P.; Lefebvre, F.; Bourgeat-Lami, E. SiOH-functionalized polystyrene latexes. A step toward the synthesis of hollow silica nanoparticles. *Chem. Mater.* **2002**, *14*, 1325.
- (256) Chen, M.; Wu, L. M.; Zhou, S. X.; You, B. A method for the fabrication of monodisperse hollow silica spheres. *Adv. Mater.* **2006**, *18*, 801.
- (257) Lou, X. W.; Archer, L. A.; Yang, Z. C. Hollow Micro-/Nanostructures: Synthesis and Applications. *Advanced Materials* **2008**, *20*, 3987.
- (258) Yamauchi, Y.; Suzuki, N.; Radhakrishnan, L.; Wang, L. Breakthrough and future: nanoscale controls of compositions, morphologies, and mesochannel orientations toward advanced mesoporous materials. *Chemical Record* **2009**, *9*, 321.
- (259) Fowler, C. E.; Khushalani, D.; Mann, S. Interfacial synthesis of hollow microspheres of mesostructured silica. *Chem. Commun.* **2001**, 2028.
- (260) Im, S. H.; Jeong, U. Y.; Xia, Y. N. Polymer hollow particles with

- controllable holes in their surfaces. *Nat. Mater.* **2005**, *4*, 671.
- (261) Lim, Y. T.; Kim, J. K.; Noh, Y. W.; Cho, M. Y.; Chung, B. H. Multifunctional Silica Nanocapsule with a Single Surface Hole. *Small* **2009**, *5*, 324.
- (262) Guan, G. J.; Zhang, Z. P.; Wang, Z. Y.; Liu, B. H.; Gao, D. M.; Xie, C. G. Single-hole hollow polymer microspheres toward specific high-capacity uptake of target species. *Adv. Mater.* **2007**, *19*, 2370.
- (263) Han, J.; Song, G. P.; Guo, R. Synthesis of polymer hollow spheres with holes in their surfaces. *Chem. Mater.* **2007**, *19*, 973.
- (264) Li, M.; Xue, J. M. Facile Route to Synthesize Polyurethane Hollow Microspheres with Size-Tunable Single Holes. *Langmuir* **2011**, *27*, 3229.
- (265) Chang, M. W.; Stride, E.; Edirisinghe, M. A New Method for the Preparation of Monoporous Hollow Microspheres. *Langmuir* **2010**, *26*, 5115.
- (266) He, X. D.; Ge, X. W.; Liu, H. R.; Wang, M. Z.; Zhang, Z. C. Synthesis of cage-like polymer microspheres with hollow core/porous shell structures by self-assembly of latex particles at the emulsion droplet interface. *Chem. Mater.* **2005**, *17*, 5891.
- (267) Shiomi, T.; Tsunoda, T.; Kawai, A.; Mizukami, F.; Sakaguchi, K. Formation of cage-like hollow spherical silica via a mesoporous structure by calcination of lysozyme-silica hybrid particles. *Chem. Commun.* **2007**, 4404.
- (268) Li, L.; Ding, J.; Xue, J. M. Macroporous Silica Hollow Microspheres as Nanoparticle Collectors. *Chem. Mater.* **2009**, *21*, 3629.
- (269) Lavergne, F. M.; Cot, D.; Ganachaud, F. Polymer microcapsules with "foamed" membranes. *Langmuir* **2007**, *23*, 6744.
- (270) Chen, Y. L.; Li, Y.; Chen, Y. X.; Liu, X. J.; Zhang, M.; Li, B. Z.; Yang, Y. G. Preparation of hollow silica spheres with holes on the shells. *Chem. Commun.* **2009**, 5177.
- (271) Shaw, R. S.; Packard, N.; Schroter, M.; Swinney, H. L. Geometry-induced asymmetric diffusion. *Proc. Natl. Acad. Sci.* **2007**, *104*, 9580.
- (272) Kanungo, M.; Deepa, P. N.; Collinson, M. M. Template Directed Formation of Hemispherical Cavities of Varying Depth and Diameter in a Silicate Matrix Prepared by the Sol-Gel Process. *Chem. Mater.* **2004**, *16*, 5535.
- (273) Khramov, A. N.; Munos, J.; Collinson, M. M. Preparation and Characterization of Macroporous Silicate Films. *Langmuir* **2001**, *17*, 8112.
- (274) Shaw, R. S. P., N.; Schroter, M. and Swinney, H. L. Geometry-induced asymmetric diffusion. *Proceedings of the National Academy of Science* **2007**, *104*, 9580.
- (275) Tong, W. J.; Gao, C. Y. Layer-by-layer assembled microcapsules: Fabrication, stimuli-responsivity, loading and release. *Chemical Journal of Chinese Universities-Chinese* **2008**, *29*, 1285.
- (276) Johnston, A. P. R.; Cortez, C.; Angelatos, A. S.; Caruso, F. Layer-by-layer engineered capsules and their applications. *Current Opinion in Colloid & Interface Science* **2006**, *11*, 203.
- (277) Venables, J. A.; Spiller, G. D. T.; Hanbucken, M. Nucleation and growth of thin-films. *Reports on Progress in Physics* **1984**, *47*, 399.
- (278) Tang, Z. Y.; Wang, Y.; Podsiadlo, P.; Kotov, N. A. Biomedical applications of layer-by-layer assembly: From biomimetics to tissue engineering. *Advanced Materials*

2006, *18*, 3203.

(279) Galajda, P.; Keymer, J.; Chaikin, P.; Austin, R. A wall of funnels concentrates swimming bacteria. *J. Bacteriol.* **2007**, *189*, 8704.

(280) Fan, H. J.; Gosele, U.; Zacharias, M. Formation of nanotubes and hollow nanoparticles based on Kirkendall and diffusion processes: A review. *Small* **2007**, *3*, 1660.

(281) Zhao, W. R.; Lang, M. D.; Li, Y. S.; Li, L.; Shi, J. L. Fabrication of uniform hollow mesoporous silica spheres and ellipsoids of tunable size through a facile hard-templating route. *Journal of Materials Chemistry* **2009**, *19*, 2778.

VITA

EDUCATION:

08/07---present: Department of Chemistry, Virginia Commonwealth University

Degree Sought: PhD (GPA : 3.72)

Ph.D. Advisor: Maryanne M. Collinson, Professor of Chemistry

09/04---07/07: Changchun Institute of Applied Chemistry, Chinese Academy of Sciences

Degree: Master (GPA: 3.17)

09/00—07/04: Department. of Chemistry, Northeast Normal University (NENU)

Degree: Bachelor of Science (GPA: 3.68)

HONORS AND AWARDS:

Albert T. Sneden III Scholarship

Philip Morris Summer Research Awards 2008

Altria academic year fellowship 2010-2011

Honor: First-class Scholarship for two academic years in NENU (Top10%/140),

Headmaster Scholarship for one academic year in NENU (Top4%/140),

Excellent Student Title for three academic years in NENU (Top10%/140)

Award in teaching skill contest in NENU

WORK EXPERIENCE

Research assistant:

06/2008-12/2008, 08/2009-08/2011 at Virginia Commonwealth University

08/2005-06/2007 at Changchun Institute of Applied Chemistry CAS

Teaching assistant:

08/2007-05/2008, 01/2009-08/2009, 08/2011-12/2011 at Virginia Commonwealth University

CONFERENCE

1. 87th Annual Meeting Virginia Academy of Science May 27-29, 2009, Size tunable hierarchical porous structures by direct templating (oral presentation).
2. ACS 238 National meeting in Washington D.C., 8-20-2009, Size tunable hierarchical templates for bimodal porous material fabrication (oral presentation).
3. Pittcon Conference & Exhibition, March 10th, 2011, Atlanta, Template-directed fabrication of well-defined hierarchical porous gold film for electrochemical applications (poster presentation).

PUBLICATIONS:

1. **Bo Zhao**, Maryanne M. Collinson, The slow passivation process of hierarchical porous gold electrodes in presence of bovine serum albumin (in preparation).
2. **Bo Zhao** and Maryanne M. Collinson, Fabrication of hierarchical porous gold

electrodes and their electrochemical properties (submitted to Journal of Electroanalytical Chemistry).

2. **Bo Zhao**, Maryanne M. Collinson, Hollow silica capsules with well defined asymmetric pores in the shell (Submitted to Langmuir).

3. **Bo Zhao**, Maryanne M. Collinson, Well-Defined Hierarchical Templates for Multimodal Porous Material Fabrication. *Chemistry of Materials* **2010**, 22(14), 4312-4319.

4. Cuikun Lin, **Bo Zhao**, Zhengling Wang, Min Yu, Huan Wang, Deyan Kong, Jun Lin Spherical SiO₂@GdPO₄:Eu³⁺ Core-Shell Phosphors: Sol-Gel Synthesis and Characterization *J. Nanosci. Nanotech.* 7(2), **2007**, 542.

5. **B. Zhao**, C.J. Zhu, X.F. Ma, W. Zhao, H.G. Tang, S.G. Cai, Z.H. Qiao, High strength Ni based composite reinforced by solid solution W(Al) obtained by powder metallurgy, *Materials Science & Engineering A* 456 (**2007**) 337-344.